HAL
open science

Dark Matter Indirect Detection with charged cosmic rays

Gaelle Giesen

To cite this version:

Gaelle Giesen. Dark Matter Indirect Detection with charged cosmic rays. High Energy Astrophysical Phenomena [astro-ph.HE]. Université Paris Sud - Paris XI, 2015. English. NNT : 2015PA112160 . tel-01246170

HAL Id: tel-01246170

https://theses.hal.science/tel-01246170v1

Submitted on 11 Jan 2016

HAL is a multi-disciplinary open access archive for the deposit and dissemination of scientific research documents, whether they are published or not. The documents may come from teaching and research institutions in France or abroad, or from public or private research centers.

L'archive ouverte pluridisciplinaire **HAL**, est destinée au dépôt et à la diffusion de documents scientifiques de niveau recherche, publiés ou non, émanant des établissements d'enseignement et de recherche français ou étrangers, des laboratoires publics ou privés.

Université Paris-Sud

Ecole Doctorale Physique en Île-de-France (ED 564)
Institut de Physique Théorique - CNRS & CEA/Saclay

Discipline : Physique

Thèse de doctorat

Soutenue le 25 Septembre 2015 par

Gaëlle Giesen

Dark Matter Indirect Detection with charged cosmic rays

Directeur de thèse :	M. Marco Cirelli	Chercheur CNRS CR1 (IPhT - CNRS & CEA/Saclay)
Composition du jury :		
Rapporteurs :	M. Julien Lavalle	Chercheur CNRS CR1 (LUP Montpelier)
	M. Nicolao Fornengo	Professeur associé (Università di Torino)
Examinateurs :	Mme Asmaa Abada	Professeur des universités (LPT-Orsay)
	M. Marco Incagli	Chercheur INFN (INFN Pisa)
	Mme Genevieve Bélanger	Chercheuse CNRS DR1 (LAPTH Annecy-le-Vieux)

Contents

1 Dark Matter: hints, constraints and models **6**
1.1 Dark Matter and Astrophysics . . . 6
1.1.1 Coma Cluster . . . 6
1.1.2 Galaxy rotation curves . . . 8
1.1.3 Halo models . . . 9
1.1.4 Bullet Cluster . . . 10
1.1.5 Massive Astrophysical Compact Halo Objects (MACHOs) . . . 11
1.2 Dark Matter and Cosmology . . . 12
1.2.1 Cosmic Microwave Background Radiation . . . 16
1.2.2 Big Bang Nucleosynthesis (BBN) . . . 18
1.2.3 Structure formation . . . 20
1.2.4 Baryon acoustic oscillation (BAO) . . . 23
1.2.5 WIMP miracle . . . 23
1.3 Dark Matter and Particle Physics . . . 26
1.3.1 Sterile neutrinos . . . 28
1.3.2 Axions . . . 30
1.3.3 Supersymmetric candidates . . . 31
1.3.4 Particles from extra dimensions . . . 33
1.3.5 Wimpzillas . . . 34
1.3.6 Primordial black holes . . . 34
1.3.7 Other candidates . . . 36
1.4 Searches for WIMPs . . . 36
1.4.1 Direct detection of dark matter . . . 37
1.4.2 Collider searches of dark matter . . . 42
1.4.3 Indirect detection of dark matter . . . 44

2 Cosmic Rays: origin and propagation **52**
2.1 Introduction . . . 52
2.2 Potential CR sources . . . 54
2.2.1 Primary source: SuperNova explosions . . . 55
2.2.2 Secondary source: spallation . . . 56
2.2.3 Ultrahigh energy CR . . . 56
2.3 Acceleration mechanisms . . . 57
2.3.1 Second-order Fermi acceleration . . . 58
2.3.2 First order Fermi acceleration . . . 59
2.4 Derivation of the transport equation in the diffusion approximation . . . 61
2.4.1 Momentum space diffusion . . . 61

2.4.2 Pitch angle scattering . . . 63
2.4.3 Convection and diffusion . . . 64
2.4.4 Full transport equation . . . 66
2.4.5 Experimental determination of the diffusion parameters . . . 69
2.5 Solar modulation . . . 71
2.5.1 Effects of CR in the heliosphere . . . 72
2.5.2 Force-field approximation . . . 75
2.6 CR Experiments . . . 77
2.6.1 PAMELA . . . 77
2.6.2 AMS-02 . . . 78
2.6.3 Fermi . . . 79
2.7 What about DM? . . . 80

3 DM indirect detection with antiprotons 81
3.1 Introduction . . . 81
3.2 Injection spectrum . . . 82
3.3 First analysis of PAMELA data- Original PPPC4DMID . . . 83
3.3.1 Primaries . . . 83
3.3.2 Astrophysical sources: secondaries . . . 84
3.3.3 Antiproton constraints from PAMELA ($K > 10$ GeV) . . . 85
3.3.4 Projected sensitivity of AMS-02 . . . 88
3.4 Including ELDR - Improved PPPC4DMID . . . 96
3.4.1 Antiproton propagation in the Galaxy . . . 96
3.4.2 Constraints using PAMELA 2012 data . . . 104
3.4.3 Sensitivity of AMS-02 . . . 107
3.5 AMS-02 Antiprotons: Secondary astrophysical component and immediate implications for DM . . . 109
3.5.1 Re-evaluation of the astrophysical antiproton background . . . 110
3.5.2 Updated constraints on Dark Matter . . . 115
3.6 Final comments . . . 117

4 Secondary photon emission from DM annihilations into electrons and positrons 118
4.1 Introduction . . . 118
4.2 Astrophysical configurations . . . 119
4.2.1 Galactic Magnetic Field . . . 119
4.2.2 Other astrophysical ingredients . . . 120
4.3 Technical outputs . . . 122
4.3.1 An improved energy loss function for $e^{\pm}$ in the Galaxy . . . 122
4.3.2 Revised halo functions for $e^{\pm}$ in the Galaxy . . . 126
4.3.3 Synchrotron halo functions . . . 129
4.3.4 Bremsstrahlung halo functions . . . 133
4.4 Summary . . . 137

5 The Galactic Center excess: charged particles at their best **138**
5.1 Introduction . . . 138
5.2 Dark Matter and Cosmic Rays: setups and tools . . . 140
5.2.1 DM Galactic distribution and DM gamma-ray flux . . . 140
5.2.2 Charged cosmic rays propagation . . . 141
5.3 Fits of the gamma-rays from DM annihilation in the GC . . . 142
5.4 Antiproton bound on $b\bar{b}$ final state . . . 146
5.5 Final comments . . . 150

6 Conclusion and discussion **151**

Appendix **155**

Foreword

This thesis work deals with the subject of Dark Matter indirect searches using charged cosmic rays, in particular antiprotons, electrons and positions and their emissions. The majority of this work has been accomplished at the Institut de Physique Théorique (IPhT) at CEA Saclay and certain parts have also been done at the Institut d'Astrophysique de Paris (IAP).

First, I would like to take the opportunity to acknowledge the contributions of certain people who have been essential for the completion of this work, directly or indirectly. I would like to thank my PhD supervisor, Marco Cirelli, for teaching me the ways of doing research, leaving space for my ideas and mistakes, while guiding me when I was lost. I would also like show my appreciation for the support of my family, especially my parents, Solange and Klaus. I would also like to thank Eric for standing by my side during good times and in stressful moments. Finally, I would like to thank my collaborators from which I learned so much: Marco Taoso, Pierre Salati, Mathieu Boudaud, Daniele Gaggero, Alfredo Urbano, Pasquale Serpico, etc...

This thesis work is structured as follows: in chapter 1, we introduce the topic of Dark Matter, the evidence for its existences in astrophysics and cosmology as well as candidates in particle physics models. Then, we turn to cosmic rays in chapter 2, where we investigate their origin and their propagation in our Galaxy. In chapter 3, we study cosmic ray antiprotons as probe for Dark Matter annihilation and decay. In chapter 4, we focus on the secondary emissions of electrons and positions from Dark Matter annihilation and decay before analyzing the Galactic Center excess in chapter 5. Finally, we conclude and discuss our results in chapter 6.

Chapter 1

Dark Matter: hints, constraints and models

At the end of the 19th century, physicists believed they had globally understood the laws covering the universe. Only two "small" problems were unresolved: the radiation of a black body and the constance of the speed of light (independent of the direction and the velocity of the source). Explaining these two phenomena led physicists to formulate the theories of quantum mechanics and special relativity, and later quantum field theory and general relativity, the two theories on which modern physics is based. Today, a lot of other mysteries in physics remain unsolved. In cosmology, for example, we can find the cosmological constant problem, the baryon asymmetry or the cosmic inflation problem. In particle physics, the Standard Model (SM) has an enormous success, especially since the discovery of the Higgs boson, the last theoretically predicted particle. However, the SM has deficiencies, such as the strong CP problem, the hierarchy problem or the existence of magnetic monopoles. In astrophysics, the origin of γ-ray bursts is unknown, as well as the mechanism of supernova explosions or the formation of 10^9 solar masses supermassive black holes at distant quasars. The nature of Dark Matter (DM) is another mystery at the interface between astrophysics, cosmology and particle physics and may be connected to other unresolved issues. Its discovery may hopefully lead us to new fields of physics.

1.1 Dark Matter and Astrophysics

Historically, the first evidences for the existence of DM begins with the study of dynamical systems, such as galaxy clusters and galaxies themselves.

1.1.1 Coma Cluster

The first strong indication for Dark Matter (or Dunkle Materie in German) has been discovered by Fritz Zwicky in 1933, while he was studying the dynamics of the Coma cluster [1]. In fact, the dynamical equations of this system could not be explained by the visible matter (stars, gas clouds, etc...) only. He applied the virial theorem to estimate the velocity due to the luminous mass and confronted it to the measurements using redshift distortion.

The virial theorem can be easily deduced by Newton's second law: In a system of N particles with mass m_i and located at $\vec{r}_i$ from the center of mass of the system, the total force $\vec{F}_i$ is

$$\vec{F}_i = m_i \frac{d^2\vec{r}_i}{dt^2}. \tag{1.1}$$

Multiplying by $\vec{r}_i$, one gets

$$\vec{r}_i \cdot \vec{F}_i = m_i \vec{r}_i \cdot \frac{d^2\vec{r}_i}{dt^2} = \frac{1}{2}\frac{d^2}{dt^2}\left(m_i \vec{r}_i^2\right) - m_i \left(\frac{d\vec{r}_i}{dt}\right)^2. \tag{1.2}$$

Now, we sum over all masses and average over time

$$\overline{\sum_i \vec{r}_i \cdot \vec{F}_i} = \frac{1}{2}\overline{\frac{d^2}{dt^2}\left(m_i \vec{r}_i^2\right)} - \overline{m_i \left(\frac{d\vec{r}_i}{dt}\right)^2}. \tag{1.3}$$

If the mass distribution has reached equilibrium, then $\overline{\frac{d}{dt}\left(m_i \vec{r}_i^2\right)} = 0$ and thus we obtain the virial theorem

$$\overline{\sum_i \frac{1}{2}\vec{r}_i \cdot \vec{F}_i} = \frac{1}{2}\overline{m_i v_i^2}, \tag{1.4}$$

where v_i is the velocity of the mass i. The right term represents the total kinetic energy of the system and the left hand side the total potential energy. In a spherically symmetric system with only the gravitational force acting, as it is the case for clusters, the force can be further written as

$$\sum_i \vec{F}_i \cdot \vec{r}_i = \sum_i \left(\sum_{j\neq i} \vec{F}_{ji}\right) \cdot \vec{r}_i = \sum_i \left(\sum_{j<i} \vec{F}_{ji}\right) \cdot (\vec{r}_i - \vec{r}_j) = -\sum_i \sum_{j<i} \left(\frac{G m_i m_j}{(\vec{r}_i - \vec{r}_j)^3}\right) \cdot (\vec{r}_i - \vec{r}_j). \tag{1.5}$$

The time average becomes

$$\overline{\sum_i m_i v_i^2} = \overline{\sum_i \sum_{j<i} \frac{G m_j m_i}{\vec{r}_i - \vec{r}_j}}. \tag{1.6}$$

The time and mass averaged squared velocity of the system can then be expressed as

$$\overline{\langle v^2 \rangle} = \frac{GM}{R}, \tag{1.7}$$

where R is the radius of the system. For example, the Coma cluster has a radius of $R = 10^{24}$ cm and consists of 800 galaxies, each with a mass of 10^9 solar masses ($M_\odot$). Zwicky computed the averaged velocity due to the luminous matter only and found

$$\sqrt{\overline{\langle v^2 \rangle}} = 80 \text{ km/s}. \tag{1.8}$$

However, using redshift distortion, the measured velocities turned out to be much larger, at least 1000-2000 km/s. To explain this discrepancy, Zwicky assumed the existence of a type of matter that would add to the total mass of the system without being seen through the telescope, i.e. DM. Clusters of Galaxies seam to be dominated by DM since $M_{cluster}/M_{vis} \simeq 6$. Surprisingly,after forty years, the paper describing these measurements *Die Rotverschiebung von extragalaktischen Nebeln* had only collected 10 citations. However, in 1980, new observations could be linked to these results, intriguing the scientific community.

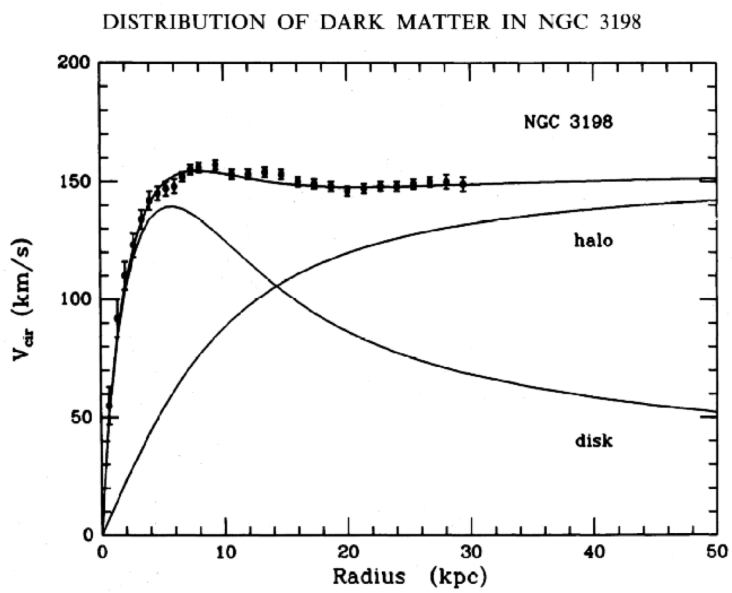

Figure 1.1: **Measurements of the rotation curve** of the galaxy NGC 3196 with the known disk and deduced halo component [3].

1.1.2 Galaxy rotation curves

In 1980, Vera Rubin, Kent Ford and Norbert Thonnard studied the dynamics of 21 galaxies within a wide range of luminosities, masses and optical radii ($L \in 3 \times 10^9 - 2 \times 10^{11}$ solar luminosities ($L_\odot$), $M \in 1 \times 10^{10} - 2 \times 10^{12} M_\odot$ and $R \in 4 - 122$ kpc) [2]. The rotation curves of these galaxies were obtained by measuring emission lines from hydrogen (Hα), nitrogen (NII) and sulfur (SII), elements in low-density gases and plasmas. The circular velocity V_c at a distance R from the center of the galaxy is related to the inclosed mass $M(r < R)$ in the following way, using Newton's law:

$$V_c = \sqrt{\frac{GM(r < R)}{R}}. \tag{1.9}$$

Thus, inside the galaxy, if the mass density $\rho(\vec{r})$ is constant and spherically symmetric (which is the case for the bulge), the enclosed mass is

$$M(r < R) = \int_V \rho(\vec{r}) dV = \rho_0 R^3. \tag{1.10}$$

And the circular velocity increases with the radius $V_c(R) \sim R$. Outside the visible part of the galaxy, we expect the circular velocity to decrease as $V_c(R) \sim R^{-1/2}$. However Rubin, Ford and Thonnard measured that the velocity was staying approximately constant, even beyond the optical edge of the galaxy. None of the galaxies had a falling rotation curve. A typical rotation curve is the one of the galaxy NGC 3198, studied in [3], and shown in figure 1.1. This rotation curve has been obtained by analyzing 21cm emission lines from hydrogen. The visible matter only extends up to 10 kpc, but the roration curve continues to be flat up to 30 kpc. The dynamics can not be explained by visible matter only. An exotic contribution has to be added to make sense of the circular velocities at the edge of the galaxy, DM dominates also in galaxies $M_{gal}/M_{visi} > 4$. This led to the idea that Dark Matter forms a giant halo in which the Galaxy disc in bathing in the middle.

1.1.3 Halo models

Today we believe that DM constitutes 70-80% of the mass of galaxies. Different types of density profiles for the halo have been proposed:

$$\begin{aligned}
\text{NFW}: \quad \rho_{\text{NFW}}(\mathbf{r}) &= \rho_s \frac{r_s}{\mathbf{r}} \left(1 + \frac{\mathbf{r}}{r_s}\right)^{-2} \\
\text{Einasto}: \quad \rho_{\text{Ein}}(\mathbf{r}) &= \rho_s \exp\left\{-\frac{2}{\alpha}\left[\left(\frac{\mathbf{r}}{r_s}\right)^{\alpha} - 1\right]\right\} \\
\text{Isothermal}: \quad \rho_{\text{Iso}}(\mathbf{r}) &= \frac{\rho_s}{1 + (\mathbf{r}/r_s)^2} \\
\text{Burkert}: \quad \rho_{\text{Bur}}(\mathbf{r}) &= \frac{\rho_s}{(1 + \mathbf{r}/r_s)(1 + (\mathbf{r}/r_s)^2)} \\
\text{Moore}: \quad \rho_{\text{Moo}}(\mathbf{r}) &= \rho_s \left(\frac{r_s}{\mathbf{r}}\right)^{1.16} \left(1 + \frac{\mathbf{r}}{r_s}\right)^{-1.84}.
\end{aligned} \tag{1.11}$$

Each of these halo profiles have different motivations, based on observations or simulations.

- The Navarro Frenk and White profile [4] was proposed to fit dark matter haloes in N-body simulations. Observations of the Milky Way and M31, the Andromeda galaxy, are compatible with the NFW profile. The mass inside a radius R can be easily computed:

$$M = \int_0^R 4\pi r^2 \rho(r) dr = 4\pi\rho_0 R^2 \left(\ln\left(\frac{R + r_s}{R}\right) - \frac{R}{R + r_s}\right). \tag{1.12}$$

- The Einasto profile [5, 6, 7] can also well reproduce the DM profiles in simulations. In addition, the density does not diverge at the center of the galaxy. EinastoB is a stepper profile, which has been introduced in [9] in order to simulate the effects baryons could have on the DM distribution [8]. The value of $\alpha = 0.11$ is motivated by numerical simulations.

- The isothermal profile is used in astrophysics to describe the density of gas clouds, but can also be used for DM density profile. Considering a perfect gas of DM in hydrostatical equilibrium with constant temperature, we start with Poisson's equation for r within the distribution

$$\nabla^2 \phi(r) = 4\pi G \rho(r). \tag{1.13}$$

  Assuming spherical symmetry,

$$\frac{1}{r^2}\frac{d}{dr}\left(r^2 \frac{d\phi(r)}{dr}\right) = 4\pi G\rho(r) \;\Rightarrow\; \frac{d\phi(r)}{dr} = \frac{4\pi G}{r^2}\int_0^r x^2 \rho(x) dx. \tag{1.14}$$

  In addition, the law of perfect gases gives us

$$P(r) = \frac{\rho(r) k_B T_0}{m_{\text{DM}}}, \tag{1.15}$$

  $P(r)$ is the pressure, k_B the Boltzmann constant and T_0 the temperature of the DM gas. And finally assuming hydrostatic equilibrium

$$\nabla P(r) = -\rho(r)\nabla\phi(r) \;\Rightarrow\; \frac{dP(r)}{dr} = -\rho(r)\frac{d\phi(r)}{dr}, \tag{1.16}$$

DM halo	DM halo parameters α	r_s [kpc]	ρ_s [GeV/cm^3]
NFW	–	24.42	0.184
Einasto	0.17	28.44	0.033
EinastoB	0.11	35.24	0.021
Isothermal	–	4.38	1.387
Burkert	–	12.67	0.712
Moore	–	30.28	0.105

Table 1.1: The **DM profile parameters** to be plugged in the functional forms of eq. (1.11).

still with spherical symmetry. Replacing $P(r)$ from equation 1.15 and $d\phi(r)/dr$ from equation 1.14, we get

$$\frac{k_B T_0}{m_{\rm DM}} \frac{d\rho(r)}{dr} = -\frac{4\pi G}{r^2} \int_0^r x^2 \rho(x) dx. \tag{1.17}$$

The solution to this equation is of the type $\rho(r) = A/r^2$.

- The Burkert profile [10] on the other hand reproduces very well the rotation curves of dwarf galaxies, which are known to be dominated by DM throughout. The Burkert profile is an empirical law that resembles a pseudo-isothermal halo.

- The Moore halo profile [11] has a steep asymptotic slope. When it was proposed, it fitted well simulations with both galactic and cluster-sized haloes and with higher precision than the original ones of Navarro Frenk and White. More recent simulations though show that this profile is too steep, but we will keep it as an extreme case in the following.

The parameters of these profiles are listed in table 1.1 and are shown in figure 1.2. For the Milky Way, these specific values are derived as discussed in [9]: Assuming that the density of DM at the location of the Sun $r_\odot = 8.33$ kpc is $\rho_\odot = 0.3$ GeV/cm^3 and the total amount of DM mass contained in 60 kpc is $M_{60} = 4.7 \times 10^{11} M_\odot$. Near the Galactic Center (GC), for $r \sim 10^{-3}$ kpc, the density of DM can change by one or two orders of magnitude depending on profile chosen. This will induce large uncertainties on potential signals from DM annihilation (and decay) in the galactic halo of the Milky Way. In fact, it is very difficult to measure directly the DM contribution of rotation curves inside the bulge of galaxies, since baryonic matter is very abundant at this location and DM is subdominant.

1.1.4 Bullet Cluster

All the effects discussed earlier could also be explained by theories of MOdified Newtonian Dynamics (MOND). As presented in [12], Newton's second law could be modified in such a way that for large accelerations, the classical Newton dynamics is restored, but for small accelerations, the circular velocity is constant. More precisely, $\vec{F} = m_g \vec{a}$ is replaced by

$$\vec{F} = m_g \mu \left(\frac{a}{a_0}\right) \vec{a} \;\; \text{with} \;\; \mu\left(\frac{a}{a_0} \gg 1\right) \simeq 1 \text{ and } \mu\left(\frac{a}{a_0} \ll 1\right) \simeq \frac{a}{a_0}. \tag{1.18}$$

This modified Newton law explains the flatness of rotation curves of galaxies at large distances from the center using only baryons and eliminates the need for DM. In fact, in the case of

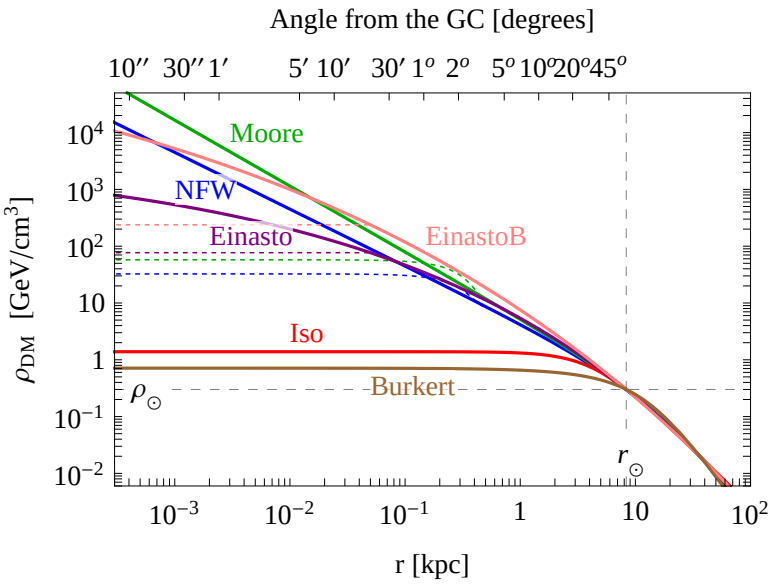

Figure 1.2: **Density of DM** as a function of the radial distance to the GC for different profiles (solid lines), as well as the modified inert part introduced in order simplify the treatment of very steep profiles in computations of the cosmic ray flux from DM annihilations and decays (dotted lines) [9]. .

gravitational systems, equation 1.18 simplifies to

$$\frac{GMm_g}{r^2} = m_g a_0 \left(\frac{v^2}{r}\right)^2 \Rightarrow v = \sqrt[4]{GM/a_0} \sim cst. \tag{1.19}$$

The relativistic generalization of MOND contains new fields that could be interpreted as DM, interacting gravitationally [13].

The best argument in favor of DM and against MOND is the Bullet Cluster, or the merging galaxy cluster 1E0657-56 [14]. Two clusterss collide, the baryons stay at the center while the gravitational potential has two lateral wells, as shown on figure 1.3. The visible matter, the hot gas detected by Chandra in X-rays and represented in pink, is interacting after the collision, while most of mass of the galaxies, observed through weak lensing in the optical images of the Hubble Space Telescope and couloured in blue, is passing through. In addition, from this system, one can deduce bounds on the self-interaction of DM [15]:

$$\sigma/m_{\rm DM} < 0.7 \text{ cm}^2/\text{g} = 1.3 \text{ barn/GeV}. \tag{1.20}$$

The Bullet Cluster is not the only example of merging galaxy clusters showing the properties of DM. The train wreck and the baby bullet are also examples, as shown in figure 1.4.

1.1.5 Massive Astrophysical Compact Halo Objects (MACHOs)

Massive Astrophysical Compact Halo Objects or MACHOs are small baryonic astrophysical objects drifting in the galaxy which emit almost no radiation and could play the role of DM. Candidates for MACHOs include black holes, neutron stars, white dwarfs, very faint red dwarfs, brown dwarfs or unassociated planets. They can be detected by gravitational microlensing of stars in near satellite galaxies and at the GC: when a MACHO crosses the line of sight of

Figure 1.3: **Optical picture by the Hubble Space Telescope of the Bullet Cluster**, where the hot gas (pink), detected by its X-ray emission, seems to be lagging behind the essential part of the mass of the cluster (blue), measured by gravitational lensing.

the star, it becomes brighter for a while, producing an anti-eclipse. Bounds on the mass of MACHOs have been computed in [16] and [17] using samples from the EROS-2 project (a MACHO dedicated project). MACHOs with masses

$$0.6 \times 10^{-7} M_\odot < M < 15 M_\odot \tag{1.21}$$

are ruled out as a major component of the Milky Way Halo, as seen on figure 1.5. In fact, there are not enough objects with masses $M > 10^{-7} M_\odot$ to explain DM. In the end, this means that the mass of one DM object has to be smaller than $m_{\rm DM} < 10^{-7} M_\odot \simeq 10^{50}$ GeV.

DM has been introduced in order to explain the behavior of gravitational systems in astrophysics, DM seams to dominate galaxies as well as clusters of galaxies. However, the nature of DM can not be determined by astrophysical objects.

1.2 Dark Matter and Cosmology

After the historical discoveries in astrophysics at galactic scales, DM also became essential on larger scales in cosmology. In fact, to explain our universe as a whole, DM is an important ingredient.

Reminder of General Relativity

General Relativity in the form of Einstein's equations relates space-time geometry and mass-energy density of the universe

$$G_{\mu\nu} = R_{\mu\nu} - \frac{1}{2} g_{\mu\nu} R = 8\pi G T_{\mu\nu} + \Lambda g_{\mu\nu}, \tag{1.22}$$

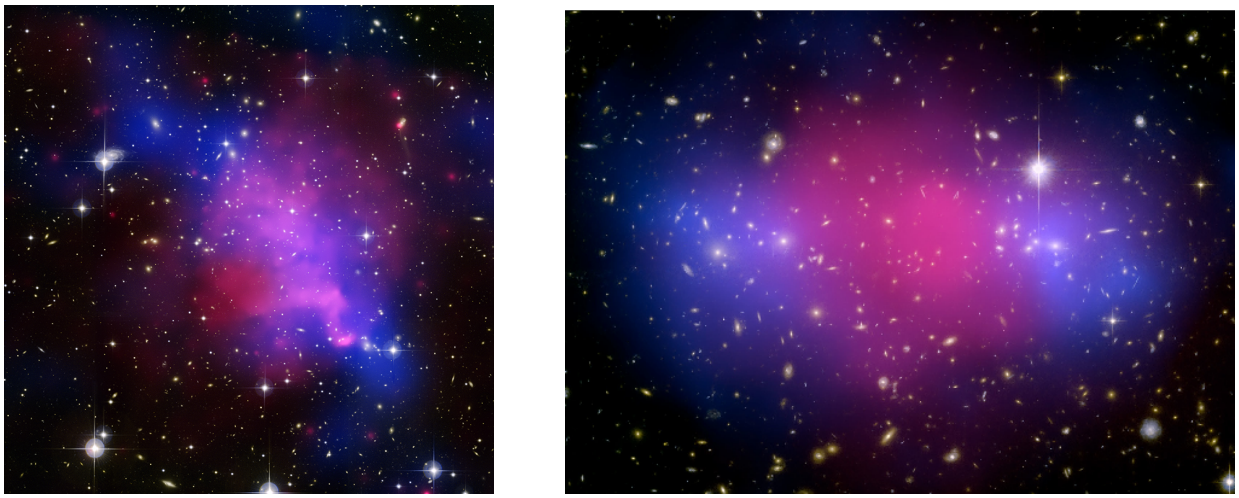

Figure 1.4: **Train Wreck** (left) and **Baby Bullet** (right), two other examples of merging cluster where the hot gas interacts in the middle while the DM has already passed through.

Λ is the cosmological constant, introduced by Einstein, which he later described as *the worst mistake of his life*, $g_{\mu\nu}$ is the metric tensor from which the curvature can be derived. The line element is

$$ds^2 = g_{\mu\nu}(x)dx^\mu dx^\nu. \tag{1.23}$$

$G_{\mu\nu}$ is a function of $g_{\mu\nu}$ and it's derivatives (through the Christoffel symbols, as detailed in the appendix) and contains all the information on the geometry of space-time. On the other hand, $T_{\mu\nu}$ is the energy-momentum tensor and is a function of all the matter fields. For a perfect fluid, which is a good description of cosmological substances, we can write:

$$T_{\mu\nu} = (\rho + p)U_\mu U_\nu + pg_{\mu\nu}, \tag{1.24}$$

where p is the pressure and ρ the density of the fluid. U^μ is the four velocity of the fluid.

Isotropic and homogeneous Friedmann-Robertson-Walker metric

Following the copernican principle which states that we are not in a special place in the universe and since the universe appears isotropic around us, we can assume that the universe is isotropic and homogeneous in every point. In practice this means that the line element can be written as

$$ds^2 = -dt^2 + a^2(t)dx^2 \tag{1.25}$$

and the metric as

$$dx^2 = \frac{1}{1 - kr^2} + r^2(d\theta^2 + \sin^2\theta d\phi^2), \tag{1.26}$$

where t is the proper time measured by a comoving (i.e. with constant spatial coordinate) observer, $a(t)$ the scale factor and k the curvature of the spatial section. The scale factor a is the same for all three directions in space and cannot depend on the position, since the universe is assumed to be isotropic an homogenous. It can thus only be a function of time. Concerning the curvature, for $k = 0$, the universe is flat, for $k = -1$ the universe is hyperbolic and for

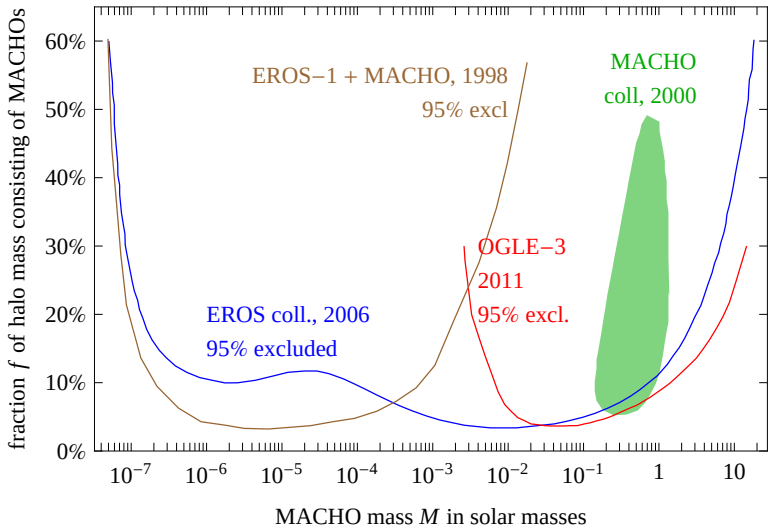

Figure 1.5: **Bounds on the fraction f of the Milky Way halo's mass which can consist of MACHOs** Results of microlensing surveys towards the Magellanic Clouds together with the region identified by the MACHO collaboration in 2000 [18].

$k = +1$ spherical. The Hubble parameter, also called Hubble constant, measures the expansion of the universe

$$H(t) = \frac{1}{a(t)}\frac{da(t)}{dt} = \frac{\dot{a}(t)}{a(t)}. \tag{1.27}$$

For this specific metric, the Einstein equations 1.22 becomes the Friedmann equations

$$\left(\frac{\dot{a}(t)}{a(t)}\right)^2 + \frac{k}{a^2(t)} - \frac{\Lambda}{3} = \frac{8\pi}{3}G\rho(t), \tag{1.28}$$

$$2\frac{\ddot{a}(t)}{a(t)} + \left(\frac{\dot{a}(t)}{a(t)}\right)^2 + \frac{k}{a^2(t)} - \Lambda = -8\pi G p(t), \tag{1.29}$$

where $\rho(t)$ is the energy density of the sum of all the matter, radiation, scalar field, etc.. contributions and p the pressure. They are related through the equation of state w

$$p(t) = w\rho(t). \tag{1.30}$$

For radiation the equation of state is $w = 1/3$, for matter $w = 0$ and for the cosmological constant $w = -1$. In fact, the energy density of the cosmological constant is then $\rho_\Lambda = -p_\Lambda = \frac{\Lambda}{8\pi G}$. On the other hand, the conservation of the energy-momentum tensor implies

$$\nabla^\mu T_{\mu\nu} = 0 \;\Rightarrow\; \dot{\rho}(t) + 3\left(\rho(t) + p(t)\right)\frac{\dot{a}(t)}{a(t)} = 0. \tag{1.31}$$

We recover Eulers continuity equation for a perfect fluid in curved space-time. Solving equations 1.28, 1.29 and 1.31 for each type of fluid (matter, radiation and cosmological constant) in a universe without curvature, we obtain the following behavior of the energy-density and the scale factor:

$$\rho(t) = \rho_0\left(\frac{a(t)}{a_0}\right)^{-3(1+w)} \qquad a(t) = a_0\left(\frac{t}{t_0}\right)^{\frac{2}{3(1+w)}}. \tag{1.32}$$

More particularly, in a matter dominated universe, the density decreases with the scale factor

$$\rho_M(t) = \rho_{0M}\left(\frac{a(t)}{a_0}\right)^{-3} = \frac{1}{6\pi G t^2}, \tag{1.33}$$

which is simply the dilution of volume due to the expansion of the universe or the first law of thermodynamics. For radiation,

$$\rho_R(t) = \rho_{0R}\left(\frac{a(t)}{a_0}\right)^{-4} = \frac{3}{32\pi G t^2}, \tag{1.34}$$

where we have the volume dilution and the redshift distortion which give the power $a(t)^{-4}$. Both $\rho_M(t)$ and $\rho_R(t)$ have a singularity at $t = 0$ which was the starting point for the elaboration of the Big Bang theory. And finally, for the cosmological constant, as the name already announces,

$$\rho_\Lambda(t) = \rho_{0\Lambda}. \tag{1.35}$$

Defining the critical density $\rho_c = \frac{3H(t_0)}{8\pi G}$, the abundances of matter, radiation and cosmological constant today $\Omega_i = \frac{\rho_i}{\rho_c}$, as well as $\Omega_k = \frac{k}{a^2(t_0)H^2(t_0)}$ the curvature abundance today, Friedmann's equation 1.28 at $t = t_0$ becomes

$$\Omega_\Lambda + \Omega_M + \Omega_R + \Omega_k = 1. \tag{1.36}$$

Thermodynamics of the universe

Another important ingredient in the understanding of cosmology is the kinetic theory in an expanding universe, i.e. Boltzmann equations. The number density of particles is defined by $n = g\int \frac{d^3p}{(2\pi)^3} f(\vec{p})$, where f is the probability to have a particle with momentum $\vec{p}$ and does not depend on the position $\vec{x}$ since the universe is supposed to be homogeneous and with g the number of spin states. The energy density is defined by $\rho = g\int \frac{d^3p}{(2\pi)^3} E f(\vec{p})$. For bosons and fermions, the distribution becomes

$$f(p) = \frac{1}{e^{\frac{E-\mu}{T}} \pm 1} \quad \text{with} \quad E = \sqrt{p^2 + m^2}, \tag{1.37}$$

μ is the chemical potential. For bosons, we use the minus sign (Bose-Einstein distribution) and for fermions the plus sign (Fermi-Dirac distribution). In the non-relativistic limit ($m \gg T$),

$$n \simeq g\left(\frac{m_x T}{2\pi}\right)^{3/2} e^{-\frac{m_x}{T}}, \tag{1.38}$$

for both bosons and fermions, and in the relativistic limit ($m \gg T$), for bosons

$$n^B \simeq \frac{\zeta(3)}{\pi^2} g_x T^3 \quad \text{and} \quad \rho^B \simeq \frac{\zeta(3)}{30} g_x T^4, \tag{1.39}$$

For fermions, we simply have $n^F = \frac{3}{4} n^B$ and $\rho^F = \frac{7}{8} n^B$. These added factors take into account Fermi blocking. In the primordial universe, at a certain temperature, certain species are relativistic ($m \ll T$) and other one which are more massive are not. In the non-relativistic case, if $\mu \ll T$, the energy density ρ decreases exponentially and thus at equilibrium the number of

non-relativistic particles is negligible with respect to the number of relativistic particles. Adding up all the contributions from relativistic bosons and fermions, the density in the primordial universe as a function of the temperature T is

$$\rho(T) = \frac{\pi^2}{30} g_*(T) T^4 \quad \text{with} \quad g_*(T) = \sum_{i=1}^{N_b} g_i \left(\frac{T_i^b}{T}\right)^4 + \frac{7}{8} \sum_{i=1}^{N_f} g_i \left(\frac{T_i^f}{T}\right)^4, \tag{1.40}$$

$g_*(T)$ accounts for the effective number of degree of freedom. At equilibrium all the temperatures are equal $T_1^b = T_2^b = .. = T_{N_b}^b = T_1^f = ... = T_{N_f}^f$. It is however possible that one species interacts to waekly (neutrinos for example) and quits thermal equilibrium and thus has a different temperature. The entropy can also be computed and for relativistic species is

$$s(T) = \frac{2\pi^2}{45} g_{*s} T^3 \quad \text{with} \quad g_*(T) = \sum_{i=1}^{N_b} g_i \left(\frac{T_i^b}{T}\right)^3 + \frac{7}{8} \sum_{i=1}^{N_f} g_i \left(\frac{T_i^f}{T}\right)^3. \tag{1.41}$$

The Boltzmann equation in an expanding universe and with a collision term I_{coll} is written as

$$\frac{\partial n}{\partial t} - H\vec{p}\frac{\partial n}{\partial \vec{p}} = I_{coll}. \tag{1.42}$$

In fact, the second term on the l.h.s of the equation represents the dilution by the expansion of the universe. Assuming that the collision term is zero at equilibrium and that the system tends to go to equilibrium, we define $N = \int d^3p\ n(p)$, and the Boltzmann equation becomes

$$\frac{\partial N}{\partial t} + 3HN = -\Gamma(N - N_{eq}), \tag{1.43}$$

N_{eq} is the equilibrium solution and Γ the interaction rate. There are two types of equilibrium:

- the kinetic equilibrium (or thermal equilibrium), characterized by the temperature T and where the particles exchange energy, the energy density being constant. A departure from kinetic equilibrium is called decoupling.
- the chemical equilibrium, characterized by the chemical potential, where the different species change number, but the number density stays constant. A departure from chemical equilibrium is called freeze-out.

The decoupling of one species with the thermal bath occurs when the interaction rate is larger than the expansion rate of the universe, i.e $\Gamma \sim H$.

1.2.1 Cosmic Microwave Background Radiation

After the Big Bang, our Universe expanded and cooled down. During this evolution, different particle species leave thermal equilibrium. Around $T \sim 3000$ K, when the universe was only 380,000 years old (redshift of $z = 1100$), photons decouple and form the Cosmic Microwave Background Radiation (CMBR). Since then the decoupled photons traveled almost freely through space and give us today useful information about the history of the universe and its composition. Today this radiation has a temperature of 2.725 K which corresponds to microwave frequencies and has been discovered by accident by Arno Penzias and Robert Wilson

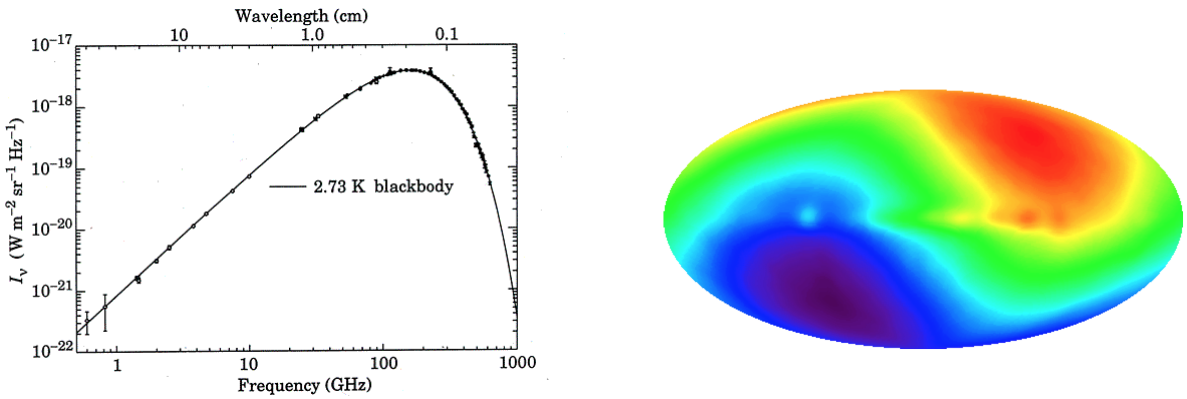

Figure 1.6: Left: **temperature measurement of the CMB** from COBE [23] with the spectrum of a blackbody at a temperature $T = 2.725$. Right: **dipole map of the CMB** from WMAP [24]. CMB maps represent the celestial sphere with a Mollweide projection, which conserves surfaces.

in 1964 [19] who were awarded with the Nobel price for this discovery in 1978. Until 1990, the CMBR had only been observed by antennas on Earth or ballons in the upper atmosphere (the Boomerang experiment). Then, the satellite COBE (COsmic Background Explorer) [20] was put into orbit with an angular resolution of 7° and in 2001 the WMAP (Wilkinson Microwave Anisotropy Probe) [21] satellite with a resolution of 0.23°. More recently, the Planck satellite [22] with a resolution of 5' was launched in 2009 and first results were published in 2013.

In first approximation, the CMBR is perfectly homogeneous and isotropic. The photons were in thermal equilibrium during decoupling and thus the spectrum is a perfect black body with a temperature of $T = 2.725 \pm 0.001$ K, as shown on left panel of figure 1.6. In fact, for a black body, the intensity as a function of frequency ν is given by

$$I(\nu) = \frac{4\pi\hbar\nu^3}{e^{\frac{2\pi\hbar\nu}{k_B T}} - 1}, \tag{1.44}$$

$\hbar$ the reduced Planck constant, k_B Boltzmann's content and T the temperature of the black body. To the second order, there is a dipolar anisotropy due the motion of our galaxy (and even solar system and Earth) with respect to the last scattering surface (LSS) of the CMB photons, as shown on the right panel of 1.6. From this dipole contribution, we can deduce that the Milky Way's velocity is of 370 km/s towards the Virgo constellation. After subtracting this contribution, anisotropies caused by the radiation emissions in our galaxies appear. After removing them, we can see the actual CMB anisotropies which are of the order $\Delta T/T \sim 10^{-5}$, shown on the left panel of figure 1.7.

The map of the temperature anisotropies of the CMB is a picture (a negative to be more precise) of the density distribution in the early universe. To extract information from these maps on our universe, we do not measure the absolute temperature at each point in the sky, but the temperature differences between two different points. We obtain the temperature variation in a certain angular direction (θ, ϕ) with respect to the averaged temperature and then we decompose it in spherical harmonics $Y_{lm}(\theta, \phi)$

$$\frac{\Delta T(\theta, \phi)}{T} = \sum_{l,m} a_{lm} Y_{lm}(\theta, \phi). \tag{1.45}$$

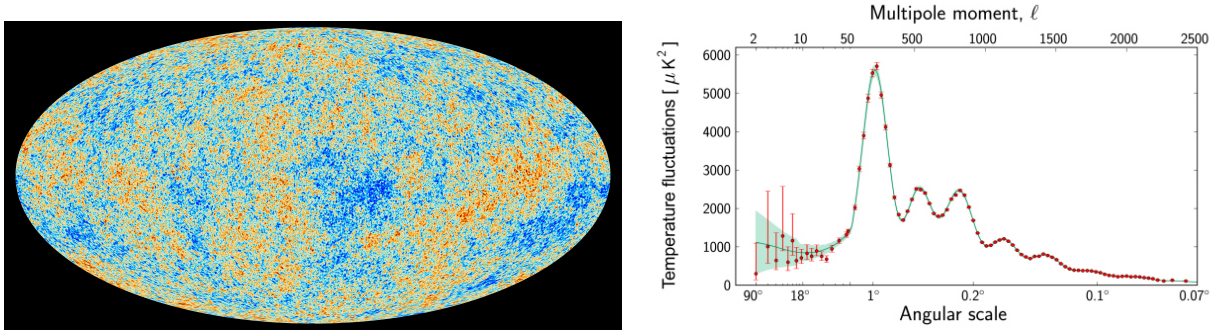

Figure 1.7: Left: **CMB temperature anisotropy map** measured by the satellite Planck [22]. Right: **CMB temperature power spectrum** as a function of the multipole l or the angular scale measured by Planck [25].

The two-point correlation function is then

$$\left\langle \frac{\Delta T(\theta,\phi)}{T} \frac{\Delta T(\theta',\phi')}{T} \right\rangle = \sum_{l,m} \sum_{l',m'} \langle a_{lm} a^*_{l'm'} \rangle \, Y_{lm}(\theta,\phi) Y^*_{l'm'}(\theta',\phi'). \tag{1.46}$$

Assuming that the universe is isotropic, $\langle a_{lm} a^*_{l'm'} \rangle = C_l \delta_{ll'} \delta_{mm'}$ is independent of m. C_l corresponds to amplitude of the multipole l and is called the power spectrum. The temperature power spectrum measured by Planck is shown in figure 1.7 on the right side.

The EE polarization spectrum and TE temperature-polarization cross-spectrum have also been computed by the Planck collaboration and different cosmological parameters can be deduced [26] (in a ΛCDM model, where CDM stands for cold dark matter, which will be discussed later), in particular:

$$\Omega_M = 0.3156 \pm 0.0091 \quad \text{and} \quad \Omega_b h^2 = 0.02225 \pm 0.00016, \tag{1.47}$$

where Ω_b is the baryon abundance and h is the reduced Hubble constant defined by $H_0 = 100h$ (km/s)/Mpc and $H_0 = 67.27 \pm 0.66$ (km/s)/Mpc. Baryons affect the minimum et maximum of the temperature fluctuations and thus change the relative heights of the CMB peaks.
To summarize, 26.8 % of the energy budget of the universe is made of DM, i.e. massive matter without a collision term in the Boltzmann equation, only 4% are baryons (and 68.3 % of dark energy, assumed to be a cosmological constant).

1.2.2 Big Bang Nucleosynthesis (BBN)

The theory of BBN gives a description of the abundances of light nuclei that formed during the first 10-20 seconds after the Big Bang. It provides us with a measurement of Ω_b, independent from the one obtained by the CMB power spectrum.

First let us describe the thermodynamical history of the universe shortly after the Big Bang. When the universe reaches a temperature of $T \sim 200$ MeV, the plasma of quarks and gluons starts to form protons and neutron, it's the strong phase transition. The plasma is then formed of p, n, $e^{\pm}$, γ, ν and $\bar{\nu}$. Around 1-4 MeV (which corresponds to the binding energy per nucleon), nucleons start to form. For temperatures under 1 MeV, the universe is essentially made of light nuclei H, ^{2}H=D, ^{3}H, ^{3}He, ^{4}He, ^{7}Li and of course still $e^{\pm}$, γ, ν and $\bar{\nu}$. Today, in the cores of stars

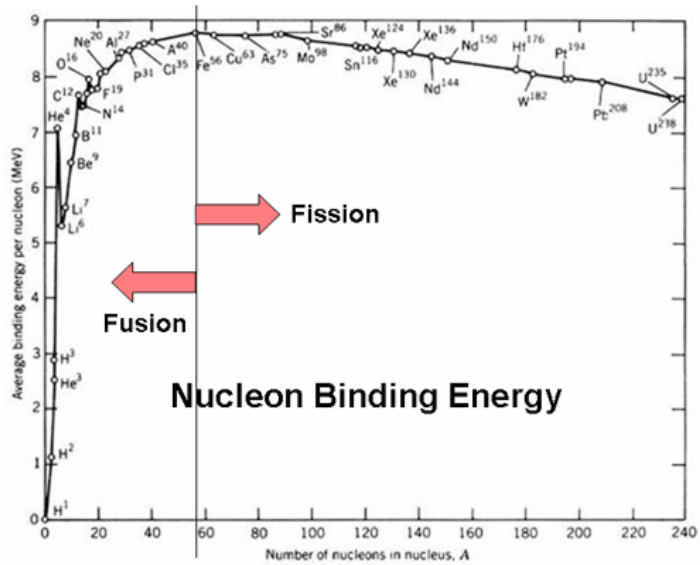

Figure 1.8: The **binding energy per nucleon** for elements [27] from hydrogen to uranium. Notice that iron ^{58}Fe is the most stable element.

nucleosynthesis continues to form heavier atoms which have to be subtracted in measurements in order to obtain the primordial abundances.

When protons and neutrons form a nucleus, energy in the amount of the binding energy is emitted. For an element X containing Z protons and $A - Z$ neutrons, the binding energy is

$$B_A = Zm_p + (A - Z)m_n - m_X > 0, \tag{1.48}$$

where m_p and m_n are the masses of the proton and the neutron respectively. We now want to compute the abundances of light elements defined as

$$X_A = \frac{An_A}{n_B}, \tag{1.49}$$

where n_A is the concentration of nuclei A and n_B the concentration of all baryons in the universe. The first reaction to take place is $p + n \rightarrow \ D + \gamma$. At thermal equilibrium, the chemical potentials satisfy $\mu_p + \mu_n = \mu_D + \mu_\gamma$ and $\mu_\gamma = 0$ because the photon is a massless particle. The number density of the different particles involved are, as we are in the relativistic limit,

$$n_p = g_p \left(\frac{m_p T}{2\pi}\right)^{3/2} e^{-\frac{m_p - \mu_p}{T}}, \tag{1.50}$$

$$n_n = g_n \left(\frac{m_n T}{2\pi}\right)^{3/2} e^{-\frac{m_n - \mu_n}{T}}, \tag{1.51}$$

$$n_D = g_D \left(\frac{m_D T}{2\pi}\right)^{3/2} e^{-\frac{m_D - \mu_D}{T}}. \tag{1.52}$$

We deduce the Saha equation, written as

$$\frac{n_p n_n}{n_D} \sim \left(\frac{m_p T}{2\pi}\right)^{3/2} e^{-\frac{\overbrace{m_p + m_n - m_D}^{=B_D}}{T}}, \tag{1.53}$$

where $B_D \simeq 2.23$ eV is the binding energy of deuterium. We can assume that the number of protons and neutrons is the same at high temperature, the reactions $n + \nu_e \leftrightarrow p + e^-$ and $n + e^+ \leftrightarrow p + \bar{\nu}_e$ being in equilibrium. Then,

$$n_p \simeq \left(\frac{m_p T}{2\pi}\right)^{3/2} e^{-\frac{B_D}{T}}, \tag{1.54}$$

and from observations we can estimate the ratio of baryons (essentially protons) and photons $\eta = \frac{n_B}{n_\gamma} = 6 \times 10^{-10}$. This means that a very small number of baryons has not been annihilated by the corresponding antibaryon and form the matter from which we are made of. The reason for this asymmetry between matter and antimatter is still a mystery and may be explained by leptogenesis scenarios. For our calculation, this means that $n_p \sim \eta n_\gamma^3$ and thus the decoupling temperature for neutrons is $T = 0.73$ MeV. From this moment on the number of neutrons and protons are not the same anymore

$$\frac{n_p}{n_n} \sim e^{-\frac{\overbrace{m_n - m_p}^{=1.293 \text{ MeV}}}{T}}. \tag{1.55}$$

The abundances of protons and neutrons for $T < 0.73$ MeV are $X_n = 1/7$ and $X_p = 6/7$. Since the neutron's lifetime is 15 min and the universe is only 4.5 min old at that time, all the neutrons will end up in nuclei, more specifically in ^{4}He because it maximizes the binding energy per nucleon for light elements, as seen on figure 1.8. And finally, under this assumption, we can compute the abundance of ^{4}He

$$X_4 = \frac{4n_{^4He}}{n_n + n_p} = \frac{2n_n}{n_n + n_p} = \frac{2}{7} \sim 0.25. \tag{1.56}$$

Helium represents 25% of the baryons in our universe, this is the prediction of hot Big Bang Nucleosynthesis and is in very good agreement with measurements, as shown on figure 1.9.

The total amount of baryons can be determined by the absorption of quasar light (the so-called Lymann-α forest). In particular, the abundance of deuterium, a very sensitive indicator of the baryon density, has been measured and agrees extremely well with the prediction of BBN and the measurements of CMB anisotropies.

1.2.3 Structure formation

Before recombination, due to the pressure of photons in the plasma, baryons are not able to grow structures. However, if structures start to form only after recombination, there is not enough time for them to grow galaxies and clusters. Another massive fluid (DM) is needed to create the potential well in which the baryons can then fall and form the observed structures:

- hot DM is relativistic when galactic size perturbations enter into the horizon $ct_U = \lambda_{gal}$ ($T \sim 1$ keV). Galaxy size inhomogeneities do not survive in this case and superclusters had to form first and then galaxies later.

- warm DM is semi-relativistic when ($T \sim 1$ keV) and inhomogeneities of dwarf-galaxies size and larger survive.

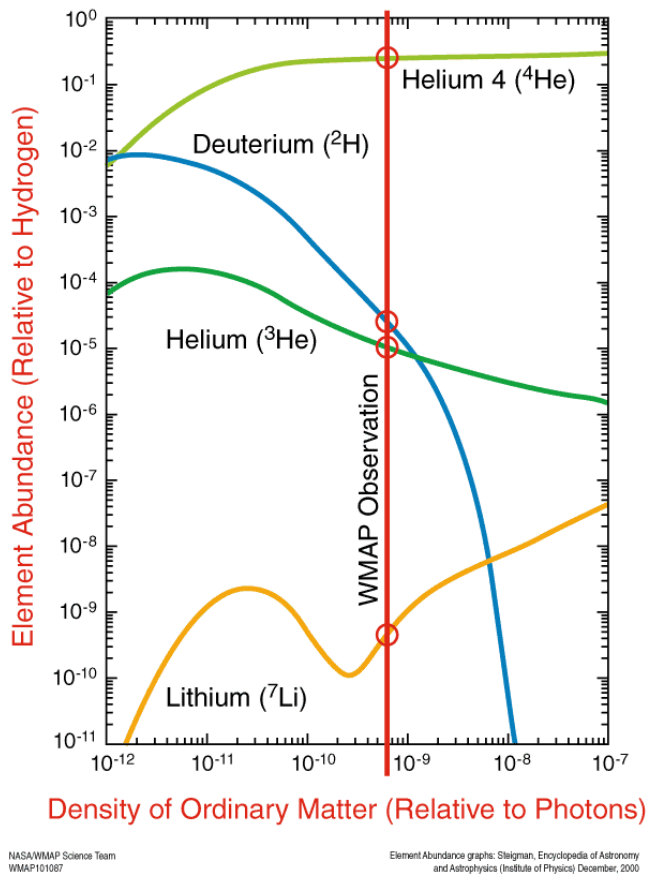

Figure 1.9: **Abundance of light elements** as a function of the density of ordinary matter in the universe ρ_b/ρ_γ in a BBN scenario. The vertical red line represents the measurement of the density of ordinary matter by WMAP and the red circles the measurements of the abundance of elements today. The abundance of deuterium is highly dependent on the ordinary matter density [28].

- cold DM is non-relativistic when ($T \sim 1$ keV) and inhomogeneities much smaller than galaxy size survive. Galaxies and clusters form in a "bottom-up"scenario by coalescence of smaller structures which from first. Small structures remain in the larger ones (DM mini-halos within galaxies).

Both cold and warm DM scenarios are in good agreement with observations of the CMB, clusters and galaxy counts, gravitational lensing and Lyman α forest, as shown in figure 1.10. In fact, hot DM is ruled out because of the lack of small structures.

Small Scale controversies of CDM

In cosmology, the model of cold DM with a cosmological constant Λ, the so-called ΛCDM model is very popular. In fact, as we have seen earlier, the CMB peaks can be very well explained in this case. However, when comparing simulations to observations, a few discrepancies arise at galactic scale:

- Very high resolution DM-only simulations find massive dense subhalos, which should have lots of stars in them, but none of the observed satellites of the Milky Way or Andromeda

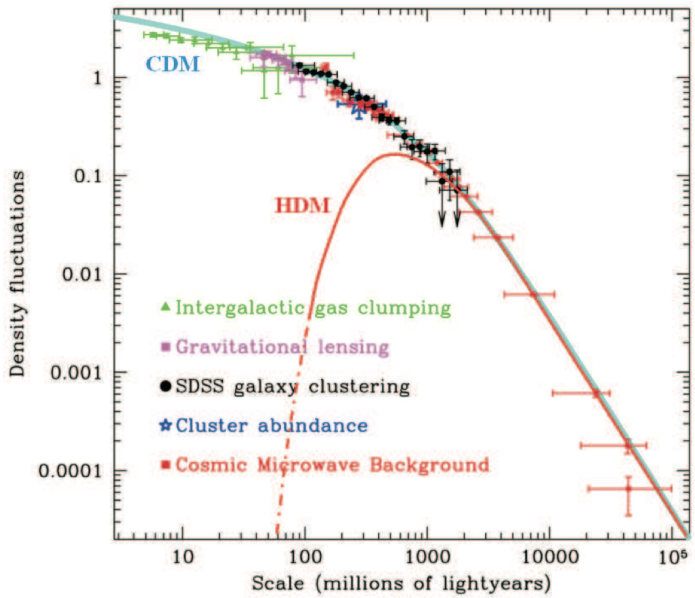

Figure 1.10: **Density fluctuations in cold and hot DM scenarios** with measurements from CMB, cluster and galaxy counts, gravitational lensing and intergalactic gas clumping. If DM is hot observed substructures can not form [29].

have stars moving as fast as expected in these very dense subhalos. This is known as the *too big too fail* problem. It is not clear how baryons would affect these simulations, they may fix the problem. Other solutions would be to consider DM self-interaction or warm DM.

- Even though the number count of galaxies seams to agree between cold DM simulations and observations, the number of dwarf galaxies differs by an order of magnitude. In fact, DM simulations predict that a galaxy of the size of the Milky Way should host hundreds of satellite galaxies, while observations show a much lower number. This is known as the *missing satellite problem*. There are two ways out of it without refusing the cold DM scenario: either the dwarf galaxies are there, but they are not luminous enough to be seen by our telescope. In other words, they did not attract enough baryons to form stars and to be detected. Or, the dwarf galaxies have been tidally stripped apart by larger galaxies and are not there anymore. In the warm DM scenario, small scales are suppressed and dwarf galaxies do not form in such a large number and the simulations would agree more with observations.

- As we have seen in section 1.1.3, N-body simulations of CDM tend to predict a cusp distribution at the center of the galaxy while observation hint towards a cored profile. This is known as the *cusp/core problem* [30]. Again, it is not clear how baryons would affect the cold DM distribution near the GC, while warm or self interacting DM could explain the cored distribution at the center of the galaxies.

1.2.4 Baryon acoustic oscillation (BAO)

In the primordial plasma, two counterbalancing forces create oscillation: gravity and radiation pressure. If we have a spherical overdensity, an acoustic wave will travel outwards, while the DM stays in the center. This sound wave travels at a speed

$$c_s = \frac{c}{\sqrt{3(1+R)}} \quad \text{with} \quad R = \frac{3\rho_b(z)}{4\rho_\gamma(z)} \sim \frac{\Omega_b}{(1+z)}. \tag{1.57}$$

Then at recombination ($z_{rec} = 1300$), when the universe becomes neutral, which is around the same time as the photons decouple ($z_{dec} = 1100$), the photons radiate away, releasing the pressure in the baryonic plasma. Thus, the spherical sound wave leaves a shell of bayons at a certain radius r_s and DM will also clump there. Finally we have two overdensities: the initial one at the center and one on the shell. This radius r_s is equal to sound horizon, which is the comoving distance a sound wave could have travelled in the photon-baryon plasma by the time of decoupling and is related to the abundances of matter an baryons

$$r_s = \int_{z_{eq}}^{\infty} \frac{c_s}{H(z)} dz = \frac{1}{\sqrt{\Omega_m H_0}} \frac{2c}{\sqrt{3 z_{eq} R_{eq}}} \ln\left(\frac{\sqrt{1+R_{rec}} + \sqrt{R_{rec}+R_{eq}}}{1+\sqrt{R_{eq}}}\right), \tag{1.58}$$

where $z_{eq} = \frac{\Omega_m}{\Omega_\gamma}$ is the redshift of the matter-radiation equality. This radius r_s is then stretched out by the expansion of the universe. If there is a galaxy at the center of the shell, there an increased probability of finding another galaxy at a distance r_s, in other words, we should find a bump in the two-point correlation function of galaxies at radius r_s. Using the abundances measured by the CMB, we find that $r_s = 150$ Mpc $= 105\ h^{-1}$ Mpc. As shown on figure 1.11, the measured value of r_s is in perfect agreement with the predictions and shows the need for a DM fluid. In fact without DM, all the baryons would have drifted away from the central density.

1.2.5 WIMP miracle

After 80 years, we do not know a lot about dark matter. Assuming that DM is in elementary particle, we know that

- DM is massive,
- DM is stable, the lifetime has to be larger than the age of the universe,
- the mass is the interval $10^{-31} \leq m_{\rm DM} \leq 10^{50}$ GeV. The lower bound comes from a DM model called fuzzy cold dark matter [32], where DM is extremely light scalar particle. For particles having reached equilibrium $0.2 - 0.7 \times 10^{-6}$ GeV $\leq m_{\rm DM}$ depending on the bosonsic or fermionic nature of DM [33].
- DM is collisionless or at least satisfies the bounds from the bullet cluster $\sigma/m \leq 0.1$ cm^2/g.
- DM is dissipationless, as opposed to baryons which cool down by radiating energy and collapse in a disk. DM should also be neutral. If DM is charged it has to be very heavy and with a very small electromagnetic coupling (Milli-charged DM, electric and magnetic

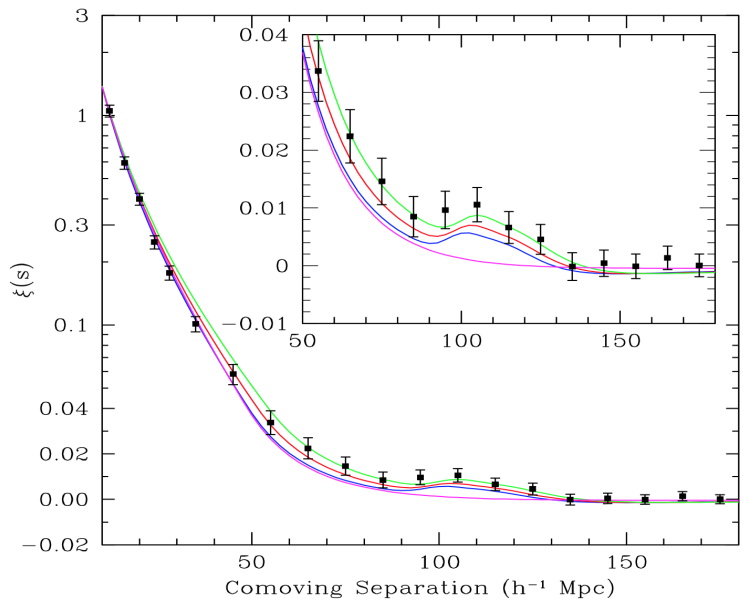

Figure 1.11: **Measurements of the two point correlation function of galaxies** from the SDSS LRG galaxy sample. The coloured lines show the prediction in a universe with $\Omega_m h^2 = 0.12, 0.13$ and 0.14 (from top to bottom), all with $\Omega_b h^2 = 0.024$. The black line shows the prediction of the correlation function in a universe with only CDM ($\Omega_b = 0$) [31] .

dipole DM, anapole DM). In fact, Charged Massive Particles (CHAMPs) with a mass of the order of $\sim 10^8$ TeV behave nearly as collisionless DM since magnetic fields would prevent these particles in the halo from entering or staying in the galactic disk. CMB and observations of large scale structure formation constrain the mili-charge of DM to be

$$Q_{DM}^2 \lesssim 3.24 \times 10^{-12} \alpha \left(\frac{m_{\rm DM}}{\rm GeV} \right), \tag{1.59}$$

where α is the electromagnetic coupling constant [34].

- The abundance of DM has to explain the CMB peaks.

Let us assume DM is made of elementary particles which where in thermal equilibrium. We want to compute the relic abundance of these particles today. We start with the Boltzmann equation 1.43, with n the particle number density of DM

$$\frac{dn}{dt} + 3Hn = -\langle \sigma v \rangle \left(n^2 - (n^{eq})^2 \right), \tag{1.60}$$

n^{eq} is the number density at equilibrium. Let us consider the non-relativistic regime $T < m_{\rm DM}$, so

$$n^{eq} = \left(\frac{m_{\rm DM} T}{2\pi} \right)^{3/2} e^{-m_{\rm DM}/T}. \tag{1.61}$$

We introduce the variables $Y = n/s$ and $Y^{eq} = n^{eq}/s$ where s is the entropy density described by equation 1.41. Entropy is conserved per co-moving volume (sa^3 =constant) and thus we can write $\frac{dn}{dt} + 3Hn = s\dot{Y}$ and replace the left hand side of equation 1.60

$$s\dot{Y} = -\langle \sigma v \rangle s^2 \left(Y - (Y^{eq})^2 \right). \tag{1.62}$$

We now define the variable $x = m_{\rm DM}/T$ and the equation becomes

$$\frac{dY}{dx} = -\frac{\langle \sigma v \rangle s}{Hx}\left(Y - (Y^{eq})^2\right). \tag{1.63}$$

For heavy DM, the thermally-average cross-section can be approximated by a non-relativistic expansion in powers of v^2,

$$\langle \sigma v \rangle = a + b\left\langle v^2 \right\rangle + O(\langle v4 \rangle) \simeq a + \frac{6b}{x}, \tag{1.64}$$

and the Botzmann equation in terms of $\Delta = Y - Y^{eq}$ becomes

$$\frac{d\Delta}{dx} = -\frac{dY^{eq}}{dx} - \underbrace{\sqrt{\frac{\pi g_*}{45}} m_{\rm DM} M_{pl}\left(a + \frac{6b}{x}\right)\frac{1}{x^2}}_{=f(x)}\Delta(2Y^{eq} + \Delta), \tag{1.65}$$

where we used the fact that the early universe has no curvature and the energy density of the cosmological constant is negligible. Friedmann's equation 1.28 gives us the rate of expansion of the universe

$$H^2 = \frac{8\pi G}{3}\rho = 1.66\sqrt{g_*}\frac{T^2}{M_{pl}}, \tag{1.66}$$

with $G = 1/M_{pl}^2$ and M_{pl} the Planck mass. We are now interested in the temperature of freeze-out of the relic DM $T_{f.o.}$ and the related variable $x_{f.o.} = m_{\rm DM}/T_{f.o.}$. Equation 1.65 has an analytical solution in two regimes (long before or long after the freeze-out)

$$x \ll x_{f.o.} \Rightarrow \Delta = -\frac{d\Delta/dx}{2f(x)Y^{eq}}, \tag{1.67}$$

$$x \gg x_{f.o.} \Rightarrow \Delta = -f(x)\Delta^2. \tag{1.68}$$

Integrating the second equation between $x_{f.o}$ and ∞ and using $\Delta(x_{f.o.}) \gg \Delta(\infty)$, we get

$$Y_\infty^{-1} = \sqrt{\frac{\pi g_*}{45}}\frac{M_{pl} m_{\rm DM}}{x_{f.o.}}\left(a + \frac{3b}{x_{f.o}}\right). \tag{1.69}$$

The present density of DM is given by $\rho_{DM} = m_{MD} n_{DM} = m_{\rm DM} s_0 Y_\infty$ with $s_0 = 2889.2$ cm^{-3} the present entropy density for Standard Model particles, in particular considering three Dirac neutrinos. The relic density of DM is then

$$\Omega_{DM} h^2 = \frac{\rho_{DM}}{\rho_c} h^2 \simeq \frac{1.07 \times 10^9 \text{GeV}^{-1}}{M_p l}\frac{x_{f.o.}}{\sqrt{g_*}}\frac{1}{a + 3b/x_{f.o}}, \tag{1.70}$$

g_* has to be evaluated at the freeze-out temperature. The relic density of DM is inversely proportional to the annihilation cross-section, as shown on figure 1.12. The freeze-out variable $x_{f.o.}$ can be estimated through the iterative solution of the equation

$$x_{f.o.} = \ln\left(c(c+2)\sqrt{\frac{45}{8}}\frac{g}{2\pi}\frac{m_{\rm DM} M_{pl}(a + 6b/x_{f.o.})}{\sqrt{g_* x_{f.o.}}}\right), \tag{1.71}$$

c is a constant around $\sim 1/2 - 1$ obtained by matching the late- and early-time solutions. The result is not dramatically affected by the value of this constant. If we want to estimate the

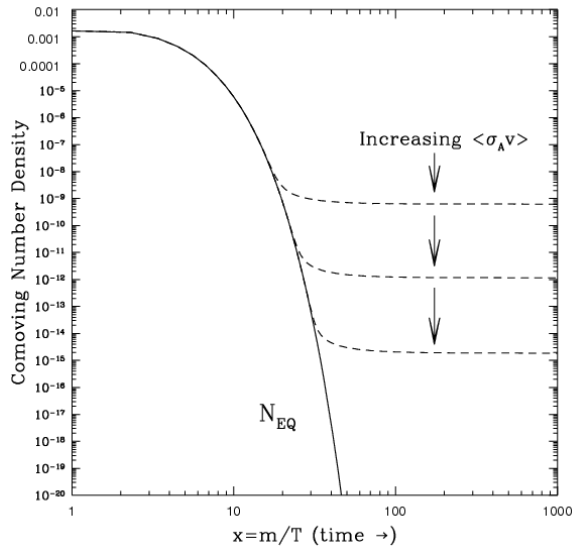

Figure 1.12: The **comoving number density of relic DM** as a function of $x = m_{\rm DM}/T$. After freeze-out, the comoving number density stays constant and depends on the annihilation cross-section [38]. Increasing $\langle \sigma v \rangle$ leads to a smaller relic abundance.

order of magnitude of the abundance of DM from a thermal relic (mass is of the order of a few GeV to few TeV), we get

$$\Omega_{DM} \simeq 0.2 \, \frac{3 \times 10^{-26} \mathrm{cm}^3/\mathrm{s}}{\langle \sigma_A v \rangle}. \tag{1.72}$$

The weak annihilation cross-section is of the order $\langle \sigma_A v \rangle \simeq G_F^2 T^2 \simeq 3 \times 10^{-26} \mathrm{cm}^3/\mathrm{s}$, with G_F the Fermi constant. So, we have found that a particle with a "heavy" mass with a weak annihilation cross-section would reproduce the DM abundance observed in our universe. This particle is called a Weakly Interacting Massive Particle, or WIMP. The fact that the thermal relic abundance of these WIMPs corresponds to the DM abundance is named the *WIMP miracle*. In [35], Lee and Weinberg assumed that $\Omega_{DM} = 1$ and found that the DM mass should be greater than 2 GeV. With the abundance obtained today the typical WIMP should be greater than 4 GeV. WIMPs are thus cold DM candidates. The upper limit on the WIMP mass is given by the so-called *unitarity bound*. In fact, if we assume the partial-wave unitarity of the S matrix, the correct thermal cross-section can only be obtained for masses smaller than 340 TeV, assuming $\Omega_{DM} = 1$ [36]. Taking into account the relic density measured by recent CMB experiments, one gets $m_{WIMP} \lesssim 80 - 120$ TeV.

If there are enough particles nearly degenerate with the DM thermal relic, but with masses m slightly greater than $m_{\rm DM}$ and if the mass difference $\Delta m = m - m_{\rm DM} \lesssim T_{f.o}$, then they are thermally accessible and their coannihilation into SM particle will affect the relic abundance of DM and have to be taken into account in the calculation [37].

1.3 Dark Matter and Particle Physics

The Standard Model (SM) of particle physics is based on a $SU(3)_c \otimes SU(2)_L \otimes U(1)_Y$ symmetry group, where $SU(3)_c$ describes the strong interaction called Quantum Chromodynamics,

$SU(2)_L \otimes U(1)_Y$ the electroweak interactions (Y the weak hypercharge $Y = B+S+C+B'+T$, with B the baryon number, S the strangeness, C the charmness, B' the bottomness and T is topness). This group undergoes a spontaneous symmetry breaking

$$SU(3)_c \otimes SU(2)_L \otimes U(1)_Y \to SU(3)_c \otimes U(1)_Q, \tag{1.73}$$

where Q is the electric charge generator. In the SM of particle physics, matter consists of fermions, namely quarks and leptons. The left-handed quarks fall onto in three $Su(2)_L$ doublets of quarks

$$Q_u = \begin{pmatrix} u_L \\ d'_L \end{pmatrix} \ , \ Q_c = \begin{pmatrix} c_L \\ s'_L \end{pmatrix} \ \text{ and } \ Q_t = \begin{pmatrix} t_L \\ b'_L \end{pmatrix}. \tag{1.74}$$

with quantum numbers $(3, 2, 1/6)$ under $SU(3)_c \otimes SU(2)_L \otimes U(1)_Y$. The quarks have a *baryon number* $B = 1/3$ and a *lepton number* $L = 0$. In the bottom line the prime $'$ denotes weak eigenstates which are related to mass eigenstates through the Cabbibo-Kobayashi-Maskawa (CKM) matrix (which we do not need to explicit here)

$$\begin{pmatrix} d' \\ s' \\ b' \end{pmatrix} = \hat{V}_{CKM} \begin{pmatrix} d \\ s \\ b \end{pmatrix}. \tag{1.75}$$

The left-handed leptons are also arranged in three generations of $SU(2)_L$

$$L_e = \begin{pmatrix} \nu_{eL} \\ e_L \end{pmatrix} \ , \ L_\mu = \begin{pmatrix} \nu_{\mu L} \\ \mu_L \end{pmatrix} \ \text{ and } \ L_\tau = \begin{pmatrix} \nu_{\tau L} \\ \tau_L \end{pmatrix} \tag{1.76}$$

wit quantum number $(1, 2, -1/2)$ under $SU(3)_c \otimes SU(2)_L \otimes U(1)_Y$. Leptons have baryon number $B = 0$ and lepton number $L = 1$. All the right-handed fields (three up-type quarks U_α, three down-type quarks D_α and three charged leptons E_α) are singlets under $SU(2)_L$, right-handed neutrinos are not present in the SM. Each particle has also an antiparticle with the same mass and opposite quantum numbers.
In the SM, interactions are mediated by bosons: gluons for the strong interaction, $W^\pm, Z^0, \gamma$ and the Higgs field H^0 for the electroweak interaction. The mass of the gauge bosons and the Higgs boson are generated by the spontaneous symmetry breaking of the SM group. A few more details can be found in the appendix.

In the SM there is no DM candidate so far, so we have to turn to models beyond the SM. For example, neutrinos are massless in the SM, however there is strong evidence from the observation of atmospheric and solar neutrinos that neutrinos oscillate from one family to another. This is only possible if they are massive. In a minimal extension of the SM, it is possible to add a neutrino mass term to the lagrangian and thus neutrinos may become ideal DM candidates, because of their very weak interactions with other SM particles. This turns out not to be the case. In fact, since neutrinos are fermions, they follow the Pauli exclusion principle and we can compute the number of neutrinos able to fit inside the potential well of a galaxy, assuming all energy levels are occupied

$$N_\nu \leq \frac{1}{2\pi} \frac{1}{\hbar^3} \int d^3p d^3x \sim p^3 r^3 \sim (m_\nu v)^3 r^3, \tag{1.77}$$

with r the radius of the galactic potential and v the velocity of the neutrinos (as well as the stars). The total mass of the neutrino halo can be

$$M_\nu \leq m_\nu N_\nu \sim m_\nu^4 v^3 r^3. \tag{1.78}$$

If we want to explain the rotation curves with the gravitational effect of neutrinos only, we have

$$M \sim \frac{rv^2}{G} \leq m_\nu N_\nu \sim m_\nu^4 v^3 r^3, \tag{1.79}$$

using Newton's second law. In the end, we find that the mass of neutrinos has to be at least

$$m_\nu \geq \left(\frac{1}{Gvr^2}\right)^{1/4} \simeq 120 \left(\frac{100 \text{ km/s}}{v}\right)^{1/4} \left(\frac{\text{kpc}}{r}\right)^{1/2} \text{ eV}. \tag{1.80}$$

For a galaxy like the Milky Way, at the position of Sun $r \sim 10$ kpc $v \sim 200$ km/s and thus we need neutrinos to have a mass $m_\nu \geq 30$ eV. For dwarf galaxies, which are dominated by DM, this conditions becomes $m_\nu \geq 1$ keV. Experiments show that $m_{\nu_e} < 2.3$ eV at 95% C.L. [39]. The mass limits on the other two neutrinos by direct measurements are not as good as the one of the electron neutrino, but the mass difference between the first and the third neutrino mass eigenstates is of the order $\Delta m_{31}^2 \simeq 3 \times 10^{-3}$ eV^2 from accelerator neutrino experiments and even $\Delta m_{21}^2 \simeq 7 \times 10^{-5}$ eV^2 for the second and first eigenstates form solar neutrinos experiments [40]. So neutrinos, even if they have a mass cannot explain rotation curves of galaxies. On top of that, the neutrino contribution to the energy of the Universe is

$$\Omega_\nu h^2 = \frac{\sum_k m_k}{94.14 \text{ eV}} < \Omega_{DM} h^2, \tag{1.81}$$

and thus neutrinos are not abundant enough in our Universe to explain DM and they would constitute hot DM.
Form a theoretical point of view, the SM of particle physics does have a few issues. For example, the weak and Planck energy scales are very different. This is called the *hierarchy problem*. This is illustrated when adding radiative corrections to the Higgs mass: the first correction is the top loop, which has to be integrated up to the cut off scale, the Planck scale. Thus the Higgs mass is expected to be of the order of the Planck scale. However, the LHC measured the Higgs mass to be 125 GeV, which is more than 15 orders of magnitude below the Planck scale. In particle physics, theories beyond the SM include very good DM candidates, with different masses and interaction cross-sections, a selection is presented in figure 1.13. We will now discuss the most popular ones in more detail.

1.3.1 Sterile neutrinos

Only left-handed neutrinos are present in the SM, right-handed neutrinos have never been observed. It may be that right-handed neutrinos do not exists or it may be that their interactions with other particles are simply too weak. In that case, they would be singlets under all gauge interactions and are thus called *sterile neutrino*, as opposed to the three active neutrinos, which are members of weak isospin doublets. Adding 1, 2 or 3 sterile neutrinos could explain the mass and the oscillations of the active ones, as well as provide a viable DM candidate.
In the most general case, if we add right-handed neutrinos ν_R, we can add a Dirac-Majorana mass term to the lagrangian

$$\mathcal{L}_{mass}^{D+M} = \mathcal{L}_{mass}^{D} + \mathcal{L}_{mass}^{ML} + \mathcal{L}_{mass}^{MR}, \tag{1.82}$$

where $\mathcal{L}_{mass}^{D} = -m_D \bar{\nu}_R \nu_L + h.c.$ is the Dirac mass term, $\mathcal{L}_{mass}^{ML} = \frac{1}{2} m_L \nu_L^T C^\dagger \nu_L + h.c$ is the Majorana mass term with left-handed neutrinos and $\mathcal{L}_{mass}^{MR} = \frac{1}{2} m_R \nu_R^T C^\dagger \nu_R + h.c$ is the Majorana

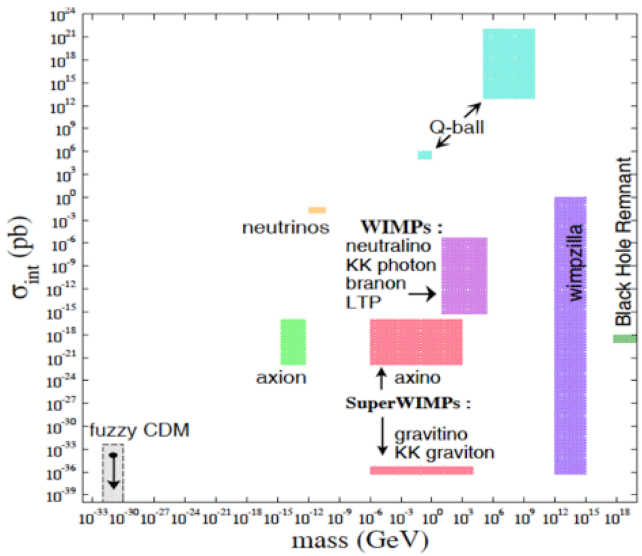

Figure 1.13: The **wide range of DM candidates** in particle physics models expressed in terms of mass and self-interaction cross-section [41].

mass term with right-handed neutrinos. If we consider m right-handed neutrinos, we can write the lagrangian 1.82 in terms of

$$N'_L = \begin{pmatrix} \nu'_L \\ \nu'^c_R \end{pmatrix} \quad \text{with} \quad \nu'_L = \begin{pmatrix} \nu'_{eL} \\ \nu'_{\mu L} \\ \nu'_{\tau L} \end{pmatrix} \quad \text{and} \quad \nu'^c_R = \begin{pmatrix} \nu'^c_{1R} \\ . \\ . \\ . \\ \nu'^c_{mR} \end{pmatrix} \tag{1.83}$$

and it becomes

$$\mathcal{L}^{D+M}_{\text{mass}} = \frac{1}{2} N'^T_L C^\dagger M^{D+M} N'_L + h.c. \quad \text{with } M^{D+M} = \begin{pmatrix} M^L & (M^D)^T \\ M^D & M^R \end{pmatrix}. \tag{1.84}$$

In general, M^D is a $3 \times m$ matrix and M^R and M^L are $m \times m$ symmetric matrices. An interesting case is when $M^L = 0$, because we can diagonalize the mass term matrix M^{D+M} and we get $m + 3$ massive Majorana neutrinos if the eigenvalues of M^R are larger than the ones of M^D. In fact, in this approximation, the mass term is

$$M^{D+M} = \begin{pmatrix} -M^D (M^R)^{-1} (M^D)^T & 0 \\ 0 & M^R \end{pmatrix}. \tag{1.85}$$

The left-handed neutrinos have a light mass while the right-handed neutrinos are much heavier, this is called the *Seesaw mechanism*. In fact increasing the eigenvalues of M^R pushes the masses of the sterile neutrinos up and those of active neutrinos down, just as if they sat on a seesaw. The weak interactions of sterile neutrinos are suppressed and thus their interaction cross-section is small enough to satisfy the bounds from the bullet cluster. The CMB is also sensitive to the number of relativistic degrees of freedom, Planck has also measured that the effective number of neutrino species is $N_{eff} = 3.15 \pm 0.23$ in agreement with the SM value of 3.046. So, sterile

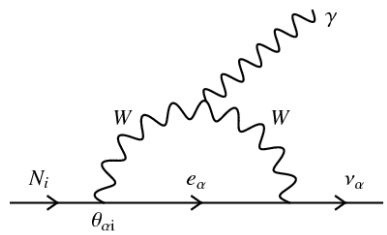

Figure 1.14: Feynman diagram of the **decay of a sterile neutrino** N_i into a active neutrino ν_α and a photon.

neutrino should be non-relativistic. In the minimal extension of the standard model νMSM, we only need to add 3 strile neutrinos in order to address the problems of neutrino oscillations, the baryon asymmetry and the nature of DM [42]. If DM is made of one type of the sterile neutrinos then they can decay through the diagram in figure 1.14 and their lifetime is

$$\tau_{\nu_{R1}} = 5 \times 10^{26} \text{ sec} \left(\frac{10^{-8}}{\Theta^2_{\alpha_1}}\right) \left(\frac{1 \text{ keV}}{m_{\nu_{R1}}}\right)^5, \tag{1.86}$$

with Θ_{α_1} the mixing of the sterile neutrino with the active neutrinos. They are produced by active-sterile neutrino oscillations and their abundance is

$$\Omega_{\nu_{R1}} h^2 \simeq 0.1 \left(\frac{\Theta^2_{\alpha_1}}{10^{-8}}\right)^2 \left(\frac{m_{\nu_{R1}}}{1 \text{ keV}}\right) \tag{1.87}$$

Typically their mass is around 1 keV and are warm DM candidates [43]. However, the parameter space allowing their thermal production has been ruled out by X-ray and Lymann-α observations. In order to maintain a viable DM candidate a lepton asymmetry has to be assumed.

1.3.2 Axions

Axions have been introduced to solve the strong CP problem. In fact, the QCD lagrangian reads

$$\mathcal{L}_{QCD} = -\frac{1}{2} Tr(F_{\mu\nu}F^{\mu\nu}) + \theta \frac{g^2}{32\pi^2} F^a_{\mu\nu} \tilde{F}^{\mu\nu a} + \bar{\psi}(i\gamma^\mu D_\mu - m e^{i\theta'\gamma_5})\psi. \tag{1.88}$$

The first term defines the gluon dynamics, the second one the QCD vacuum (CP violating) and the last one the kinetic and mass term of quarks. We would expect $\theta \sim O(1)$, but the electric dipole moment of the neutron is directly related to this parameter

$$|d_n| \simeq 5 \times 10^{-16} \theta \tag{1.89}$$

and experimentally $|d_n| < 10^{-25}$, thus $\theta < 10^{-10}$. The fact that θ is so small is called the *strong CP problem*. Peccei and Quinn introduced a global $U(1)_{PQ}$ symmetry which spontaneously breaks at a large energy scale E [44]. $\theta = a/f_a$ becomes a dynamical variable, where a is the axion field and f_a the decay constant and the QCD lagrangian becomes

$$\mathcal{L}_{QCD} = -\frac{1}{2} Tr(F_{\mu\nu}F^{\mu\nu}) + \bar{\psi}(i\gamma^\mu D_\mu - m e^{i\theta'\gamma_5})\psi + \left(\theta - \frac{a}{f_a}\right) \frac{g^2}{32\pi^2} F^a_{\mu\nu} \tilde{F}^{\mu\nu a} + \frac{1}{2}\partial_\mu \partial^\mu a. \tag{1.90}$$

superfield	SM particle	Spin	Superpartner	Spin	$SU(3)_c \otimes SU(2)_L \otimes U(1)_Y$
Q_α	$\begin{pmatrix} u_L \\ d_L \end{pmatrix}$	1/2	$\begin{pmatrix} \tilde{u_L} \\ \tilde{d_L} \end{pmatrix}$	0	$(3, 2, 1/6)$
U^c_α	$\bar{u}_R$	1/2	$\tilde{u}^*_R$	0	$(\bar{3}, 1, -2/3)$
D^c_α	$\bar{d}_R$	1/2	$\tilde{d}^*_R$	0	$(\bar{3}, 1, 1/3)$
L_α	$\begin{pmatrix} \nu_L \\ e_L \end{pmatrix}$	1/2	$\begin{pmatrix} \tilde{\nu_L} \\ \tilde{e_L} \end{pmatrix}$	0	$(1, 2, -1/2)$
E^c_α	$\bar{e}_R$	1/2	$\tilde{e}^*_R$	0	$(1, 1, 1)$
H_1	H_1	0	$\tilde{H}_1$	1/2	$(1, 2, +1/2)$
H_2	H_2	0	$\tilde{H}_2$	1/2	$(1, 2, -1/2)$
G^a	g	1	$\tilde{g}$	1/2	$(8, 1, 0)$
W_i	W_i	1	$\tilde{W}_i$	1/2	$(1, 3, 0)$
B	B	1	$\tilde{B}$	1/2	$(1, 1, 0)$

Table 1.2: **Field content of the minimal supersymmetric standard model:** SM fields and superpartners, adapted from [47].

When the universe cools down, around the QCD epoch $T < 1$ GeV, the vacuum effects tilt the potential, explicitly breaking the symmetry and the axion gets a mass $m_a \sim \frac{f_\pi m_\pi}{f_a}$ and the CP symmetry is restored [45, 46]. The coherent oscillations of the axion field create a condensate, with density

$$\Omega_a h^2 \simeq 0.3 \left(\frac{f_a}{10^{12} \text{ GeV}} \right)^{7/6} \simeq \frac{10^{-5} \text{ eV}}{m_a}. \tag{1.91}$$

Even though the mass of the axion is very small $m_a \sim 10^{-(6-2)}$ eV, their velocity today is of the order $v_a \sim 10^{-17} c$ and thus are a good cold DM candidate. They could also be produced thermally, but would be hot DM and not be abundant enough.

1.3.3 Supersymmetric candidates

Supersymmetry, consisting of introducing a symmetry relating bosons and fermions, is a way to solve the *hierarchy problem*, the huge difference between the electroweak and Planck energy scales, illustrated by the radiative directions to the mass of the Higgs boson. Fermion masses increase only logarithmically, but scalar masses increase quadratically with energy. Adding supersymmetric particles with similar masses but opposite spin, allows to write the radiative correction to the higgs mass as

$$\delta m_s^2 \sim \left(\frac{\alpha}{2\pi} \right) (\Lambda^2 + m_B^2) - \left(\frac{\alpha}{2\pi} \right) (\Lambda^2 + m_F^2) = \left(\frac{\alpha}{2\pi} \right) (m_B^2 - m_F^2), \tag{1.92}$$

where Λ is the high-energy cut-off of new physics. The new generator Q changes fermions into bosons and vise-versa

$$Q \left| fermion \right\rangle = \left| boson \right\rangle \quad \text{and} \quad Q \left| boson \right\rangle = \left| fermion \right\rangle . \tag{1.93}$$

The minimal supersymmetric extension of the standard model or Minimal Supersymmetric Standard Model (MSSM) has one supersymmetric field for each SM particle. It is the minimal number of SUSY particles necessary to include all the SM fields: quarks and leptons get scalar superpartner, namely *squarks* and *sleptons*, to each gauge field a fermonic superpartners is

associated, called *gluinos*, *winos* and *binos* and finally there is an additional Higgs field and thus one 1/2 spin *higgsino* to each Higgs boson. In this way, both up- and down-type quarks get masses at electroweak symmetry breaking. All these fields and particle eigenstates are presented in table 1.2 and 1.3. An important feature in SUSY is the conservation of R-parity, introduced to counter the proton decay and where R is a new quantum number defined as

$$R = (-1)^{3B+L+2S}, \tag{1.94}$$

SM particles have $R = +1$ and all particles have $R = -1$. The conservation of this parity ensures that SUSY particles can only decay into an odd number of other SUSY particles (and maybe SM particles). Thus, the Lightest Supersymmetric Particle (LSP) is stable, can only be destroyed by pair annihilation and has zero electric and color charge. In fact, otherwise, the LSP could have formed heavy isotopes with baryonic matter. These characteristics of the LSP make it a perfect DM candidate. There are three candidates for the LSP in the MSSM

- the *sneutrino*: if we want it to be responsible for the whole DM relic density in the universe, the cross-section has to be high and has already been ruled out by direct detection experiments (a subject that we will talk about later), see for example [49], even though there may be some way to get out of it [50].

- the *gravitino*, which would interact very weakly and thus be almost impossible to detect and not very interesting from a phenomenological point of view.

- the *lightest neutralino*, which is the lightest of the four Majorana fermionic eigenstates from the mixing of the bino $\tilde{B}$, the wino $\tilde{W}^3$ and the two higgsinos $\tilde{H}_1^0$ and $\tilde{H}_2^0$. The lightest neutralino $\tilde{\chi}_1^0$ is a linear combination of these four fields

  $$\tilde{\chi}_1^0 = N_{11}\tilde{B} + N_{12}\tilde{W}^3 + N_{13}\tilde{H}_1^0 + N_{14}\tilde{H}_2^0. \tag{1.95}$$

  In order to be responsible for the entire DM in the universe (i.e. to have the correct relic density), the annihilation cross-section of the neutralino needs to be of the order

  $$\langle \sigma v \rangle \sim 1 \text{ pb} \sim \alpha/(150 \text{ GeV})^2, \tag{1.96}$$

  it has the correct mass and the electroweak interaction strength to make it a perfect WIMP candidate. Neutralinos annihilate mostly into fermions, such as top and bottom quarks or τ leptons, or gauge bosons $W^\pm$ and Z^0, as well as final states containing the Higgs boson. The corresponding diagrams can be found, among others, in [51].
  If $\tilde{\chi}_1^0$ is mostly higgsino or wino, it has to be very heavy (around 1 TeV) to have the correct abundance. Lighter masses are also possible, but the correct abundance is reached by non-thermal mechanism.
  If $\tilde{\chi}_1^0$ is mostly bino, a lot of the parameter space has already been ruled out by LEP, in the remaining one the relic density is higher that the abundance of DM and thus new contributions to the cross-section have to be considered.

If the MSSM is extended, other potential DM candidate arise. For example, the *right-handed sneutrino* is a viable DM candidates [52], or the supersymmetric partner of the axion, *axinos* as well. As the gravitino, the axino has smaller cross-sections than the typical WIMP and thus difficult to detect.
The subject of SUSY theories is a vast topic and only a few of many ideas are presented here. We only focussed on the most popular candidates and introduced them quickly. In fact, it would be impossible to review in only a few pages all of the candidates and their phenomenology.

SM particles and fields		SUSY partners			
		Interaction eigenstates		Mass eigenstates	
Symbol	Name	Symbol	Name	Symbol	Name
$q = u, d, c, s, b, t$	quark	$\tilde{q}_L$,$\tilde{q}_R$	squark	$\tilde{q}_1$,$\tilde{q}_2$	squark
$l = e, \mu, \tau$	lepton	$\tilde{l}_L$,$\tilde{l}_R$	slepton	$\tilde{l}_1$, $\tilde{l}_2$	slepton
$\nu = \nu_e, \nu_\mu, \nu_\tau$	neutrino	$\tilde{\nu}$	sneutrino	$\tilde{\nu}$	sneutrino
g	gluon	$\tilde{g}$	gluino	$\tilde{g}$	gluino
$W^\pm$	W-boson	$\tilde{W}^\pm$	wino	$\tilde{\chi}^\pm_{1,2}$	chargino
H^-	Higgs boson	$\tilde{H}^-_1$	higgsino		
H^+	Higgs boson	$\tilde{H}^+_2$	higgsino		
B	B-field	$\tilde{B}$	bino	$\tilde{\chi}^0_{1,2,3,4}$	neutralino
W^3	W^3-field	$\tilde{W}^3$	wino		
H^0_1	Higgs boson	$\tilde{H}^0_1$	higgsino		
H^0_2	Higgs boson	$\tilde{H}^0_2$	higgsino		
H^0_3	Higgs boson				

Table 1.3: **Particle content of the minimal supersymmetric model:** interaction and mass eigenstates, adapted from [47] and [48].

1.3.4 Particles from extra dimensions

In the attempt to unifying electromagnetism and gravity, Kaluza introduced the concept of extra dimensions [53]. We seem to be living in a universe with 3 space dimensions and 1 time dimension. However, it may be possible that other dimensions appear at higher energies. The hierarchy problem may also be resolved in these theories. The idea is that our 3+1 dimensional space-time, the so-called brane, is embedded in a $3 + \delta + 1$ space-time, the bulk. The hierarchy problem can then be addressed when the extra dimensions are compactified on circles of radius R, which lowers the Planck scale to an energy close to the electroweak scale. In brane world scenarios, the SM fields are confined on the brane while gravity can propagate in the bulk. In the case of universal extra dimensions, all fields, including SM bosons and fermions, can propagate in the extra dimensions. These theories provide viable DM candidates, as shown in [54].

Upon compactification of the extra dimension, all fields propagating in the bulk have their momentum quantized $p^2 \sim 1/R^2$ and thus a set of Fourier expanded modes appear, called Kaluza-Klein (KK) states. To us, in the brane, these KK states seem as a series (a tower) of states with masses $m_n = n/R$, where n in the mode number. In a similar fashion as in supersymmetry where R-parity ensures the stability of the LSP, in extra dimension it is the KK-parity $(-1)^n$ that stabilizes the Lightest Kaluza-Klein Particle (LKP). KK parity can be seen as a translation by πR with a flip of sign of all odd states in the KK Fourier decomposition of the bulk fields. In models with five or six dimensions and a compactification radius of TeV^{-1}, the first KK excitation of the hypercharge gauge boson, the photon, or of the neutrino are viable DM candidates. They have masses around the TeV and their annihilation cross-section is of the order

$$\sigma v \simeq 0.6 \text{ pb} \left(\frac{m_{KK}}{1 \text{ TeV}}\right)^2 . \tag{1.97}$$

Thus they are typical WIMPs. For example, the *KK-photon* annihilates mostly into charged lepton pairs and quark pairs. The *KK-neutrino* annihilates as well into quark pairs, charged leptons and of course neutrinos, for a mass of 1 TeV, the cross-section is 1.3 pb.

1.3.5 Wimpzillas

Superheavy long-lived particles have been suggested to explain the existence of Ultra-High Energy (UHE) cosmic rays with energies above $\sim 10^{18}$ eV. In fact up to this energy, cosmic rays are of solar and galactic origin. One explanation is the production of UHE cosmic rays due to the decay or annihilation of superheavy DM particles, called *wimpzillas* [55, 56].

These superheavy long-lived particles can be gravitationally produced from vacuum fluctuations during the transition from inflation to a matter- or radiation-dominated era, resulting from the non-adiabatic expansion of the background spacetime. In this scenario, the DM creation is similar to the generation of gravitational perturbations during inflation, the seeds of large scale structures [1]. The mass of the DM particle is of the order of the mass of the inflaton $m_\phi \sim 10^{13}$ GeV. Due to this large mass, DM never thermalizes and the abundance does not depend on weak couplings to other particles (as it is the case for the WIMP). More precisely, for masses $0.04 \lesssim m_X/H_I \lesssim 2$, where m_X is the mass of the wimpzillas and $H_I \sim m_\phi$ the Hubble constant after inflation, the abundance of X is of the order of 1 and does not overclose the universe. As the abundance is almost independent of any details of the non-gravitational interactions of the X field, the cross-sections with other particles may also be very large, X is then called a *simpzilla*.

1.3.6 Primordial black holes

Primordial Black Holes (PBH) are a non-elementary DM candidates and do not need an extension of the SM of particle physics. They could be produced from density fluctuations during inflation. If we assume that the whole mass in the horizon is absorbed into a PBH, in a radiation dominated universe, its mass is

$$\begin{aligned} M_{PBH} &= \frac{4\pi\sqrt{3}M_{pl}^3}{\sqrt{\rho_f}} \simeq 10^{32}\ \mathrm{g}\left(\frac{g_*}{100}\right)^{-1/2}\left(\frac{T_f}{\mathrm{GeV}}\right)^{-2} \\ &\simeq 2.8\times 10^{46}\ \mathrm{g}\left(\frac{g_*}{100}\right)^{-1/6}\left(\frac{k_f}{\mathrm{Mpc}^{-1}}\right)^{-2}, \end{aligned} \tag{1.98}$$

where ρ_f is the energy density, T_f the plasma temperature and k_f the comoving wavenumber corresponding to the Hubble horizon at formation of the PBH. They are naturally long-lived, as the lifetime of a PBH is

$$\tau_{PBH} \simeq 10^{64}\left(\frac{M_{PBH}}{2\times 10^{33}\ \mathrm{g}}\right)^3 \text{ years.} \tag{1.99}$$

And they are collisonless, as their size is

$$r \sim 10^{-8}\ \mathrm{cm}\left(\frac{M_{PBH}}{10^{20}\ \mathrm{g}}\right). \tag{1.100}$$

Different constraints apply on the mass of the PBH as a DM candidate, as shown on figure 1.15:

[1] A small difference remains between the quantum generation of energy density fluctuations and DM particle creation: in the case of DM, the inflaton does not dominate the mass density of the universe.

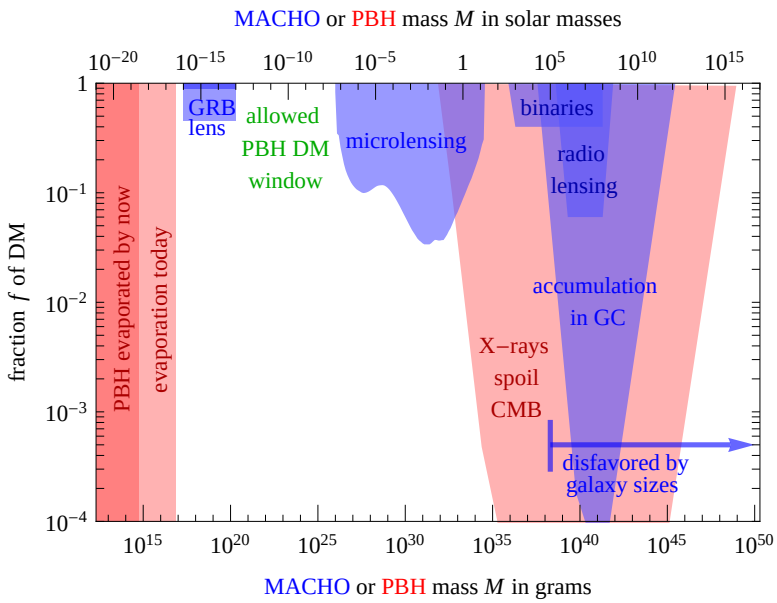

Figure 1.15: **Bounds on the fraction f of DM consisting of PBH** The blue bounds apply to any MACHO, including Primordial Black Holes (PBH), and the red bounds only to PBHs. Bound from the Kepler satellite are not shown in this plot [18].

- As we can see from equation 1.99, Black holes having a mass $M_{PBH} < 5 \times 10^{14}$ g would have evaporated by now due Hawking radiation [57].
- For masses $10^{15} \lesssim M_{PBH} \lesssim 10^{16}$ g, the PBH would emit γ-rays with energies of the order $E \sim 100$ MeV, which are not measured in the extra-galactic γ-ray background.
- For masses $10^{18} \lesssim M_{PBH} \lesssim 10^{20}$ g, femto-lensing of γ-ray bursts predicts that the abundance of PBH can only account for 10% of DM in the universe.
- For masses $10^{24} \lesssim M_{PBH} \lesssim 10^{26}$ g, Kepler can constrain PBH, even though it is designed to search for extra-solar planets, detecting the decreasing luminosity of the star when the planet passes by. For PBH, it is the opposite phenomenon appears: the luminosity of the star increases when a PBH passes through the line of sight [58].
- For masses $10^{26} \lesssim M_{PBH} \lesssim 10^{34}$ g, microlensing from the MACHO surveys exclude PNB as DM.
- Masses between $10^{33} \lesssim M_{PBH} \lesssim 10^{40}$ g are constrained by the CMB since they would affect BBN.

PBH in the mass range $10^{16} \lesssim M_{PBH} \lesssim 10^{22}$ g can be constraints by neutron stars: In a DM rich environment, PBH would have been captured by neutron stars of white dwarf and destructed the remnant by accretion. The number of neutron stars in globular clusters, where a high concentration of DM is expected, can thus constrain this mass range [59]. It is however very difficult to model the neutron star physics and the constraints can easily be weakend [60].

Finally the window $10^{20} \lesssim M_{PBH} \lesssim 10^{24}$ g is unconstrained. Also entropy arguments play in favor of PBH as DM [61]. No discrete symmetries need to be added to the SM of particle physics, but standard slow-roll scalar field inflation can not have the dynamics to form a sharp

peak in density perturbations necessary for the formation of PBH. Non-standard cosmological models have to be considered. For example, in multiple inflation scenarios, explosive particle production between the inflation periods can produce the sharp peaks in density fluctuations and PBH can form later [62, 63].

1.3.7 Other candidates

As we have seen, typical WIMPs appear naturally in certain theories, but also other candidates for DM are theoretically motivated. A few other examples are the following:

- *Asymmetric DM*: Since a particle-antiparticle asymmetry in present for the SM, it could also be the case for the DM sector, requiring non-self conjugated DM candidates. Assuming that the asymmetry for the baryons A_B and the one for DM A_{DM} are generated by similar physics, we get

$$\frac{\Omega_{DM}}{\Omega_b} \simeq \frac{n_{DM} m_{\rm DM}}{n_B m_N} \simeq \frac{m_{\rm DM}}{m_N}, \tag{1.101}$$

  where $m_N = m_p \simeq 1$ GeV is the mass of a nucleon. Since $\Omega_{DM}/\Omega_b \simeq 5$, the mass of the asymmetric DM candidate would be $m_{\rm DM} \simeq 5$ GeV [64].

- *Q-balls* are non-topological solitons (localized field configurations) which are stable due to conservation of charge Q. In fact, solitons represent the configuration with the lowest energy per unit charge. They appear, for example, in a theory with bosonic particles and an attraction between particles of same charge Q. A ball of bosonic particles is then created and stable against fission and evaporation, due to the attractive force. More precisely, the minimum of the energy functional

$$E = \int d^3x \left[(\partial_t \phi)^2 + (\nabla\phi)^2 + U(\phi^*\phi)\right], \tag{1.102}$$

  keeping the charge

$$Q = i \int d^3x \left[\phi^*(\partial\phi) - (\partial\phi^*)\phi\right] \tag{1.103}$$

  fixed is a spherically symmetric non-topological solution $\phi(r,t) = e^{i\omega t}\phi(r)$, if the minimum of $\frac{U(\phi^*\phi)}{\phi^*\phi}$ exists at $\phi_0 \neq 0$. In the SM, the only global symmetries are the ones associated with the baryon and lepton number B and L, but none of the scalar field carry them. In the MSSM however, there are 49 scalar fields carrying either B or L and may be stable in theories with gauge-mediated supersymmetry breaking. The mass of these objects scale as

$$m_Q \simeq \frac{4\pi\sqrt{2}}{3}\Lambda Q^{3/4}, \tag{1.104}$$

  where $\Lambda \sim 1 - 10$ TeV is the scale of the supersymmetry breaking. The charge $Q \sim 10^8 - 10^{20}$ for a B-ball and $Q > 10^{32}$ for a L-ball, to ensure it hasn't evaporated yet [65].

1.4 Searches for WIMPs

The thermal WIMP is very attractive candidate for DM from a theoretical point of view, it accounts for the correct relic abundance of DM in the universe and is predicted to exist

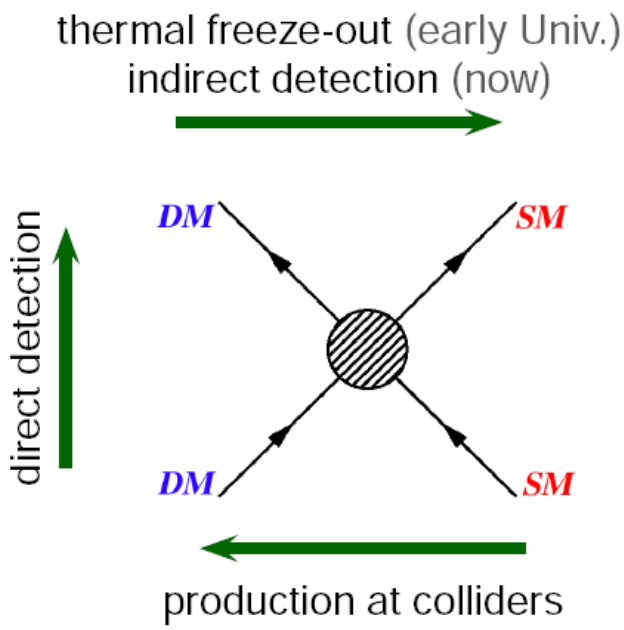

Figure 1.16: **Effective diagram representing the processes involving DM and SM particles:** annihilation, scattering and production, depending on the direction of the arrow of time [66].

in theories with supersymmetry or extra-dimensions. From an experimental point of view, its existence may be proven in different ways, giving the opportunity of cross-checking its potential characteristics. In fact, looking at the diagram in figure 1.16, depending on the arrow of time, WIMPs can be either produced at colliders through the collision of SM particles, directly detected through their scattering with a target material or indirectly detected through their annihilation in the halo (or in the Sun) and the extra contribution to cosmic rays. In the following, we will use consider DM as WIMPs, if the contrary is not explicitly written.

1.4.1 Direct detection of dark matter

Direct detection is based on the idea that if the Milky Way's halo is composed of WIMPs, then we are bathing in them and due to the velocity of the Sun circling around the GC, the WIMP flux on Earth should be of order $10^5(100\ \mathrm{GeV}/m_{\mathrm{DM}})\ \mathrm{cm}^{-2}\mathrm{s}^{-1}$. Even though WIMPs interact weakly, a very small fraction of them should recoil on a nucleus imparting a small amount of energy. The velocity of the WIMP wind in the laboratory frame is $v_\odot = 220 \pm 20$ km/s and $\beta = v/c \sim 0.73 \times 10^3$. Since the scattering occurs in the extremely non-relativistic regime, we can estimate the recoil energy

$$E_R \simeq \frac{1}{2} m_{\mathrm{DM}} \beta^2 c^2 \simeq 27\ \mathrm{keV} \left(\frac{m_{\mathrm{DM}}}{100\ \mathrm{GeV}} \right). \tag{1.105}$$

The idea is to detect this energy deposition in a target mass against an overwhelming number of background events. More precisely, the recoil energy is related to the scattering angle in the center of mass θ^*:

$$E_R = \frac{\mu_N^2 v^2 (1 - \cos\theta^*)}{m_N}, \tag{1.106}$$

where v the velocity of the DM particles and $\mu_N = m_{\rm DM} m_N/(m_{\rm DM}+m_N)$ is the WIMP-nucleus reduced mass. The differential event rate, measured in counts/kg/day (or dru=differential rate unit), is defined as

$$\frac{dR}{dE_R} = \frac{\rho_\odot}{m_N m_{\rm DM}} \int_{v_{min}}^{\infty} v f(v) \frac{d\sigma}{dE_R}(v, E_R) dv, \tag{1.107}$$

with ρ_0 the local WIMP density, m_N the nucleus mass, $f(v)$ the DM speed distribution and $d\sigma/dE_R$ the WIMP-nucleon cross-section. The minimum WIMP velocity which can cause a recoil of energy E_R is

$$v_{min} = \sqrt{\frac{m_N E_R}{2\mu_N^2}}. \tag{1.108}$$

The event rate is then found by integrating over all recoil energies, E_T being the threshold energy,

$$R = \int_{E_T}^{\infty} dE_R \frac{\rho_0}{m_N m_{\rm DM}} \int_{v_{min}}^{\infty} v f(v) \frac{d\sigma}{dE_R}(v, E_R) dv. \tag{1.109}$$

Particle Physics input

The WIMP-nucleon cross-section can be separated into a spin-independent and a spin-dependent contributions

$$\frac{d\sigma}{dE_R} = \left(\frac{d\sigma}{dE_R}\right)_{SI} + \left(\frac{d\sigma}{dE_R}\right)_{SD}. \tag{1.110}$$

Introducing the form factors $F(E_R)$ encoding the dependence on the momentum transfer $q = \sqrt{2m_N E_R}$ and accounting for the coherence loss, the spin and scalar components can be added coherently

$$\frac{d\sigma}{dE_R} = \frac{m_N}{2\mu^2 v^2} \left[\sigma_{SI}^0 F_{SI}^2(E_R) + \sigma_{SD}^0 F_{SD}^2(E_R)\right], \tag{1.111}$$

where σ_{SI}^0 and σ_{SD}^0 are the spin-independent and -dependent cross-sections at zero momentum transfer. If the DM field is named χ, the spin-independent contribution arises from scalar-scalar and vector-vector couplings such as

$$L \supset \alpha_q^S \bar{\chi}\chi\bar{q}q + \alpha_q^V \bar{\chi}\gamma_\mu\chi\bar{q}\gamma_\mu q \tag{1.112}$$

and can be written as

$$\sigma_{SI}^0 = \frac{4\mu}{\pi} \left[Z f_p + (A-Z) f_n\right]^2, \tag{1.113}$$

where Z and A are the number of protons and nucleons and f_p and f_n the couplings to protons and neutrons. In the case where the couplings are similar, σ_{SI} is proportional to A^2. Thus, the spin-independent cross-section is sensitive to high values of A.
The spin-dependent cross-section arises from couplings of the WIMP to the quark axial curent, such as

$$L \supset \alpha_q^A (\bar{\chi}\gamma^\mu\gamma_5\chi)(\bar{q}\gamma_\mu\gamma_5 q) \tag{1.114}$$

and is expressed in terms of the total angular momentum of the nucleus J and the expectation value of the spin content of proton and neutron $\langle S_{p,n}\rangle = \langle N|S_{p,n}|N\rangle$, with N the nucleus:

$$\sigma_{SD}^0 = \frac{32\mu^2}{\pi} G_F^2 \frac{J+1}{J} \left[a_p \langle S_p\rangle + a_n \langle S_n\rangle\right]^2, \tag{1.115}$$

where the coefficients a_p and a_n are effective WIMP-proton and WIMP-neutron couplings. As expected, the spin-dependent cross-section grows with the square of nucleus's spin. It is common to define the enhancement factor

$$C_A = \frac{8}{\pi}\frac{J+1}{J}\left[a_p\left\langle S_p\right\rangle + a_n\left\langle S_n\right\rangle\right]^2, \tag{1.116}$$

which can be decomposed in a proton and a neutron contribution $C_A = \left(\sqrt{C_A^p} + \sqrt{C_A^n}\right)^2$ with

$$C_A^p = \frac{8}{\pi}\frac{J+1}{J}\left(a_p\left\langle S_p\right\rangle\right)^2 \quad \text{and} \quad C_A^n = \frac{8}{\pi}\frac{J+1}{J}\left(a_n\left\langle S_n\right\rangle\right)^2. \tag{1.117}$$

The ratios $C_A^p/C_A = \frac{4}{3}\left\langle S_p\right\rangle\frac{J+1}{J}$ and $C_A^n/C_A = \frac{4}{3}\left\langle S_n\right\rangle\frac{J+1}{J}$ independent of the WIMP model and characterizes the target mass. The values of these coefficients for different elements can be found in table 1.4.

Nucleus	A	Z	J	$\langle S_p\rangle$	$\langle S_n\rangle$	C_A^p/C_A	C_A^n/C_A
F	19	9	1/2	+0.477	−0.004	9.10×10^{-1}	6.40×10^{-5}
Na	23	11	3/2	+0.248	+0.020	1.37×10^{-1}	8.89×10^{-4}
Al	27	13	5/2	−0.343	+0.030	2.20×10^{-1}	1.68×10^{-3}
Si	29	14	1/2	−0.002	+0.130	1.60×10^{-5}	6.76×10^{-2}
Cl	35	17	3/2	−0.083	+0.004	1.53×10^{-2}	3.56×10^{-5}
K	39	19	3/2	−0.180	+0.050	7.20×10^{-2}	5.56×10^{-3}
Ge	73	32	9/2	+0.030	+0.378	1.47×10^{-3}	2.33×10^{-1}
Nb	93	41	9/2	+0.460	+0.080	3.45×10^{-1}	1.04×10^{-2}
Te	125	52	1/2	+0.001	+0.287	4.00×10^{-6}	3.29×10^{-1}
I	127	53	5/2	+0.309	+0.075	1.78×10^{-1}	1.05×10^{-2}
Xe	129	54	1/2	+0.028	+0.359	3.14×10^{-3}	5.16×10^{-1}
Xe	131	54	3/2	−0.009	−0.227	1.80×10^{-4}	1.15×10^{-1}

Table 1.4: **Properties of different nuclei** used for DM indirect detection, adapted from [67].

Astrophysics input

To compute the differential event rate (equation 1.107), we need the measurement of the local DM density $\rho_\odot = \rho(r = r_\odot)$, with $\rho_\odot$ the solar radius, as well as the velocity distribution $f(v)$. In direct detection experiments, the standard value of the location of solar system in the Galaxy is $r_\odot = 8.5$ kpc [68] [2]. The local DM density can be obtained by measuring the galaxy rotation curve of the Milky Way and microlensing [69] and is of the order $0.1 - 0.5$ cm^{-3}. A more recent study gives $\rho_\odot = 0.30 \pm 0.05$ [70]. Thus, in general, the standard value is $\rho_\odot = 0.3$ GeV/cm^3. In the Standard Halo Model (SHM), the speed distribution is assumed to be a isotropic and Gaussian (or Maxwellian)

$$f(v) = \frac{1}{\sqrt{2\pi}\sigma}\exp\left(-\frac{v^2}{2\sigma^2}\right), \tag{1.118}$$

where the speed distribution is related to the circular speed of the Sun v_c by $\sigma = \sqrt{3/2}v_c \simeq 270$ km/s, as $v_c = 220\pm20$ km/s [71]. This velocity distribution corresponds to an isothermal sphere

[2] In section 1.1.3, we used a slightly different value, namely $r_\odot = 8.33$ kpc, this is based on more recent measurements

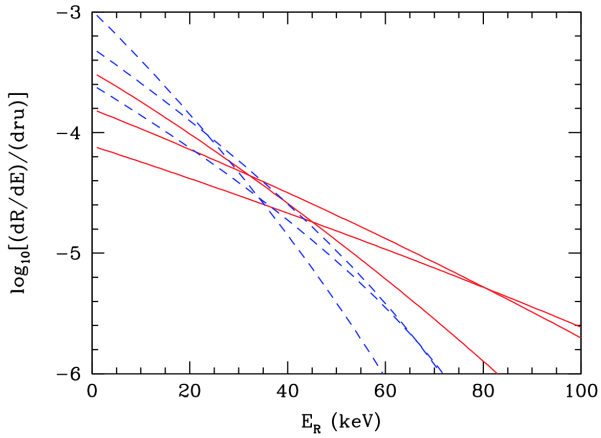

Figure 1.17: **Spin-independent differential rate** as a function of recoil energy, for WIMP masses $m_{\rm DM} = 50$, 100 and 200 keV (from top to bottom at $E_R = 0$) and $\sigma_{SI} = 10^{-44}$ cm^{-2}. The red lines represents a target of Germanium and dashed blue lines Xenon [72].

with density profile $\rho(r) \propto r^{-2}$, as we have seen in section 1.1.3. Particles with speed greater than the local escape speed are not gravitationally bound. The function 1.118 extends out to infinite radii and thus the speed distribution in this model must be truncated by hand, typically $v_{esc} = 650$ km/s.

Energy dependence

For the SHM, the differential event rate in equation 1.107 becomes

$$\frac{dR}{dE_R} \simeq \left(\frac{dR}{dE_R}\right)_0 F^2(E_R) \exp\left(-\frac{E_R}{E_c}\right), \tag{1.119}$$

with $(dR/dE_R)_0$ the event rate when $E \to 0$ keV and $E_c = c_1 2\mu_N v_c^2/m_N$ the characteristic energy scale. The parameter c_1 depends on the target nuclei and is of order 1. The total event rate, presented in figure 1.17 for the spin-independent case, declines with growing recoil energy. The decrease in rate is steepest for heavy target nuclei. At zero momentum transfer, the differential event rate is the highest for Xenon, compared to germanium. The energy spectrum also depends on the WIMP mass, which can then be reconstructed from the energies of detected events. A larger target mass will probe heavy DM, while for light WIMPs the event rate above the detector threshold energy E_T can be small.

Time dependence

Since the Earth is rotating around the Sun, the differential event rate has a time dependance, especially an annual modulation. In summer, the Earth rotates in the same direction as the rotation of Sun and the WIMP wind is increased. In winter, it is the other way around. The Earth's orbital speed around the Sun ($v_e \simeq 30$ km/s) is significantly smaller than the Sun's circular speed around the galactic center ($v_c \simeq 220$ km/s) and thus the differential event rate can be expanded in a Taylor series

$$\frac{dR}{dE_R} \simeq \left(\frac{d\bar{R}}{dE_R}\right) [1 + \Delta(E_R) \cos\alpha(t)], \tag{1.120}$$

where $\alpha(t) = 2\pi(t - t_0)/T$ with $T = 1$ year and $t_0 = 150$ days. This seasonal effect changes the amplitude of a WIMP signal by 1-10%.

Detection principles

Different methods can be used to detect the energy deposition of a WIMP scattering off a nucleus: scintillation in crystals/liquids, ionization in crystals/liquids, bubble formation in liquids/gel and thermal/athermal heating in crystals. Experiments searching for the annual modulation of the WIMP signal look for one type of observable. For example, CoGeNT [73] uses ionization while DAMA/LIBRA [74], DEAP/CLEAN [75] and KIMS [76] use scintillation. On the other hand, experiments which are integrating the potential DM events need to use a combination of two signals in order to reject the background efficiently. XENON [77], LUX [78] and DarkSide [79] use both ionization and scintillation signals. Furthermore, CRESST [80] detects the scintillation and the phonon signal of nuclear recoil and CDMS [81] and Edelweiss [82] the ionization and photon signal. Finally, superheated droplet detectors, such as COUPP [83] and PICASSO [84] search for bubbles due to the phase transition of liquid to gas.

The detection of a WIMP is in principle easy as it should interact with the nucleus and not the electrons in the target mass. In the materials used, scattering of atomic nuclei leads to different physical effects than scattering from an electrons and thus electron recoil can be rejected. However, neutrons from environmental radioactivity or the spallation of cosmic rays muons may interact with the nucleus and look like a WIMP. To minimize these background events, the experiments are placed in deep underground laboratories and have a lot of shielding.

Constraints and signals hints

Assuming the SHM, events or their absence can be interpreted in terms of the WIMP mass and WIMP-nucleon cross-section. In fact, several experiments have reported excess events over the expected background, such as the DAMA annual modulation signal or the CRESST and CDMS II Silicon events. These regions are represented by closed contours on figure 1.18 while other experiments exclude these same parameter spaces (straight lines on the plot). Future experiments (dashed lines) will further probe these regions, as well as the regions where the scattering of neutrinos with nuclei represent an irreducible background. Neutrinos can come from the Sun (the B^7 and B^8 production), the atmosphere and diffuse supernova.

At low WIMP masses, different experiments probe different part of the velocity distribution, especially the high velocity tail. Precise cosmological N-body simulations, such as the Via Lactea II simulation [86], reproduce galaxies with the characteristics of the Milky Way. However, the speed distribution of the DM particles do not exactly follow a Maxwelian function. The comparison between different experiment may be more difficult than expected [87]. Another way of expressing constraints or signal regions is in a halo-independent approach [88]. For the spin independent component, the total event rate can be expressed as

$$R = \int_{E_T}^{\infty} \frac{1}{2\mu^2\sigma_p}\sigma_{SI}^0 F_{SI}^2(E_R)\underbrace{\frac{\sigma_p\rho_\odot}{m_{\mathrm{DM}}}\int_{v_{min}}^{\infty} v f(v,t)dv}_{=\tilde{\eta}(v_{min},t)}, \tag{1.121}$$

where σ_p is the WIMP-proton cross-section. Changing our integration variable from E_R to v_{min} through equation 1.108, the total rate can be written as

$$R = \int_0^{\infty} dv_{min}\frac{2}{m_N\sigma_p}\sigma_{SI}^0 F_{SI}^2 v_{min}\tilde{\eta}(v_{min},t) = \int_0^{\infty} dv_{min}\mathcal{R}^{SI}(v_{min})\tilde{\eta}(v_{min},t), \tag{1.122}$$

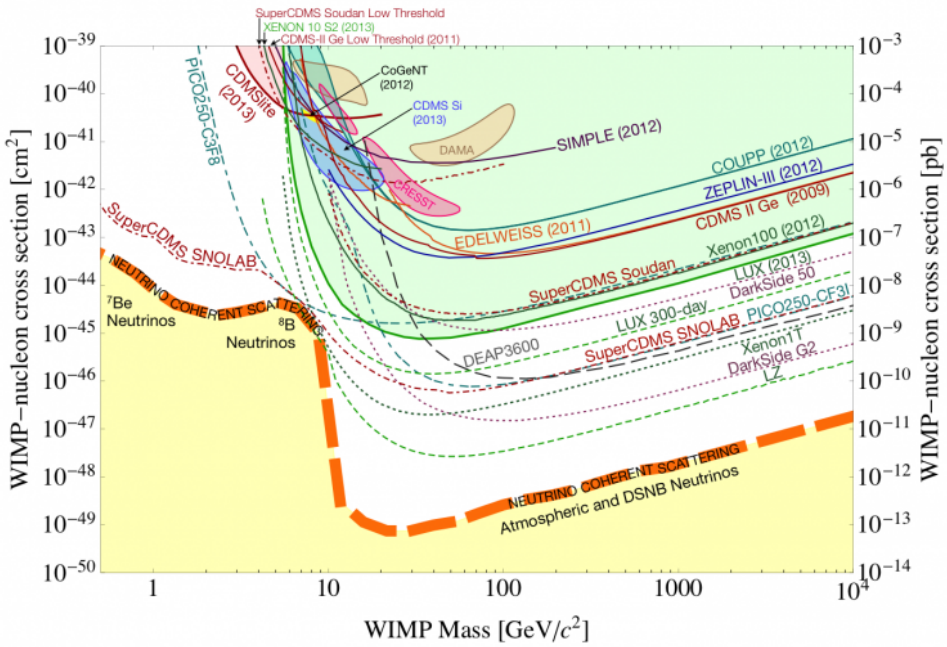

Figure 1.18: **Exclusion limits (continuous lines), signal regions (closed contours) and future sensitivities (dashed lines) on the spin-independent WIMP-nucleon cross-section** from different direct detection experiments. The yellow band represents the region where coherent scattering of neutrinos on nuclei becomes important [85].

where $\mathcal{R}^{SI}(v_{min})$ is the response function of the detector. The time-dependence in $\tilde{\eta}$ is Taylor expanded as previously for the differential event rate and upper limits as well as signals can be represented in the $(v_{min}, \tilde{\eta}(v_{min}))$-plane, once the mass of the WIMP is fixed. Assuming isospin-conserving couplings $f_n = f_p$ or even isospin-violating couplings $f_n/f_p = -0.7$, it is still difficult to reconcile experiments with positive signals and those with negative results [89].

1.4.2 Collider searches of dark matter

After the discovery of the Higgs boson by the CMS and ATLAS collaborations [90, 91], these experiments search for new physics. One of these phenomena is the DM pair production at colliders through the reaction $pp \to \chi\bar{\chi}$. Since WIMPs interact very weakly, they will fly away from the detector without ever being seen. However they will carry a lot of energy out of the detector and thus the signature of DM production is missing energy. In order to select events that may produce these invisible particles, we need to see an initial state radiation: the quarks emit a gluon (and then a jet), γ, W or Z boson, providing a kick into the transverse plane. Thus, the final states used for collider searches of DM are Mono-X (where X is g, γ, W or Z)+ missing transverse energy $\not{E}_T$ or missing transverse momentum $\not{p}_T$. Since the X particles are emitted from the incoming legs, the relative rates of these radiations are determined by the SM.

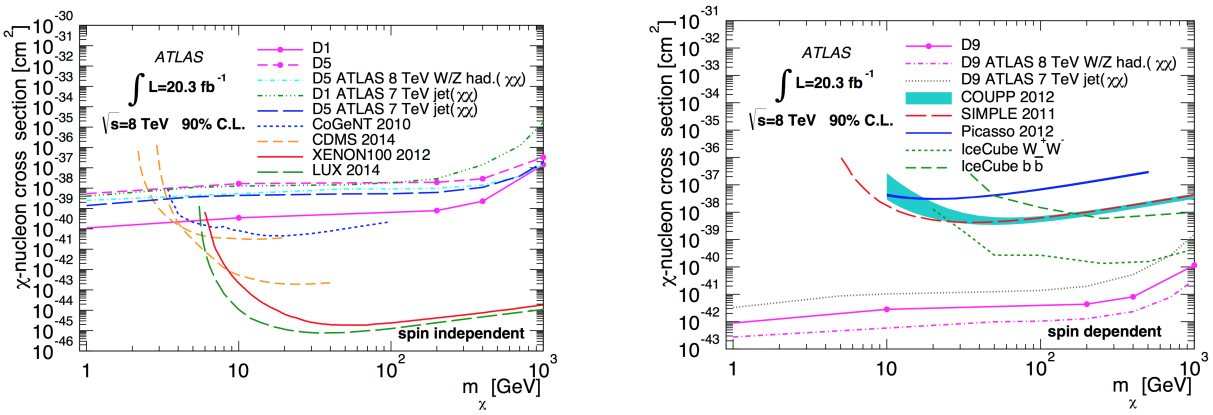

Figure 1.19: **ATLAS bounds on dark matter** in events with a Z boson and missing transverse momentum in pp collisions at $\sqrt{s} = 8$ TeV in a naïve EFT approach. Events with large missing transverse momentum and two oppositely-charged electrons or muons consistent with the decay of a Z boson are analyzed [92].

DM production cross-sections are very model-dependent. The only way to have model-independent constraints is to use an Effective Field Theory approach (EFT), like the Fermi theory of weak interactions. We assume that the interaction between the DM and SM particles is mediated by an unknown and unresolved mediator of mass M. The interaction in figure 1.16 is then effectively modeled by a four-point interaction. The mass scale of the unknown interaction is then $M_* = M/\sqrt{g_1 g_2}$, where g_1 and g_2 are the couplings of the mediator to DM and SM fields. The EFT lagrangian describing the interactions of DM with SM contains operators with dimension $d > 4$ in order to be renormalizable.

The effective operators describing the pair production can be found in [93], where the DM-field χ can be a Dirac fermion (operators D1-D14), a complex scalar (operators C1-C6) or a real scalar (operators R1-R4). The EFT approach is accurate in describing the microscopic physics for scattering at low enough center-of-mass energy E_{cm}, below a certain cutoff scale M_{cut}, which depends on the mass of the mediator M in the underlying microscopic theory. But it is unknown to the EFT and is thus treated as a free parameter, as are the DM mass m_{DM} and the interaction scale M_*, in the regime where $E_{cm} < M_{cut}$.

The EFT can predict the DM annihilation cross-section determining the relic density, present annihilation important for indirect detection, as well as scattering of a nucleus in direct detection experiments. In fact all these processes take place at safely small E_{cm}. For collider searches, it is however different and thus needs extra treatment. In fact, certain events may occur at center-of-mass energies higher than the cutoff scale. These events can be discarded and the bounds on the DM production cross-section can be obtained in a very conservative way by using only events in the validity region of the EFT. The limits are expressed in the (m_{DM}, M_*)-plane for different values of M_{cut} [94] and for different operators. For $M_{cut} = 8$ TeV, the limit on M_* is the same as the one in a naïve EFT, where no restriction on the center-of-mass energy is imposed. In this approach and for some operators, the bounds on the scale M_* can be translated into bounds on the WIMP-nucleon cross-section. As we can see on figures 1.19 and 1.20, collider searches are very powerful for low mass WIMPs, where direct detection experiments loose their sensitivities and are thus complementary. However, the presented bounds are only valid in a naïve EFT approach, i.e. when mediator is massive enough. If the mediator is lighter

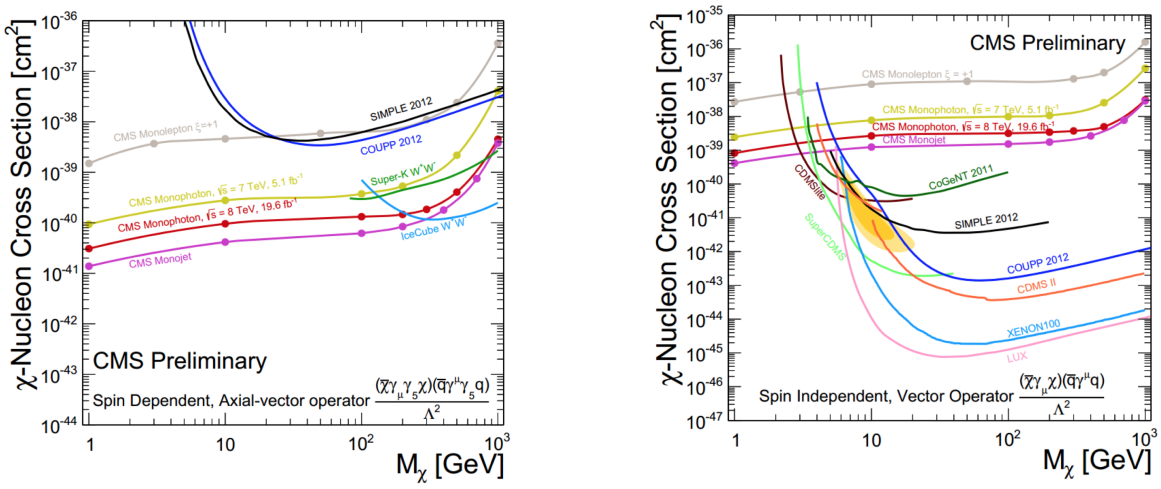

Figure 1.20: **CMS bounds on dark matter** mono-photon searches for the D8 operator on the right and D5 operator on the left in a naïve EFT approach [95].

than ~ 8 TeV, the bounds need to be relaxed (almost independently of the DM mass).

Apart from the EFT approach, simplified models can also be a way to probe DM in an almost model-independent way. Comparing two different simplified models giving rise to the same EFT operator shows that the EFT approach excludes the parameter space which is still unconstrained [94]. The presented bounds on EFT operator should thus be treated with caution.

Searches of other BSM theories could also give us a hint on the nature of DM. For example if supersymmetric particles were found at LHC, the next step in DM searches would be to look out for neutralinos. The collaborations at LHC are also searching for lepto-quarks (found in grand unification theories), lepton flavor violation, compositeness of leptons and quarks, etc.. In the full LHC Run I (luminosity of 20 fb^{-1} and $\sqrt{s} = 8$ TeV), no evidence for new exotic physics has been found confirming the validity of the SM up to these energies [96]. The future of DM collider searches still lies in the LHC since the Run II will provide us with new data at higher luminosity and energy.

1.4.3 Indirect detection of dark matter

The idea behind indirect detection is, as the name says, not to measure DM directly, but to detect the products or effects of its annihilation. In today's universe, annihilations or decay in galaxy halos will produce cosmic rays. As we have seen earlier, WIMPs can annihilate or decay into various channels (quarks, leptons, bosons and maybe other noes particles such an intermediate vector V which then decays into leptons). These particles are or will produce cosmic rays, that we can detect at Earth, such as photons, neutrinos or antimatter particles (positrons, antiprotons and antideuteron).

Gamma-rays

Photons (and neutrinos) from DM annihilation travel through space undisturbed and their flux at Earth is

$$\frac{dR}{d\Omega dE} = \frac{1}{2}\frac{\langle\sigma v\rangle}{m_{\rm DM}^2}\sum_i BR_i \frac{dN_\gamma^i}{dE_i} \times J(\Delta\Omega), \tag{1.123}$$

where BR_i is the branching ratio into different primary channels, $\frac{dN_\gamma^i}{dE_i}$ the photon spectrum and $J(\Delta\Omega)$ the "J-factor" contains all the astrophysical information and defined by

$$J(\Delta\Omega) = \int_{\Delta\Omega} d\Omega \int_{l.o.s.}^{\infty} ds\ \rho_{DM}^2\left(r(s)\right), \tag{1.124}$$

with s the line of sight, related to the distance to the center of the halo r. There are different targets for γ-ray searches, each having advantages and disadvantages, shown in table 1.5 : the **Galactic Center (GC)** of our Galaxy, **dwarf Spheroidal galaxies (dSph)** gravitationally bound to the Milky Way, **clusters of galaxies**, **dark satellites**, DM satellites in which no stars have formed, the **galactic diffuse emission** and the **isotropic background**, the redshifted contributions of all galaxies in the universe. Limits from the γ-rays emitted by our neighboring galaxy Andromeda (M31) are not very competitive.

target region	advantages	inconveniences
Galactic Center	high concentration of DM close proximity → spectral features as smoking gun	uncertainty on the DM profile important population of γ-ray sources diffuse emission from cosmic rays
dSph	no γ-ray point sources no intrinsic diffuse emission no substructures	"ultra-faint" satellites recently reevaluated uncertainties on DM distribution
Dark satellites	smoking gun confirmation of ΛCDM	not found yet
Clusters	DM dominated bright sources	unknown substructures uncertainty on the mass profile
Galactic diffuse emission	spectral and spatial distribution can be used	astrophysical diffuse emission
Isotropic background	spectral and spatial distribution can be used	halo and subhalo abundance as a function of redshift to be modeled contribution of astrophysical sources

Table 1.5: **DM γ-ray sources**, their advantages and inconveniences.

Since the J-factor grows as the DM density squared, the best targets are the ones with a high concentration of DM, such as the GC, clusters, dwarf spheroidal galaxies and hypothetically dark satellites. Several difficulties can arise: Since the halo density profile in the inner part of our Galaxy is unknown, the GC is subject to high uncertainties. Substructures, predicted by ΛCDM model, will enhance the γ-ray signal, as their concentration in DM is very high. However modeling their contribution is difficult due to their unknown density and number. Diffuse emission from cosmic rays and γ-ray point sources also need to be modeled and add uncertainties to the γ-ray signal from WIMP annihilations. Gamma-ray experiments can be ground-based or on orbit around the Earth. Ground-based telescopes are Imaging Atmospheric Cherenkov Telescopes (IACT). As for neutrino telescopes, a γ-ray photon passing through the atmosphere will produce an electromagnetic cascade and a shower of electromagnetic particles. Ground-based experiments indirectly observe the γ-ray photon by detecting the secondary particles and the Cherenkov light, due to the interaction of the photon with the Earth's atmosphere. These experiments include MAGIC [97], VERITAS [98] and HESS [99]. In low-Earth orbit, the Fermi satellite, has two instruments on board: the gamma-ray monitor and the Large Area Telescope (LAT) [100], the successor of the EGRET [101] mission onboard the COMPTON-GRO satellite. A γ-ray photon entering the LAT converter foils will produce an electron/positron pair, which can be tracked.

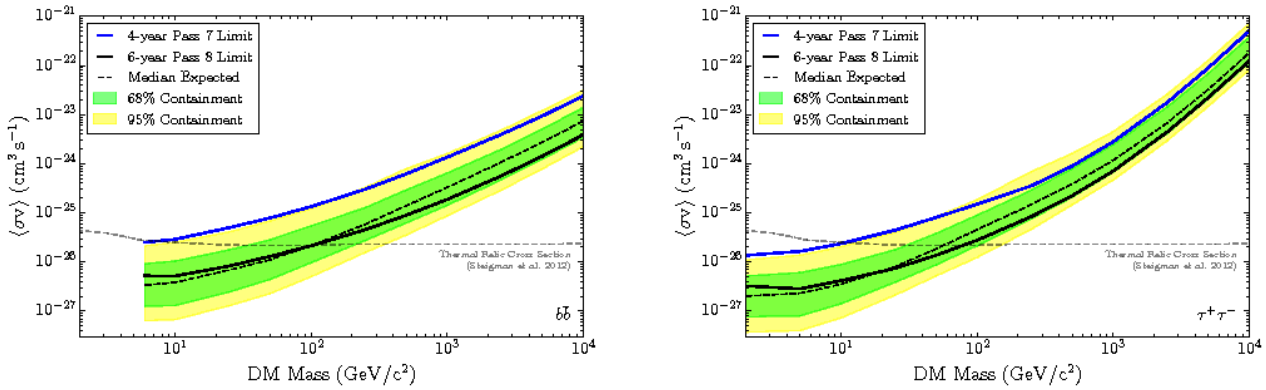

Figure 1.21: **Constraints on DM from a combined analysis of 15 dSph** using 4- and 6-years of Fermi-LAT data and Pass 7 and the new Pass 8 event-level analysis, respectively. [105].

At the Galactic Center, an excess of γ-rays has been observed by these experiments and can be interpreted as the annihilation of DM, for example, into $b\bar{b}$ with a mass of $m_{\rm DM} = 30 - 40$ GeV and annihilation cross-section $\langle\sigma v\rangle = 1.4 - 2 \times 10^{-26}$ cm^{3}s^{-1} [102]. We will further discuss this excess and constraints form antiprotons in chapter 3.
A line in γ-rays is usually called the golden channel, as no known astrophysical processes could explain it. At the GC, a line around 130 GeV was discovered in 2012 [103, 104]. In the end, the signal does not seem to be caused by DM annihilations, but by a combination of instrumental effects and statistical fluctuations.
Dwarf spheroidal galaxies are very popular targets from DM searches and a combined analysis puts very stringent constraints on the DM annihilation cross-section, as shown in figure 1.21. However, very recently, a dwarf galaxy newly discovered by the Dark Energy Survey (DES), called Reticulum 2, may show an excess in γ-ray emission [106].

Neutrinos

Neutrinos from DM annihilations are produced and travel through space in the same way as photons. The typical targets are the GC, halo, dwarf galaxies and clusters. The only difference is that they are more difficult to detect, since they interact very weakly with other SM particles. Like direct detection experiments, neutrino detectors are based underground or underwater, limiting the background. In fact, neutrinos are observed by their muon tracks in the detector produced in charged current interaction inside or close to the detector. The muons will travel through the detector volume at a speed higher than the speed of light in the detection material and emit Cherenkov light. Neutrino telescopes are kilometer-scale experiments of large arrays of photo-multipliers, deep in the ice or the water. Currently searching for DM annihilation products are the IceCube experiment [107], situated at the South-Pole, and ANTARES [108] in the Mediterranean sea, close to Toulon in France.

Limits on annihilation cross-section are not very competitive with other types of indirect searches. In fact, for a DM mass of 100 GeV and annihilation into quarks, the upper bounds lie at least two orders of magnitude higher than constraints from Fermai-LAT. They become competitive for very high masses, close to the unitarity bound. In the case of annihilation into leptons, the bounds from neutrino telescopes are comparable to the ones obtained by γ-ray experiments and become more stringent for DM masses above 1 TeV.

In searching for DM, neutrino telescopes are much more relevant for the WIMP-nucleon cross-section, like direct detection experiments. In fact, DM particles are captured by any massive body, such as the Sun (or the Earth), by scattering off the nuclei, losing energy and thus accumulating at the center. They will annihilate and create high energy neutrinos, which can then be detected at Earth, even after their oscillations and interactions with the dense matter of the Sun. Neutrinos from nuclear fusion are typically much less energetic than the ones induced by DM annihilations in the Sun. The absence of these high energy neutrinos imposes constraints on the spin-dependent scattering cross-section of DM particles with hydrogen nuclei as well as on the spin-independent cross-section of DM with other nuclei. These bounds are very competitive with current direct detection experiments, but also depend on the annihilation channel. As expected, annihilations into leptons would give rise to a larger neutrino flux than annihilations into quarks, as shown on figure 1.22. For example, for the τ-channel, the limits from IC79 (IceCube using only 79 out of the 86 photo-multiplier strings) and ANTARES on the WIMP-nucleon cross-section are 2 orders of magnitude stronger than the ones from the direct detection experiment COUPP [109].

Charged particles

The sources and propagation of charged particles in the Galaxy will be discussed in detail in chapter 2, constraints on antiprotons in chapter 3 and constraints from photon emission from electrons and positrons in chapter 4. Anti-particles are used for DM searches since they are very rarely produced in astrophysical processes. For example, the antiproton flux is 10^4 times smaller than the one from protons, the same is true for positrons. DM annihilation should produce the same amount of particles and antiparticle [3] and even a small contribution from DM annihilation could be detectable over the background. These charged cosmic rays need to be detected from space without the influence of the atmosphere. The latest results on cosmic rays are provided by AMS-02, a magnetic spectrometer measuring particle fluxes on the International Space Station (ISS) since 2012 [112]. The experiment is supposed to last for two decades and has an exceptional precision.

The astrophysical contribution to the positron fraction $\phi(e^+)/(\phi(e^+) + \phi(e^-))$ is expected to decrease with energy. However, as we can see on the left of figure 1.23, for energies above 10 GeV, the positron fraction is rising. This is known as the positron or PAMELA excess, as it has been first measured with high accuracy by the PAMELA experiment [115], a spectrometer on board a Russian satellite launched in 2006. Confirmed by AMS-02 and together with a hard (electron+positron) spectrum measured by Fermi-LAT, this excess suggests an additional source of primary positrons. WIMPs with masses $m_{\rm DM} \gtrsim 1$ TeV annihilating into leptonic channels with a cross-section of the order of 10^{-23} cm^{3}s^{-1} could produce these extra positrons. The annihilation cross-section is very high compared to the thermal one and thus an enhancement mechanism, such as substructures or Sommerfeld enhancement, would be necessary to keep this interpretation alive [116]. Astrophysical sources may also be the reason for this excess and the hard (electron+positron) spectrum. Local SuperNovaRemnants (SNR) [117] and pulsars may be the cause: one single close-by mature pulsar, such as Monogem or Gemiga or the sum of pulsars in the Milky Way population could be the source of these positrons. [118, 119]. A way of testing the hypothesis of one single pulsar can be to measure the positron anisotropy.

Antiprotons measured by PAMELA, on the other hand, can be explained by astrophysical secondaries only, as shown on the right panel of figure 1.23, and thus a very powerful probe to

[3] unless DM is asymmetric [64, 110]

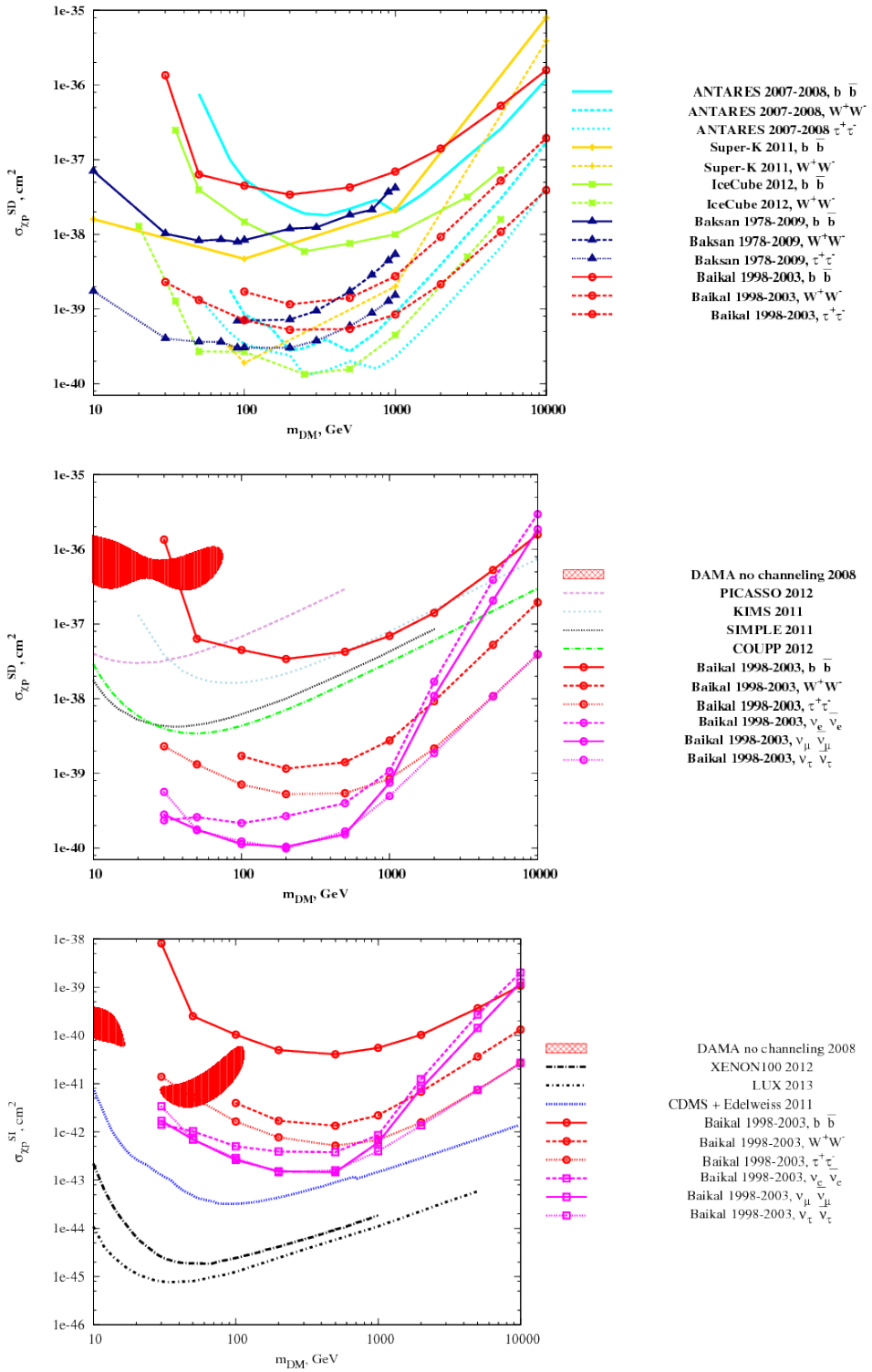

Figure 1.22: **Limits on spin-dependent and -independent WIMP-nucleon cross-section from neutrino telescopes** First row: Baikal, ANTARES, Baksan, IceCube and SuperKamiokande 90% CL limits on the spin-dependent elastic cross-section of DM particles on protons. Second row: Comparison of Baikal 90% CL limits on the spin-dependent elastic cross section of DM particles on protons with the results of direct searches: DAMA, PICASSO, KIMS, SIMPLE and COUPP. Bottom row: Comparison of Baikal 90% CL limits on the spin-independent elastic cross section of DM particles on protons with the results of direct searches: DAMA, CDMS/Edelweiss, XENON and LUX [111].

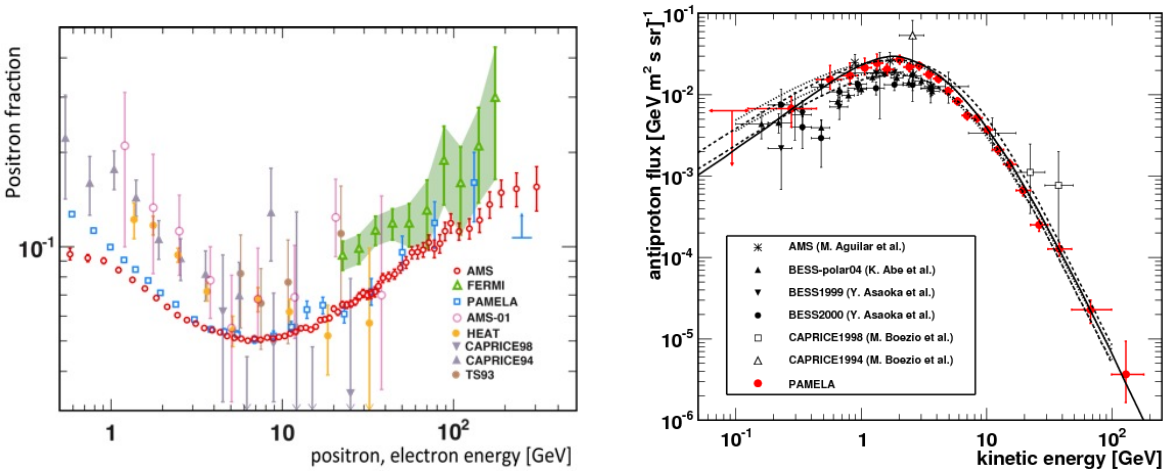

Figure 1.23: **The positron fraction** measured by different experiments and presented by AMS-02 at ICRC in 2013 [113] and **antiproton flux** measured by several experiments, in particular PAMELA [114]. The different measurements had been taken at different times and thus at different solar activities which explains the discrepancy for energies $E \lesssim 10$ GeV.

constrain DM. Antideuterons (the bound states of an antiproton and an antineutron) could also be produced by WIMP annihilations via coalescence and provide a smoking gun signature of DM. In fact, the DM signal, even though it is very small, would be orders of magnitude higher than the astrophysical background, as seen on figure 1.24. In fact, the astrophysical background is obtained from the spallation of cosmic ray protons hitting hydrogen or helium atoms in the interstellar medium (see section 2.2.2). In this type of reactions, the outgoing antideuteron has a high momentum. In DM annihilations, the reaction takes place almost at rest and the antideuteron has a very low momentum. Thus, the contribution from DM annihilation peaks at a lower energy than the one from standard astrophysical processes.
Detecting only one sub-GeV antideuteron in cosmic rays would be a game changing event in terms of WIMP searches. Current constraints are provided by BESS [121], but also AMS-02 can detect antideuterons [122], as well as the future experiment General AntiParticle Spectrometer (GAPS) [123, 124]. It will be dedicated balloon or satellite experiment slowing down the antideuteron inside the detector, which will forme an exotic atom in an excited state and decay emitting a characteristic X-ray and pion radiation. A successful prototype flew on a balloon in 2012 and the actual experiment should fly in 2017. Note that also antihelium may be a probe for DM, but is even more difficult to detect than antideuteron [125].

Constraints from CMB

In the early universe, DM annihilations are responsible for the abundance today, but also inject energy into the plasma and have an effect on the thermal history of the universe which reflects on the power spectrum of the CMB. More precisely, the energy released by DM annihilation is

$$\left.\frac{dE}{dt}\right|_{DM}(z) = \rho_c^2 \Omega_{DM}^2 (1+z)^6 f(z) \frac{\langle \sigma v \rangle}{m_{\rm DM}}, \tag{1.125}$$

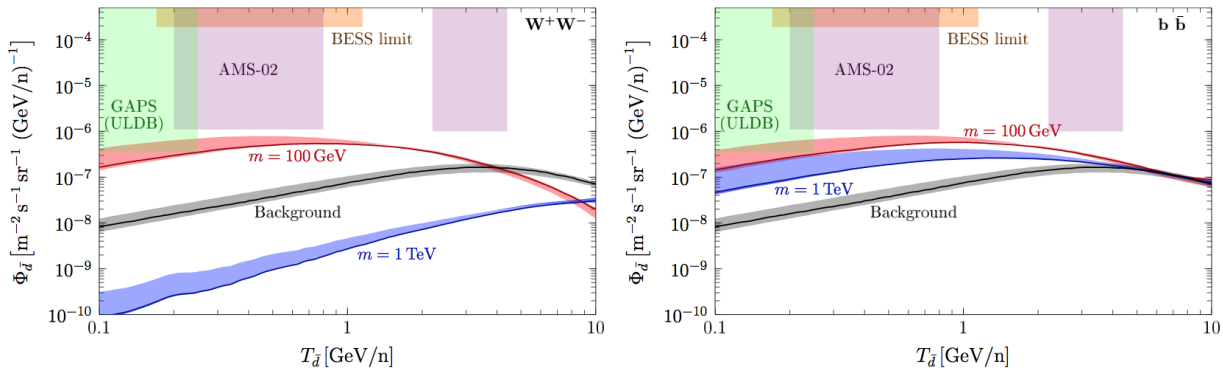

Figure 1.24: **Maximum antideuteron flux** from dark matter annihilations assuming a NFW dark matter halo profile and a value of the coalescence momentum $p_0 = 192$ MeV. The black line is the expected background and the shaded area show the propagation uncertainty [120].

where $f(z)$, the fraction of energy absorbed by the plasma and takes values between $\sim 0.3 - 1$ depending on the annihilation channel [126]. This energy will then ionize, excite and heat the plasma and specifically the hydrogen atoms inhibiting recombination. The parameter encoding the DM characteristics is $p_{ann}(z) = f(z)\langle\sigma v\rangle / m_{\rm DM}$, which generally depends on the redshift z, but can be taken constant to a very good approximation [127]. Depending on the value of the annihilation parameter p_{ann}, we have a damping of the CMB peaks, temperature as well as polarization. The latest constraints on this parameter comes from Planck [26]

$$p_{ann} < 3.4 \times 10^{-28}\ \mathrm{cm^3 s^{-1} GeV^{-1}} \tag{1.126}$$

at 95 % confidence level, varying all the other cosmological parameters of ΛCDM and using TT, EE, TE spectra, as well as lensing data.

Example of non-WIMP DM searches: X-rays

Warm DM, such as keV sterile neutrinos, cannot produce the same signatures as WIMPs. As we have seen earlier, sterile neutrinos are also very good DM candidates. They can decay into SM neutrinos plus a photon or two monochromatic photons with an energy corresponding to half the sterile neutrino mass, i.e. X-rays. The ideal targets are the same as for γ-ray searches: nearby clusters of galaxies or nearby galaxies such as Andromeda or local dwarf spheroidal galaxies. Recently, an unknown emission line in X-rays has been discovered using XMM-Newton in the Andromeda galaxy and the Perseus galaxy cluster [128]. An independent analysis of Chandra data of staked galaxy clusters showed the same results: an unexplained line with energy $E \simeq 3.5$ keV is present in DM dominated systems [129]. If this signal is due to the decay of a sterile neutrino, the mass should be $m_s = 7.1$ keV, as shown on figure 1.25. Another possibility is that this line is due to an atomic transition, for example from potassium [130].

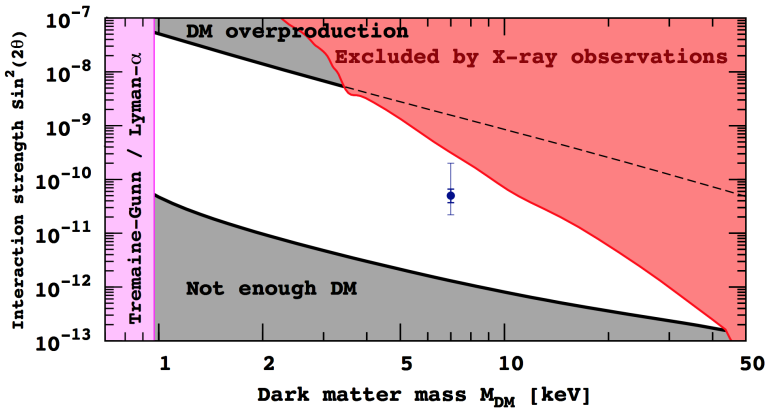

Figure 1.25: **Interpretation of the 3.5 keV-line from the Andromeda galaxy (M31)** detected by XMM-Newton as the decay of sterile neutrino DM and previous constraints [128].

Chapter 2

Cosmic Rays: origin and propagation

2.1 Introduction

Cosmic Rays (CR) were discovered in 1912 by Victor Hess due to their ionization effect using portable electroscopes on board atmospheric balloons [131]. Before Hess's experiments, electric charges had been detected in electroscopes on Earth, even in those with thick shielding. The source of this ionizing radiation was assumed to be terrestrial, for example due to radioactivity in minerals. However, in 1910, Theodore Wulf measured the ionization at the bottom and on the top of the Eiffel tower and found that the radiation flux on the top was too big to be due to ground radiation only. Then, balloon experiments were launched into the atmosphere, but they suffered from instrumental defects. Hess was the first to design instruments that would stand the temperature and pressure conditions at higher altitudes. He was able to demonstrate that the ionization flux first decreases with altitude before increasing rapidly, concluding that the main radiation source should be located outside the atmosphere. In addition, during the near-total eclipse of the Sun on April 7th 1912, Hess found that the ionization did not decrease, thus excluding the Sun as source of the radiation. The origin had to be further out in space. This discovery was then confirmed by Robert Millikan in 1925 who named this ionizing radiation *cosmic rays*. Hess shared the Nobel prize in 1936 with Carl David Anderson, who detected a CR positron in a cloud chamber [132]. In fact, the positron left a track corresponding to a particle with electron mass, but opposite charge.

Today, CR are a large field of study and many different experiments, ground- and space-based have been developed to detect them. Their energy spectrum is presented on the left panel in figure 2.1. CR extends up to energies of 3×10^{20} eV and have a few spectral features. In fact, the spectrum can be described by a power law

$$\frac{dN}{dE} \simeq E^{-\gamma} \tag{2.1}$$

with an index $\gamma = 2.7$ up to energies of 5×10^{15} eV, then the spectrum steepens to an index of $\gamma = 3.1$ up to energies 3×10^{18}, where it flattens again to an index $\gamma = 2.7$. The first spectral transition is called the *knee* and the second one the *ankle*. There is also another small feature around energies of 3×10^{17} eV called the *second knee*.
Above $\sim 5 \times 10^{10}$ GeV, protons interact with CMB photons with a center-of-mass energy close to 1.232 GeV, the mass of the Δ hadron. The cross-section of this resonance is very large and thus any source of cosmic-rays should have an exponential cutoff, the Greisen-Zatsepin-Kuzmin (GZK) cutoff [133, 134], and the universe should be opaque to these energies. In

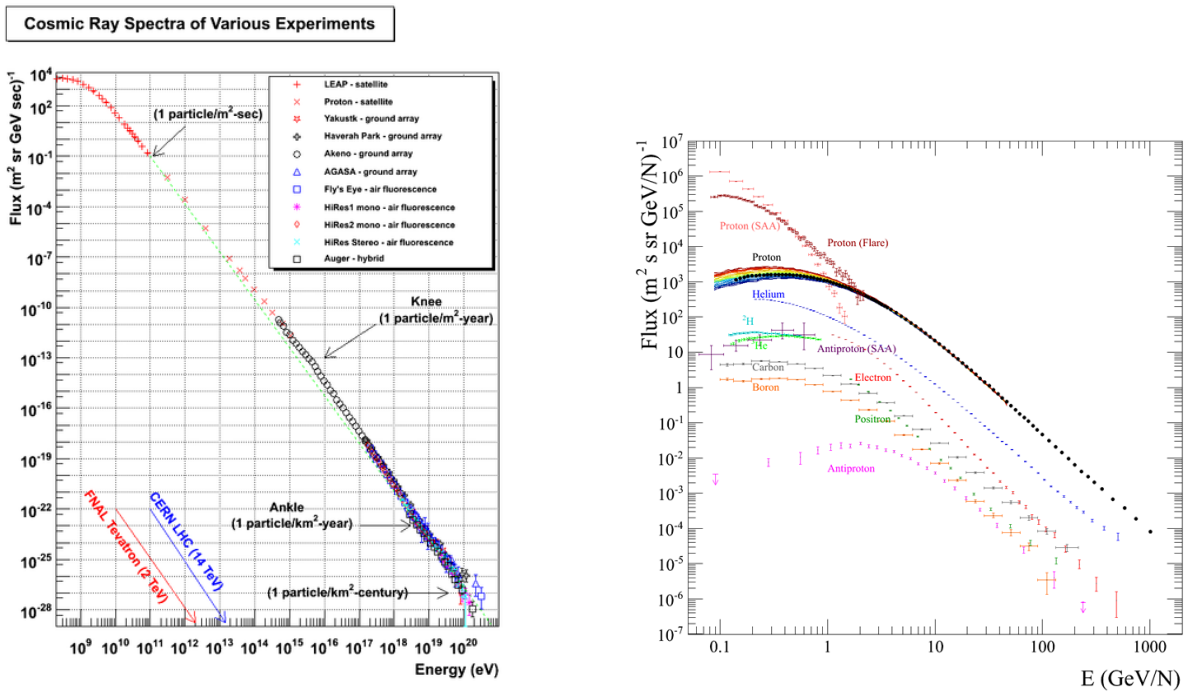

Figure 2.1: **CR spectrum and composition** Left: Energy spectrum of CR measured by different experiments [138]. We can see the events measured by AGASA and FLY'S EYE above the GZK-cutoff, as well as the suppression of the spectrum observed by HiRes and AUGER. Right: Composition of CR, distinguishing between solar or galactic origin [139].

the 1990's, observations made by the experiments AGASA and FLY'S EYE appeared to show events above the GZK-cutoff, around 5×10^{19} eV [135]. However, the HIRES experiment and the AUGER observatory found a suppression in the UHECR spectrum at the correct energy [136, 137], thus concluding that the previous results were incorrect. As shown on the right panel of figure 2.1, 99% of CR are nuclei and about 1% are electrons. Out of these nuclei, 90% are protons (hydrogen nuclei), 9% are helium nuclei (alpha particles), and about 1% are nuclei of heavier elements. Antimatter, positrons and antiprotons, only represents a small fraction of CR. Except for a small hint at 10^{18} eV, there is no anisotropy in CR measured at Earth [140] which indicates that they do not travel in straight lines as photons and neutrinos. More specifically, there is no signature from the galactic disk.

The chemical composition of the hadronic component of CR is presented on figure 2.2. In general, the abundances are similar to those found in the solar system and the interstellar medium. The abundances of protons (not shown in the figure) and helium however are smaller in CR than in the solar system. On the other hand, lithium, beryllium and boron are much more abundant in CR than the interstellar medium. The abundances of odd-Z elements are larger in CR than in the solar system. Explaining these similarities and differences has been the work of cosmic ray physicists since their discovery.

In the following we will briefly discuss the sources of CR, then explain the acceleration mechanisms, before introducing their transport equation in the Galaxy.

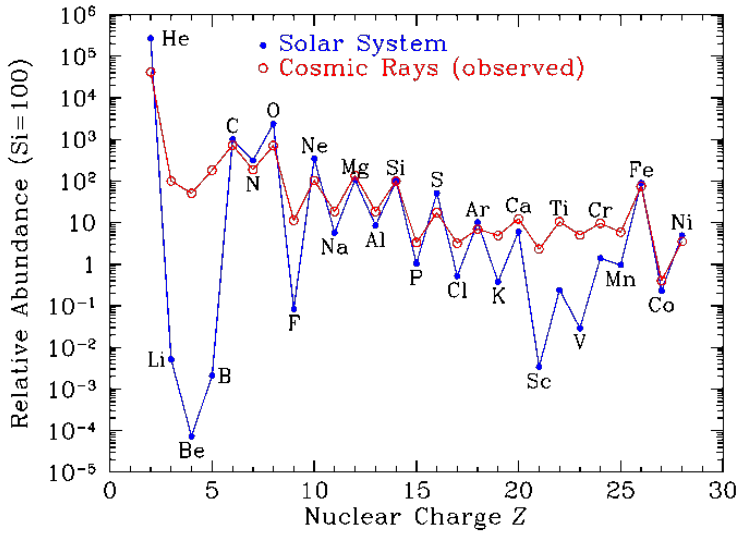

Figure 2.2: **Composition of the hadronic component of CR** as a function of the atomic number, measured at an energy of 1 TeV/nucleon [141] and arbitrarily normalized in such a way that the abundance of silicon is 100.

2.2 Potential CR sources

Up to a few GeVs, the source of CR can be identified as the solar wind; ultrahigh energy CR ($T > 10^{18}$ eV) are extragalactic (as we will explain in section 2.2.3). For energies in between, the CR are of galactic origin. Since the chemical composition of CR at 1 TeV/nucleon is similar to the one found in the solar system and the InterStellar Medium (ISM), it is usually assumed that CR originate from stellar-like sources.

The radioactive isotope ^{10}Be has a β-decay half-life of $\sim 3 \times 10^6$ years and its observed abundance suggests that local CR nuclei have an age of $t_{CR} \sim 10^8$ yr. The energy density of hadronic CR is of the order of $\omega_{CR} \sim 10^{-12}$ erg/cm^3. We typically assume that CR propagate in a cylindrical region with radius $R = 20$ kpc and a half-height of $L = 10$ kpc (see section 2.4.4), thus the volume of the CR confinement region is

$$V_{CR} = 2\pi R^2 L \sim 7 \times 10^{68} \ \ \text{cm}^3. \tag{2.2}$$

The total CR energy is $E_{CR} = \omega_{CR} V_{CR} \sim 10^{56}$ erg. And thus the luminosity of CR in our Galaxy is

$$L_{CR} = \frac{E_{CR}}{t_{CR}} \sim 10^{40} \ \ \text{erg/s}. \tag{2.3}$$

The Sun's CR luminosity is $L_{CR\odot} \sim 10^{25}$ erg and assuming solar type stars are the only source of CR we would obtain a total luminosity of $L_{CR\odot} M_G / M_\odot \sim 10^{25} 10^{11} \sim 10^{36}$ erg/s [142]. Clearly, normal (Sun-like) stars cannot provide the correct amount of CR. Other types of stars can be considered and especially their explosions.

2.2.1 Primary source: SuperNova explosions

At the end of its lifetime, a star explodes into a SuperNova (SN), a very short but highly energetic phenomenon. The explosion releases an energy of $10^{49} - 10^{50}$ erg (without the contribution of neutrinos) and expels its content into space. Hydrogen and all the elements synthesized by the star through nuclear fusion are injected into the ISM [143]. The SN explosion also creates thus a shockwave and the ejected matter stretches out into space, creating a nebula, the SuperNova Remanent (SNR). In terms of power, the SNR contribution is $10^{40} - 10^{42}$ erg/s, which is the correct amount of energy for CR and thus could be a possible sources of hadronic and leptonic galactic CR.

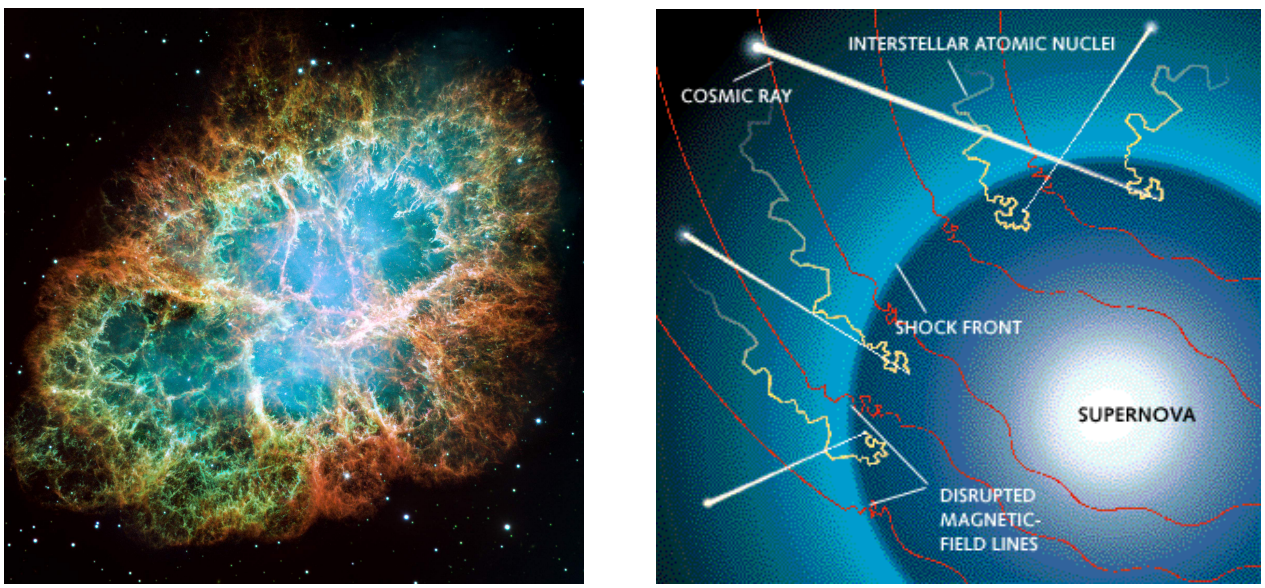

Figure 2.3: Left: **The Crab nebula** (galactic coordinates $l = 184,5575°$ and $b = -5,7843°$) is a young SNR, photographed by the Hubble Space Telescope. The SN exploded in 1024 and was witnessed by Japanese and Chinese astronomers. The diameter of the nebula is 3 pc today and the material is expanding at 1 500 km/s into space. At the center, we can find a pulsar, the crabe pulsar or PSR B0531+21, rotating 30 times per second around its own axis, it is most energetic pulsar known [144]. Right: **Acceleration of interstellar nuclei** to CR energies in the shockwave of a SNR [145].

SN explosions are supposed to occur every 30 years in the Milky Way, but have never been observed in our Galaxy since the invention of the telescope. In fact, the last directly observed supernova in the Milky Way was Kepler's Star of 1604 (SN 1604), remnants of two more recent supernovae have been found retrospectively. The closest SN explosion observed with telescopes is SN1987A in the Magellanic Clouds, a dwarf galaxy orbiting the Milky Way. SN explosions in other galaxies are very frequently obverted though. The historical explosion SN1054 in our Galaxy has been observed by Japanese and Chinese astronomers in the year 1024. Today we can see the remanent, the Crab nebula, shown in figure 2.3.

SN are classified according to their absorption lines of different chemical elements that appear in their spectra. The first element for division is the presence or absence of a line caused by hydrogen. The spectrum of type I SN does not contain hydrogen lines. In fact, the star at the origin of the explosion burned all hydrogen atoms during nuclear fusion and has converted them into heavier elements. They are further subcategorized: type Ia SN do not

contain helium lines, but silicon ones. They are used as cosmic standard candles in cosmology, for example for the measurement of the accelerated expansion of the universe. Type Ib and Ic SN contain helium lines, but no silicon, they are classified depending on their abundance of helium. Finally type II SN do present hydrogen lines and can also be classified depending on the helium abundance. Type Ib and II SN emerge from the explosion of hot, short-lived and massive ($8 - 10\ M_\odot$) OB-stars. They dominate the SN population, as opposed to SNIa explosions. Cosmic ray acceleration could also occur directly as the supernova is ejecting matter into interstellar space

The role of SN in CR physics is twofold: first, the explosion injects nuclei in the ISM, consisting mostly of hydrogen, helium, carbon, nitrogen and oxygen [146]. And second, the expanding SNR shell hitting the ISM accelerate the particles present to CR energies (at least up to the ankle) in a diffusive shock, as shown on the right panel of figure 2.3. CR acceleration could also occur directly as the supernova is ejecting matter into interstellar space. SN are thus called the *primary* source of CR. Also electrons seam to be accelerated by the same shock acceleration processes as nuclei [147]. Other possible sources for galactic CR include stellar winds of hot OB-stars [148] (massive stars emitting ultraviolet radiation) or pulsars.

2.2.2 Secondary source: spallation

Spallation is a nuclear reaction in which a nucleus is hit by an incoming particle (neutron, proton, etc...) or a gamma-ray (with an energy of ∼50 MeV to a few GeV). The target nucleus is decomposed into an atom with a lighter atomic mass, emitting particles, such as neutrons, protons, light nuclei (deuterium, helium or lithium) or antimatter (antiprotons, antideuteron). Spallation is a common process in primordial nucleosynthesis, in the upper atmosphere and in CR propagation.

More specifically, for CR, target nuclei are generally hydrogen and helium atoms, but also carbon, nitrogen and oxygen, present in the ISM. Spallation processes are both a source and a loss term, as it lowers the abundance of the target and incoming particles, the *primaries* and increases the one of the resulting emitted particles, the *secondaries*. As we have seen, the chemical abundances of light nuclei (lithium, beryllium and boron) are much larger in CR than in the solar system. In fact, thermonuclear reactions in the center of the Sun bypass these light elements and galactic CR impinging on the ISM give birth to them [149]. The reaction we are considering is

$$p_{CR} + {}^{A}_{Z}N_{ISM} \rightarrow {}^{A'}_{Z'}N + X, \tag{2.4}$$

with $A' < A$ and/or $Z' < Z$ and X is the emitted particle. For example, the destruction of primary carbon nuclei is responsible for the abundance of boron in CR.

Antiprotons are also produced by the CR protons hitting hydrogen and helium atoms in the ISM, for example through the reaction

$$p_{CR} + H_{ISM} \rightarrow p + p + p + \bar{p}. \tag{2.5}$$

In fact, antiprotons are difficult to be produced by any other astrophysical processes. The astrophysical background of antideuterons is produced in the same type of reaction, as well.

2.2.3 Ultrahigh energy CR

For completeness, we quickly present ultrahigh energy CR ($T > 10^{18}$ eV). These CR cannot be trapped inside our Galaxy by magnetic fields. In fact, the Larmor radius, corresponding to the

radius of the circular motion of a charged particle, is defined as

$$r_g = \frac{mv_\perp}{ZeB}, \tag{2.6}$$

with $v_\perp$ the velocity of the particle in the direction perpendicular to the magnetic field B. For protons above 10^{15} eV, the Larmor radius is of the order of the scale of the galactic magnetic irregularities, which trap the CR inside the Galaxy. Thus, CR with higher energies must have an extragalactic origin. Possible accelerators for ultrahigh energy CR include pulsars, neutron stars, gamma-ray bursts, active galactic nuclei [150] and of course DM.

As we have already mentioned before, CR with energies above 5×10^{19} eV will interact with CMB photons and produce pions with a center-of-mass energy close to 1.232 GeV, the mass of the Δ hadron, in the reaction

$$p + \gamma_{2.7K} \to \Delta^+ \to p + \pi^0. \tag{2.7}$$

Since the cross-section of this resonance is very large, the universe should be opaque to these energies and the spectrum should have an exponential cutoff, the Greisen-Zatsepin-Kurmin cutoff, at this energy. As we have seen earlier certain experiments measured events above the cutoff, these results were then disproved by more recent data. Particles with energies above the cutoff should originate from a source at a distance of $50 - 100$ Mpc or closer in order to reach us before interacting with CMB photons and which is in contradiction with the previous argument.

2.3 Acceleration mechanisms

Global and static magnetic fields cannot change the energy of a particle, but only change the momentum components. Electric fields are needed for acceleration to occur. Regular acceleration takes place in a large scale electric field. This is however very difficult to achieve in astrophysical environments because of the high electrical conductivity of astrophysical plasmas[1]. Stochastic acceleration can be achieved when small scale electrical fields are present

$$\left\langle \vec{E} \right\rangle = 0 \qquad \left\langle \vec{E}^2 \right\rangle \neq 0. \tag{2.8}$$

Small scale random magnetic fields are then generated and will scatter particles when the resonance is achieved and thus isotropize the particle distribution in the reference frame of the turbulences.

Different types of acceleration mechanisms where proposed to explain the power law behavior of the energy spectrum of CR, in particular by Fermi. The differential equation expressing the variation of the number density should have the following contributions

$$\frac{dN}{dt} = \text{ diffusion } + \text{ energy gain/loss } + \text{ sources } + \text{ leaks } . \tag{2.9}$$

The analysis of meteorites showed that the flux of CR has been constant for at least 10^9 years. Thus usually the time derivative is assume to be negligible and all the components on the right hand side cancel out. In fact, numerical codes or semi-analytical methods solve the transport equation in steady-sate condition, which is a valid approximation.

[1] A few exceptions exist: For example, in rotating magnetic fields, such as pulsars or rotating black holes, electric fields are created.

2.3.1 Second-order Fermi acceleration

In 1949, Fermi proposed a stochastic model in which charged particles are accelerated by successive scattering off magnetic clouds. Let us assume a particle with mass m and velocity v is injected with an energy E and scatters off a cloud of mass $M \gg m$ with speed V at an angle θ. If $(E, \vec{p})$ is the 4-vector before the scattering associated to the particle with mass m and $(E', \vec{p}')$ the 4-vector in the center of mass (which coincides with the magnetic cloud since $m \ll M$), we have

$$E' = \gamma \left(E + V p_x\right), \tag{2.10}$$

$$p'_x = \gamma \left(p_x + V \frac{E}{c^2}\right), \tag{2.11}$$

with $\gamma = \sqrt{1 - (V^2/c^2)}$ and $p_x = p \cos\theta$. After the scattering, the center of mass energy has not changed and only p_x changes sign. If we go back to the initial system, the particle's energy is

$$E'' = \gamma \left(E' - V(-p_x)\right) = \gamma^2 \left(E \left(1 + \frac{V^2}{c^2}\right) + 2V p_x\right). \tag{2.12}$$

To second order in V/c, we obtain

$$E'' \simeq E + 2E\frac{V^2}{c^2} + 2p_x V \tag{2.13}$$

and thus the energy gained during this scattering is

$$\frac{E'' - E}{E} \simeq 2\frac{V^2}{c^2} + 2\frac{V}{c} v \cos\theta. \tag{2.14}$$

The fractional energy change can be both positive and negative, depending on whether the particle-cloud scattering is head-on or tail-on. In the relativistic regime, the probability of scattering as a function of the angle θ is

$$Prob(\theta) \simeq \gamma \left(1 + \frac{V}{c}\cos\theta\right). \tag{2.15}$$

Since head-on collisions are more probable than tail-on ones, the energy of the particle should globally increase. In fact, averaging over all angles in the second term of equation 2.14, for $v = c$ is

$$\left\langle \frac{2V\cos\theta}{c} \right\rangle = \frac{2V}{c} \frac{\int Prob(\theta)\cos\theta \sin\theta d\theta}{\int Prob(\theta)\sin\theta d\theta} = \frac{2}{3}\left(\frac{V}{c}\right)^2 \tag{2.16}$$

and thus the averaged gained energy is

$$\left\langle \frac{E'' - E}{E} \right\rangle \simeq \frac{8}{3}\left(\frac{V}{c}\right)^2. \tag{2.17}$$

This expression shows that the energy depends only on at second order in V, hence the name *second-order* Fermi acceleration. Assuming the distance between two magnetic irregularities along a field line is L, the time between collisions for a particle on a trajectory with an angle

ϕ with respect to the magnetic field line is $L/(c\cos\phi)$ and the average value is $2L/c$, thus the energy growth rate is

$$\frac{dE}{dt} \simeq \frac{\Delta E}{E}\frac{E}{\Delta t} = \frac{8}{3}\left(\frac{V}{c}\right)^2 \frac{E}{2L/c} = \frac{4}{3}\left(\frac{V}{cL}\right)^2 E = \epsilon E. \tag{2.18}$$

In the end, we want to estimate the spectrum in energy, i.e. dN/dE, neglecting diffusion and assuming there are no sources of energy E. The gain and leak terms in equation 2.9 can be written as

$$\frac{dN(E)}{dt} = \frac{\partial}{\partial E}\left(N(E)\frac{dE}{dt}\right) + \frac{N(E)}{T}. \tag{2.19}$$

Here, we are model the Galaxy as a leaky box: particles are confined in the halo with a global magnetic field, once they touch the edge of the propagation region, they escape the propagation region and can travel into intergalactic space. T is the typical time scale of leaks, and is independent of the energy E. At equilibrium $dN/dE = 0$, both contributions cancel out,

$$\frac{\partial N(E)}{\partial E} = -\frac{N(E)}{E}\left(\frac{1}{\epsilon T} + 1\right). \tag{2.20}$$

The solution to this equation is a power law $N(E) \propto E^{-\alpha}$ with $\alpha = 1+1/(\epsilon T)$. Moving magnetic fields are the source of electric fields and particles propagating in this environment change their momentum. The induced electric field is responsible for this type of particle acceleration, the scattering leads to momentum transfer. Magnetic irregularities can exist in any plasma excited by stellar ultraviolet radiation, stellar winds, supernova explosions and the energetic particles moving through. However, magnetic irregularities in our Galaxy have a velocity $10^{-4}c$. The mean free path is of the order of a parsec and thus we can expect one collision per year. The gain in energy would not be sufficient to explain the observed energies. In the final transport equation, we will include a term describing these effects.

The essence of Fermi's model can be summarized as followed: if the leaking probability of a collision is P, after k collisions we would have $N = N_0 P^k$ and if the change in energy per collision is $\Delta E = \gamma^c E$, starting from an energy E_0 after k collisions, we will have an energy

$$E = E_0(1+\gamma^c)^k, \tag{2.21}$$

and thus the number density is

$$\frac{N}{N_0} = \left(\frac{E}{E_0}\right)^{\frac{\ln P}{\ln(1+\gamma^c)}}. \tag{2.22}$$

and the energy spectrum is

$$N(E)dE = cst \times E^{-1+\ln P/\ln(1+\gamma^c)}dE. \tag{2.23}$$

Hence it predicts a power law. This is a very general and natural result, that can be applied to different astrophysical processes, not only the one of magnetic clouds.

2.3.2 First order Fermi acceleration

Bell proposed in 1978 another model in which cosmic particles get accelerated by supersonic wavefronts of ionized gas, as it may be the case during SuperNova (SN) explosions, as shown

on the right panel of figure 2.3. Assuming the gas has a pressure P, a temperature T and a density ρ and is at rest in front of the wavefront, in the reference frame of the wavefront, the gas upstream has a velocity v_1 and downstream a velocity v_2. The conservation of mass dictates

$$\vec{\nabla} \cdot (\rho v) = 0 \quad \Rightarrow \quad \rho_1 v_1 = \rho_2 v_2 \tag{2.24}$$

and the conservation of momentum is written as

$$\vec{\nabla} \cdot (P + \rho v) = 0 \quad \Rightarrow \quad P_1 + \rho_1 v_1^2 = P_2 + \rho_2 v_1^2. \tag{2.25}$$

Finally, Bernoulli's conservation of energy implies

$$\vec{\nabla} \cdot \left(\frac{1}{2}\rho v^3 + \frac{\gamma}{\gamma - 1} v P \right) = 0 \quad \Rightarrow \quad \frac{1}{2}\rho_1 v_1^3 + \frac{\gamma}{\gamma - 1} v_1 P_1 = \frac{1}{2}\rho_2 v_2^3 + \frac{\gamma}{\gamma - 1} v_2 P_2, \tag{2.26}$$

where $\gamma = C_p/C_V$ is the ratio of the specific heat of a gas at a constant pressure to specific heat at a constant volume. Aside from the trivial solution in which all quantities remain spatially constant, there is the discontinuous solution:

$$\frac{\rho_2}{\rho_1} = \frac{u_1}{u_2} = \frac{(\gamma + 1) M_1^2}{(\gamma - 1) M_1^2 + 2}, \tag{2.27}$$

$$\frac{p_2}{p_1} = \frac{2\gamma M_1^2}{\gamma + 1} - \frac{\gamma - 1}{\gamma + 1}, \tag{2.28}$$

$$\frac{T_2}{T_1} = \frac{(2\gamma M_1^2 - \gamma(\gamma - 1))\left((\gamma - 1) M_1^2 + 2\right)}{(\gamma + 1)^2 M_1^2}, \tag{2.29}$$

with the downstream Mach number $M_1 = v_1/c_s = U/c_s$ ($c_s = \sqrt{\gamma p/\rho}$ is the sound speed in the gas at rest and U the velocity of the wavefront). In the limit of a strong shock front ($M_1^2 \gg 1$), the shock solution simplifies to

$$\frac{\rho_2}{\rho_1} = \frac{u_1}{u_2} = \frac{\gamma + 1}{\gamma - 1}, \tag{2.30}$$

$$\frac{p_2}{p_1} = \frac{2\gamma M_1^2}{\gamma + 1}, \tag{2.31}$$

$$\frac{T_2}{T_1} = \frac{2\gamma(\gamma - 1) M_1^2}{(\gamma + 1)^2}. \tag{2.32}$$

Shocks behave as very efficient heating machines and a large fraction of the incoming pressure is converted into internal energy of the gas behind the shock front.
Finally, in the case of a monoatomic gas $\gamma = 5/3$, thus $\rho_2/\rho_1 = v_2/v_1 = 4$ and $v_2 = U/4$. In the frame of the gas at rest in downstream of the wavefront, we see the gas upstream of the wavefront traveling at a speed $V = 3U/4$. Using the same arguments as for the second-order Fermi model, the energy variation is

$$\gamma^c = \left\langle \frac{\Delta E}{E} \right\rangle = \frac{4}{3}\frac{V}{c} = \frac{U}{c}. \tag{2.33}$$

This variation is in first order in velocity. The reason is that a each shock the particle gain energy, none of shock can slow it down. In the end, the particles will bounce back and forth inside the shock wave, gaining energy at each collision and accelerate them to the needed CR energies.

2.4 Derivation of the transport equation in the diffusion approximation

The differential equation describing the time evolution of the distribution of charged particles in a plasma with long-range interaction is a collisionless Boltzmann equation and is called *Vlasov equation*. Defining the six-dimensional Lorentz-invariant distribution function $f(\vec{x}, \vec{p}; t)$ of position $\vec{x}$, relativistic momentum $\vec{p}$ and time t, the relativistic Vlasov equation is written as

$$\frac{\partial f}{\partial t} + \vec{v} \cdot \frac{\partial f}{\partial \vec{x}} + \frac{\partial}{\partial \vec{p}} \left(\vec{F} f \right) = 0, \tag{2.34}$$

where $\vec{F} = \frac{d\vec{p}}{dt}$ is the force acting on the particles. In acceleration mechanisms in astrophysics and especially first and second order Fermi acceleration, CR particles acquire their energy by small increments, like in a biased random walk, both in real and momentum space. This random motion can be treated in the diffusion approximation, giving rise to spatial and momentum space diffusion terms in the final transport equation.

More precisely, a biased random walk represents a system in which the probability that the particle changes its momentum and its trajectory at a certain time t depends only on its recent events and not on the complete history of the particle. This is also called a *Markov process*. These processes are described by the *Fokker-Planck equation*, which is written as

$$\frac{\partial f}{\partial t} = -\sum_{i=1}^{N} \frac{\partial}{\partial x_i} \left[D_i^1(x_1, ..., x_N) f \right] + \frac{1}{2} \sum_{i=1}^{N} \sum_{j=1}^{N} \frac{\partial^2}{\partial x_i \partial x_j} \left[D_{ij}^2(x_1, ..., x_N) f \right], \tag{2.35}$$

where $D_i^1(x_1, ..., x_N)$ is the drift coefficient and $D_{ij}^2(x_1, ..., x_N)$ the diffusion tensor. The biased nature of the random walk determines the different coefficients and components of the tensor. The full transport equation for charged CR in the Galaxy can be obtained directly by computing the components in equation 2.35, as in [151].

Another way of deriving the transport equation is to start from the Vlasov equation 2.34 and to derive the collision operator

$$\left(\frac{\partial f}{\partial t} \right)_c = \frac{\partial f}{\partial t} + \vec{v} \cdot \frac{\partial f}{\partial \vec{x}} \tag{2.36}$$

approximating the forcing term $\partial(\vec{F} f)/\partial \vec{p}$ and changing the Vlasov equation 2.34 into a Boltzmann equation with a collision term and thus also into a Fokker-Planck equation. This approach in presented in [152] and the one we are going to sketch in the following.

The ultimate goal is to describe particle acceleration by magnetohydrondynamical turbulences in a moving fluid. First, we will focus on momentum diffusion, then spatial transport taking into account spatial gradients and finally add the motion of the scattering medium. The first effect will give rise to momentum space diffusion, the second to spatial transport and the third to spatial diffusion and convection.

2.4.1 Momentum space diffusion

Since the energy changes in a each collision is small, we can use the Fokker-Planck formalism which applies to Markov processes: the probability of change $\Delta\vec{p}$ in momentum during Δt

is assumed to depend on $\vec{p}$ and $\vec{x}$ and not the complete history of the particle. Thus the distribution function after a time Δt can be written as

$$f(\vec{p}, \vec{x} + \vec{v}\Delta t; t + \Delta t) = \int d\Delta\vec{p}\ \Psi(\vec{p} - \Delta\vec{p}, \Delta\vec{p}) f(\vec{p} - \Delta\vec{p}, \Delta\vec{p}), \tag{2.37}$$

$\Psi(\vec{p}, \Delta\vec{p}) d\Delta\vec{p}$ is the element of probability for changing the momentum $\vec{p}$ to $\vec{p} + \Delta\vec{p}$ in time Δt with $\int d\Delta\vec{p}\ \Psi(\vec{p}, \Delta\vec{p}) = 1$. Expanding in a Taylor serie, we have

$$\begin{aligned}\left(\frac{\partial f}{\partial t}\right)_c &= \frac{f(\vec{p}, \vec{x} + \vec{v}\Delta t; t + \Delta t) - f(\vec{p}, \vec{x}; t)}{\Delta t} = \frac{\int d\Delta\vec{p}\ \Psi(\vec{p} - \Delta\vec{p}, \Delta\vec{p}) f(\vec{p} - \Delta\vec{p}, \Delta\vec{p}) - f(\vec{p}, \vec{x}; t)}{\Delta t} \\ &= \frac{\partial f}{\partial t} + \vec{v} \cdot \frac{\partial f}{\partial \vec{x}} = -\frac{\partial}{\partial \vec{p}} \left[f(\vec{p}, \vec{x}; t) \left\langle \frac{\Delta\vec{p}}{\Delta t} \right\rangle - \frac{1}{2} \frac{\partial}{\partial \vec{p}} \left(f(\vec{p}, \vec{x}; t) \left\langle \frac{\Delta\vec{p}\Delta\vec{p}}{\Delta t} \right\rangle \right) \right],\end{aligned} \tag{2.38}$$

with the Fokker-Planck coefficients are defined as

$$\left\langle \frac{\Delta\vec{p}}{\Delta t} \right\rangle = \frac{1}{\Delta t} \int d\Delta\vec{p}\ \Psi(\vec{p}, \Delta\vec{p}) \Delta\vec{p}, \tag{2.39}$$

$$\left\langle \frac{\Delta\vec{p}\Delta\vec{p}}{\Delta t} \right\rangle = \frac{1}{\Delta t} \int d\Delta\vec{p}\ \Psi(\vec{p}, \Delta\vec{p}) \Delta\vec{p}\Delta\vec{p}. \tag{2.40}$$

A simplification of the Fokker-Planck equation arises, when the recoil of the scatter can be ignored, such that $\Psi(\vec{p}, -\Delta\vec{p}) = \Psi(\vec{p} - \Delta\vec{p}, \Delta\vec{p})$ and using again a Taylor expansion and integrating over $\Delta\vec{p}$

$$\frac{\partial}{\partial \vec{p}} \left[\left\langle \frac{\Delta\vec{p}}{\Delta t} \right\rangle - \frac{1}{2} \left\langle \frac{\Delta\vec{p}\Delta\vec{p}}{\Delta t} \right\rangle \right] = 0. \tag{2.41}$$

The Fokker-Planck coefficients vanish for small values of the momentum $\vec{p}$ and thus

$$\left\langle \frac{\Delta\vec{p}}{\Delta t} \right\rangle = \frac{1}{2} \left\langle \frac{\Delta\vec{p}\Delta\vec{p}}{\Delta t} \right\rangle. \tag{2.42}$$

The Fokker-Planck equation becomes

$$\frac{\partial f}{\partial t} + \vec{v} \cdot \frac{\partial f}{\partial \vec{x}} = \frac{\partial}{\partial \vec{p}} \left(\bar{D}_{pp} \frac{\partial f}{\partial \vec{p}} \right), \tag{2.43}$$

with the momentum space diffusion tensor defined as

$$\bar{D}_{pp} = \frac{1}{2} \left\langle \frac{\Delta\vec{p}\Delta\vec{p}}{\Delta t} \right\rangle. \tag{2.44}$$

In the case of isotropic scattering by an isotropic distribution of scatters moving at a velocity $v_a \ll c$, the momentum change of the particle is $\Delta p = -(\vec{p} \cdot \vec{v_a})/v$ and if L is the collision mean free path, the momentum space diffusion tensor is diagonal $\bar{D}_{pp} = D_{pp}\mathbb{1}$ with

$$D_{pp} = \frac{p^2 \langle v_a^2 \rangle}{3vL}. \tag{2.45}$$

This is a traditional second-order Fermi process. In fact, the velocity of the scattering centers is *squared*. The coefficient is also proportional to the squared momentum of the particles and inversely proportional to the collision free path. This expression is only valid in the non-relativistic limit.

2.4.2 Pitch angle scattering

Particles have to be able to leave the acceleration region in order to maintain a steady state solution. Spatial transport is thus needed. Earlier, we introduced a simple escape term $-f/T$. In this case, spatial gradients are not included. Modeling the Galaxy as a leaky box is very good approximation for CR and we will apply this approach to scattering on plasma waves.

Let us assume a random magnetic field component perpendicular to the global magnetic field B_0 with $\delta B \ll B_0$. In the reference frame of the wave, the equation of motion is

$$\frac{d\vec{p}}{dt} = \frac{q}{c}\vec{v} \times (\vec{B}_0 + \delta\vec{B}). \tag{2.46}$$

Splitting the momentum into one parallel and two perpendicular components, the perpendicular components cannot change their modulus, while the parallel one is defined by

$$\frac{d\vec{p}_\parallel}{dt} = \frac{q}{c}\left|\vec{v}_\perp \times \delta\vec{B}\right| \quad \text{and} \quad p_\parallel = p\mu, \tag{2.47}$$

where $\mu = (\vec{p}\cdot\vec{B})/pB$ is the particle's pitch angle, obeying the equation of motion in the wave rest frame

$$\frac{d\mu}{dt} = \frac{q}{pc}v(1-\mu^2)^{1/2}\delta B\cos\left((\Omega - kv\mu)t + \psi\right), \tag{2.48}$$

with the Larmor frequency $\Omega = qB_0/mc\gamma$, k the wave vector and ψ the phase of the wave. The mean value of the pitch angle variation over a long time vanishes $\langle\Delta\mu\rangle_t = 0$ and averaging upon the random phase of the wave, we have

$$\langle\Delta\mu(t')\Delta\mu(t'')\rangle_\psi = \frac{q^2v^2(1-\mu^2)\delta B^2}{2c^2p^2}\cos\left((\Omega - kv\mu)(t'-t'')\right). \tag{2.49}$$

Integrating over time, we obtain the pitch angle diffusion coefficient

$$\begin{aligned}\langle\Delta\mu(t')\Delta\mu(t'')\rangle_t &= \frac{q^2v^2(1-\mu^2)\delta B^2}{2c^2p^2}\int dt'\int dt''\cos\left((\Omega - kv\mu)(t'-t'')\right)\\ &= \frac{q^2v^2(1-\mu^2)\delta B^2}{2c^2p^2}\delta\left(k - \frac{\Omega}{v\mu}\right)\Delta t,\end{aligned} \tag{2.50}$$

where $\delta(x)$ is the Dirac function defined as $\delta(0) = 1$ and $\delta(x) = 0$ elsewhere. Only resonant waves with $k_{res} = \Omega/v\mu$ interact strongly with the particles and in the limit $t \to \infty$, the random change in pitch angle can be described by a diffusion coefficient

$$\nu = \left\langle\frac{\Delta\theta\Delta\theta}{\Delta t}\right\rangle = \frac{\pi q^2 v\delta B^2}{p^2c^2\mu}\delta(k - k_{res}). \tag{2.51}$$

In general, the particle does not encounter one single wave, but rather an energy density $\mathcal{E}(k)$ in waves of different modes. Integrating over all wave numbers, the pitch angle diffusion coefficient becomes

$$\nu = \frac{\pi}{4}\Omega\frac{k_{res}\mathcal{E}(k_{res})}{B_0^2/8\pi} \sim \Omega\left\langle\left(\frac{\delta B}{B_0}\right)^2\right\rangle, \tag{2.52}$$

making explicit the essential physical expression of the angular diffusion as given by the Larmor frequency times the power of magnetic field perturbation. The distribution is expected to be

driven to isotropy, i.e. to be μ-independent, over a time scale of a few ν^{-1}. At each resonance, the particle changes its pitch angle by $\Delta\theta \sim \delta B/B_0$ with a random sign. The Vlasov equation with spatial gradients becomes the Fokker-Planck equation

$$\left(\frac{\partial f}{\partial t}\right)_c = \frac{\partial f}{\partial t} + \vec{v}\cdot\vec{\nabla}_x f = \frac{\partial}{\partial \mu}\left(D_{\mu\mu}\frac{\partial f}{\partial \mu}\right) = \frac{\partial}{\partial \mu}\left((1-\mu^2)\nu\frac{\partial f}{\partial \mu}\right). \tag{2.53}$$

2.4.3 Convection and diffusion

When the particle's mean free paths are sufficiently short, the spatial transport described in the section 2.4.2 can be treated as a diffusion process [153]. We generalize the Vlasov equation to particle transport in a non-stationary medium taking into account the motion of the scattering medium and thus obtaining a convection term in our equation.

We consider the motion of the scattering centers in the shock front moving at a velocity $\vec{u}$. To keep the calculation as simple as possible, we will use a non-inertial reference frame with mixed coordinates: time and position will be taken in the laboratory frame and the momentum in the plasma frame. The primed coordinates will refers to the laboratory frame, while the unprimed ones to the plasma frame. At first order in u, the distribution function can be written as

$$\begin{aligned} f'(\vec{x}', \vec{p}', t') &= f(\vec{x}', \vec{p}' = \vec{p} - m\vec{u}, t') \\ &= f(\vec{x}', \vec{p}' = \vec{p}, t') - m\vec{u}\,\frac{\partial f(\vec{x}', \vec{p}' = \vec{p}, t')}{\partial \vec{p}'}. \end{aligned} \tag{2.54}$$

The Vlasov equation in the laboratory frame is still

$$\frac{\partial f'(\vec{x}', \vec{p}', t')}{\partial t'} + \vec{v}'\frac{\partial f'(\vec{x}', \vec{p}', t')}{\partial \vec{x}'} = -\frac{\partial}{\partial \vec{p}'}\left(\frac{d\vec{p}'}{dt} f'(\vec{x}', \vec{p}', t')\right) \tag{2.55}$$

and in the non-inertial frame to first order in u and assuming $\partial u/\partial t = 0$ it becomes

$$\frac{\partial f(\vec{x}', \vec{p}, t')}{\partial t'} + (\vec{v} + \vec{u})\cdot\frac{\partial f(\vec{x}', \vec{p}, t')}{\partial \vec{x}'} - \vec{p}\cdot\frac{\partial \vec{u}}{\partial \vec{x}'}\cdot\frac{\partial f(\vec{x}', \vec{p}, t')}{\partial \vec{p}} = -\frac{\partial}{\partial \vec{p}}\left(\frac{d\vec{p}}{dt} f(\vec{x}', \vec{p}, t')\right). \tag{2.56}$$

Now, we introduce a vector $\vec{n}(\vec{x}', t')$ parallel to the magnetic field at any point $\vec{x}'$ in space. The local pitch angle μ is thus the angle between $\vec{p}$ and $\vec{n}$. The distribution function f should be independent of the gyrational phase ϕ, the angle describing the circular motion of the particle around the axis of the local magnetic field $\vec{B}$. Thus $f(\vec{x}', \vec{p}, t') = f(\vec{x}', p, \mu, t')$ and we can average the terms in equation 2.56 over ϕ

$$\left\langle \vec{v}\frac{\partial f}{\partial \vec{x}'}\right\rangle_\phi = \mu v\vec{n}\cdot\frac{\partial f}{\partial \vec{x}'} + \frac{1}{2}(1-\mu^2)v\frac{\partial \vec{n}}{\vec{x}'}\cdot\frac{\partial f}{\partial \mu}, \tag{2.57}$$

$$\left\langle \vec{p}\cdot\frac{\partial \vec{u}}{\partial \vec{x}'}\cdot\frac{\partial f}{\partial \vec{p}}\right\rangle_\phi = \left[\frac{1}{2}(1-\mu^2)\frac{\partial \vec{u}}{\partial \vec{x}'} + \frac{1}{2}(3\mu^2-1)\vec{n}\cdot\frac{\partial \vec{n}\cdot\vec{u}}{\partial \vec{x}'}\right] p\frac{\partial f}{\partial p}. \tag{2.58}$$

And the full Vlasov equation 2.56 becomes

$$\begin{aligned} \frac{\partial f}{\partial t'} + (\mu v\vec{n} + \vec{u})\cdot\frac{\partial f}{\partial \vec{x}'} - \left[\frac{1}{2}(1-\mu^2)\frac{\partial \vec{u}}{\partial \vec{x}'} + \frac{1}{2}(3\mu^2-1)\vec{n}\cdot\frac{\partial(\vec{n}\cdot\vec{u})}{\partial \vec{x}'}\right] p\frac{\partial f}{\partial p} + \frac{1}{2}(1-\mu^2)v\frac{\partial \vec{n}}{\partial \vec{x}'}\cdot\frac{\partial f}{\partial \mu} \\ = \frac{\partial}{\partial \mu}\left(\frac{1}{2}(1-\mu^2)\nu\frac{\partial f}{\partial \mu}\right), \end{aligned} \tag{2.59}$$

where we used the pitch angle coefficient from equation 2.53. The distribution function f in the scattering medium is approximately isotropic and since $u \ll v$, we can expand f in terms of u/v: $f = f_0 + f_1 + f_2$ with $f_n = O(u/v)^n f_0$. At 0th-oder, we get

$$\frac{\partial}{\partial \mu}\left(\frac{1}{2}(1-\mu^2)\nu\frac{\partial f_0}{\partial \mu}\right) = 0, \tag{2.60}$$

confirming that f_0 is totally isotropic, i.e. independent of μ. At 1-st order, we have an equation for f_1

$$\mu v\vec{n}\frac{\partial f_0}{\partial \vec{x}'} = \frac{\partial}{\partial \mu}\left(\frac{1}{2}(1-\mu^2)\nu\frac{\partial f_1}{\partial \mu}\right) \quad \Rightarrow \quad \frac{\partial f_1}{\partial \mu} = -\frac{v}{\nu}\vec{n}\cdot\frac{\partial f_0}{\partial \vec{x}'} \tag{2.61}$$

And finally at 2-nd order

$$\begin{aligned}\frac{\partial f_0}{\partial t'} + \vec{u}\cdot\frac{\partial f_0}{\partial \vec{x}'} + \mu v\vec{n}\cdot\frac{\partial f_1}{\partial \vec{x}'} - \left[\frac{1}{2}(1-\mu^2)\frac{\partial \vec{u}}{\partial \vec{x}'} + \frac{1}{2}(3\mu^2-1)\vec{n}\cdot\frac{\partial(\vec{n}\cdot\vec{u})}{\partial \vec{x}'}\right]p\frac{\partial f_0}{\partial p} \\ + \frac{1}{2}(1-\mu^2)v\frac{\partial \vec{n}}{\partial \vec{x}'}\frac{\partial f_1}{\partial \mu} = \frac{\partial}{\partial \mu}\left(\frac{1}{2}(1-\mu^2)\nu\frac{\partial f_2}{\partial \mu}\right).\end{aligned} \tag{2.62}$$

Averaging over μ and replacing 2.61, we obtain

$$\frac{\partial f_0}{\partial t'} + (\vec{u}\cdot\nabla)f_0 - \nabla\left(\vec{n}D_{\parallel}(\vec{n}\cdot\nabla)f_0\right) = \frac{1}{3}(\nabla\cdot\vec{u})p\frac{\partial f_0}{\partial p}, \tag{2.63}$$

where the μ-averaged diffusion coefficient is diffined as

$$D_{\parallel}(\vec{x}', \vec{p}, t') = \left\langle \frac{1}{2}(1-\mu^2)\frac{v^2}{\nu}\right\rangle_{\mu}. \tag{2.64}$$

Now we have a transport equation for the isotropic part of the distribution function f_0 and at the order at which we are working it does not matter whether we measure it in the wave frame or the inertial frame, thus $f_0 = f_0(\vec{x}, p, t)$. The equation contains a convection and a diffusion term (on the right hand side), as well as an adiabatic energy loss term (on the left-hand side). We can add momentum space diffusion, as obtained in equation 2.43, to the spatial diffusion in a coherent way, for the isotropic distribution function $f(\vec{x}, p, t)$

$$\frac{\partial f}{\partial t} + (\vec{V_c}\cdot\nabla)f - \nabla\left(\vec{n}D_{\parallel}(\vec{n}\cdot\nabla)f\right) = \frac{1}{3}(\nabla\cdot\vec{V_c})p\frac{\partial f}{\partial p} + \frac{1}{p^2}\frac{\partial}{\partial p}\left(p^2 D_{pp}\frac{\partial f}{\partial p}\right), \tag{2.65}$$

$\vec{V_c}$ becomes a compromise velocity between the velocity of the background $\vec{u}$ and the one of the plasma waves $\vec{v_a}$. The momentum diffusion coefficient also obtains a contribution from the pitch angle scattering. It is however always proportional to $D_{pp} \propto v_A^2$, the plasma wave velocity *squared*. The exact formulas can be found in [152] equation 3.41, here we do not need to go in such detail. Finally, energy losses (other than adiabatic) and source terms have not been taken into account until now, but have to be added to the full transport equation in order to describe the propagation in the Galaxy faithfully.

In the next section, we will present the model used in CR propagation, called the Halo Diffusion Model. In this model the spatial and momentum diffusion terms, as well as convection, can be approximated and have a simple analytical form.

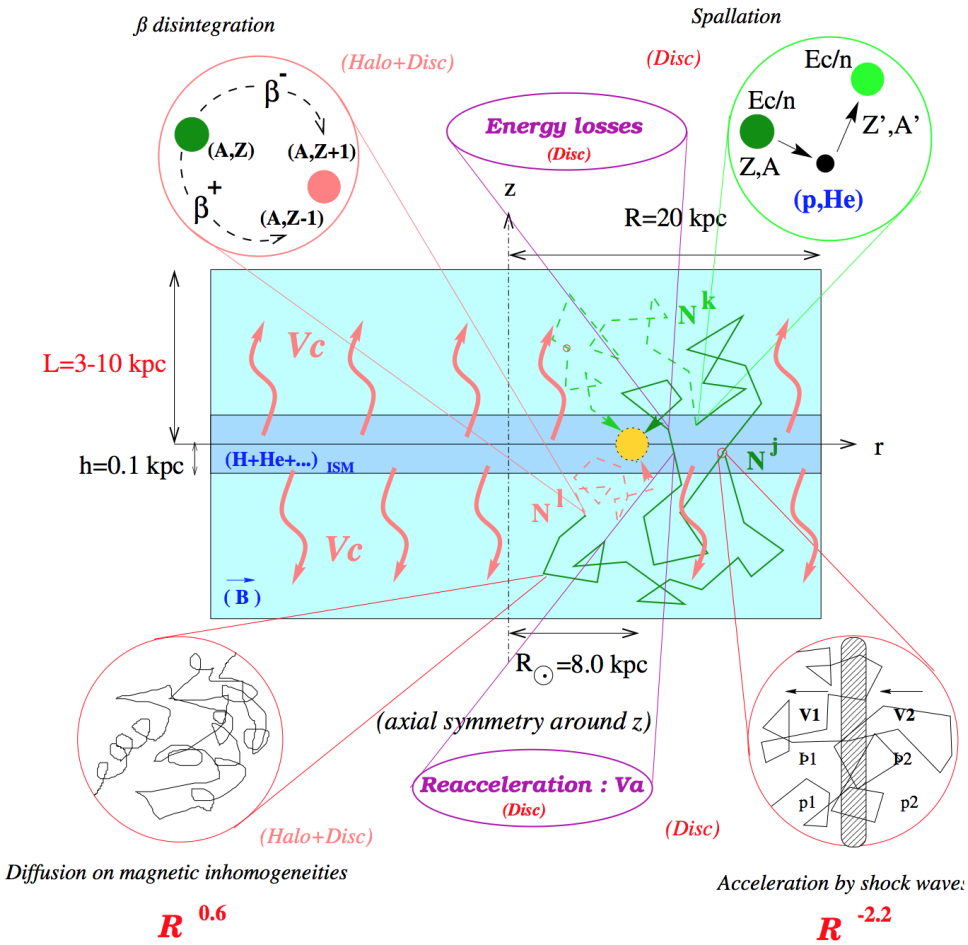

Figure 2.4: **Schematic edge-on view of the HDM** of our Galaxy with CR acceleration sources, diffusive, convective and energy loss processes [154].

2.4.4 Full transport equation

The Halo Diffusion Model (HDM) is used to describe CR propagation in our Galaxy and is represented in figure 2.4. The Galaxy consists of two cylindrical regions with radius R and a cylindrical symmetry. The disk with a half height h is embedded in the diffusive halo with a half-height $L \gg h$ (typically L is 10-100 times larger than h). The diffusive halo is a leaky box: particles are assumed to be confined in the halo with a global magnetic field, once they touch the edge of the halo, they escape the propagation region and can travel into intergalactic space.

Essentially, the disk is a particular region of the diffuse region, because of the stars and the ISM it contains. Primary sources in the from of SNR as well as secondary sources, due to spallation of primary CR on the ISM, are present. SN explosions and radiation pressure of stars create a convective wind away from the disk and the adiabatic expansion is responsible for adiabatic losses of CR. Energy losses in the disk are an additional ingredient in the propagation of nuclei and especially of electrons and positrons.

In the entire diffusive halo, random motion of CR in magnetic inhomogeneities is modeled as spatial diffusion. Since the diffusion centers have a non-zero velocity, also a momentum space

diffusion is present. This diffusive reacceleration is very effective in the disk and is thus not modeled in the rest of the diffuse region.

Starting from equation 2.65, where we already have spatial diffusion, convection, adiabatic losses and momentum space diffusion we have to add other terms in order to take into account all the effects that are important for the CR propagation:

- energy losses (other than adiabatic), for example due to ionization, or in the case of electrons, due inverse Compton scattering, synchrotron emissions and bremsstrahlung,
- spallation, as presented in section 2.2.2, is a source for secondary particles and a loss term for primary CR species,
- particle decay,
- radioactive decay transforming a nucleus j into a lighter nucleus i,
- particle production from nucleus type j to i,
- primary sources, such as assumed to be SN explosions discussed in section 2.2.1, but also DM annihilation and decay as we will see later.

Finally, the full transport equation for $N_i(t, \vec{r}, p)$, the isotropic number density of cosmic-ray nuclei of type i (and even electrons and positrons, when the source term is correctly accounted for) can be written as

$$\begin{aligned}\frac{\partial N_i}{\partial t} =& \nabla \cdot \left(D_{xx} \cdot \nabla N_i - \vec{V_c} N_i \right) + \frac{\partial}{\partial p} \left[D_{pp} p^2 \frac{\partial}{\partial p} \left(\frac{N_i}{p^2} \right) \right] + \frac{\partial}{\partial p} \left[\left(\frac{p}{3} \nabla \cdot \vec{V_c} + b_i \right) N_i \right] \\ & - \left(nv\sigma_i + \frac{1}{\tau_i} \right) N_i + \sum_{j<i} \left(nv\sigma_{ij} + \frac{1}{\tau_{ij}} \right) N_i + S_i, \end{aligned} \tag{2.66}$$

On the right hand side the first term accounts for spatial diffusion with D_{xx} is the *spatial diffusion* tensor, the second term for convection with $\vec{V_c}$ the *convection* velocity and the forth term $\frac{p}{3}\nabla \cdot \vec{V_c}$ represent the *adiabatic momentum loss* rate. These terms can be recovered by following the discussion in section 2.4.3. The third expression on the right hand side describes momentum diffusion (or second-order Fermi acceleration), discussed in section 2.4.1. In the case of an isotopic distribution function the momentum space diffusion in equation 2.43 becomes

$$\frac{\partial}{\partial \vec{p}} \left(\bar{D}_{pp} \frac{\partial f}{\partial \vec{p}} \right) = \frac{\partial}{\partial p} \left(D_{pp} \frac{\partial f}{\partial p} \right) \tag{2.67}$$

with D_{pp} the *momentum diffusion* coefficient. The fifth term in equation 2.66 represents energy losses due to ionization or other energy-loss mechanisms with $b_i = -\frac{dp}{dt}$ the *momentum loss* rate. Finally in the last terms, we take into account the other effects enumerated above: n is the number density of the ISM), v the particle speed in the ISM, σ_i the total *spallation* cross-section, τ_i *decay time*, σ_{ij} *particle production* cross-section from nucleus type j to i, τ_{ij} the *radioactive decay* time from nucleus species j to i and S_i *primary cosmic-ray source injection* rate.

Let us discuss the most important terms in more detail and present the approximations used in the HDM for CR propagation.

Astrophysical primary sources

As we have seen in section 2.2.1, SN explosions are most likely the astrophysical primary sources of CR. The injection spectrum for nuclei is assumed to be a power law in momentum; the distribution of sources is chosen to reproduce the γ-ray signal found by EGRET and FERMI [155, 156] or on the basis of pulsar and progenitor star surveys [157], which are more peaked distributions than those empirically obtained by γ-rays. The source are assumed to continuously spread along the disk and are steadily accelerating charged particles.

Diffusion and convection

Magnetohydordynamical turbulences in a plasma are called Alfvén waves, named after Hannes Alfvén who won the Nobel prize in Physics in 1970 for his work in plasma physics. These dispersionless waves represent the oscillation of ions, as well as the magnetic field. The ion mass density has the role of inertia and the magnetic field line tension the one of restoring force. The propagation velocity of these waves is

$$v_A = \frac{B}{\sqrt{\mu_0 \rho}}, \tag{2.68}$$

where B is the magnetic field strength, μ_0 the vacuum permeability and $\rho = \sum n_s m_s$ the total mass density of charged particles in the plasma. Alfvén waves are responsible for the spatial diffusion and since these scattering centers have a proper velocity they are also responsible for momentum space diffusion. The two diffusion coefficients are thus related to each other, as we will see in the following.

The spatial diffusion coefficient is assumed to depend on the rigidity of the particles $R = pc/Ze$ with an exponent δ, other dependence can also be added, as we will see in the following. Different codes exist in order to solve equation 2.66: `Galprop` [158] and `DRAGON` [159] solve the equation in fully numerically, while `USINE` [160] solves it in a semi-analytical approach. The spatial and momentum diffusion coefficient differ slightly from one code to another, but describe the same effects and fit very well the CR data.

- In `GalProp` the spatial diffusion coefficient has the form $D_{xx} = D_0 \beta \left(R/R_0\right)^\delta$ with $R_0 = 4$ GV and the momentum diffusion coefficient is

  $$D_{pp} = \frac{4p^2 v_a^2}{3\delta(4-\delta^2)(4-\delta)D_{xx}}. \tag{2.69}$$

  As in equation 2.45, we recover the dependence in v_a^2 as well as in p^2. The mean free path L is then linked to the spatial diffusion coefficient. In fact, D_{xx} appears at the denominator in 2.69, essentially expressing the fact that the more efficiently cosmic rays diffuse in space, the fewer collisions there are and the weaker the energy diffusion.

- In the case of the `DRAGON` code, the spatial diffusion coefficient is written as $D_{xx} = D_0 \beta^\eta \left(R/R_0\right)^\delta e^{-z/z_t}$ with $R_0 = 3$ GV. The relation with the momentum diffusion coefficient is the same as for `GalProp`.

- In `USINE`, spatial diffusion has the same form as in `GalProp`, but with $R_0 = 1$ GV. The transport equation 2.66 is written for the number density as a function of energy

$\psi(\vec{x}, E, t) = dn/dE$ and thus the momentum space diffusion is treated as an energy diffusion in the no-recoil hard sphere scattering center approximation [161]

$$D_{EE} = \frac{2}{9} \frac{v_a^2 E^2 \beta^4}{D_{xx}(E)}. \tag{2.70}$$

Finally, convection is assumed to be in the direction of the symmetry axis of the cylinder, i.e. along the z-axis. In the `USINE` code, adiabatic losses are supposed to take place only inside the disk and thus in the thin disk approximation $\nabla \cdot \vec{V_c} \simeq V_c/h$, as the value of the convective wind is $-V_c$ at $-h$ and $+V_c$ at $+h$. In `DRAGON`, convection increases away from the disk (see parameters in table 2.2).

Energy Losses

For nuclei, energy losses due to Coulomb interaction and ionization can be modeled in the disk, for energies below 10 GeV, they do not represent an important contribution to the propagation, as shown in figure 2.5. For electrons however, these losses, as well as bremsstrahlung and Inverse Compton scattering on InfraRed (IR) radiation and stellar light have to be fully taken into account. In the entire halo, energy losses due to synchrotron radiation and Inverse Compton (IC) on CMB photons have also to be added. This will be further investigated in chapter 4.

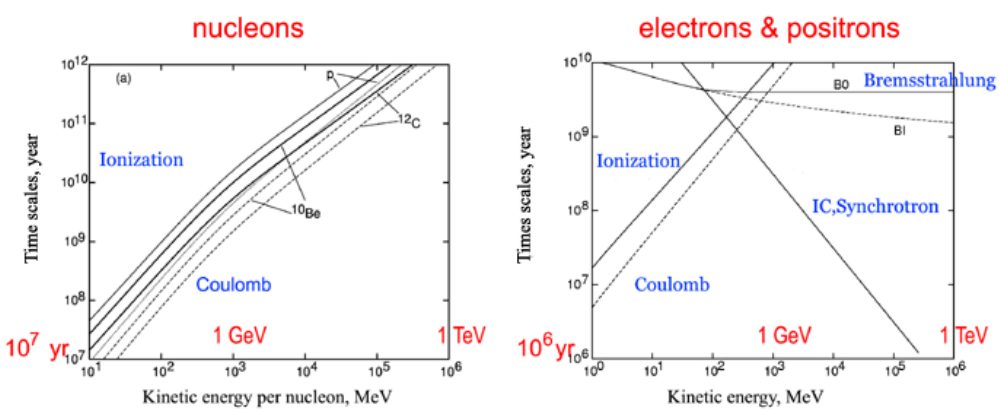

Figure 2.5: **Energy loss time scale for nucleons and electron/positions** in neutral and ionized hydrogen for gas densities of $n_H = n_{HII} = 0.01$ cm^{-3} and equal energy densities of photons and magnetic field $U = U_B = 1$ eV cm^{-3} [162]. The importance of an energy loss rate in the propagation of CR is inversely proportional to the time scale.

2.4.5 Experimental determination of the diffusion parameters

Different types of nuclei can be sensitive to different propagation parameters. Therefore using available measurements allows us to constrain the values of these parameters and to find precise models able to reproduce all the abundances and spectra. Stable secondary particles, such as lithium (Li), beryllium (Be) and boron (B) (but also scandium (Sc), titanium (Ti) and vanadium (V)) can give us information on the ratio L/D_0, while radioactive secondaries (beryllium ^{4}Be, aluminum ^{26}Al, chlorine ^{36}Cl or manganese ^{54}Mn) probe the halo size L and the diffusion

coefficient D_0 separately. In addition secondary to primary ratio (typically B/C) are sensitive to D_0 and the energy dependence of the diffusion coefficient δ [163]. The relative abundance of radioactive secondaries (^{10}Be/^{9}Be) probes the halo size L as large diffusion volume increases the probability of radioactive decay of the isotope and thus a smaller ratio is recovered at Earth. K-capture isotopes (vanadium ^{49}V, chromium ^{51}Cr) decay by absorbing an electron and have a short lifetime in the ISM. They are sensitive to reaccelerating and solar modulation (discussed below). In general, light nuclei (up to oxygen) have experienced propagation through large galactic regions and inform us on the averaged propagation parameters [161] while radioactive isotopes with short lifetimes and heavy nuclei give us useful insight into the Local InterStellar medium (LIS) [158].

`USINE`

Using the `USINE` code, references [164, 165] derive propagation parameters satisfying the measurements of CR data. Three models are proposed, in agreement with the B/C data from NASA HEAO 3 satellite [166], as well as data from balloons and the ISEE 3 experiment. The parameters for the three models are shown in figure 2.1. They are named in relation with their antiproton flux from DM annihilation: MIN (MAX) minimize (maximize) the antiproton signal from DM. MED gives a antiproton flux in the middle of MIN and MAX.

Model	δ	D_0 [kpc^2/Myr]	V_c [km/s]	L [kpc]	v_a [km/s]
MIN	0.85	0.0016	13.5	1	22.4
MED	0.70	0.0112	12	4	52.9
MAX	0.46	0.0765	5	15	117.6

Table 2.1: **CR propagation parameters using** USINE **code** for nuclei and electrons/positrons in the Galactic halo (from [164, 165]). δ and D_0 diffusion parameters, V_c is the velocity of the convective wind, L is the half-thickness of the diffusive cylinder and v_a is the velocity of the reaccelerating scattering centers.

The propagation model MIN has already been disfavored due to its small thickness of the diffusion cylinder. Studies on synchrotron emission, radio maps and low energy positron spectrum exclude a diffusion halo scale smaller than 2 kpc at 3σ level [167]. Moreover, a bayesian analysis on B/C, ^{10}Be/^{9}Be ratios and carbon and oxygen spectra suggests a thickness in the interval $[3.2, 8.6]$ kpc at 95% confidence level [168]. The analysis in [169] also disfavor a 1 kpc thickness, although the observation region is not optimized and the results are weakened by the inclusion of DM. And finally positron measurements from PAMELA exclude the MIN model [170].

`DRAGON`

In a similar way, propagation parameters can be derived with the `DRAGON` code, they are presented in 2.2. Five benchmark models are shown, in a similar fashion as for MIN MED and MAX. Their classification is however different:

- The THN, KRA and THK models assume the same value of δ – corresponding to a Kraichnan-type turbulence in the Quasi-Linear Theory (QLT) – but different values for the height z_t of the diffusion cylinder: THN corresponds to a very thin diffusion zone (0.5 kpc), KRA assumes 4 kpc and THK applies if the diffusion zone is as thick as 10 kpc.

Model	δ	η	D_0 [10^{28} cm^2 s^{-1}]	$\frac{dV_c}{dz}$ [km s^{-1} kpc^{-1}]	z_t [kpc]	v_a [km/s]
KRA	0.50	-0.39	2.64	0	4	14.2
KOL	0.33	1	4.46	0	4	36
CON	0.6	1	0.97	50	4	38.1
THK	0.50	-0.15	4.75	0	10	14.1
THN	0.50	-0.27	0.31	0	0.5	11.6
THN2	0.50	-0.27	1.35	0	2	11.6
THN3	0.50	-0.27	1.98	0	3	11.6

Table 2.2: **CR propagation parameters using** DRAGON **code** for the 5 standard profiles of [171] (upper portion of the table) as well as of the modified 'thin' setups (lower portion).

- The KOL model instead assumes a $\delta = 1/3$ (which is given by Kolmogorov turbulence in QLT), with a diffusive characteristic height fixed at 4 kpc.
- The CON model includes strong convective effects with $v_{conv}(z = 0) = 0$ and $dv_{conv}/dz \neq 0$ (but the diffusive height is still fixed at 4 kpc).

QLT is the simplest theory describing turbulences in a plasma far from equilibrium. Assuming an incompressible and isotropic plasma, the Kolmogorov and Kraichnan spectra can be obtained by choosing different magnetic field configurations: when the mean magnetic field dominates the fluctuations, we obtain a Kraichnan energy spectrum, while when the magnetic field fluctuations are stronger than the mean magnetic field, the spectrum is Kolmogorov-like. These energy spectra give rise to the diffusion coefficients with $\delta = 1/2$ (KRA= strong mean field) and $\delta = 1/3$ (KOL= strong fluctuations).

Using these parametrization, small halo scales are also disfavored. For example in [167] the authors claim a 5-σ exclusion for models with $z_t < 2$ kpc, with the best fit obtained from both synchrotron profiles and spectra being located around $z_t \simeq 8$ kpc. Other works show similar results [172, 173, 174]: e.g. in [174] the authors model several radio maps of the Galaxy as superpositions of an isotropic component plus the Galactic synchrotron emission, and obtain a preference for large halos in agreement with [167]. In order to investigate more carefully different choices for the thickness of the diffusion zone, we define two more THN-type models with, respectively, $z_t = 2, 3$ kpc.

2.5 Solar modulation

The outer solar atmosphere, also called the solar corona, is a very hot plasma which turns into a continuous plasma stream of coupled particles and magnetic fields: the *solar wind*. It encounters the ISM and a heliospheric bubble is created, separated by the heliopause from the ISM. Since the Sun is moving with respect to the ISM, an asymmetry with a bow shock and a heliotail is shaped, as shown in figure 2.6. In addition, due to the rotation of Sun around it's own axis, the magnetic field lines form a spiral, the Parker spiral. The two Voyager spacecrafts, launched in 1977, have observed the changes the solar wind undergoes at the heliospheric termination shock and the heliopause [175, 176].
Energetic particles can be produced inside the heliosphere, for example during solar flares ions can be accelerated up to energies of a few GeV and electrons to a few 100 MeV. Other pro-

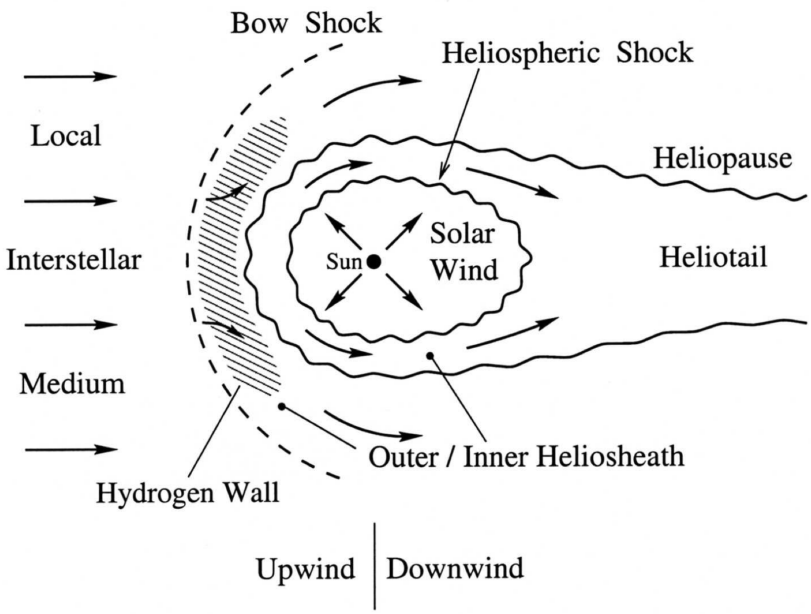

Figure 2.6: **Model of the heliosphere** in the rest frame of the Sun where the plasma flow of the ISM is compressed to form a bow shock [177].

duction mechanisms include coronal mass ejections and even emission of electrons by planetary magnetospheres, such as the one of Jupiter.

2.5.1 Effects of CR in the heliosphere

When entering the heliosphere, galactic CR encounter the solar wind, reshaping their energy spectrum up to energies of $\sim$ 20 GeV (for protons). The observed temporal variation of the CR intensity is called *solar modulation*. Corrections due to modulation effects are even used in archeology and in planning the flight path of commercial passenger jets [178]. For CR propagation, two periodic effects have to be considered: first, an anticorrelation between solar activity, undergoing an 11-year cycle and measured by the Sun spot number for example, and CR intensity has been well established. Second, the 22-year cycle related to the reversal of the Heliospheric Magnetic Field (HMF) at each period of extreme solar activity has also to be taken into account. The 27-day solar rotation and the daily variations due to the Earth's rotation are usually neglected, since their effect on CR are very small.

Transport equation

The effects on the propagation of CR in the heliosphere can be described with a transport equation, a diffusion-convection equation similar to the one for the propagation in the Galaxy. In fact, CR transport was first derived in the case of propagation in the heliosphere by Parker [179]. The Parker equation for the number density $N(\vec{x}, p, t)$, related to the distribution function $f(\vec{x}, p, t)$ through $N(\vec{x}, p, t) = 4\pi p^2 f(\vec{x}, p, t)$, can be written as

$$\frac{\partial f}{\partial t} = \nabla \cdot (\mathbf{K}_s \cdot \nabla) - \left(\vec{V} + \langle v_d \rangle\right) \cdot \nabla f + \frac{1}{p^2}\frac{\partial}{\partial p}\left(\frac{p^3}{3}(\nabla \cdot \vec{V}) f\right) + S, \tag{2.71}$$

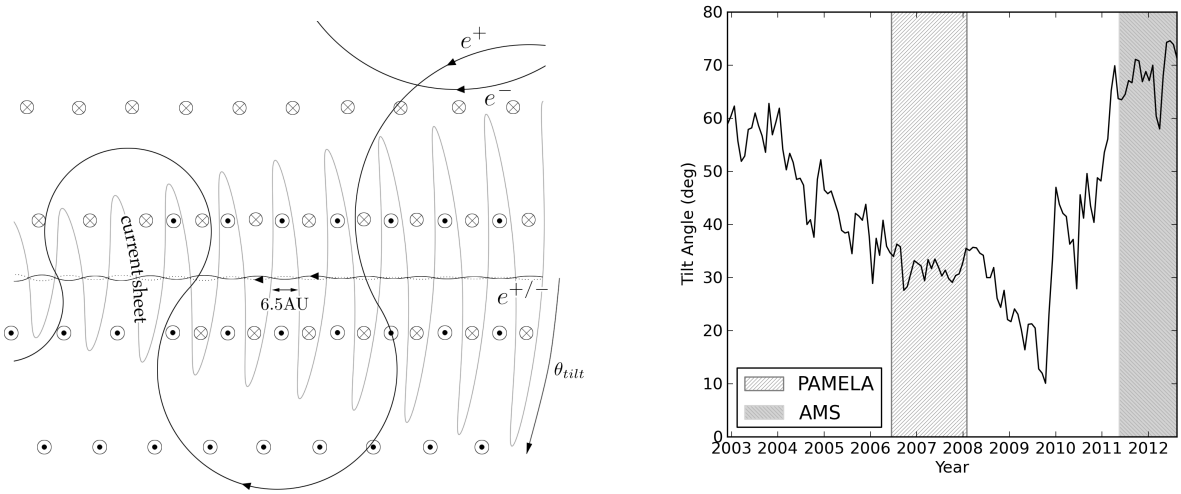

Figure 2.7: **Measurement of the tilt angle** left: A schematic of the heliospheric magnetic field: the rapidly oscillating grey line indicates the current sheet. The latitudinal extent of the current sheet is specified by the tilt angle $\alpha = \theta_{tilt}$. The trajectories of electrons and positrons are also shown. right: Measurements of the tilt angle for PAMELA and AMS-02 data taking periods [183].

with $\mathbf{K}_s$ the symmetrical diffusion tensor, $\vec{V}$ the solar wind velocity, $\langle v_d \rangle$ the averaged particle drift velocity due to gradients and curvatures in the global HMF and the adiabatic losses usually expressed as $\frac{1}{p^2}\frac{\partial}{\partial p}\left(\frac{p^3}{3}(\nabla \cdot \vec{V})f\right) = \frac{1}{3}(\nabla \cdot \vec{V})\frac{\partial f}{\partial \ln p}$. Second-order Fermi acceleration can be neglected in the case of heliospheric propagation. An elegant simplification can been applied to this equation: the averaged drift velocity for an isotopic or weakly anisotropic distribution is expressed as

$$\langle v_d \rangle = \frac{\beta P}{3} \nabla \times \frac{\vec{B}}{B}, \tag{2.72}$$

with $P = p/q$ the rigidity, and can be absorbed into the diffusion tensor as an antisymmetric component [180]. In fact, we can define the diffusion tensor

$$\mathbf{K} = \begin{pmatrix} \kappa_\parallel & 0 & 0 \\ 0 & \kappa_\perp & -\kappa_T \\ 0 & \kappa_T & \kappa_\perp \end{pmatrix}, \tag{2.73}$$

with $\kappa_T = \beta P/3B$ and where $\kappa_\parallel$ and $\kappa_\perp$ are the diffusion coefficient parallel and perpendicular to the background magnetic field and equation 2.71 becomes

$$\frac{\partial f}{\partial t} = \nabla \cdot \left(\mathbf{K} \cdot \nabla - \vec{V} f\right) + \frac{1}{p^2}\frac{\partial}{\partial p}\left(\frac{p^3}{3}(\nabla \cdot \vec{V})f\right) + S. \tag{2.74}$$

The parallel diffusion coefficient for example, is simply $\kappa_\parallel = \lambda_\parallel v/3$ and for momentum $P > 0.1$ GeV, the parallel mean free path can be modeled as

$$\lambda_\parallel \propto \lambda_0 \left(\frac{P}{\mathrm{GeV}}\right)^\delta \left(\frac{B_0}{B}\right), \tag{2.75}$$

with B_0 the Solar Magnetic Field strength at Earth. Thus the parallel diffusion coefficient is inversely proportional to the SMF strength B [181] and the rigidity dependence has an

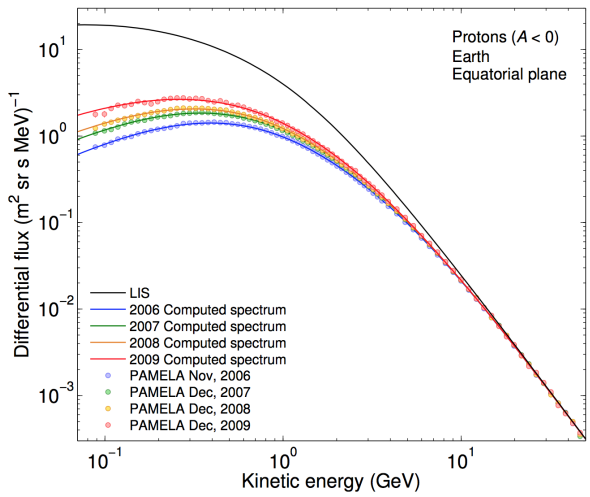

Figure 2.8: **Proton spectra measured by** PAMELA at different conditions of the solar cycle and computed spectrum using the full Parker equation [184] .

exponent δ, as in the propagation of CR in the Galaxy. The perpendicular components can also be modeled [182].
Since polarities are opposite in the northern and southern hemispheres of the Sun, an interface where the intensity of the SMF is null is formed. This plane is called the heliospheric current sheet (HCS). If the magnetic poles were perfectly aligned with the rotation axis of the poles, the HCS would be a plane perpendicular to the rotation axis. But since the magnetic poles are not aligned with the rotation axis, the HCS oscillates and has a "skirt"-like shape. We then define the angle between the magnetic pole and the axis of rotation as the tilt angle α, as shown on the left panel of 2.7. During the 11-years of the solar activity cycle, the magnetic poles migrate towards the Sun's equator, increasing the tilt angle until they cross the equator at solar maximum and reverrse the polarity of the HMF. Thus, the value of the tilt angle depends on the solar activity and its time evolution from 2003 to 2013 is shown on right panel of figure 2.7.
Numerical codes solving the full Parker equation reproduce very well the measured spectra, as shown on the right panel of figure 2.8 for the proton spectrum measured at different periods of the solar cycle.

Gradient and curvature drift

On top of the strength of the solar wind, particle drift cannot be neglected in solar modulation. Cycles where the magnetic field is directed outward in the northern and inward in the southern magnetic hemisphere are referred to as $A > 0$ cycles and during $A < 0$ cycles, the magnetic field is oriented in the opposite direction. In $A > 0$ cycles, positively charged particles drift inward at the poles and then downward from the poles toward the current sheet (near the equator). During $A < 0$ cycles, particles drift inward along the current sheet (near the equator) and then upward toward the poles, as shown on figure 2.9.
CR of opposite charge will reach the Earth from different heliospheric directions, particles with opposite charges will experience solar modulation differently. Not only does the flux of particles change according to the solar activity and HFM configuration, but we can also expect the flux

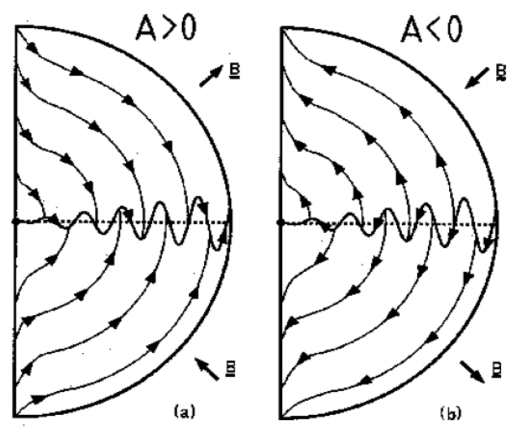

Figure 2.9: **Drifts for positively charged CR** during $A > 0$ and $A < 0$ HMF polarity cycle. During $A >$ cycles, the particles drift inwards, while in $A < 0$ cycles, they drift outwards [185] .

of antiparticles to be different from the one of particles.

2.5.2 Force-field approximation

If we want to follow the entire particle's journey from their production to their detection at Earth, we need to model both the galactic and the heliospheric propagation, with two transport equations. Using the full Parker equation after the transport equation 2.66 is a complicated exercise. Thus we are now going to introduce a successful approximation, called the force-field approximation, in order to take into account solar modulation in a simple and phenomenological correct frame. To sketch the approximation first proposed by Gleeson and Axford [186], we start from equation 2.74 and use $\nabla \cdot \vec{v} = \nabla(\vec{v}f) - \vec{v} \cdot \nabla f$

$$\frac{df}{dt} = \nabla \cdot \left(\mathbf{K}\nabla f - \vec{V}f\right) + \frac{1}{p^2}\frac{\partial}{\partial p}\left(\frac{p^3}{3}\nabla \cdot (\vec{V}f)\right) - \frac{1}{p^2}\frac{\partial}{\partial p}\left(p^2 \ \left(\frac{p}{3}\vec{V}\frac{\nabla f}{f}\right) \ f\right) + S. \tag{2.76}$$

Writing the adiabatic loss as $\langle \dot{p} \rangle = \frac{p}{3}\vec{V} \ \nabla f/f$, we further simply the equation to

$$\frac{df}{dt} = \nabla \cdot (\mathbf{K}\nabla f) + \frac{p}{3}\frac{\partial}{\partial p}\left(\nabla(\vec{V}f)\right) - \frac{1}{p^2}\frac{\partial}{\partial p}\left(p^2 \langle \dot{p} \rangle f\right) + S. \tag{2.77}$$

We can define the Compton-Getting coefficient $C = -1/3 \, \partial \ln f / \partial \ln p$, one third of the spectral index of a power law spectrum in momentum space, and the transport equation is a continuity equation

$$\frac{df}{dt} = \nabla \cdot \left(\mathbf{K}\nabla f - C\vec{V}f\right) - \frac{1}{p^2}\frac{\partial}{\partial p}\left(p^2 \langle \dot{p} \rangle f\right) + S, \tag{2.78}$$

where we can define the flux $S = \mathbf{K}\nabla f - C\vec{V}f$. Our goal is to find an analytical solution making a few approximations. Following the arguments in [187], we assume

- a steady-state solution $\partial f/\partial t = 0$,
- no sources are present inside the heliosphere $S = 0$,

- spherical symmetry and defining $\mathcal{K}$ as a single, effective radial coefficient, the structure of the magnetic field is lost,
- adiabatic losses $\langle \dot{p} \rangle$ are negligible compared to the other terms in the equation.

We obtain an equation in the weak-modulation approximation which is most accurate in the inner heliosphere and in which oppositely directed convective and diffusive flows nearly cancel out

$$\frac{Vp}{3}\frac{\partial f}{\partial p} + \mathcal{K}\frac{\partial f}{\partial r} = 0. \tag{2.79}$$

At the boundary of the modulation region, we have a constant solution $f(r,p) = f_b(r_b, p_b)$ along the contours satisfying $dp/dr = Vp/3\mathcal{K}$. Performing the change of variable from momentum p to rigidity $P = A/Z\sqrt{K(K+2m_0)}$, with K and m_0, the kinetic and rest mass per nucleon, respectively, the equation becomes

$$\frac{VP}{3\mathcal{K}}\frac{\partial f}{\partial P} + \frac{\partial f}{\partial r} = 0 \tag{2.80}$$

and the coefficient in front of the first term has dimension of potential per unit length, or field. This is why this approximation is called the *force-field approximation*. Assuming the diffusion coefficient is separable $\mathcal{K}(r,P) = \beta\kappa_1(r)\kappa_2(P)$, the solution of the equation 2.80 is

$$\int_P^{P_b} \frac{\beta\kappa_2(P')}{P'} dP' = \int_r^{r_b} \frac{v(r')}{3\kappa_1(r')} \equiv \phi(r). \tag{2.81}$$

If $\kappa_2 \sim P$ and $\beta \sim 1$, the force-field potential (also called Fisk potential) becomes $P_b - P = \phi$ [188], $P_b =$ is the rigidity at the boundary of the modulation region. By definition, the modulation potential causes energy change, however in the beginning we neglected adiabatic losses. By chance, it can be shown that the force-field energy loss $VP/3\mathcal{K}$ is an upper bound to the true adiabatic loss [189].

In the end, the energy spectrum at Earth $d\Phi_\oplus/dK$ is obtained by "rescaling" the rigidity of the particles before they enter the heliosphere

$$\frac{d\Phi_\oplus}{dK}(K) = \frac{d\Phi_{\text{LIS}}}{dK}\left(K + \frac{Ze}{A}\phi\right)\frac{K(K+2m)}{\left(K+m+\frac{Ze}{A}\phi\right)^2 - m^2}. \tag{2.82}$$

All these approximations are valid for kinetic energies above a few 100 MeV/nucleon [188, 190]. If the diffusion coefficient is not separable, then we have to assume $P_b - P = f(\phi, P)$. The force-field approximation is particularly successful in describing the solar modulation of proton and helium nuclei and reproduces well the shapes obtained by observations [191, 192] as well as numerical simulations with the full Parker equation [193]. In fact, simulated proton data with the dedicated numerical code `HelioProp` ([182, 194]) can be reproduced by using a force-field, as shown in table 2.3.

In practice, we will use the force-field approximation in order to model the effects of solar modulation on the fluxes of galactic CR. Before analyzing experimental data, it may be useful to study the values of the force-field potential for protons and antiprotons and thus determine an interval that we can use later in our analysis. For this purpose, we use the code `HelioProp`, obtain modulated fluxes for protons and antiprotons in different heliospheric propagation setups and fit the force-field potential. We considered a range of heliospheric propagation setups, in order to include all possible scenarios, in which:

- The polarity of the SMF and tilt angle were fixed to the appropriate values for the PAMELA data taking period. Since the data are dominated by the exceptional 2008-2009 solar minimum, a low value of the tilt angle is expected. In agreement with [195] we considered a value of 10°, which was also used in [194] to model leptonic data.
- The mean free path in the heliosphere (a free parameter which is generally fit to the data) was allowed to vary in a quite extreme range, from 0.01 AU to 0.4 AU.
- Also other parameters such as the normalization of the magnetic field and the ratio between perpendicular and parallel diffusion coefficients were varied within very wide ranges.

Then, for every `HelioProp` run we found the Fisk potential that provided the best fit of the modulated proton and antiproton spectra separately. We see that the force-field potential for antiprotons is not necessarily equal to the one of the protons. In a traditional force-field approximation, both force-fields should be equal, since charge-dependent effects due to drifts are neglected. In order to go beyond this simple approximation, we will consider the antiproton force-field to be different from the one of protons and still use equation 2.82. This is not a fair approach in the strict sense, but it allows us to take into account charge dependent effects in a very simple framework, without having to use complicated numerical codes.
The two force-fields typically do not differ by more than 50%. Moreover, these dedicated runs find that the value for antiprotons tends to be larger than the one for protons, at least for conditions of solar activity featuring a negative polarity of the solar magnetic field, a tilt angle of the heliospheric current sheet of about 20-40 degrees (both assumptions being appropriate for the PAMELA data taking period) and a parallel mean free path of protons at Earth not smaller than ~ 0.05 AU [196]. Only if the mfp assumes very small values one can have a Fisk potential for protons larger than the one for antiprotons. For electrons, solar modulation is more complicated. Even though electrons with energies $E \sim 1 - 100$ MeV are relativistic, and $\beta = 1$ holds, the diffusion coefficient $\mathcal{K}$ is independent of the rigidity and the approximations done for nuclei in equation 2.81 cannot be performed. Thus, the force-field is insufficient to describe the modulation and does not have dimension of a potential.

2.6 CR Experiments

In the following chapters, we will analyze data from different experiments: antiproton data from PAMELA and AMS-02 as well as γ-rays from Fermi-LAT. Let us first present shortly theses experiments.

2.6.1 PAMELA

The Payload for Antimatter Matter Exploration and Light-nuclei Astrophysics (PAMELA) is a module on board the Resurs-DK1 Russian satellite, launched on June 15th 2006. It is the first satellite-based experiment designed for the detection of CR, focussing on antimatter (positrons and antiprotons).
The most important result presented by the collaboration in 2008 is the rise in the positron fraction from 10 to 60 GeV, shown on the left panel of figure 1.23. The majority of astrophysical sources would predict a falling positron fraction thus the rise is know as the *PAMELA or*

polarity	tilt angle α [°]	m.f.p. λ_0 [AU]	δ [-]	ϕ_p [GV]	$\phi_{\bar{p}}$[GV]	rel. diff. [%]
-1.00	10.00	0.05	0.30	1.18	1.18	0.00%
-1.00	10.00	0.05	0.50	1.18	1.18	0.00%
-1.00	10.00	0.05	1.00	1.12	1.12	0.00%
-1.00	10.00	0.10	0.30	1.06	1.10	3.77%
-1.00	10.00	0.10	0.50	1.02	1.10	7.84%
-1.00	10.00	0.10	1.00	1.02	1.10	7.84%
-1.00	10.00	0.20	0.30	0.78	0.96	23.08%
-1.00	10.00	0.20	0.50	0.74	0.90	21.62%
-1.00	10.00	0.20	1.00	0.60	0.74	23.33%
-1.00	10.00	0.30	0.30	0.60	0.82	36.67%
-1.00	10.00	0.30	0.50	0.54	0.76	40.74%
-1.00	10.00	0.30	1.00	0.46	0.58	26.09%
-1.00	10.00	0.40	0.30	0.36	0.46	27.78%
-1.00	10.00	0.40	1.00	0.48	0.72	50.00%
-1.00	20.00	0.05	0.30	1.46	1.18	-19.18%
-1.00	20.00	0.05	1.00	1.28	1.12	-12.50%
-1.00	20.00	0.40	0.30	0.48	0.72	50.00%
-1.00	20.00	0.40	1.00	0.36	0.46	27.78%
-1.00	40.00	0.05	0.30	1.56	1.18	-24.36%
-1.00	40.00	0.40	0.30	0.50	0.70	40.00%
-1.00	40.00	0.40	1.00	0.38	0.44	15.79%
-1.00	60.00	0.05	0.30	1.50	1.86	24.00%
-1.00	60.00	0.05	1.00	1.18	1.34	13.56%
-1.00	60.00	0.40	0.30	0.50	0.66	32.00%
-1.00	60.00	0.40	1.00	0.40	0.42	5.00%

Table 2.3: **Solar modulation parameters used in** `HelioProp` in order to simulate the Sun's effect and fitted force-field potentials for protons and antiprotons

positron excess. This result confirmed suspicions after the HEAT experiments also pointed towards a rise in the positron fraction. However, the error bars on the measurements were large and at these energies the experiment was limited by particle identification: it may have not been able to distinguish between a proton and a positron. Thus, it is truly PAMELA which established the rise. On the other hand, no excess was found in the antiproton flux, as seen on the right panel of figure 1.23.

The PAMELA experiment also confirmed the presence of antiprotons in the Van Allen radiation belts while passing through the South Atlantic Anomaly (SAA). The Van Allen belts are donut-shaped rings of charged particles trapped by the Earth's magnetic field. In 2011, it was well known that the belts contained protons and electrons, PAMELA confirmed theoretical models predicting also the presence of antiprotons. They originate from the interaction of CR with the upper atmosphere before being trapped by the Earth's magnetic field.

2.6.2 AMS-02

The Alpha Magnetic Spectrometer (AMS) is a particle physics detector on board the International Space Station (ISS). The prototype AMS-01, a simplified version of the detector, was flown on board the Space Shuttle *Discovery* during flight STS-91 in 1998 and exposed it to

the space environment. The prototype measured CR fluxes, thus proving the feasibility of the mission. The real experiment AMS-02 was then launched on May 16th 2011 onboard the Space Shuttle *Endeavor* carrying it to the ISS. The module was installed on the space station three days later. For a long time, it was not sure if AMS-02 could be brought to the ISS. In fact, after the tragic accident of the Space Shuttle *Columbia*, NASA reduced Shuttle flights. Other ways of delivering the experiment to the space station were investigated, but fortunately on its last flight (the second to last flight of the entire Space Shuttle program) *Endeavor* brought the experiment to its location.
The AMS-02 experiment was first supposed to contain a cryogenic, superconducting magnet. After the announcement of the extension of the ISS's operational time, the collaboration decided to integrate the non-superconducting magnet used for the prototype mission. Thus, the experiment should be able to measure CR fluxes through the entire lifetime of the ISS, until 2020 or longer.
The first results announced by AMS-02 concern positrons. In fact, the experiment measured the position fraction up to energies of 275 GeV with an unprecedented precision. The data may show a flattening of the rise around 275 GeV, as shown on figure 1.23. In addition, no anisotropy was found by AMS-02 in the positron flux. Very recently, the antiproton over proton ratio was presented at CERN. We will discuss these measurements and the implications for DM in the next chapter.

2.6.3 Fermi

The Fermi Gamma-ray Space Telescope (previously named Gamma-ray Large Area Space Telescope or GLAST) is the successor of the EGRET mission and was brought into low Eath orbit on June 11th 2008 by a Delta II rocket. The mission is designed to observe high-energy phenomena in the universe, such as understanding the mechanisms of particle acceleration in active galactic nuclei (AGN), pulsars, and SNR, study supermassive blackholes, merging neutron stars, etc.. It has two main instruments on board: the Gamma Burst Monitor (GBM), measuring gamma ray energies of 8 keV up to 30 MeV with a temporal resolution of two microseconds and the Large Area Telescope (LAT) measuring gamma rays with energies of 20 MeV to 300 GeV. The LAT has a very large field of view, over 2 steradian (1/5 of the entire sky) and has a high sensitivity above 10 GeV.
The Fermi satellite is responsible for numerous astrophysical discoveries, such as a gamma-ray pulsar at the center of a SNR, quiet in other wavelengths to the measurement of the gamma radiation from a micro quasar. It has also measured the most violent gamma- ray bust ever seen emitting the energy equivalent to 5 solar masses in 60 seconds. In November 2010, the collaboration announced the detection of two gamma-ray and x-ray bubbles around the Milky Way. The bubbles, named *Fermi Bubbles*, extend about 10 kpc above and below the center of the Galaxy. There are many results from the Fermi-LAT which have implications for DM indirect detection. In the following, we will in particular focus on the GeV excess. In fact, the collaboration found that the Galactic Center produces more high-energy gamma rays than can be explained by known astrophysical sources. This is known as the *Galactic Center excess* and could be due to DM. We will investigate this interpretation in chapter 5.

2.7 What about DM?

On top of the known astrophysical sources, DM pair annihilations or decay can also be a primary source of CR and can thus be added in the source term S of equation 2.66 for different types of CR species. In fact, these CR will also propagate through the diffusion halo and the heliosphere before being measured at Earth, by ground- or space-based experiments. In pursuing the goal of identifying DM or better constraining it, searching for a contribution from DM annihilation and decay is a powerful approach, complementary to direct detection experiments and collider searches.

The ultimate proof for existence of DM would be a signal in different CR species. It is thus important to be able to perform multi-messenger analyses in a coherent framework and therefore to develop a set of coherent, model independent tools. A step in this direction is presented in the following chapters. The Poor Particle Physicist Cookbook for Dark Matter Indirect Detection (`PPPC4DMID`) provides tools in form of mathematica interpolation functions that can be easily used by the community in order to search for DM in CR. More precisely, on the `PPPC4DMID` website, propagated CR fluxes at Earth and intermediate functions, such as energy loss and halo functions (described in chapter 4), for different astrophysical configurations can be downloaded.

The purpose of this thesis work is twofold: develop and improve the tools in the `PPPC4DMID` and use them in order to search for a DM contribution in CR data. We will begin with antiprotons, which are very sensitive to DM. Their astrophysical background is due to the spallation of proton and helium CR on the ISM. The spectra of these species are measured by CR experiments and can be easily incorporated into the propagation equation. We will analyze PAMELA data as well as study the sensitivity of the AMS-02 experiment, using the antiproton fluxes from the original `PPPC4DMID` [9]. Then, we will improve these fluxes by implementing energy losses and diffusive reaccelerating in the propagation equation and reevaluate the constraints on DM using the same PAMELA data and the forecast for AMS-02. Finally, with the recently presented AMS-02 antiproton over proton ratio, we tackle the question of a DM signal and derive bounds on the annihilation cross-section and the decay rate of DM.
Then we move on to electrons and positrons from DM annihilation and decay and their secondary radiation due to the $e^{\pm}$ energy losses. We improve the energy loss function of $e^{\pm}$ by adding ionization and bremsstrahlung losses to the existing functions in the `PPPC4DMID`. We then evaluate the halo functions for secondary emissions, such as inverse compton, bremsstrahlung and synchrotron. These functions can then be used in order to evaluate the DM contribution at different wavelengths.
Finally, we will address the GC excess, where both antiprotons and secondary emissions from $e^{\pm}$ are used in a coherent framework: the GC excess has been measured in γ-rays by the Fermi satellite and interpreted as a DM annihilation signal. Secondary emissions have to be included in order to determine the correct annihilation channel, mass and cross-section. In addition, antiprotons can set contains on the hadronic channels in different propagation models.

Chapter 3

DM indirect detection with antiprotons

3.1 Introduction

Since the initial proposal to use antiprotons as probe for DM [197], many studies have stressed the importance of this channel, including several recent ones [198]- [202]. This is both for intrinsic and contingent reasons. An intrinsic reason is that the production of antiprotons is rather universal in DM models: as long as DM particles annihilate or decay into quarks or gauge bosons $\bar{p}$ copiously emerge from the hadronization process. Also annihilation or decay into leptons produces antiprotons, thanks to ElectroWeak corrections, the emission of EW gauge bosons from the final state particles, such as the one shown on figure 3.1.

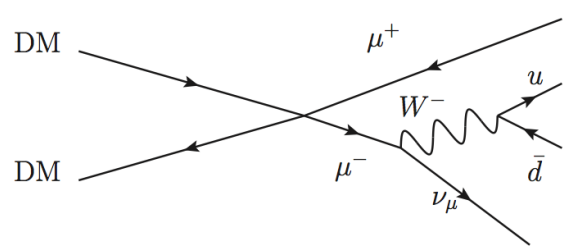

Figure 3.1: **Example of a diagram leading to ElectroWeak corrections** in the antiproton flux from DM annihilation (or decay). The emitted W-boson decays into quarks which will then contribute to the total antiproton flux, after hadronization.

Other reasons are that the determination of the astrophysical background is relatively under control (at least if compared to other channels) and that the Galactic propagation of antiprotons can be better modeled than the one of other charged particles. A contingent reason, on the other hand, is that in other channels (most notably positrons and gamma rays) sizable excesses have shown up, which cannot be easily attributed neither to DM nor to known astrophysical processes. Until their origin is clarified, they greatly limit the robustness of DM analyses based on these channels. Finally, another motivation stems from the great precision of the $\bar{p}$ data already available from the PAMELA satellite and the even better precision from AMS-02.

3.2 Injection spectrum

We consider several different annihilation or decay channels, in a model independent way. Following [9], we consider a complete array of annihilation or decay channels, in a model independent way. They consist in the following 2×23 cases:

$$\left.\begin{array}{rr} \text{annihilation} & \text{DM DM} \\ \text{decay} & \text{DM} \end{array}\right\} \rightarrow \left\{\begin{array}{l} e_L^+ e_L^-,\ e_R^+ e_R^-,\ \mu_L^+ \mu_L^-,\ \mu_R^+ \mu_R^-,\ \tau_L^+ \tau_L^-,\ \tau_R^+ \tau_R^-, \\ q\bar{q},\ c\bar{c},\ b\bar{b},\ t\bar{t},\ \gamma\gamma,\ gg, \\ W_L^+ W_L^-,\ W_T^+ W_T^-,\ Z_L Z_L,\ Z_T Z_T, \\ hh, \\ \nu_e \bar{\nu}_e,\ \nu_\mu \bar{\nu}_\mu,\ \nu_\tau \bar{\nu}_\tau, \\ VV \rightarrow 4e,\ VV \rightarrow 4\mu,\ VV \rightarrow 4\tau. \end{array}\right. \tag{3.1}$$

Here the subscripts $_{L,R}$ denote the *L*eft-handed and *R*ight-handed polarizations for the leptons and $_{L,T}$ the *L*ongitudinal or *T*ransverse ones for the gauge boson: since EW corrections act differently on the different polarizations, it is important to keep them separate. In the end, the full antiproton spectrum is obtained by adding the contributions coherently: for each lepton species $\phi_l = 1/2(\phi_{l_L} + \phi_{l_R})$ and for gauge bosons $\phi_{GB} = 1/3\phi_{GB_L} + 2/3\phi_{GB_T}$. $q = u, d, s$ denotes a light quark and h is the SM Higgs boson, with its mass fixed at 125 GeV. The last three channels denote models in which the annihilation or decay first happens into some new (light) boson V which then decays into a pair of leptons. As for the DM mass, we consider the range $m_{\rm DM} = 5\,\text{GeV} \rightarrow 100\,\text{TeV}$ (annihilation) or $m_{\rm DM} = 10\,\text{GeV} \rightarrow 200\,\text{TeV}$ (decay).

In practice the spectral shape of the resulting $\bar{p}$ fluxes from all these channels are not very different, due to the qualitative fact that $\bar{p}$ are the final product of a complex hadronization process which 'washes out' possible distinguishing features, as shown in figure 3.2. Moreover, some of the channels yield $\bar{p}$ spectra which are practically indistinguishable, both in terms of shape and normalization. This is the case for $b\bar{b}$ and $t\bar{t}$ (of course for the range of DM masses in which both are kinematically allowed), for W^+W^- and ZZ as well as for $\mu^+\mu^-$ and $\tau^+\tau^-$). Therefore, for all practical purposes, only four of the channels lead to actually different results ($b\bar{b}, W^+W^-, \mu^+\mu^-$ and $\gamma\gamma$) and thus we will mainly focus on these in the following. Along these same lines of argument, the results for other channels that we do not consider can be safely deduced from channels with similar spectra: for instance, the hh channel is equivalent to the $b\bar{b}$ one, the e^+e^- is equivalent to the $\mu^+\mu^-$ one etcetera. Alongside with the 'traditional' quark and weak gauge boson channels (collectively: 'hadronic channels'), we consider leptonic channels ($\mu^+\mu^-, \tau^+\tau^-$) and a direct $\gamma\gamma$ channel. Antiprotons are produced in these channels because we take into account electromagnetic and electroweak corrections. Not surprisingly, the yield of $\bar{p}$ from these processes is suppressed and therefore the resulting constraints will probably be much weaker than for hadronic channels. Nevertheless, we include these channels for completeness and for the interest that they have carried in recent years for the interpretation in terms of DM of the PAMELA and Fermi $e^\pm$ anomalies and of the 135 GeV line in Fermi data.

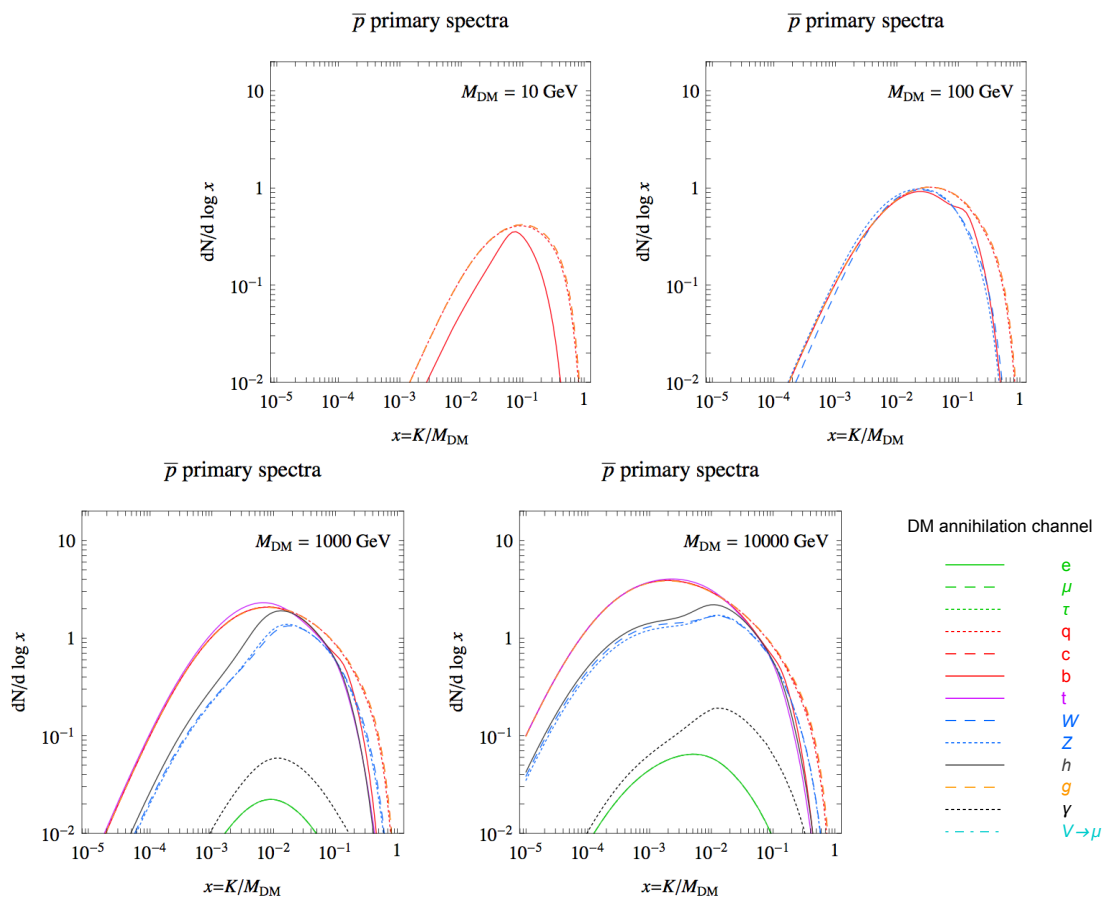

Figure 3.2: **Primary antiproton fluxes** from DM annihilation for different channels and DM masses [9]. Spectra from DM decay can be simply obtained by rescaling the DM mass from the annihilation spectra $m_{\rm DM} \to m_{\rm DM}/2$.

3.3 First analysis of PAMELA data- Original PPPC4DMID

First, we will use a simplified version of the propagation equation and model the astrophysical background as a power law above kinetic energies of $K > 10$ GeV, in order to avoid solar modulation effects[1]. In fact, in the analysis of PAMELA we will focus only on these data points. Later, we will include the entire energy spectrum in a more rigorous analysis.

3.3.1 Primaries

Primary antiprotons correspond to the $\bar{p}$ flux produced by DM annihilations or decays in the galactic halo. For the transport equation 2.66, they constitute a source term S which reads

$$S_{\bar{p}}^{\rm prim} = \frac{1}{2}\left(\frac{\rho}{M_{\rm DM}}\right)^2 f_{\rm inj}^{\rm ann}, \qquad f_{\rm inj}^{\rm ann} = \sum_f \langle \sigma v \rangle_f \frac{dN_{\bar{p}}^f}{dK} \qquad \text{(annihilation)}, \tag{3.2}$$

[1]In section 2.5, we saw that solar modulation can affect antiproton energies up to ~ 20 GeV, thus in the range of $10-20$ GeV, there might be a small impact that we are not modeling. However these small effects can be absorbed into the parameters of the power law background.

$$S_{\bar{p}}^{\rm prim} = \left(\frac{\rho}{M_{\rm DM}}\right) f_{\rm inj}^{\rm dec}, \qquad f_{\rm inj}^{\rm dec} = \sum_f \Gamma_f \frac{dN_{\bar{p}}^f}{dK} \qquad \text{(decay)}. \tag{3.3}$$

The above formulæ show the factorization of the source term in a portion that depends essentially on astrophysics (the DM density distribution ρ) and in a portion ($f_{\rm inj}^{\rm ann/dec}$) that depends on the particle physics model. Here $dN_{\bar{p}}/dK$ are the antiproton spectra per single annihilation or decay event and f runs over all the channels with $\bar{p}$ in the final state, with the respective thermal averaged cross-sections σv or decay rate Γ.

The source of antiprotons from DM annihilations or decay depend on the distribution of DM in the galactic halo. We consider the various DM halo profiles, presented in section 1.1.3. After their production, the antiprotons are subject to propagation in the galactic environment, described by the transport equation in section 2.4.4. In a first time, we will consider a simplified version of the equation, neglecting energy losses and momentum diffusion (second-order Fermi acceleration). In fact, these effects are minimal for antiprotons and nuclei in general at kinetic energies above 10 GeV. Thus, the master equation for the energy and space distribution function $f = dn/dK$ for antiproton CR becomes

$$\frac{\partial f}{\partial t} - D_{xx}(K)\cdot\nabla^2 f + \frac{\partial}{\partial z}\left\{\text{sign}(z)\, f\, V_{\rm conv}\right\} = S, \tag{3.4}$$

where the spatial diffusion coefficient is $D_{xx}(K) = D_0\beta\,(p/p_0)^\delta$ and with $p = \sqrt{K^2 + 2m_p K}$ the antiproton momentum. The propagation parameters used in this equation are listed in table 2.1. The propagated fluxes are shown on figure 3.3. As mentioned before, propagation models are named after their (antiproton) fluxes from DM annihilation or decay potentially recovered as earth: the set denoted by 'MIN' ('MAX') corresponds to a minimal (maximal) final yield of $\bar{p}$ and therefore they bracket the uncertainty. The halo model also adds an uncertainty on the antiproton spectrum from DM, especially for annihilations, as the DM distribution is squared in the primary source term.

3.3.2 Astrophysical sources: secondaries

Secondary antiprotons, produced by standard CR processes (essentially the spallation of primary protons on the ISM, as described in section 2.2.2), represent the astrophysical background fro DM searches. In a first approach, we do not calculate such background ourselves, but use instead the determination obtained by [171]. There, the two extreme cases are the Kolmogorov (KOL) and Kraichanian (KRA) models: we choose a spectrum which goes roughly through the middle of these (for illustration, it is the one plotted in figure 3.4) and will be refer to as the 'fixed background'. To model the uncertainty of such background function: we let the amplitude vary by 10% and the spectral index by ± 0.05. This envelops fairly generously the different models and the astrophysical uncertainties. Technically, we just multiply the fixed background by $A\,K^p$ (where K is the antiproton kinetic energy), and allow $A \in [0.9, 1.1]$ and $p \in [-0.05, 0.05]$. In the following, we will marginalize with respect to the A and p parameters, i.e. we will identify the values that give the best fit for a given assumed signal and a given set of data. We refer to this procedure as 'varying background'. In absence of a signal, the best fit background with respect to the PAMELA data is obtained with an amplitude of $A_0 = 1.08$ and a slope $p_0 = -0.05$: it gives a $\chi_0^2(A_0, p_0) = 4.62$ for 8 data points (we always restrict to kinetic energies $K > 10$ GeV).

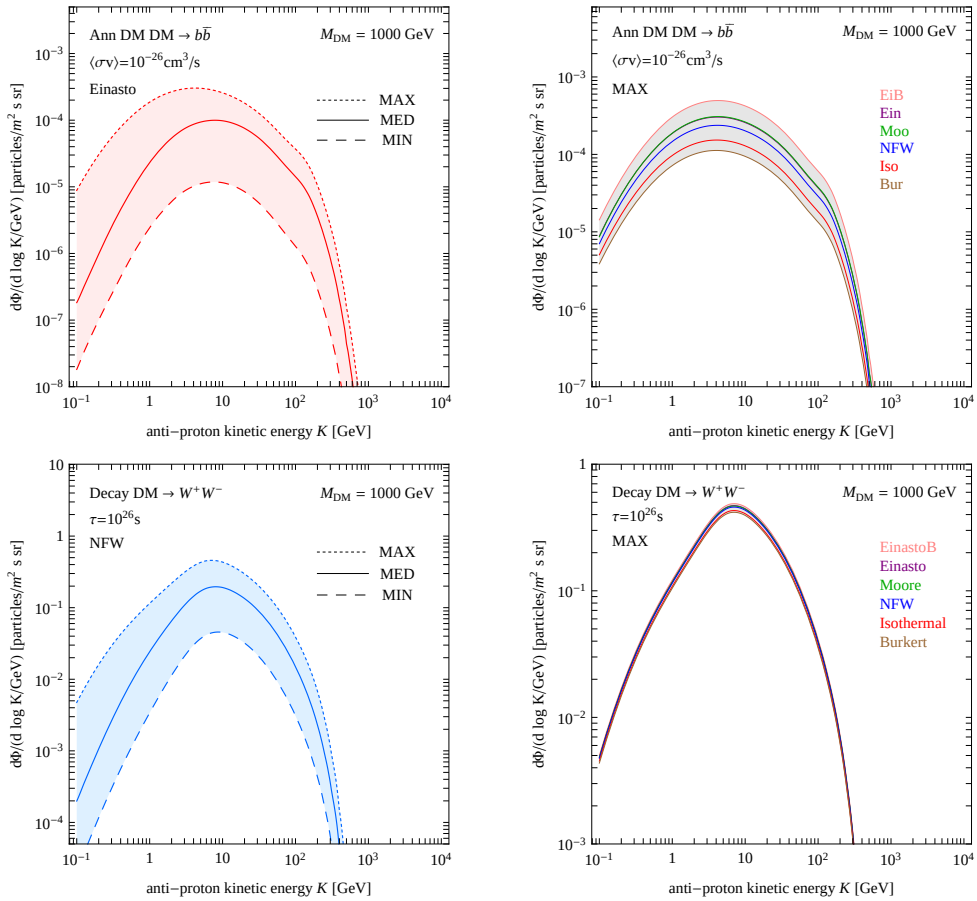

Figure 3.3: **Astrophysical uncertainty on the antiproton flux** due propagation and halo profile for annihilation into $b\bar{b}$ and decay into W^+W^- [9].

In previous analyses (e.g. [203]), the background used was the one in [204] with wider intervals for the variating amplitude (40%) and slope (±0.10). The obtained uncertainty band was thus broader and these choices would allow to fit the PAMELA data slightly better. However, we decide to make use of the function deduced from [171] since this analysis takes recent CR and especially proton spectra into account and the uncertainties are clearly smaller. It is of course possible to get the same larger bandwidth from the new background by increasing the amplitude and the slope. A power law (above 10 GeV) is expected to follow from most astrophysical processes, it may not always be strictly the case. In fact, some astrophysical sources, such as supernova remnants [205] or plasma phenomena [206], could induce a different spectrum. However, such deviations from an effective power law are typically expected at energies higher than those of our interest [207]. We will add certain effects in section 3.4 and reevaluate the constraints, as well as the AMS-02 sensitivity.

3.3.3 Antiproton constraints from PAMELA ($K > 10$ GeV)

The data provided by the PAMELA satellite [114] and reproduced in figure 3.4, extend from kinetic energies of less than 1 GeV to about 180 GeV (although we use only the portion above 10 GeV to avoid the effects of solar modulation).

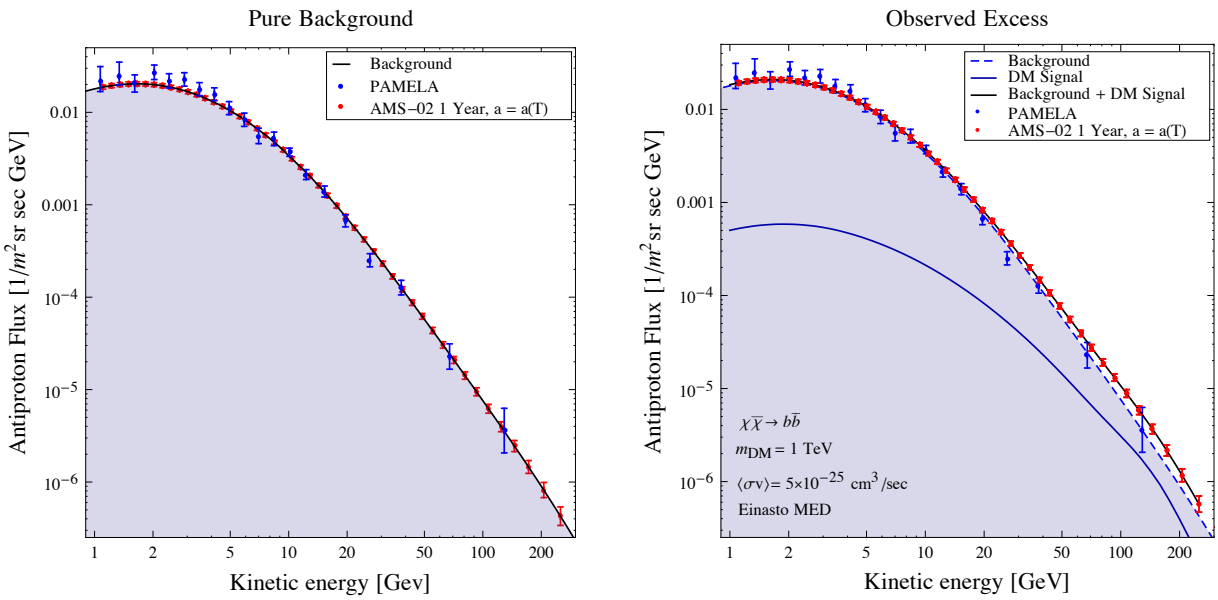

Figure 3.4: **Examples of antiproton fluxes and data.** Left Panel: astrophysical $\bar{p}$ background, superimposed to the current data from PAMELA and to one of our realizations of mock data from the AMS-02 experiment. Right Panel: the same but including a contribution from DM annihilation giving rise to an excess on top of the background which could be detected by AMS-02. The example chosen is DM annihilating into $b\bar{b}$ with $m_{\rm DM} = 1\ TeV$ and $\langle\sigma v\rangle = 5\times10^{-25}$ cm^{3}s^{-1} for an Einasto halo profile and MED propagation parameters. The mock data does not take into account the fact that during the AMS-02 data taking period solar conditions are different than the ones for the PAMELA data dating period

The total antiproton flux is given by the sum of the DM and the astrophysical contributions,

$$\phi_{\rm tot}(m_{\rm DM}, \langle\sigma v\rangle; A, p) = \phi_{\rm DM}(m_{\rm DM}, \langle\sigma v\rangle) + \phi_{\rm bkg}(A, p). \tag{3.5}$$

For fixed values of the DM particle mass $m_{\rm DM}$ and the thermally averaged annihilation cross-section $\langle\sigma v\rangle$, the astrophysical background is optimized within the uncertainty bandwidth in order to minimize the χ^2 of the total flux with respect to the data. During this procedure, the optimal values of the amplitude $A_{\rm opt} \in [0.9, 1.1]$ and the slope $p_{\rm opt} \in [-0.05, 0.05]$ are determined. Then, to find the exclusion contour in the $(m_{\rm DM}, \langle\sigma v\rangle)$-plane, the required condition is

$$\Delta\chi^2(m_{\rm DM}, \langle\sigma v\rangle) = \chi^2(m_{\rm DM}, \langle\sigma v\rangle; A_{\rm opt}, p_{\rm opt}) - \chi^2_0(A_0, p_0) < 4. \tag{3.6}$$

We show the resulting contours in figures 3.19 (for annihilating DM) and 3.6 (for decaying DM). In the left panels we have fixed the astrophysical parameters to a fiducial choice: the halo model is chosen to be Einasto and the propagation parameters to be MED. The constraints on $\langle\sigma v\rangle$ reach the level of $\sim 10^{-25}$ cm^3/sec for the quark or gauge boson channels, at a DM mass of about 100 GeV. For decaying DM, the constraints on the lifetime τ reach $\sim$ few $\times\ 10^{27}$ sec. The bounds for the exotic channels ($\gamma\gamma$ and leptons) are much less stringent, as expected. The constraint from the leptonic channels is lifted below $m_{\rm DM} \simeq 300$ GeV, consistently with the fact that EW corrections are effective only for large $m_{\rm DM}$ [208]. The $\gamma\gamma$ constraint exhibits two regimes: at $m_{\rm DM} \lesssim 300$ GeV some $\bar{p}$ are produced by γ showering; at $m_{\rm DM} \gtrsim 300$ GeV

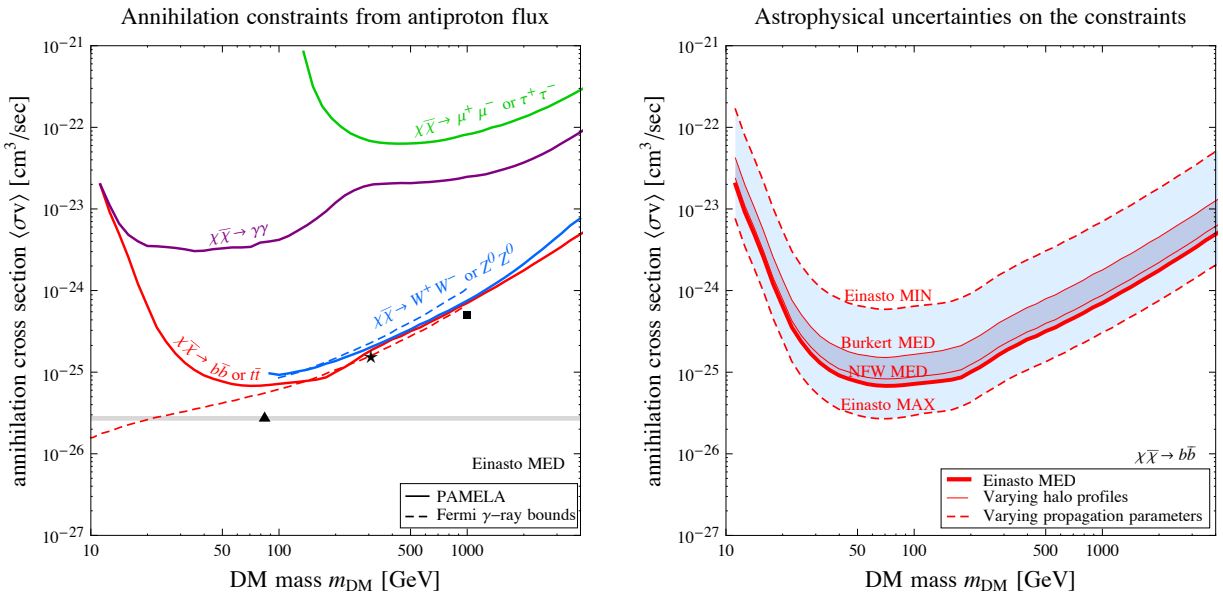

Figure 3.5: **Annihilating DM: current constraints.** Left Panel: current constraints from the antiproton measurements by PAMELA, for different annihilation channels. The areas above the curves are excluded. The dashed lines reproduce the γ-ray constraints from [209], for the same channels. The symbols individuates the parameters used for the analyses in section 3.3.4 while the horizontal band signals the thermal relic cross-section. Right Panel: illustration of the impact of astrophysical uncertainties: the constraint for the $b\bar{b}$ channel spans the shaded band when varying the propagation parameters (dashed lines) or the halo profiles (solid lines).

EW corrections set in and increase the $\bar{p}$ yield, resulting in a constraint that follows the shape of the leptonic one.

These results show that, for the hadronic channels, the constraints inferred from the data of PAMELA are already competitive with (or even slightly better than) the bounds from Fermi γ-rays (reported as dashed lines in figures 3.19 and 3.6, respectively from [209] (See also [210] and [211]), for both annihilating and decaying DM. This is a non-trivial conclusion, especially considering that the prospects of improvement in γ-rays are arguably less promising than in antiprotons (the Fermi satellite will at most double the statistics in the final years of its lifetime, while for antiprotons AMS-02 can in principle accumulate high precision data for several years to come).

On the other hand, the astrophysical uncertainties for antiprotons are non-negligible: the choice of propagation parameters and halo profile can change the constraints by one or two orders of magnitude, as illustrated in the right panels of figures 3.19 and 3.6. The impact of changing the propagation parameters from MIN to MAX is particularly important as it accounts by itself for more than a one order of magnitude shift in the bounds. At this point, we should remember that the propagation model MIN has already been disfavored due to its small thickness of the diffusion cylinder. As expected, the impact of changing the halo profile is more important for the annihilation case than for the decay one.

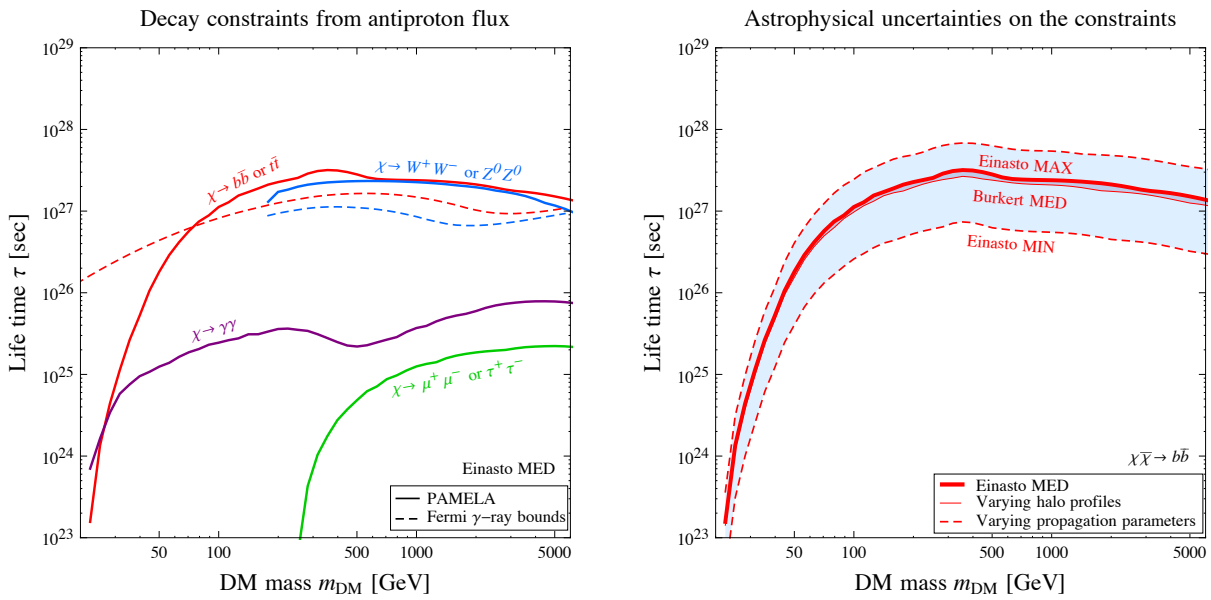

Figure 3.6: **Decaying DM: current constraints.** Left Panel: current constraints from the antiproton measurements by PAMELA, for different decay channels. The areas below the curves are excluded. The dashed lines reproduce the γ-ray constraints from [211]. Right Panel: illustration of the impact of astrophysical uncertainties: the constraint for the $b\bar{b}$ channel spans the shaded band when varying the propagation parameters (dashed lines) or the halo profiles (solid lines).

3.3.4 Projected sensitivity of AMS-02

In order to study the reach of the upcoming early AMS-02 antiproton results on DM, we need to produce mock AMS-02 data and their associated error bars, which we do by implementing the following procedure. We adopt a linear approximation of the rigidity resolution of AMS-02 as given in [212]

$$r(K) = \frac{\Delta K}{K} = 0.0042 \times K + 0.1, \tag{3.7}$$

where K is the kinetic energy of the incoming antiproton. This allows us to determine a realistic $\bar{p}$ energy binning. We assume that the $\bar{p}$ flux will be measured up to 300 GeV (we will use only the portion above 10 GeV, as already discussed, for a total of 27 simulated data points), thus extending the range of PAMELA to higher energies. Next, we need to estimate the errors on the measurement of the antiproton flux. The number of collected and reconstructed antiprotons in AMS-02 in a given bin i centered around a kinetic energy K_i will be given by

$$N_i = \epsilon\, a(K_i)\, \phi(K_i)\, \Delta K_i\, \Delta t, \tag{3.8}$$

where ϵ is the efficiency, a the geometrical acceptance of the apparatus (which is in general a function of the energy), ϕ the antiproton flux, ΔK the width of the kinetic energy bin and Δt the exposure time. Assuming a Poisson distribution ($\Delta N = \sqrt{N}$), the statistical error on the antiproton flux in bin i is therefore

$$\Delta\phi_i\,|_{stat} = \sqrt{\frac{\phi(K_i)}{\epsilon\, a(K_i)\, \Delta K_i\, \Delta t}}. \tag{3.9}$$

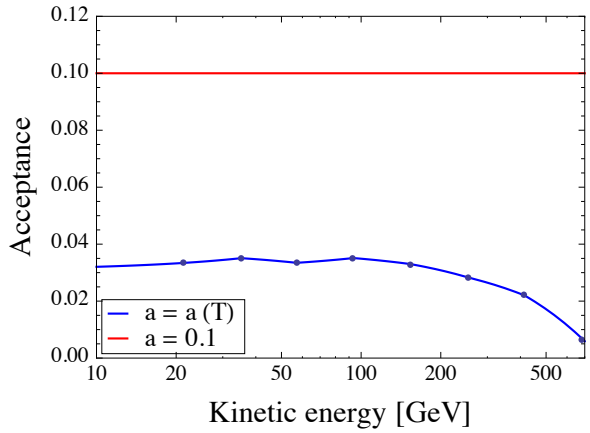

Figure 3.7: **Modelisation of the acceptance of the** AMS-02 **detector** for the realistic case (blue) [215] and the optimistic constant function (red).

We assume systematic errors of 5% based on the analysis in [213] and we sum them in quadrature with the statistical ones. The $\bar{p}$ efficiencies of the different subdetectors of AMS-02 are expected to be close to 1 (or in any case well above 0.9) for the whole range of energies of our interest [214]. Therefore we set the overall efficiency $\epsilon = 1$. The modelisation of the acceptance of the experiment is the most critical point and the one which is least accessible from outside the collaboration. We will therefore consider two options, as shown in figure 3.7:

1. $\Delta t = 1$ year and an acceptance $a = 0.147$ m^2 sr for 1 GeV $< K <$ 11 GeV, but an energy dependent one (contained roughly in the interval $a \sim 0.02 \div 0.04$ m^2 sr) for energies $K >$ 11 GeV, by interpolating the points in fig. 8 of [215];

2. $\Delta t = 3$ years with a constant acceptance for all energies $a = 0.1$ m^2 sr.

The second case is obviously much more optimistic, as it gives rise to a much larger accumulated statistics. The first case might be more realistic though: in AMS-02, the identification of antiprotons at high energy will likely have to rely on the use of the calorimeter, thus reducing the pure geometrical acceptance of the experiment. We can expect the real data to lie in between these two scenarios. The resulting set of mock data (for option 1, for definiteness) is reproduced in figure 3.4, both for a scenario with no excess (left) and for a scenario where an excess over background is detected (right).

Foreseen constraints

First, we consider a scenario in which the measurements of AMS-02 do not show an antiproton excess and the data points follow the background, as represented on figure 3.4 on the left. We generate the mock data using the 'fixed background' spectrum function. We then compute the constraints for annihilation and decay of DM with the same method discussed in section 3.3.3 (therefore, in particular, implementing the 'varying background' procedure). We believe this 'workflow' to be realistically similar to an actual data analysis. The results are presented in figure 3.8.
It is apparent that, with AMS-02, the constraints can be improved by about an order of magnitude or slightly less with respect to PAMELA. For the $b\bar{b}$ channel (and for the $t\bar{t}$ one, when

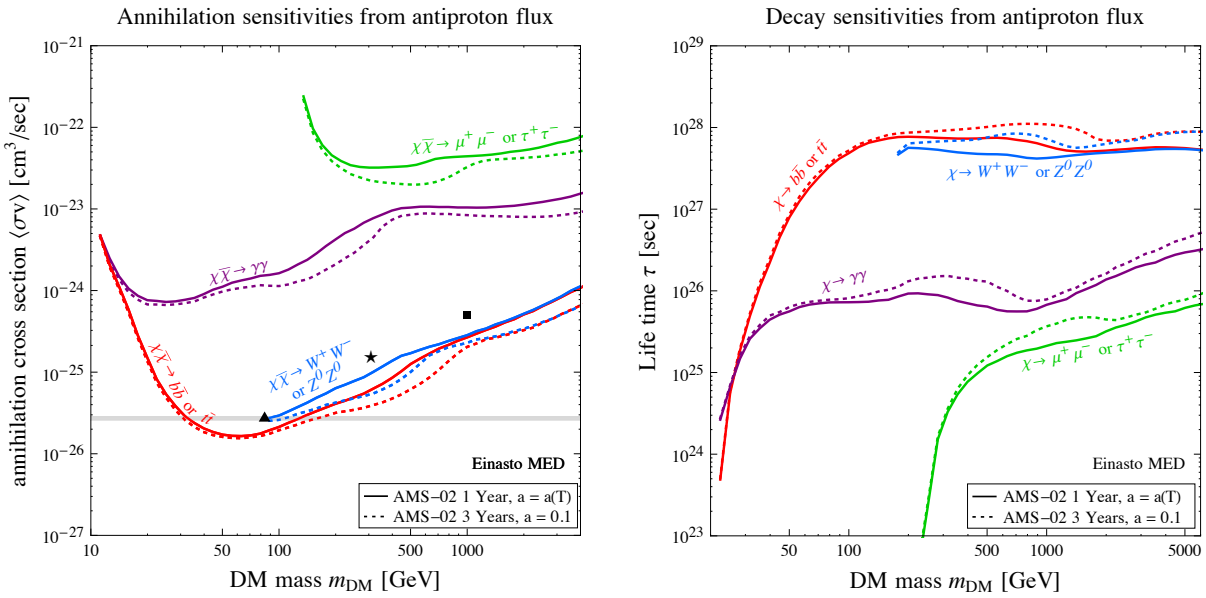

Figure 3.8: **Annihilating and decaying DM: future sensitivities.** Left panel: the sensitivity of early AMS-02 antiproton measurements for different channels. The solid lines assume 1 year of data taking and a realistic acceptance, the dotted lines assume 3 years of data taking and an optimized acceptance. The rest of the notations are like in figure 3.19. Right panel: the same for the case of decaying DM.

kinematically open) the bounds will reach the thermal value of the annihilation cross-section (2.7×10^{-26} cm^3/sec) in the range of masses $30 - 200$ GeV. The more optimistic choice for the acceptance and the operating time (option 2 in 3.3.4) improves the projected reach by at most another half an order of magnitude or so, except at low masses (i.e. low energies) where the systematic errors dominate.

We only show the curves corresponding to the 'Einasto, MED' choice of astrophysical parameters: other choices would modify the bounds in the same way we discussed in section 3.3.3. However, we also mention that a significant collateral improvement expected from AMS-02 will be to reduce the astrophysical uncertainties: using low energy spectra and the B/C ratio, as described above [167, 168], the propagation of CR should be better pinned down and the error band reduced. In [171] a similar analysis has been performed, for annihilating DM. Our results in figure 3.8 (left) compare almost directly with their figure 17, albeit on a reduced range of masses and for the specific models that they consider. The constraints that we find are less stringent than theirs by about one order of magnitude. We attribute this to the fact that they assume a larger acceptance and, possibly, to their use of a larger range of energies.

Reconstruction capabilities

We now consider a scenario in which an identifiable excess is detected by AMS-02 in the antiproton flux and it is attributed to DM, and we study how well it will be possible to reconstruct the underlying DM properties. We focus only on annihilating DM, for definiteness. We need to assume values of the DM mass and annihilation cross-section which are still allowed by the PAMELA data, but which would be probed by AMS-02. We therefore select three benchmark models:

- ▲ $m_{\rm DM} = 85\,{\rm GeV}$ $\langle\sigma v\rangle = 2.7\times10^{-26}\,{\rm cm^3\,s^{-1}}$,
- ★ $m_{\rm DM} = 300\,{\rm GeV}$ $\langle\sigma v\rangle = 1.5\times10^{-25}\,{\rm cm^3\,s^{-1}}$,
- ■ $m_{\rm DM} = 1\,{\rm TeV}$ $\langle\sigma v\rangle = 5\times10^{-25}\,{\rm cm^3\,s^{-1}}$,

which are denoted by the corresponding symbols in figures 3.19, 3.8 and 3.9. Each of these models represents a different region of interest in the ($m_{\rm DM}$,$\langle\sigma v\rangle$)-plane:

- ▲ The cross-section corresponds to the thermal annihilation cross-section, favored by cosmological observations. Because of the relatively small mass, the DM signal affects mainly energies below 10 GeV (which are not considered in this analysis).
- ★ The $\bar{p}$ signal sits squarely in the energy range probed by AMS-02 . For the given mass, the cross-section is chosen at the limit of the exclusion contour of PAMELA. The analysis of this model should be the most straightforward.
- ■ The DM signal starts to have an important contribution for energies around 100 GeV, where larger uncertainties are present. The lack of data for high energies should pose problem for the reconstruction of this model.

We assume an Einasto halo profile and we fix MED propagation parameters. We sum the $\bar{p}$ flux resulting from these DM models to the 'fixed background' and we generate the corresponding mock data, plotted in figure 3.4, right. We thus determine *a posteriori* the regions of the parameter space which would be identified, at a given C.L., by a blind analysis of such data.

Mass and cross-section for $b\bar{b}$ channel

First we assume that the annihilation channel is fixed and known: $\chi\bar{\chi}\to b\bar{b}$ with 100% Branching Ratio (BR). In the left panels of Fig. 3.9 we show the regions identified at 90% and 99% C.L. (corresponding to $\Delta\chi^2 = 4.61, 9.21$ for 2 d.o.f.), with the ellipse corresponding to the 'fixed background' hypothesis and the extended shaded areas corresponding to the implementation of the 'variating background' procedure.

- ★ We focus first on the results for this model. We see that $m_{\rm DM}$ is determined fairly well, within 50% of the true value or so. For a fixed cross-section, values of the mass which are smaller than the true value are more quickly disfavored than values which are larger than the true one. This is consistent with expectations since, for small masses, the signal will have its maximum at small energies, which are measured more precisely.
  We also notice that the ellipse corresponding to the 'fixed background' analysis displays the degeneracy between $m_{\rm DM}^{-2}$ and $\langle\sigma v\rangle$, since the product of these two quantities appears in the determination of the DM flux. On the other hand, the 'variating background' analysis destroys this simple analytical dependence.
- ▲ Here, we display only the 90% C.L. contours: the 99% ones would artificially extend to very low DM masses, as a consequence of the 10 GeV cut imposed by solar modulation. From the point of view of the χ^2, the points in the 99% contour would favor a pure background. The shape is unusual probably because of the cut at 10 GeV.

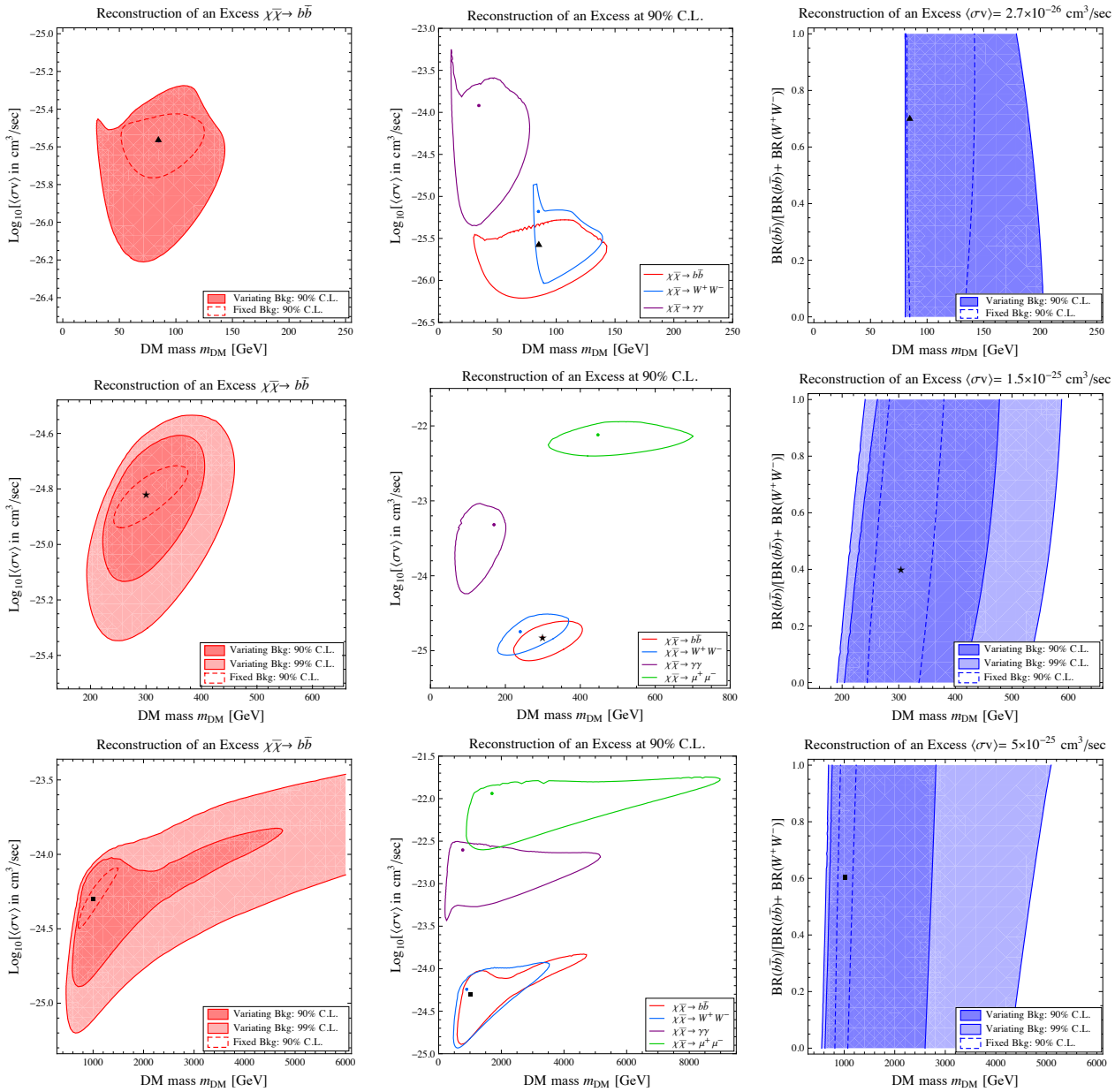

Figure 3.9: **Reconstruction capabilities of DM properties by** AMS-02**.** Left Panels: Reconstruction of the mass and the cross-section assuming an annihilation into $b\bar{b}$. The true point is indicated by a symbol; the contours delimit the regions that AMS-02 would identify, at the indicated C.L. and given the indicated assumptions on the background. Middle Panel: Reconstruction of the mass and the cross-section without knowing a priori the annihilation channel. The true point is indicated by the symbol; the other points and the contours indicate the best fits and the 90% C.L. regions that AMS-02 would identify for other annihilation channels. Right Panels: Reconstruction of the mass and the branching ratio for a fixed cross-section and annihilation into $b\bar{b}$ and W^+W^-. The symbols represent the model used to produce the mock data.

Fixed annihilation channel (true signal: **100% $b\bar{b}$**)	mass $m_{\rm DM}$ [GeV]	cross-section $\langle\sigma v\rangle$ [cm^{3}s^{-1}]	$\Delta\chi^2$ with respect to a pure background
$\chi\chi \to b\bar{b}$	84.9	$2.7 \cdot 10^{-26}$	-10.5
$\chi\chi \to W^+W^-$	84.8	$6.6 \cdot 10^{-26}$	-10.3
$\chi\chi \to \gamma\gamma$	57.4	$1.0 \cdot 10^{-24}$	-5.7
Fixed cross-section $\langle\sigma v\rangle$ [cm^{3}s^{-1}] (true signal: $\mathbf{70\%\, b\bar{b} + 30\%\, W^+W^-}$)	mass $m_{\rm DM}$ [GeV]	relative branching ratio	$\Delta\chi^2$ with respect to a pure background
2.7×10^{-26}	84.9	0.7	-5.4

Table 3.1: Best fit reconstructions of a signal from a 85 GeV DM candidate with $\langle\sigma v\rangle = 2.7 \times 10^{-26}\ cm^3\, s^{-1}$ (model ▲). See text for details.

Fixed annihilation channel (true signal: **100% $b\bar{b}$**)	mass $m_{\rm DM}$ [GeV]	cross-section $\langle\sigma v\rangle$ [cm^{3}s^{-1}]	$\Delta\chi^2$ with respect to a pure background
$\chi\chi \to b\bar{b}$	300	$1.5 \cdot 10^{-25}$	-21.0
$\chi\chi \to W^+W^-$	240	$1.9 \cdot 10^{-25}$	-19.7
$\chi\chi \to \gamma\gamma$	169	$4.8 \cdot 10^{-24}$	-9.8
$\chi\chi \to \mu^+\mu^-$	447	$7.6 \cdot 10^{-23}$	-19.2
Fixed cross-section $\langle\sigma v\rangle$ [cm^{3}s^{-1}] (true signal: $\mathbf{40\%\, b\bar{b} + 60\%\, W^+W^-}$)	mass $m_{\rm DM}$ [GeV]	relative branching ratio	$\Delta\chi^2$ with respect to a pure background
1.5×10^{-25}	300	0.4	-13.0

Table 3.2: Best fit reconstructions of a signal from a 300 GeV DM candidate with $\langle\sigma v\rangle = 1.5 \times 10^{-25}\ cm^3\, s^{-1}$ (model ★). See text for details.

Fixed annihilation channel (true signal: **100% $b\bar{b}$**)	mass $m_{\rm DM}$ [GeV]	cross-section $\langle\sigma v\rangle$ [cm^{3}s^{-1}]	$\Delta\chi^2$ with respect to a pure background
$\chi\chi \to b\bar{b}$	999	$5 \cdot 10^{-25}$	-15.7
$\chi\chi \to W^+W^-$	886	$5.8 \cdot 10^{-24}$	-15.1
$\chi\chi \to \gamma\gamma$	765	$2.5 \cdot 10^{-22}$	-14.5
$\chi\chi \to \mu^+\mu^-$	1711	$1.1 \cdot 10^{-22}$	-14.8
Fixed cross-section $\langle\sigma v\rangle$ [cm^{3}s^{-1}] (true signal: $\mathbf{60\%\, b\bar{b} + 40\%\, W^+W^-}$)	mass $m_{\rm DM}$ [GeV]	relative branching ratio	$\Delta\chi^2$ with respect to a pure background
5×10^{-25}	999	0.6	-15.3

Table 3.3: Best fit reconstructions of a signal from a 1 TeV DM candidate with $\langle\sigma v\rangle = 5 \times 10^{-25}\ cm^3\, s^{-1}$ (model ■). See text for details.

- The 99% C.L. region extends to very large masses as the signal moves into the region in which the measurements are least precise. In addition, as the signal affects large kinetic energies, any contribution with a mass > 1 TeV can fit the the data at 99% C.L. provided the cross-section is large enough.

In all cases, the annihilating cross-section is determined within an order of magnitude at best.

Mass and the cross-section for different annihilation channels

Next, we use still a single annihilation channel ($\chi\bar{\chi} \to b\bar{b}$ with 100% BR) to produce the mock data and we investigate how the same signal could be interpreted in terms of a different channel. The results are shown in the central panels of figure 3.9, where the contours enclose the 90% C.L. regions for the indicated channels. Not surprisingly, interpreting the data in terms of annihilation into the W^+W^- channel identifies a region which is very similar (a part for the kinematical cut in the ▲ case) to the one corresponding to the 'true' $b\bar{b}$ annihilation, since the $\bar{p}$ spectra and the yields of the two channels are very similar. On the other hand, interpreting the data in terms of annihilation into $\gamma\gamma$ ($\mu^+\mu^-$) would result in reconstructing a DM mass smaller (larger) than the true one and a cross-section much larger than the true one. In tables 3.2 and 3.3 (upper parts) we report the best fit values of DM mass and annihilation cross-section (identified by a colored point in figure 3.9) for each channel. We also report, in the last column of the tables, the $\Delta\chi^2$ of each one of these points with respect to a pure background hypothesis. [2] We see that, while the $b\bar{b}$ channel does still obtain the overall best fit, all the other channels also fit the data similarly well, so that it is not practically possible to reconstruct the 'true' configuration. In addition, we remind that a channel like $t\bar{t}$ (when kinematically open) is practically indistinguishable from $b\bar{b}$ and therefore constitutes an additional degeneracy.

The $\Delta\chi^2$ numbers allow to draw another conclusion: all channels for the ★ and ■ models (with the possible exception of the borderline case of the $\gamma\gamma$ channel in the ▲ model) improve sufficiently the χ^2 that an excess can quite clearly be identified. This might be surprising if, for instance, judging by eye from the right panel of fig. 3.4. However, as long as a power-law assumption (with the assumed uncertainty band) for the background is justified, this statistical conclusion is sound. If one allows for the possibility that the background shows features mimicking the hump produced by DM (or that it might consist of a superposition of power-laws, or that the uncertainty band in much larger...), then of course these conclusions evaporate, as warned in section 3.3.2. On the other hand, for the ▲ model the improvement of χ^2 over the pure background becomes quite thin: an actual reconstruction will be very challenging.

Branching Ratio

Finally, we produce mock data with a mixed annihilation into $b\bar{b}$ and into W^+W^- and we investigate whether it is possible to reconstruct the Branching Ratio. The results in the right panels of figure 3.9 show that it is not possible. While the determined best fit falls on top or very close to the true value (see the last lines of the tables 3.1, 3.2, 3.3), the 90% and 99% C.L. regions span the entire range of BR. This is due to the similarity of the $b\bar{b}$ and W^+W^- spectra

[2] More precisely, what we do is the following. We generate the mock data using a 'fixed background + signal' flux. We then try and interpret them in terms of a 'variating background' with free A and p: the best of such variating backgrounds has a χ^2 of χ^2_0. We then add back the signal, assuming different annihilation channels, and we see how much the χ^2 improves with respect to χ^2_0. These improvements are the numbers we quote in the last column of the tables.

and it reinforces the conclusions of the analyses above. In particular, these conclusions highlight that it will be important to carry on a *multi-messenger* analysis (i.e. including signals in γ rays, neutrinos etc) in order to break the degeneracies and obtain a convincing reconstruction.

Exploring the potential of the PAMELA and AMS-02 measurements of the flux of CR antiprotons to constrain DM, we have analyzed, in a model independent way, several annihilation and decay channels, a large range of masses and assessed the impact of astrophysical uncertainties. Our main results can be schematized as follows.

- The current $\bar{p}$ constraints using PAMELA measurements are very strong both for annihilating (see figure 3.19 left) and decaying (see figure 3.6 left) DM, for the hadronic channels. Adopting fiducial choices for the halo profile and propagation parameters ('Einasto, MED'), they are as strong as (or even slightly stronger than) the most stringent gamma ray constraints from the FERMI satellite.

- The astrophysical uncertainty band associated to different choices for the halo profile and the propagation parameters, however, spans between one and two orders of magnitude (see figure 3.19 right and figure 3.6 right).

- The upcoming AMS-02 measurements (assuming 1 year of accumulated data and a realistic acceptance for the experiment) have the power to improve the constraints, assuming that no signal is seen, by slightly less than one order of magnitude (see fig. 3.8). In particular, AMS-02 will probe the thermal value of the annihilation cross-section in the range $m_{\rm DM} \simeq 30 - 200$ GeV for the $b\bar{b}$ (or $t\bar{t}$) channel.

- If a convincing excess is measured by AMS-02 and it is attributed to annihilating DM, the data will allow to somewhat constrain the underlying DM properties, but a full reconstruction will be quite challenging (see figure 3.9). The main reason is that the $\bar{p}$ spectra from different channels are quite similar one to another (as a result of the hadronization process smoothing out differences) and not very different from the shape of the pure background, so that degeneracies are impossible to break.

  - Restricting to the 'traditional' hadronic annihilation channels ($b\bar{b}$, $t\bar{t}$, W^+W^-, ZZ), in the most favorable case in which $m_{\rm DM} \sim$ few hundreds GeV (and therefore the signal falls in the energy range best measured by AMS-02) it will be possible to reconstruct the DM mass within 50%. For smaller values of $m_{\rm DM}$ (below ~ 100 GeV) or larger ones (above ~ 1 TeV) the reconstruction capability worsens somewhat.
  - Still restricting to the hadronic channels, the determination of the annihilation cross-section will be possible within an order of magnitude independently of the mass range.
  - If other annihilation channels are allowed, the data will not allow to discriminate among them and the determination of the annihilation cross-section becomes impossible.
  - If several of the hadronic channels are open at the same time, it will not be possible to determine the relative branching ratios.

In summary, we find that antiprotons are a very relevant tool to constrain DM annihilation and decay, on a par with gamma rays for the hadronic channels. PAMELA data and AMS-02 data

allow to probe large regions of the parameter space. On the other hand, using $\bar{p}$ to reconstruct the DM properties in case of positive detection will be very challenging, except for favorable scenarios.

3.4 Including Energy Losses and Diffusive Reacceleration (ELDR) - Improved PPPC4DMID

In the previous analysis, we showed the potential of antiprotons as DM indirect detection messenger. It is clearly timely to refine previous predictions of antiproton production from astrophysics and from DM, in order to obtain fluxes as accurate as possible to be compared with the precise data. This is what we aim to do in this section. In particular, we upgrade previous computations by incorporating energy losses and diffusive reacceleration (second-order Fermi acceleration) and use the full spectrum. We anticipate that these effects have a sizable impact on the low energy portion of the spectrum. Hence, they cannot be neglected anymore if one aims at precision predictions, especially at low energies. One should nevertheless keep in mind that other sources of uncertainties could also possibly play a role, yet to be determined, such as the nuclear antiproton production cross-sections or the way CR propagation is modeled. We provide numerical results in the form of fit functions for the astrophysical fluxes (see section 3.4.1) and in the form of a new release of the PPPC4DMID for what concerns the DM fluxes.

3.4.1 Antiproton propagation in the Galaxy

We address the main points concerning how to treat the full propagation of antiprotons, including all the effects that we neglected previously. In particular, we focus on the process of energy losses (in particular tertiary production) and diffusive reacceleration, as well as solar modulation in the force-field approximation.

Full transport equation in the Galaxy

Starting from 2.66, we consider the effects of energy losses and diffusive reacceleration, we obtain the complete master equation for the energy and space distribution function $f = dn/dK$ for antiprotons:

$$\frac{\partial f}{\partial t} - D_{xx}(K)\cdot\nabla^2 f + \frac{\partial}{\partial z}\left\{\mathrm{sign}(z)\, f\, V_{\mathrm{conv}}\right\} + \frac{\partial}{\partial E}\left\{b(K,\vec{x})f - \mathcal{K}_{\mathrm{EE}}(K)\frac{\partial f}{\partial E}\right\} = S. \tag{3.10}$$

The diffusion term is modeled as previously: $D_{xx}(K) = \mathcal{K}_0\,\beta\,(p/\mathrm{GeV})^{\delta}$. However, the fourth term (inside the energy derivative) accounts for energy losses, which are in general energy and space dependent. The thin disk approximation leads to write $b(K,\vec{x})$ as $2h\delta(z)\,b(K)$, where $h = 100$ pc is the half-height of the disk. We will now fully include them in our detailed analyses. The last term of the l.h.s. represents diffusive reacceleration or second-oder Fermi acceleration.

On the right hand side, the equation features the source term S, which can contain different contributions. The spallation of high-energy CR on the interstellar gas produces antiprotons (the secondaries) which are the source of the astrophysical background. The annihilations or decays of DM produce primary antiprotons, as described in section 3.3.1. S contains also a sink term, due to the annihilations of the antiprotons on the interstellar gas. Such a term reads

$-2h\delta(z)\,\Gamma_{\rm ann}$ where the δ function effectively localizes the interactions only in the disk where the ISM sits. The annihilation rate $\Gamma_{\rm ann}$ is equal to $(n_{\rm H}+4^{2/3}n_{\rm He})\sigma^{\rm ann}_{\bar{p}p}v_{\bar{p}}$, where $n_{\rm H}=0.9$ cm^{-3} and $n_{\rm He}=0.1$ cm^{-3} stand for the ISM hydrogen and helium densities, while $v_{\bar{p}}$ denotes the velocity of the incoming antiproton. The annihilation cross-section $\sigma^{\rm ann}_{\bar{p}p}$ is borrowed from [216, 217], and we have multiplied it by a factor of $4^{2/3}\sim 2.5$ to account for the different geometrical cross-section on helium in an effective way. Notice that antiprotons also collide elastically on interstellar H and He. Since they are preferentially scattered forward, this process has no effect and does not contribute to the sink term in S. Last but not least, S contains a source term (or rather 'recycling' term) corresponding to tertiary antiprotons, discussed in the next subsection together with energy losses and diffusive reacceleration.

In order to solve the transport equation 3.10, we model the magnetic halo of the Milky Way as described in section 2.4.4. The CR densities $f\equiv dn/dK$ are assumed to be axi-symmetric. They are expanded along the radial direction as a series of Bessel functions of zeroth-order

$$f(r,z,E)=\sum_{i=1}^{+\infty}F_i(z,E)\,J_0\left(\alpha_i\,r/R\right). \tag{3.11}$$

Since α_i is the $i^{\rm th}$ zero of J_0, the density vanishes at $r=R$. The Bessel transforms $F_i(z,E)$ also vanish at the vertical boundaries $z=\pm L$ of the diffusive halo. The transport equation is solved for each Bessel order i and the antiproton flux at the Earth is derived as explained in [218, 204].

The Energy Losses including tertiaries, and Diffusive Reacceleration ('ELDR')

Three processes of energy loss are encoded in the negative coefficient b. First, like any other nuclear species, antiprotons undergo ionization losses in the interstellar neutral matter, whose composition has been given above. Then, Coulomb energy losses take place on the fraction of the ISM that is completely ionized. That mechanism is dominated by scatterings on thermal electrons, for which we have used a density of 0.033 cm^{-3} and a temperature of 3×10^5 K. These two effects are discussed in [219] and [163], where complete expressions may be found for the energy loss rate b. Finally, convective processes also induce a loss of energy through the conservation of the CR density in phase-space. This leads to an adiabatic energy loss in the thin disk approximation

$$b_{\rm adia}(K,\vec{x})=-\frac{1}{3}\left\{\nabla_x\cdot\vec{V_{\rm conv}}(\vec{x})\right\}\frac{p^2}{E}\xrightarrow{\rm ave}b_{\rm adia}(K)=-\frac{V_{\rm conv}}{3h}\frac{p^2}{E}, \tag{3.12}$$

as already mentioned in section 2.4.4.

As anticipated, the term 'tertiary antiprotons' identifies the particles emerging from inelastic and non-annihilating interactions of primary or secondary antiprotons on the ISM. An antiproton can collide on a proton at rest and transfer enough energy to excite it as a Δ resonance. The $\bar{p}$ typically loses a fraction of its energy and is effectively reinjected in the flux with a degraded momentum. This mechanism redistributes antiprotons towards lower energies, hence flattening their spectrum as first remarked by [220]. The rate for the production of tertiary antiprotons is given by

$$S^{\rm ter}_{\bar{p}}(\vec{x},E_{\bar{p}})=\int_{E_{\bar{p}}}^{+\infty}\frac{d\sigma_{\bar{p}p\to\bar{p}X}}{dE_{\bar{p}}}(E'_{\bar{p}}\to E_{\bar{p}})\,n_{\rm H}(\vec{x})\,v'_{\bar{p}}\,f(\vec{x},E'_{\bar{p}})\,dE'_{\bar{p}}\;-\;\sigma_{\bar{p}p\to\bar{p}X}(E_{\bar{p}})\,n_{\rm H}(\vec{x})\,v_{\bar{p}}\,f(\vec{x},E_{\bar{p}}). \tag{3.13}$$

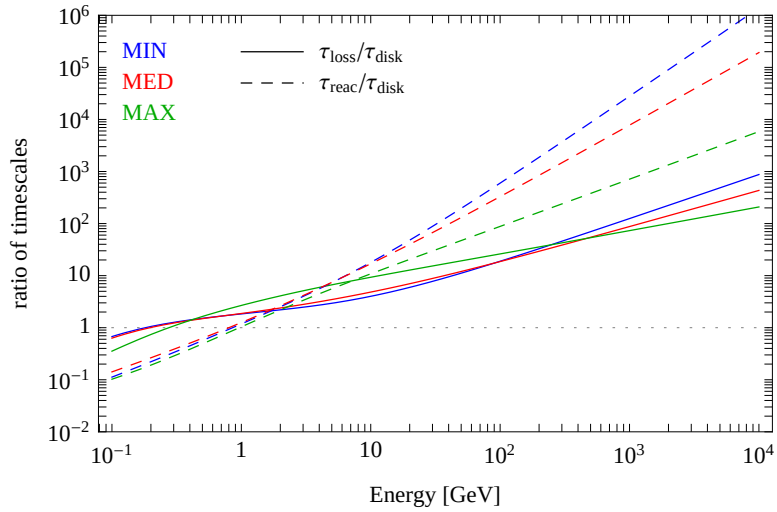

Figure 3.10: The **timescale ratios** $\tau_{\rm loss}/\tau_{\rm disk}$ (solid) and $\tau_{\rm reac}/\tau_{\rm disk}$ (short dashed) are plotted as a function of the antiproton kinetic energy K. The blue, red and green curves respectively stand for the three canonical models MIN, MED and MAX of CR propagation as defined in table 2.1.

In this expression, the differential cross-section for inelastic and non-annihilating interactions has been approximated by

$$\frac{d\sigma_{\bar{p}p\to\bar{p}X}}{dE_{\bar{p}}}(E'_{\bar{p}}\to E_{\bar{p}}) = \frac{\sigma_{\bar{p}p\to\bar{p}X}(E'_{\bar{p}})}{K'_{\bar{p}}}. \tag{3.14}$$

Following [220], we assume that an antiproton undergoing such a reaction has final kinetic energy $K_{\bar{p}}$ uniformly distributed between 0 and its initial value $K'_{\bar{p}}$. The total inelastic and non-annihilating cross-section $\sigma_{\bar{p}p\to\bar{p}X}$ has been borrowed from [217] where, above a kinetic energy of 13.3 GeV, it is approximated by the inelastic proton-proton cross-section.

At high energy, the second term in relation 3.13 is dominant. The antiproton energy distribution is depleted for the benefit of the low-energy tail of the spectrum where the first term contributes most. Notice also that the tertiary production rate is proportional to the hydrogen density, which should be rescaled by a mere factor of$(n_{\rm H} + 4^{2/3}n_{\rm He})$ to take also into account the helium component of the ISM. Finally, a global factor of $2h\delta(z)$ should be added in the thin disk approximation.

The last term in the l.h.s. of the transport equation 3.10 accounts for diffusive reacceleration. The second order Fermi acceleration boils down into a diffusion in energy space whose coefficient may be expressed in equation 2.70. Other forms are possible as in equation 2.69 and are used in other codes, like `GalProp` and `DRAGON`. We will nevertheless keep the relation in equation 2.70 for our study because it is this particular form that has been used in [161] to constrain the CR propagation parameters from the B/C tracer, and to define in [165] the canonical models MIN, MED and MAX.

As inelastic and non-annihilating interactions result into a discontinous variation of the antiproton energy, they will be associated in this analysis to the continuous energy losses described by the $b(K)$ coefficient. The latter comes into play in the transport equation together with diffusive reacceleration. These three processes will hence be switched on or off together, and are hereafter denoted generically by the acronym 'ELDR'. In order to get a flavor of the

relative importance of the various mechanisms which come into play in CR transport, we should compare their timescales. To this end, we define the three timescales $\tau_{\rm disk}$, $\tau_{\rm loss}$ and $\tau_{\rm reac}$. Space diffusion and Galactic convection can be combined together in a one dimensional slab model to yield the typical confinement timescale inside the disk

$$\tau_{\rm disk} = \frac{h}{V_{\rm conv}} \left[1 - \exp\left(-\frac{V_{\rm conv} L}{D_{xx}} \right) \right] . \tag{3.15}$$

At low energy, convection dominates and $\tau_{\rm disk} \simeq h/V_{\rm conv}$ is constant. Above a few GeV, diffusion takes over since D_{xx} is an increasing function of kinetic energy K, and the usual escape time $\tau_{\rm disk} \simeq hL/D_{xx}$ of the Leaky Box model is recovered. The typical timescale for energy losses is instead defined by $\tau_{\rm loss} = -K/b(K)$. Above a few GeV, ionization and Coulomb losses are negligible with respect to adiabatic losses, and $\tau_{\rm loss}$ becomes equal to the constant $3h/V_{\rm conv}$. Finally, the diffusive reacceleration timescale $\tau_{\rm reac}$ is defined by the ratio $K^2/D_{\rm EE}(K)$. As soon as $\beta \simeq 1$, this timescale increases with energy like $9D_{xx}/2v_a^2$.

The ratios $\tau_{\rm loss}/\tau_{\rm disk}$ (solid) and $\tau_{\rm reac}/\tau_{\rm disk}$ (short dashed) are displayed in figure 3.10 as a function of antiproton kinetic energy K, for the three CR propagation canonical models MIN, MED and MAX defined in table 2.1. Above 1 GeV, all ratios exceed unity, and $\tau_{\rm disk}$ is the smallest timescale. Convection and space diffusion are the dominant processes, with the latter taking over the former above a few GeV. That is why simple approaches like the Leaky Box or infinite slab models reproduce well the B/C observations. For kinetic energies smaller than 1 GeV, the short dashed curves are below the dotted horizontal line (with critical value 1) and diffusive reacceleration becomes the dominant mechanism. Although never dominant, energy losses slightly deplete the high energy part of the antiproton spectrum and replenish its low energy tail, flattening it. Possible bumps showing up in the injected spectra are partially erased once energy losses come into play. As expected, we also find that inelastic but non-annihilating interactions, which are responsible for the tertiary production of antiprotons, have qualitatively the same effect, albeit with a somewhat lesser extent. Diffusive reacceleration tends to smooth globally the antiproton spectrum. Although inducing qualitatively the same effect at low energy as the two other mechanisms, that process tends on the contrary to slightly replenish the high-energy part of the antiproton spectrum. As featured by the $\tau_{\rm reac}/\tau_{\rm disk}$ curves of figure 3.10, diffusive reacceleration is more and more effective along the MIN–MED–MAX sequence of CR transport models. Once all these mechanisms are combined, their global effect depends on the relative importance of diffusive reacceleration with respect to energy losses. As indicated in figure 3.10, the $\tau_{\rm reac}/\tau_{\rm loss}$ ratio significantly decreases from the MIN to the MAX configurations. In the MIN and MED cases, the antiproton spectrum is slightly depleted at high energies when the 'ELDR' effects are included, whereas the opposite effect is observed for the MAX model where diffusive reacceleration counterbalances energy losses.

Solar modulation ('SMod') effects in a force-field approximation

In the final portion of their journey, antiprotons penetrate into the sphere of influence of the Sun and are subject to the phenomenon of solar modulation (denoted with the abbreviation 'SMod' hereafter), described in section 2.5. We will use the force-field approximation defined by equation 2.82 with $Z = A = 1$ for protons and antiprotons. The force-field or Fisk potential ϕ_F parameterizes the effect of the solar modulation on CRs and with the notation ϕ_F, we will always refer to the Fisk potential *for antiprotons*. For the analysis of the PAMELA data, we choose a conservative interval 0.1 GV $< \phi_F <$ 1.1 GV (see table 2.3). However, for the

AMS-02 data, we will want to be even more conservative and choose 0 GV $< \phi_F <$ 2 GV, motivated by the different values of the tilt angle during the PAMELA and AMS-02 data taking periods.

The antiproton astrophysical flux

We now briefly review the computation of the two main antiproton input components: the background, from astrophysics, and the primary signal, from DM annihilations or decays, including the effects neglected in section 3.3.

The astrophysical antiproton background is produced by the collisions of high-energy CR protons and helium nuclei on the ISM, which is assumed here to be mostly composed of hydrogen and helium. In the case of the interactions between CR protons and hydrogen atoms, the source term takes the following form

$$S_{\bar{p}}^{\rm sec}(\vec{x}, E_{\bar{p}}) = \int_{E_p^0}^{+\infty} \frac{d\sigma_{p{\rm H}\to\bar{p}X}}{dE_{\bar{p}}}(E_p \to E_{\bar{p}})\, n_{\rm H}(\vec{x})\, v_p\, f_p(\vec{x}, E_p)\, dE_p. \tag{3.16}$$

We use the injection proton and helium CR fluxes at the Earth as measured by the PAMELA experiment [221][3]. Following previous studies [218, 204], the Bessel transforms of these fluxes are calculated for each CR propagation model in order to derive the proton and helium densities f_p and f_α all over the Galactic magnetic halo. The radial profile of the sources of primary CR nuclei comes into play and can be determined from pulsar and surpernova remnant surveys. We have used here the parameterization of [223], slightly modified by [224].

In the case of a proton impinging on a hydrogen atom at rest, the production rate peaks around a few GeV. The energy of the projectile must actually exceed a threshold of $E_p^0 = 7m_p$. In the Galactic frame, where the target is at rest, the differential production cross-section of the previous relation is given by the integral

$$\frac{d\sigma_{p{\rm H}\to\bar{p}X}}{dE_{\bar{p}}} = 2\pi k_{\bar{p}} \int_0^{\theta_{\rm max}} \left(E_{\bar{p}} \frac{d^3\sigma}{d^3k_{\bar{p}}} \right)_{\rm LI} d(-\cos\theta), \tag{3.17}$$

where θ is the angle between the momenta of the incoming proton and the produced antiproton. In the center of mass frame, which drifts with a velocity $\beta_{\rm CM} = \{(E_p - m_p)/(E_p + m_p)\}^{1/2}$ with respect to the Galactic frame, the antiproton energy cannot exceed a value of

$$E^*_{\bar{p},{\rm max}} = \frac{s\, -\, 9\, m_p^2\, +\, m_p^2}{2\sqrt{s}}, \tag{3.18}$$

where $\sqrt{s} = \{2m_p(E_p + m_p)\}^{1/2}$ is the total energy of the reaction. In equation 3.17, the energies E_p and $E_{\bar{p}}$ have been fixed and the angular integral runs from $\theta = 0$ up to a maximal value of $\theta_{\rm max}$ for which

$$\cos\theta_{\rm max} = \frac{1}{\beta_{\rm CM} k_{\bar{p}}} \left(E_{\bar{p}} - \frac{E^*_{\bar{p},{\rm max}}}{\gamma_{\rm CM}} \right). \tag{3.19}$$

The Lorentz invariant differential cross-section $E_{\bar{p}}\,(d^3\sigma/d^3k_{\bar{p}})$ depends on the antiproton rapidity $y = \tanh^{-1}(k_{\bar{p}\parallel}/E_{\bar{p}})$ and transverse mass $m_T^2 = m_p^2 + k_{\bar{p}\perp}^2$. We have used a new parameterization recently proposed by [225] instead of the Tan and Ng fitting relations [216, 217]. As mentioned by [204], the transverse mass m_T should be preferred to the angular variable

[3] Technically, we employ a numerical fit of those data performed by T. Delahaye [222].

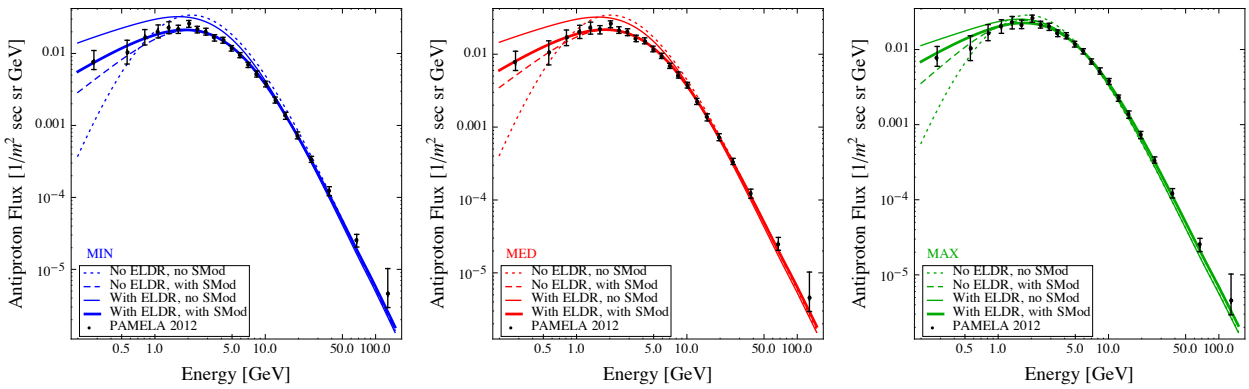

Figure 3.11: The **astrophysical background (secondary) antiproton spectra** with/without SMod and with/without ELDR, for the MIN, MED, MAX propagation models (left to right). Superimposed are the data points from PAMELA.

$\cos\theta$ in the integral 3.17 whenever the maximal angle $\theta_{\max}$ is small, under penalty of numerical errors. Antiprotons can also be produced in reactions involving helium nuclei either in the cosmic radiation or in the ISM. We have used the same procedure as discussed in [204].

Notice finally that antineutrons are also produced, and should be taken into account as they subsequently decay into antiprotons. It has been so far conventionally assumed that the antineutron and antiproton production rates are equal insofar as isospin symmetry should hold. A global factor of 2 was generally assumed in order to account for antineutrons. But measurements by the NA49 experiment [226] of the differential antiproton multiplicity in pp and np collisions point towards a different conclusion, as noticed by [227]. In the case of antineutrons, the production cross-section should be multiplied by an unknown factor $N_{\rm IS}$ such that

$$\frac{d\sigma_{p{\rm H}\to\bar{n}X}}{dE_{\bar{n}}} = N_{\rm IS}\,\frac{d\sigma_{p{\rm H}\to\bar{p}X}}{dE_{\bar{p}}}. \tag{3.20}$$

For conservativeness, we have assumed $N_{\rm IS}$ to lie in the range from 1 to 1.5, so that our calculations can be rescaled by a factor $A \equiv (1 + N_{\rm IS})/2$ which has been varied freely from 1 to 1.25 in order to improve the quality ot the fits.

In figure 3.11, we plot the fluxes that we obtain for the MIN, MED and MAX models in order to compare now quantitatively these astrophysical $\bar{p}$ fluxes with PAMELA 2012 data [297]. To better assess the impact of our additional effects, three cases are considered:

- first, we consider only the data points with kinetic energies $K > 10$ GeV and we neglect solar modulation, as in the previous analysis;
- second, we add solar modulation (allowing the Fisk potential to vary in the range 0.1 GV $< \phi_F <$ 1.1 GV and the normalization A within 1 and 1.25), using kinetic enrages $K > 10$ GeV;
- third, we use the whole energy spectrum (still taking solar modulation into account). For each one of these cases, we compare the χ^2 with and without ELDR. In table 3.4, we present the best fit Fisk potential ϕ_F and the corresponding χ^2 value.

In general, the agreement between the astrophysical fluxes and the data, that we achieve by including ELDR and SMod, is very good, with a value of the reduced χ^2 which is below 1 for all configurations as soon as SMod is included. This is significant and essentially implies that little room is left for exotic contributions such as those from DM. A few fine features are however worth noticing.
(i) Taking into account solar modulation improves the fits considerably even above 10 GeV, especially for the MIN and MED configurations. This is because the datapoints between 10 and 50 GeV have such an exquisite precision that even the limited modification of solar modulation above 10 GeV has an impact.
(ii) Adding ELDR has a limited impact above 10 GeV (improving or worsening the χ^2 only by fractions of a point in most cases). However, when the whole spectrum is considered, then ELDR allows a significantly better agreement.

	MIN			MED			MAX		
	χ^2/dof	A [-]	ϕ_F [GV]	χ^2/dof	A [-]	ϕ_F [GV]	χ^2/dof	A [-]	ϕ_F [GV]
K > 10 GeV no SMod									
No ELDR	35.07/7	1.00	-	12.85/7	1.0	-	2.21/7	1.21	-
With ELDR	36.43/7	1.00	-	15.44/7	1.0	-	2.19/7	1.20	-
K > 10 GeV with SMod									
No ELDR	3.07/6	1.14	1.10	1.77/6	1.22	1.05	1.44/6	1.25	0.17
With ELDR	3.29/6	1.25	0.79	2.24/6	1.25	0.69	1.70/6	1.25	0.26
Whole spectrum with SMod									
No ELDR	15.63/21	1.00	0.66	8.23/21	1.12	0.74	10.16/21	1.25	0.46
With ELDR	9.65/21	1.22	0.74	6.95/21	1.24	0.70	6.38/21	1.25	0.38

Table 3.4: χ^2 **of the astrophysical $\bar{p}$ flux** with respect to PAMELA 2012 data, with and without ELDR, in three cases. We also report the best fit values for the addition parameters A and ϕ_F, where applicable.

To conclude this analysis, we provide some useful approximating functions to the astrophysical fluxes presented above. They read:

$$\log\left(\frac{\Phi_{\rm bkg}}{1/{\rm m}^2\ {\rm sec\ sr\ GeV}}\right) = \sum_{i=0}^{8} a_i \log^i\left(\frac{K}{\rm GeV}\right), \tag{3.21}$$

with the coefficients a_i as presented in table 3.5 for MIN, MED and MAX propagation models. These functions reproduce our results within 5% in the range of energies 0.2 GeV $\leq K \leq$ 800 GeV. They remain accurate within 20% all the way up to 10 TeV. For the convenience of the reader, we also provide an approximating function (labelled 'average' in table 3.5, not to be confused with MED) which corresponds to a flux that sits in the middle of the highest and lowest astrophysical fluxes, at all energies. We stress that of course it is preferable to use the functions adapted to the MIN, MED or MAX scenarios, as applicable, rather than this 'average' function. Nevertheless, the latter can allow for a quick scenario-independent estimate. In that case, the uncertainty due to the propagation can be taken into account as follows: for energies in the range 0.1 GeV $\leq K \leq$ 450 GeV, the uncertainty is of 30% above and below; up to 1.7 TeV the uncertainty is 50% and it reaches $\sim$ 70% at 10 TeV.

Recently, [227] and [228] have revisited the computation of the secondary antiproton flux. (The latter has also obtained new antiproton constraints on DM annihilation, on which we will comment later.) Our results essentially agree with the findings of the former so we mostly comment here on the latter. Such work bases its computation on a large set of propagation

	a_0	a_1	a_2	a_3	a_4	a_5	a_6	a_7	a_8
MIN	-1.5116	0.37991	- 0.69686	- 0.92051	0.17873	0.34161	- 0.19910	0.04154	- 0.00309
MED	-1.5079	0.34279	- 0.71347	- 0.89053	0.18914	0.32518	- 0.19223	0.04022	- 0.00299
MAX	-1.6192	0.34986	- 0.69943	- 0.86758	0.19016	0.30858	- 0.18192	0.03777	- 0.00279
'average'	-1.5594	0.35685	- 0.69211	- 0.89153	0.17990	0.32460	- 0.18875	0.03911	- 0.00289

Table 3.5: **Coefficients for the approximating functions** of the astrophysical flux, assuming $A = 1$ and $\phi_F = 0$ for MIN, MED and MAX propagation scenarios and for the 'average' case.

parameter determined in [168], via a full bayesian scan of CR data, and its crucial result is that the secondary $\bar{p}$ flux is found to systematically undershoot the $\bar{p}$ data by PAMELA (the resulting 'antiproton excess' can then be fit with a DM contribution as discussed in ref. [228]). Similar results had been anticipated in previous works [229]. However, other set of studies [230, 227] do not reach the same conclusion and, in particular, this is at odd with what we find: as discussed, we obtain a secondary flux which is well in agreement with PAMELA data for any one of the propagation models we consider and essentially across the whole range of energies (see e.g. figure 3.11). There might be many origins for this difference and it is difficult to pin down any single one, as discussed in previous works and as the authors of [228] also very nicely point out. Firstly, we notice that [228] considers two values of the Fisk potential for antiprotons which are smaller or equal to the value for protons, while we do not restrict to this situation. Actually, computations based on `HelioProp` show a preference for $\phi_F^{\bar{p}} > \phi_F^p$ during the PAMELA data taking period (see table 2.3). While in first approximation a large $\phi_F^{\bar{p}}$ would tend to reduce the $\bar{p}$ spectrum further, it is possible that the interplay with other effects mentioned below produces the opposite effect. Secondly, the models considered in [228], with one exception, do not include convection. Adding convection would generically have the effect of reducing an antiproton excess, as also recognized in [228] [4]. Thirdly, the primary proton spectrum considered in [228] (a broken power law with a break at 10 GV) differs from the one we use based on PAMELA data. Finally, we introduce an additional degree of freedom (linked to the antineutron production, as discussed above) which affects the overall normalization of the $\bar{p}$ flux and which is not taken into account in [228]. It is conceivable that a combination of these individually small effects works in the direction of explaining away the difference.

In any case, the comparison with the detailed work in [228] shows how crucial is the impact of the 'fine points' in the calculation of the secondaries. We will have to keep this in mind and proceed with maximal caution.

The DM antiproton signal including 'ELDR'

Also the DM signal needs to be reevaluated since energy losses and diffusive reacceleration have been added to the transport equation. Figure 3.12 presents the DM antiproton spectra (for some representative choices of masses) computed and propagated as discussed in the previous sections. We show the spectra from the previous release of PPPC4DMID (Release 3.0) compared with the spectra from our current calculation, with and without ELDR. The previous PPPC4DMID and the new calculation without ELDR agree very well (with small residual differences due to the different computational techniques), which is expected and reassuring. Including ELDR, the main effect is the one of having the spectrum 'squat': the peak decreases, the low energy tail is softened and the high energy portion can be somewhat raised. It is

[4] Moreover, position-dependent convection and diffusion can have a very interesting impact [231].

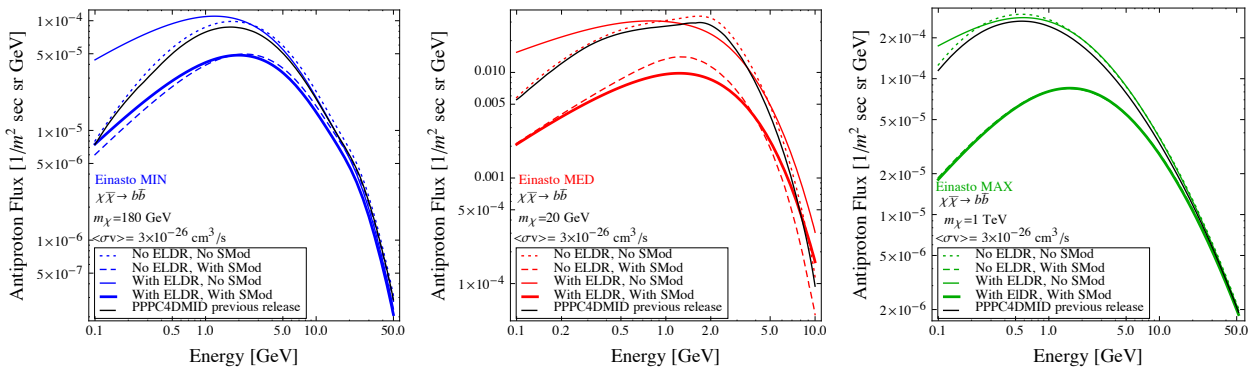

Figure 3.12: Comparison of the **antiproton flux from DM** annihilating into $b\bar{b}$ for an Einasto profile with/without SMod, with/without ELDR and with the previous PPPC4DMID flux, for the three propagation models MIN, MED, MAX and for three chosen masses.

interesting to note that this leads also to a non-zero $\bar{p}$ flux *above the nominal endpoint* of the spectrum at $K = m_{\rm DM}$, thanks to the (re)acceleration experienced by some of those antiprotons which had been produced with energies already close to such endpoint.

The antiproton spectra including ELDR are our most refined output possible for this observable and constitute our final result. We compute them for all the channels and range of masses spelled out in section 3.2 and we put them at public disposal in the new release of PPPC4DMID (Release 4.0). Solar modulation, being inherently epoch-dependent, is not included in the numerical product, but can be easily implemented with the use of equation 2.82 in a force-field approximation.

3.4.2 Constraints using PAMELA 2012 data

With the astrophysical background discussed in section 3.4.1 and the fluxes from DM annihilation obtained in section 3.4.1, we can now compute the constraints on DM in the usual 'mass vs. annihilation cross-section' plane. We do not aim here at an exhaustive scan of annihilation channels and DM profiles, but rather to show the impact on some specific examples. For definiteness, we focus on annihilations into $\bar{b}b$ and an Einasto profile.

At a practical level, we use the same method as previously, but with other parameters: for each propagation model, we add the contributions of the astrophysical flux and the DM, so that the total flux is

$$\Phi_{\rm tot}(m_{\rm DM}, \langle\sigma v\rangle; A, \phi_F) = \Phi_{\rm bkg}(A, \phi_F) + \Phi_{\rm DM}(m_{\rm DM}, \langle\sigma v\rangle, \phi_F), \tag{3.22}$$

where ϕ_F is the Fisk potential and A the amplitude over which we both marginalize. Then, for each mass $m_{\rm DM}$, we solve the following equation in $\langle\sigma v\rangle$

$$\chi^2_{\rm DM}(m_{\rm DM}, \langle\sigma v\rangle; A, \phi_F) - \chi^2_0 = 4, \tag{3.23}$$

where χ^2_0 is the chi square of the best fit background, found in table 3.4.

The results obtained with data from PAMELA 2012 [297] are presented in figure 3.13. For each propagation model, we distinguish four different cases: taking into account only the data

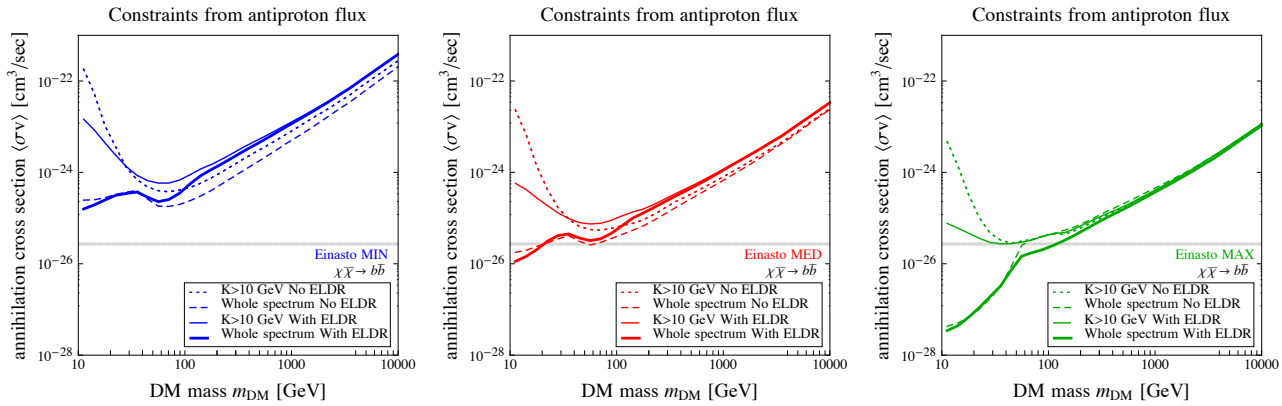

Figure 3.13: **Antiproton constraints** on DM annihilating into $b\bar{b}$ for an Einasto profile with or without ELDR, for $K > 10\,\text{GeV}$ or the whole spectrum and for the three propagation models MIN, MED, MAX. Solar modulation is marginalized over as explained in the main text.

points with energies $K > 10$ GeV or for the whole spectrum and with or without ELDR. In figure 3.14 we keep only the 'whole spectrum' case and compare the three propagation scenarios.

For the MIN and MED propagation models, we observe that the constraints with ELDR are stronger at small masses and weaker at large masses than the ones obtained without these effects. In fact, as we have seen in section 3.4.1, including ELDR means depopulating states with high energies and adding them to lower energies. Thus, with ELDR the astrophysical background as well as the DM signal are lower at high energies leaving more freedom for a large mass DM contribution and relaxing the constraints. At low masses, the situation is the opposite: the astrophysical background and the DM signal are higher with ELDR and thus the constraints are stronger. For MAX, the effect is almost absent or actually inverted. This can be qualitatively understood in the light of the discussion of the relative importance of reacceleration and energy losses presented in section 3.4.1. In short, while for MIN and MED the effect of energy losses is dominant at high energies, for MAX it is counterbalanced by diffusive reacceleration, the astrophysical and DM spectra slightly increase and hence the constraints are faintly stronger.

The other prominent feature in the bounds is the 'hump' below $m_{\text{DM}} \sim$40 GeV, especially visible for the MIN and MED cases. It originates from another rather complex interplay, this time among the effect of SMod, the size of the experimental error bars and the shape of the spectra. Indeed, for DM masses of the order of 20−40 GeV, the DM $\bar{p}$ spectrum peaks at the same energy (≈ 2 GeV) and has the same shape as the astrophysical background. By playing with an appropriate choice of the Fisk potential, more room can be freed for the DM, hence the constraints relax. Above ~ 40 GeV, instead, the DM component mostly contributes to data points above ~ 5 GeV: here the error bars are smaller and the SMod effect cannot effectively act as a compensation to DM, hence the constraints are more stringent.

Before moving on, we comment on another subtle result, which is not directly visible in the plots of figure 3.13 but which can be inferred by closely scrutinizing the χ^2 of the fits: the inclusion of ELDR is important in the computation of $\bar{p}$ fluxes from low mass DM because, without it, a DM signal can even slightly improve the χ^2 and therefore be artificially favored. We show two specific, cherry-picked examples in table 3.6. Focussing for definiteness on the first case (the 20 GeV DM), we see that: when ELDR is correctly included, the fit with respect

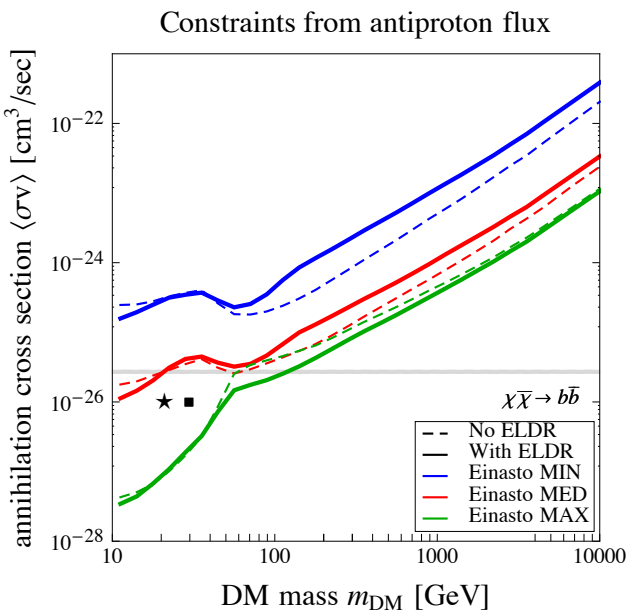

Figure 3.14: **Summary of the antiproton constraints** on DM annihilating into $b\bar{b}$ for an Einasto profile with or without ELDR for the three propagation models MIN, MED, MAX. The symbols represent the DM cases listed in table 3.6.

to the one of a pure astrophysical background is very slightly worsened ($\Delta\chi^2 = 0.04$ in this example); if instead ELDR effects are neglected, the fit can be ameliorated (by 3.78 points in this example), inducing an unfounded preference in favor of DM. Qualitatively, the origin of this effect can be understood by looking at the best fit background in figure 3.11: without ELDR, the astrophysical component typically passes just below the first few data points; adding a DM contribution can push the curve up and improve the χ^2. This does not happen when ELDR is added, as the astrophysical background fits the data better at these low energies. We will come back to this issue in more detail when discussing AMS-02 projections in the next section.

Symbol	$m_{\rm DM}$ [GeV]	$\langle\sigma v\rangle$ [cm^{3}s^{-1}]	No ELDR			With ELDR		
			A[-]	ϕ_F [GV]	$\Delta\chi^2$	A[-]	ϕ_F [GV]	$\Delta\chi^2$
★	20	10^{-26}	1.20	0.98	-3.78	1.25	0.86	0.04
■	30	10^{-26}	1.15	0.90	-1.66	1.25	0.82	0.17

Table 3.6: **Examples of the $\Delta\chi^2$ of the fit to** PAMELA **data** with respect to a pure background case obtained by adding a DM contribution (with the specified parameters), with or without ELDR in the MED propagation model.

Antiproton constraints based on PAMELA data like the ones that we obtain here have also been deduced recently in [232] and [228]. Our constraints are consistent with our previous analysis of section 3.3 (except that that work had not included ELDR), while the constraints in [232] are more stringent than ours and those in [228] are much looser. While a detailed case-by-case comparison is difficult, the choice of the astrophysical background (on which we commented extensively in section 3.4.1 in connection with [228]) plays probably the major role in explaining the differences.

As a rather general conclusion, the different aspects of our analysis and the comparisons with other results show how critical the fine details of background and signal fluxes (ELDR, SMod, interplay with the propagation setups) are to establish the constraints. These should be therefore handled with great care.

3.4.3 Sensitivity of AMS-02

Before the AMS-02 data were announced (we will discuss those in section 3.5), we have estimated the sensitivity of the antiproton measurements to DM annihilation. This is what we present in this section, taking into account all the previously neglected effects, as well as the full mock data. We produced simulated AMS-02 data by putting the points on the MED curve of the astrophysical background, computed including ELDR and a Fisk potential $\phi_F = 0.6$. The binning in energy and the error bars are computed in the same way as in section 3.3.4. The mock data points obtained in this way are presented in figure 3.15. We then apply the same fitting procedure that we used in the previous section, including in particular the marginalization over the value of the Fisk potential.

First, we check the quality of the fits with background only. The results are shown in table 3.7. We correctly find that $\chi^2 = 0$ for the MED case with ELDR and the correct Fisk potential is recovered. The fit remains very good also for MIN and MAX, at the condition of adjusting the Fisk potential to a respectively larger/smaller value than the true one. If ELDR are neglected, the χ^2 worsens dramatically. This is not surprising given the small error bars of the mock data: the best fit curves undershoot the data for the first 15 points and overshoots them at high energies. Next, we add a DM component and compute the sensitivity of AMS-02

	MIN		MED		MAX	
	χ^2/d.o.f.	ϕ_F [GV]	χ^2/d.o.f.	ϕ_F [GV]	χ^2/d.o.f.	ϕ_F [GV]
Whole spectrum with SMod						
No ELDR	645/65	0.81	385/65	0.74	385/65	0.45
With ELDR	19.6/65	0.62	0/65	0.60	30.8/65	0.35

Table 3.7: **Fits of mock** AMS-02 **data** with astrophysical antiprotons only, with or without ELDR.

to DM annihilation, in the usual plane $(m_{\rm DM}, \sigma v)$, on the basis of the mock data. The results are shown in figure 3.15. The behavior of the sensitivity curve is very similar to the actual limits obtained with PAMELA data in the previous section. The limits at large DM masses are more constraining when ELDR are not taken into account; at low masses, it is the opposite. The curves show the 'hump' at ~ 40 GeV already discussed in the previous section.

Another relevant feature on which we want to comment is the significant worsening of the mock constraints for $m_{\rm DM} \lesssim 100$ GeV when ELDR are not taken into account. This arises, in this exercise we are performing, from the same mechanism we discussed in the previous subsection, now enhanced by the foreseen accuracy of the AMS-02 data. Indeed, without ELDR a pure background can not acceptably fit the data (as shown in table 3.7). The χ^2 can be significantly improved by introducing a DM component, hence the constraints relax. This may even lead to believe that a DM signal is hidden at low masses while instead it is just a poor modelisation of the background which is at play. If fact, table 3.8 shows that a DM with a mass $m_{\rm DM} = 20$ GeV (and the other parameters as listed) ameliorates the χ^2 by a large amount. It sits indeed in the region allowed by the 'No ELDR' curve in fig. 3.15. By correctly including ELDR, however, the $\Delta\chi^2$ becomes positive again and the point sits in the excluded

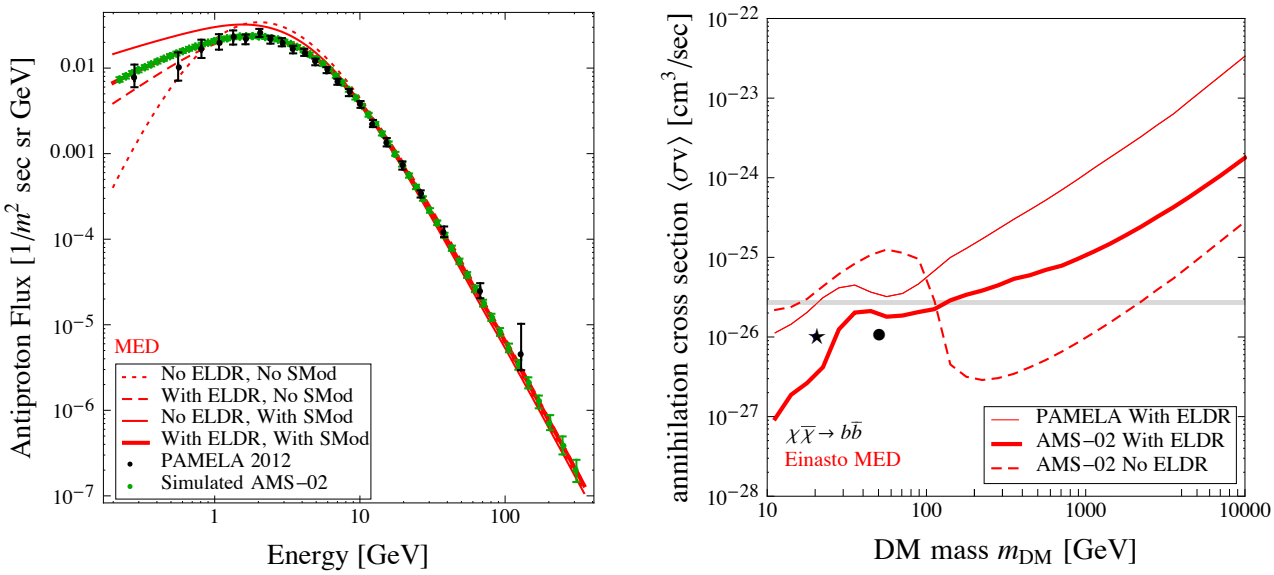

Figure 3.15: **Predictions of** AMS-02 **sensitivity**. Left: mock data points for the $\bar{p}$ flux measured by AMS-02 after 1 year of data-taking and for a Fisk potential $\phi_F = 0.6$ GV. Right: Sensitivity of AMS-02 to DM annihilating into $b\bar{b}$ for an Einasto profile with or without ELDR, for the MED propagation model. The symbols represent the DM cases listed in Table 3.8.

region. While the precise values of the χ^2 have relatively little meaning here, being based on mock data, the point that they illustrate is valid. The general lesson, not surprisingly, is that the robustness of any DM identification in future data, especially at low energies, will have to be based on a careful understanding of the appropriate background, including in particular fine effects such as ELDR.

Symbol	$m_{\rm DM}$ [GeV]	$\langle\sigma v\rangle$ [cm^{3}s^{-1}]	No ELDR			With ELDR		
			A [-]	ϕ_F [GV]	$\Delta\chi^2$	A [-]	ϕ_F [GV]	$\Delta\chi^2$
★	20	10^{-26}	1.19	0.86	-342	1.25	0.78	21.6
●	50	10^{-26}	1.19	0.74	-100	1.23	0.66	1.17

Table 3.8: (Analogously to table 3.6), **examples of the $\Delta\chi^2$ of the fit to mock** AMS-02 data with respect to a pure background case obtained by adding a DM contribution (with the specified parameters), with or without ELDR in the MED propagation model.

Lastly, we note that with AMS-02 it is possible to exclude a thermal cross-section for $m_{\rm DM} < 150$ GeV. This holds using the mock data generated assuming a normalization $A = 1.24$ and this is also the result we obtain with the real $\bar{p}/p$, as will see in section 3.5.2. Gamma ray searches, e.g. from dwarf galaxies, are currently probing similar ranges [233], which shows how competitive the antiproton constraints can be.

In summary, the constraints show that the subtle effects, ELDR in particular, modify the bounds by up to a factor of a few (typically loosening them) even at large masses. The sensitivity analysis shows that AMS-02 will be able to improve on current constraints by up to more than one order of magnitude and probe the thermal annihilation cross-section for DM masses as

large as 150 or 300 GeV (depending on the actual results). Perhaps more importantly, our analysis also shows that appropriately including the subdominant effects is crucial for a correct interpretation of the data: without them, one can e.g. easily obtain a 'false positive' in favor of a DM signature. We have presented a concrete example where this indeed happens.

We are aware that we have only dealt here with a subset of the possible refinements for the calculation of the DM antiproton signal and its background. CR transport may also be a source of sizable uncertainty, which has been so far constrained from probes such as the B/C ratio. As the production of antiprotons from high-energy protons and helium nuclei takes place in the same astrophysical sites as the fragmentation of carbon into boron, using the B/C ratio has proved to be an efficient tool to constrain the antiproton predictions. We anticipate that the antiproton background will not be much affected by the assumptions about the geometry of the magnetic halo. This is less clear for the antiproton DM signal. Alternatively, assuming that spallation reactions take place inside the acceleration sites and yield an astrophysical component of primary antiprotons could possibly modify the DM predictions.

In conclusion, this analysis shows the non-trivial complications connected to the use of antiprotons from astrophysics and from DM, especially at low DM masses, but also their very important probing power, if correctly mastered, for the upcoming future of DM indirect searches.

3.5 AMS-02 Antiprotons: Secondary astrophysical component and immediate implications for DM

In this section we analyze data from the Alpha Magnetic Spectrometer (AMS-02) onboard the International Space Station (ISS), the most advanced detector for indirect DM searches via charged CR flux measurements. The positron fraction has already been published [234, 235], confirming the rise at energies above 10 GeV detected previously by PAMELA [115, 236] and Fermi [237]. The sum of electrons and positrons [238] as well as their separate fluxes [239] have also been published, thus drawing a coherent and extremely precise picture of the lepton components of CR's. Despite the fact that DM interpretations of the positron and, more generally, leptonic 'excesses' have been attempted (for a review see [240]), even before the advent of AMS-02 it had been recognized that explanations involving astrophysical sources were both viable and favored (for a review see [241]), a conclusion reinforced by updated analyses (see [117, 242], and references therein, for recent assessments).

The AMS-02 Collaboration has now presented its preliminary measurements of the $\bar{p}/p$ ratio [243], with an improved statistical precision and energy range extending to 450 GeV. It is therefore crucial and timely to re-examine the situation and update existing results. In addition, AMS-02 has published the measurement of the proton (p) spectrum [244] and presented the measurement of the helium (α) one [243], in qualitative agreement with the previous determinations by PAMELA [221], but now with unprecedented precision and detail. This is important for our purposes since the p and α spectra are crucial input ingredients in the computation of the secondary antiproton flux, which is the minimal astrophysical antiproton background for indirect DM searches. Hence, with the release of these exquisitely precise datasets, AMS-02 provides a coherent, high-statistics—albeit preliminary—picture in the hadronic component of CR's too, allowing for a scrutiny of possible exotic contributions.

3.5.1 Re-evaluation of the astrophysical antiproton background

The main ingredients of the computation for the '(secondary) astrophysical $\bar{p}$ source term' are: i) the injection p and α primary fluxes from galactic sources, ii) the collision cross-sections, iii) the propagation details, as we have seen in the previous section. In this section, we will try to quantify the different uncertainties of the astrophysical background.

For the p and α spectra needed in i), as mentioned above we use the data that have just been released by AMS-02 [244, 243]. The spectra are measured up to a rigidity of 1.8 and 3 TV for p and α nuclei, respectively, and, as already reported by the PAMELA Collaboration [221], they cannot be described by a single power law: a hardening at energies higher than ∼300 GV is observed for both. At the practical level, we perform our own fits of the AMS-02 data points. For both p and α fluxes, we used the following rigidity dependent function (in particles $\mathrm{cm}^{-2}\,\mathrm{s}^{-1}\,\mathrm{sr}^{-1}\,\mathrm{GV}^{-1}$)

$$\Phi = C \cdot (1 - \beta e^{\lambda R}) \cdot \left(\frac{R}{R+\phi_F}\right)^2 \cdot (R+\phi_F)^{\gamma} \cdot \left[1 + \left(\frac{R+\phi_F}{R_B}\right)^{\frac{\Delta\gamma}{s}}\right]^s. \tag{3.24}$$

We proceed in two steps: first γ, $\Delta\gamma$, R_B, s are fixed using the high energy part ($R > 45$ GV) of the spectrum. Then C, α and β are determined over the all energy range. The value of the Fisk potential which gives the best χ^2 for our fits is $\phi_F = 0.62$ GV, the upper bound of the interval set in [244]. The values of the best-fit parameters are reported in table 3.9.

	p	α
C	23566± 30	4075± 2
λ	-0.519 ± 0.007	-0.163 ± 0.004
β	1.21 ± 0.02	0.41 ± 0.02
γ	-2.849 ± 0.002	-2.795 ± 0.009
R_B	355 ± 33	284 ± 38
$\Delta\gamma$	0.146 ± 0.02	0.162 ± 0.009
s	0.0325± 0.0131	0.078± 0.035
χ^2_{ndof}	29.02/(73-7)	2.62/(54-7)

Table 3.9: **Best-fit values for p and α fluxes**, measured by AMS-02 .

The uncertainties on the slope of the p and α spectra at high energies, $\Delta\gamma_{p,\alpha}$, induce an uncertainty band on the predicted astrophysical $\bar{p}/p$ ratio. In figure 3.16, top left panel [5], we show the result of our computation of the ratio with such uncertainty band. For the distribution of the sources of primary CR p and α, which can be determined from pulsar and supernova remnant surveys, we use the parameterization of [223], slightly modified as in [224].

We use the same ingredients as described in the previous section (section 3.4): for $\sigma_{p\mathrm{H}}$ we use the new parameterization recently proposed by [225], instead of the traditional fitting relations given in [216, 217]. For the cross-sections of the other reactions we use the prescription of [204]. We also consider the contribution of antineutron production: on the basis of isospin symmetry, one would consider the production cross-section for antineutrons (e.g. $\sigma_{p\mathrm{H}\to\bar{n}\mathrm{X}}$ and

[5] Each of the panels of the figure has to assume a choice for the uncertainties presented in the other panels. e.g. the first panel assumes definite values for the collision cross-sections, a model for $\bar{p}$ propagation and a value for the Fisk potential. They are always chosen to be the central values, e.g MED, the fiducial cross-section and 0.62 GV for this example.

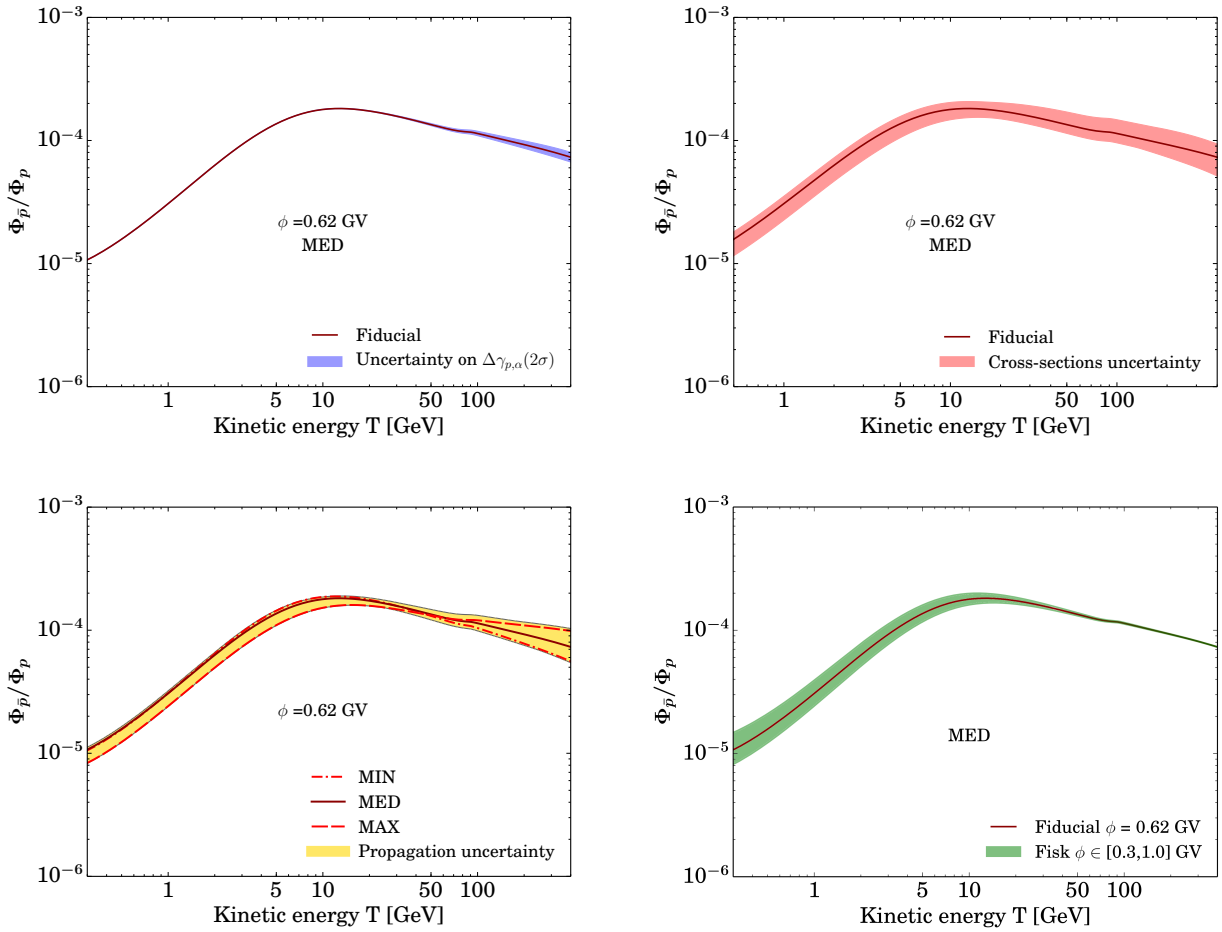

Figure 3.16: Illustration of the individual **partial uncertainties for secondary antiprotons.** The colored bands represent the uncertainties on the input p and α fluxes (upper left panel), $\bar{p}$ production cross-sections in the interstellar medium (upper right panel), Galactic propagation (lower left panel) and Solar modulation (lower right panel).

the others) as equal to those for antiprotons; the antineutrons then rapidly decay and provide an exact factor of 2 in the $\bar{p}$ flux. However, as pointed out in [225, 227] and it may be that this naïve scaling does not apply and that the antineutron cross-section is larger by up to 50% with respect to the $\bar{p}$ one.

Assessing uncertainties for reactions involving He is even more challenging, since no data are present, and predictions are based on semi-empirical nuclear models calibrated on data involving either protons or heavier nuclei (see [245]). For sure, uncertainties involving these reactions are at least as large in percentage as the one of the pH reaction, an assumption we will do in the following. More conservative assumptions would only make the error larger, and strengthen our main conclusion on the level of agreement of the data with a purely secondary antiproton flux. All these cumulated effects contribute to an uncertainty band for the astrophysical $\bar{p}/p$ ratio which is represented in figure 8 of [225] and which we will adopt: it varies from about 20% to at most 50% (at large energies and in the most conservative conditions). In figure 3.16, top right panel, we show our prediction for the $\bar{p}/p$ ratio with this uncertainty envelope.

Once produced, antiprotons have to propagate in the local Galactic environment before they

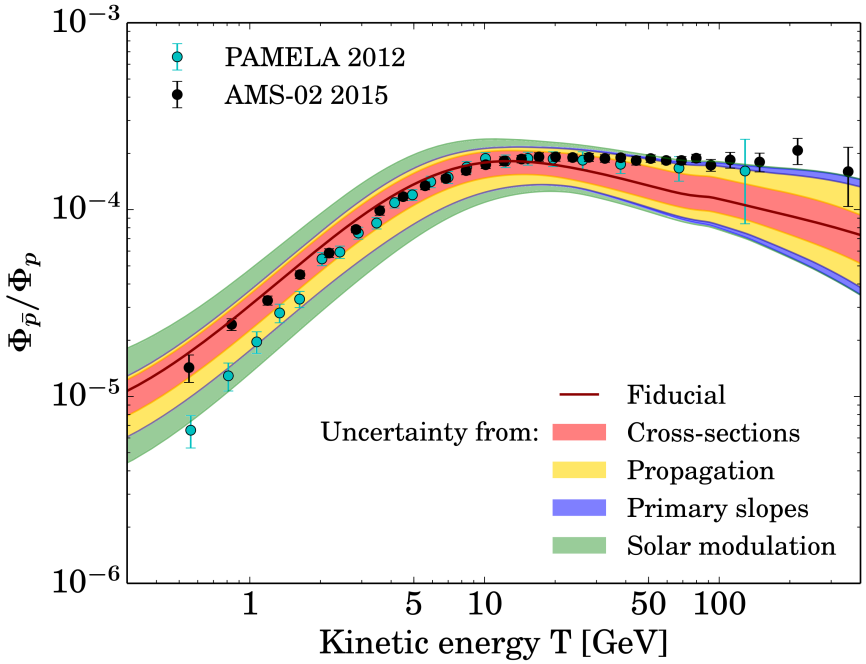

Figure 3.17: The **combined total uncertainty on the predicted secondary $\bar{p}/p$ ratio**, superimposed to the older PAMELA data [297] and the new AMS-02 data. The curve labelled 'fiducial' assumes the reference values for the different contributions to the uncertainties: best fit proton and helium fluxes, central values for the cross-sections, MED propagation and central value for the Fisk potential. We stress however that the whole uncertainty band can be spanned within the errors.

are collected at Earth. We deal with this process in the usual way, by solving semi-analytically the full transport equation for a charged species in a 2D cylindrical 'thick halo' model of the Galaxy, as described in section 3.4. We take into account $\bar{p}$ annihilation, energy losses, 'tertiary production', and diffusive reacceleration. Besides these effects, the propagation parameters governing diffusion and convection are as usual codified in the MIN, MED and MAX. Note that these have not (yet) been revised on the light of recent secondary data like the preliminary B/C ratio of AMS-02, so the viability of these predictions for the $\bar{p}/p$ ratio (which extends for instance to higher energies) is not trivially expected to hold.

In figure 3.16, lower left panel, we show the impact of the propagation uncertainty. The curves which are labelled MIN, MED and MAX represent the modification which occurs by choosing these standard sets. The shaded yellow area envelops the results obtained by sampling more widely the propagation parameter space that has been shown in [218] to be compatible with the B/C ratio and finding the values that minimize and maximize the secondary, rather than primary, $\bar{p}/p$ flux. Notice that the shaded yellow area does not coincide with the MIN-MED-MAX envelope (see in particular between 50 and 100 GeV): this is not surprising, as it just reflects the fact that the choices of the parameters which minimize and maximize the $\bar{p}/p$ secondaries are slightly different from those of the primaries. However, the discrepancy is not very large. We also notice for completeness that an additional source of uncertainty affects the energy loss processes. Among these, the most relevant ones are the energy distribution in the outcome of inelastic but non-annihilating interactions or elastic scatterings to the extent they

do not fully peak in the forward direction, as commonly assumed [218]. Although no detailed assessment of these uncertainties exists in the literature, they should affect only the sub-GeV energy range, where however experimental errors are significantly larger, and which lies outside the main domain of interest of this article.

Finally, $\bar{p}$'s are subject to the phenomenon of solar modulation in the heliosphere. As in the previous section, we describe this process in the force field approximation with a conservative interval for the Fisk potential $\phi_F = [0.3, 1.0]$ GV $\simeq \phi_F^p \pm 50\% \, \phi_F^p$, motivated by the dedicated analysis in section 2.5.2. In figure 3.16, bottom right panel, we show the computation of the ratio with the uncertainties related to the values of the Fisk potential in the considered interval. Notice finally that the force field approximation, even if 'improved' by our allowing for different Fisk potentials for protons and antiprotons, remains indeed an "effective" description of a complicated phenomenon. Possible departures from it could introduce further uncertainties on the predicted $\bar{p}/p$, which we are not including. However it has been shown in the past [**?**] that the approximation grasps quite well the main features of the process, so that we are confident that our procedure is conservative enough.

Figure 3.17 constitutes our summary and best determination of the astrophysical $\bar{p}/p$ ratio and its combined uncertainties, compared to the new (preliminary) AMS-02 data. The crucial observation is that the astrophysical flux, with its cumulated uncertainties, can reasonably well explain the new datapoints. Thus, our first —and arguably most important— conclusion is that, contrarily to the leptonic case, there is no clear antiproton excess that can be identified in the first place, and thus, at this stage, no real need for primary sources. This also means that, at least qualitatively, one expects a limited room left for exotic components, such as DM. Indeed in the following section we will proceed to compute the constraints on it.

However, before we can do so, we have to identify specific sets of astrophysical parameters to describe the background. We fix in turn MIN, MED and MAX and we vary the solar modulation potential in the given interval. We model the uncertainties of the production cross-sections term by allowing a renormalization of the background with an energy dependence and an amplitude A as dictated by the analysis presented above (namely, an uncertainty modulated as the pink band of figure 3.16). With this strategy, we look for the best fitting values of the amplitude A and of the potential ϕ_F and we trace the corresponding $\bar{p}/p$ spectra. In concrete terms, for each propagation model, we minimize the chi-square $\chi_0^2(A, \phi_F)$ with respect to the AMS-02 data and hence determine the best fit amplitude A_0 and Fisk potential ϕ_F^0. We show in figure 3.18 the different cases.

Even within the limitations of the data like those we are dealing with (namely their preliminary nature, their errors only partially accounted for and the partial collection time with respect to the full lifetime of the experiment), we can see that the MIN propagation scheme predicts an astrophysical background that can *not* reproduce the new $\bar{p}/p$ data points above 30 GeV. The MED scheme provides a barely decent fit (still good up to $\sim$ 30 GeV but rapidly degrading after) while choosing MAX the data can be well explained across the whole range of energies. We have explicitly computed the corresponding χ^2 to support the above statements, with the MIN, MED, MAX cases yielding 106, 58 and 41, respectively (for 28 degrees of freedom). Given the preliminary nature of the data, of course they have only an indicative significance. This is our second conclusion:the preliminary $\bar{p}/p$ AMS-02 data seem to prefer a model, such as MAX, characterized by a relatively mild energy dependence of the diffusion coefficient at high energies. Although it is too early to draw strong conclusions, this is an interesting observation and it goes in the same direction as the preference displayed by the

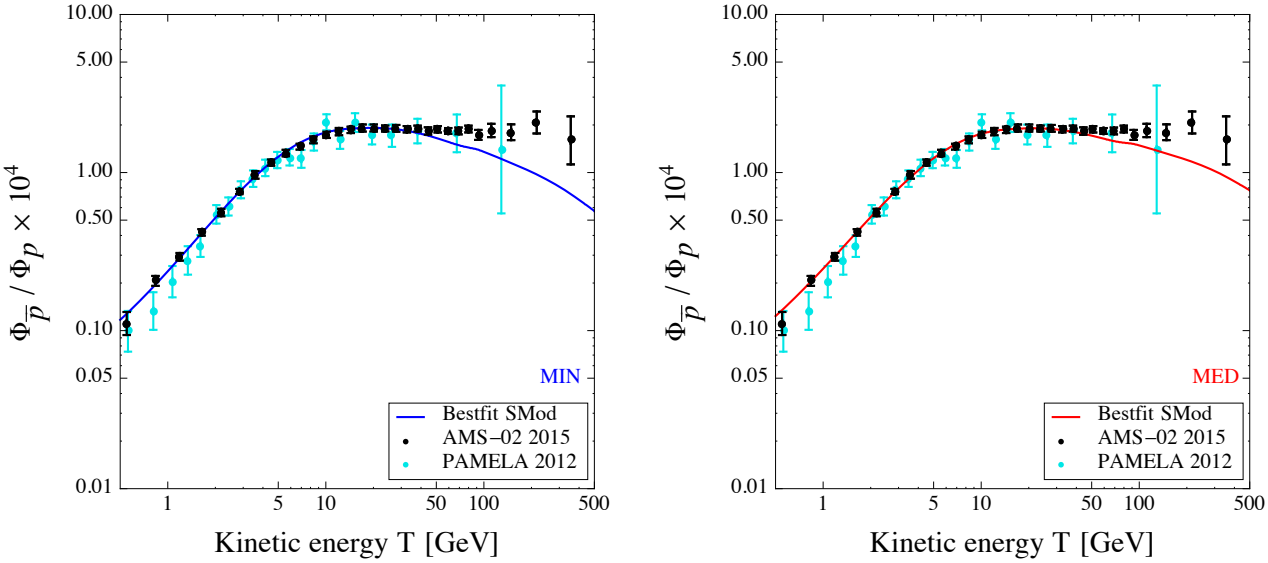

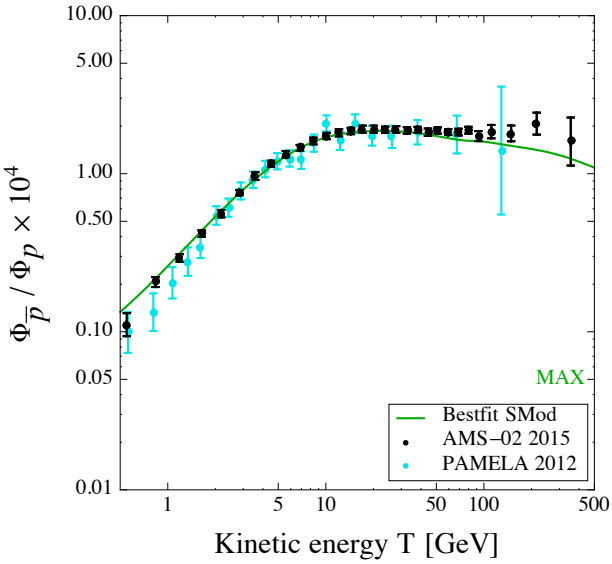

Figure 3.18: The **best-fit secondary** antiproton fluxes originating from astrophysics, for the MIN, MED and MAX cases, compared to the new AMS-02 data and the previous PAMELA data. Each case assumes a different value for the normalization amplitude A and for the Fisk potential.

preliminary B/C AMS-02 data [**?**] [6].

It would of course be tempting to interpret the room left in the MIN and MED cases at large energies as an exotic contribution from DM. However we insist that this would be a wrong deduction in two respects: as long as a model within the uncertainties can fit the data, failure of other models just means a better selection of the background rather than evidence for an extra component; in any case, a new assessment of the viable propagation parameter space would be needed before any conclusion is drawn.

[6] It is also backed by the results recently reported in [246]—appeared after the first version of this paper in pre-print form—based on fits to PAMELA B/C, p and He data.

3.5.2 Updated constraints on Dark Matter

We obtain the $\bar{p}$ fluxes at Earth (post-propagation) from the numerical products provided in [9], version 4 and obtained in the previous section. Notice that these include the subtle effects of energy losses, tertiaries and diffusive reacceleration which are important to reach a detailed prediction.

We consider the same four primary annihilation (or decay) channels: DM DM $\to b\bar{b}$, W^+W^-, $\mu^+\mu^-$ and $\gamma\gamma$. We also consider two representative DM Galactic profiles: Einasto and Burkert, with the precise functional forms and definitions of the parameters as in 1.1.3. The former possesses a peaked distribution towards the Galactic center and hence typically results in a more abundant yield of antiprotons with respect to the latter, which features a core in the inner few kpc.

We remind that, in section 3.5.1, we have obtained the re-evaluated astrophysical background fluxes and their uncertainties. In particular, we have computed the fluxes for the MIN, MED and MAX cases, displayed in figure 3.18. Armed with those and with the fluxes from DM as just presented, we can now compute the constraints in the usual planes 'mass $m_{\rm DM}$ vs. thermally averaged annihilation cross-section $\langle\sigma v\rangle$' or 'mass $m_{\rm DM}$ vs. decay rate Γ'. We repeat the procedure from the previous section and derive constraints on DM. It makes sense to derive constraints only within the propagation schemes that provide a decent explanation of the background. MAX is the favored scheme. MED provides overall a worse but still reasonable fit to the data, so that we will employ it. In addition, (see figure 3.18, middle panel) at small energies ($T \lesssim 30$ GeV) its fit is good, thus meaningful constraints on relatively light DM ($m_{\rm DM} \lesssim 300$ GeV) can be derived. We discard instead the MIN case.

The results that we obtain with this strategy are presented in figure 3.19 for the DM annihilation case and in figure 3.20 for the DM decay case. In the left panels we fix a benchmark DM profile (Einasto) and the MED propagation model, and show the constraints for the different particle physics channels introduced above. We see for example that the thermal annihilation cross-section $\langle\sigma v\rangle = 3 \cdot 10^{-26}\,{\rm cm}^3/{\rm s}$ is now touched by the exclusion line for $m_{\rm DM} \sim 150$ GeV for the $\bar{b}b$ channel. In the right panels we explore the impact of changing the propagation parameters or the DM distribution. As already highlighted several times in the literature, the effect is sizable and can reach a factor of up to an order of magnitude. For instance, the previously quoted limit for the mass of a thermal relic can vary between 90 and 250 GeV for the range of models explored here. Of course, as MAX maximizes by definition the DM $\bar{p}$ yield, its constraints are much stronger than those of the MED case. Turning the argument around, if the preference for MAX-like propagation schemes hinted at by preliminary AMS-02 data is confirmed, AMS-02 itself has the unprecedented possibility to exclude $m_{\rm DM} \lesssim 250$ GeV for thermal annihilation cross-section in the $\bar{b}b$ channel.

This analysis is very preliminary and there is still room for improvements. First and foremost, the release of the final $\bar{p}/p$ measurement with systematic and statistical errors fully accounted for. Yet, even a preliminary analysis allows to show that antiprotons confirm themselves as a very powerful probe for CR physics and for DM in particular. Actually, considering the puzzling excesses (with respect to the originally predicted astrophysical background) of undetermined origin in the electron and positron fluxes, considering the complicated background of most gamma-ray searches and considering the challenges of neutrino detection, $\bar{p}$'s might arguably still be the most promising avenue in DM indirect searches, since improving the knowledge of the background is relatively easier than for other channels and so perhaps seeing the emergence of a clear signal is possible. In this respect, the AMS-02 experiment

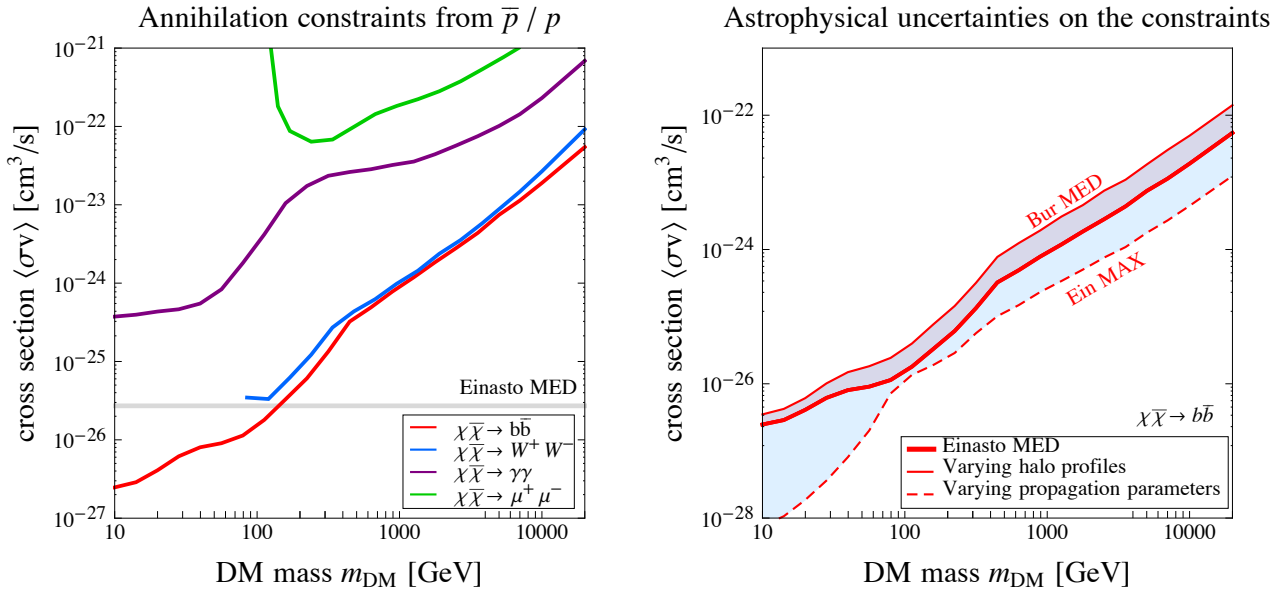

Figure 3.19: **Annihilating DM: current constraints.** Left Panel: current constraints from the antiproton to proton ratio measurements by AMS-02, for different annihilation channels. The areas above the curves are excluded. Right Panel: illustration of the impact of DM-related astrophysical uncertainties: the constraint for the $b\bar{b}$ channel spans the shaded band when varying the propagation parameters (dashed lines) or the halo profiles (solid lines). Notice that in the MIN case the analysis is not sensible, hence not shown here (see text for details).

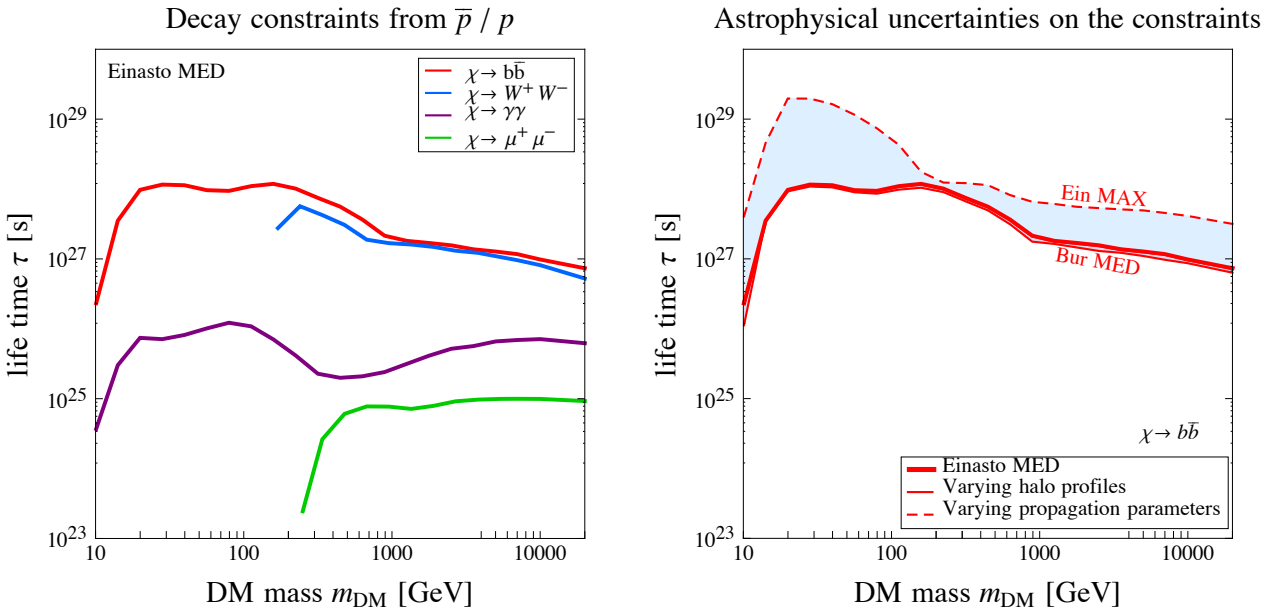

Figure 3.20: **Decaying DM: current constraints.** Left Panel: current constraints from the antiproton to proton ratio measurements by AMS-02, for different decay channels. The areas below the curves are excluded. Right Panel: illustration of the impact of DM-related astrophysical uncertainties: the constraint for the $b\bar{b}$ channel spans the shaded band when varying the propagation parameters (dashed lines) or the halo profiles (solid lines). Notice that in the MIN case the analysis is not sensible, hence not shown here (see text for details).

can play a crucial role. So far it has essentially confirmed the results of previous experiments (most notably PAMELA), but it has done so with an impressively improved accuracy: the qualitative picture in DM indirect searches has been left largely unchanged by it, but AMS-02 has allowed improved pinning down of the parameters and tightening of the constraints. In this context, while follow-up releases of antiproton data (e.g. pure fluxes, extended energy range or enlarged statistics) will obviously be welcome, it is urgent to address first one of the main current limitations in the field of charged CRs, namely the determination of the propagation parameters. In this respect, analyzing the upcoming reliable and accurate light nuclei measurements from AMS-02 will provide the community with a very powerful leverage for any search of exotics in CR's. At that point it will be possible to assess whether or not excesses are present in antiproton data, for instance if the current small deficit increases in significance (although identifying their origin will remain very challenging [247]).

3.6 Final comments

In this chapter of the thesis we have dealt with antiprotons as a tool for DM indirect searches. After computing constraints on DM based on the antiproton flux measured by PAMELA in a simplified approach, we added the neglected effects (energy-losses, including tertiary production, diffusive reaccelerating and solar modulation in a force-field approximation). Antiprotons are a very powerful and sensitive probe of DM and with the precision of recent experiments these effects have to be taken into account and can change the conclusion on exotic contributions. The secondary background is provided in terms of an analytical function and the DM signal can be downloaded on the PPPC4DMID webpage. All of these computation have been done for the three propagation parameter sets, namely MIN, MED and MAX.

Finally, we analyzed the preliminary AMS-02 results on the $\bar{p}/p$ ratio, using the new p flux published by AMS-02 and the preliminary AMS-02 results presented on the α flux. We have re-evaluated the secondary astrophysical predictions for the $\bar{p}/p$ ratio. We have accounted for the different sources of uncertainties: namely on the injection fluxes, on the production cross-sections, on the propagation process and those connected to solar modulation. Our first and main result is that there is no unambiguous antiproton excess that can be identified in the first place, and thus, at this stage, no real need for primary sources of antiprotons. Within errors, secondary astrophysical production alone can account for the data. This conclusion is highly non-trivial, since we relied on updates of *existing* propagation schemes, which were not necessarily expected to work in the high precision and extended energy regime made accessible by AMS-02.

Next, we enter in the merit of which propagation schemes do account for the data, taking into account the other uncertainties. We find that the data seem to prefer a model, such as MAX, characterized by a relatively mild energy dependence of the diffusion coefficient at high energies. If confirmed, this would go in the same direction as other indications already obtained in different channels, as discussed above. In fact, like the B/C, the $\bar{p}/p$ is a secondary to primary ratio and is thus sensitive to the slope of the diffusion parameter δ. The previous data set form PAMELA was in agreement with all threes propagation models. An important application concerns updated constraints on DM: within the framework of the propagation schemes that it is sensible to use, we derive bounds that are more stringent by about one order of magnitude with respect to the previous ones, as expected from our sensitivity studies.

Chapter 4

Secondary photon emission from DM annihilations into electrons and positrons

4.1 Introduction

Positrons are also charged antiparticles used for DM indirect detection. As we have seen earlier, an excess in the positron flux, as well as in the positron+electron flux, has been detected by Pamela, Fermi, Hess and recently AMS-02. Looking for DM directly in the leptonic channels can thus be challenging, hence another interesting strategy consists in looking for the emissions produced by the interactions of relativistic electrons and positrons, injected by DM annihilations (or decays), with the galactic environment. These emissions go under the collective name of 'secondary radiation' and are essentially of three kinds: (i) radio waves due to the synchrotron radiation of the $e^{\pm}$ on the galactic magnetic field; (ii) gamma rays due to the bremsstrahlung processes on the galactic gas density; (iii) gamma rays due to the Inverse Compton scattering (ICS) processes on the interstellar radiation field.

They have received different attention in the literature. Synchrotron emission has been considered since a long time in regions close to the GC, characterized by a large intensity of the magnetic field [248]. Its relevance in wider regions of interest in the Galaxy has also been highlighted [249, 250, 251, 252, 253, 254, 255, 256, 257, 258, 259]. Bremsstrahlung gamma rays have mostly been neglected for what concerns DM studies. Recently, however, their importance has been recognized, especially in connection with searches for relatively light (10-40 GeV) DM signals from the GC [260, 261, 262, 263, 264], analyses in chapter 5. Finally, ICS gamma rays have been identified as an important component of the DM gamma ray spectrum mainly in conjunction with the models of leptophilic DM featuring a large annihilation cross-section, proposed in the wake of the lepton excesses (see e.g. [265, 266, 267, 268, 269, 270] and many subsequent works).

All these signatures are potentially very relevant and promising. Their practical use, however, depends on a number of different choices, i.e. related to the unknown magnetic field configuration, to the unknown propagation parameters of electrons and positrons in the Galaxy, to the unknown gas distribution, to the unknown profile of DM etc. Some of these uncertainties are also shared with other possible signals from DM in other Indirect Detection channels. A step towards model independent tools in order to identify DM is what we would like to make here.

More precisely, the purpose of this chapter is to provide state-of-the-art tools allowing the computation of synchrotron and bremsstrahlung radiation for any (weak-scale) DM model, for a set of possible astrophysical configurations that bracket the current sensible ranges of the uncertainties. This follows the spirit of previous papers ([9, 271]): the concrete goal is to enable the 'DM model builder' to readily compute the synchrotron and bremsstrahlung phenomenology of their model without having to fiddle with the underlying computations or even with the intervening astrophysics, but just by choosing which configurations to adopt (and being able to adopt the same choices consistently for other indirect detection channels). On the way to achieve that, we have to upgrade some ingredients used to accurately compute the population of DM-induced electrons and positrons, namely the energy loss function and the $e^{\pm}$ halo functions. In the spirit of [9, 271] we always employ semi-analytical methods rather than fully numerical ones, in order to better control the relevant physics.

4.2 Astrophysical configurations

First, we spell out the astrophysical ingredients that we use to compute the propagation of electrons and positrons, especially the energy loss function, and ultimately the synchrotron and bremsstrahlung signals. While there certainly exist some interdependences between the parameters entering in these astrophysical ingredients (for instance, the thickness of the CR diffusive halo L is related to the vertical extent of the galactic magnetic field, since a far reaching magnetic field determines a thick CR confinement box) it is beyond our scope to impose such correlations by hand. Our aim is to provide the full range of possible choices and it is up to the user to choose sensible combinations. In order to consider inter-dependencies self-consistently one is better off choosing a fully numerical approach to the propagation of CR, such as by using `GalProp` [158] or `Dragon` [159].

4.2.1 Galactic Magnetic Field

Our Galaxy has a complicated magnetic field structure, and dedicated efforts by several groups have been performed in order to map it: for some recent overviews and sets of references see for instance [272, 273, 274, 275]. We recall here the salient features of the inferred magnetic field and then define the simplified functional form that we will adopt.

The total galactic magnetic field $\vec{B}_{\rm tot}$ is the sum of a large scale regular $\vec{B}_{\rm reg}$ and a turbulent $\vec{B}_{\rm turb}$ component. These, in turn, can be decomposed in different contributions, including disk and halo fields. The regular magnetic field is caused by dynamo effects in the galaxy and it can be studied with Faraday rotation measurements of nearby pulsars and high latitude radio sources, or with measurements of the polarized synchrotron intensity. On the other hand, the turbulent magnetic fields are tangled by turbulent gas flows and can be traced looking for their unpolarized synchrotron emission. Recent models of the galactic magnetic fields have been proposed e.g. in [276, 277, 278, 279, 274].

Rather than the detailed magnetic field geography, the overall intensity is more important for our purposes. While we keep in mind that the complicated cartography sketched above can have an impact on the determination of the energy losses of electrons and on the synchrotron emission from DM, we choose to model the disk field strength by a double exponential in z and

in r, as proposed e.g. by [280] and [281] for the radial part. Namely, we use

$$B_{\rm tot} = B_0 \exp\left(-\frac{r - r_\odot}{R_D} - \frac{|z|}{z_D}\right) \tag{4.1}$$

where $r_\odot = 8.33$ kpc is the location of the Sun. We then adopt several configurations for the values for the parameters B_0, r_D and z_D, as shown in the table in fig. 4.1:

- Model 1 (MF1 for "Magnetic Field 1" hereafter) is the configuration used in [9] and very similar to the one used in the original `GalProp` code (it differs by the normalization factor B_0, which has changed a few times in the `GalProp` literature [280, 163, 162]).
- Model 2 ("MF2") is loosely based on the findings of [276] (and previous [281]). Following one of the models in [276] we take a value of 2.1 μG for the intensity of the disk regular field at solar location (we report it to our value for $r_\odot$); we then add an intensity of 3 μG to account for the random component. The resulting field is steeper in r and in z than MF1 and reaches slightly higher values at the GC.
- Model 3 ("MF3") is modeled following [282]. It is substantially higher at the location of the Earth and has larger scale heights both in r and in z, i.e. it extends much farther out in both directions.

4.2.2 Other astrophysical ingredients

In this section we recall the other astrophysical ingredients involved in the computations. We illustrate most of them in figure 4.1 (except for DM profiles which are shown in figure 1.2 and propagation parameters which can be found in table 2.1). As a general rule, we want to use state-of-the-art but standard ingredients, in order to allow easy comparison with other work.

- The **DM density profile** in the Galaxy. We adopt the 6 standard profiles as defined in section 1.1.3.
- Electron and positron **propagation parameters**. These have to be plugged in the diffusion-loss equation 2.66, correctly accounting for source terms and energy losses. While an updated assessment of the validity of these ranges of parameters would be welcome, as seen in section 3.5.1, we continue using the standard values reported here also for consistency reasons.
- **InterStellar Radiation Field** (ISRF). As mentioned in section 2.4.4, electrons and positrons propagating in the galactic halo lose energy by Inverse Compton scattering on the ambient light. A detailed description of this radiation field is therefore important in order to reliably compute the energy losses. We adopt the latest radiation maps extracted from `GalProp` [283]. These replace the ones formerly used in the literature, and in particular in [9]. In figure 4.1 we draw the two maps in two sample locations (at the Earth and near the galactic center) and compare them. One clearly sees the three different components (StarLight SL, InfraRed IR and the CMB blackbody spectrum). The current map is much more detailed and normalization differences of the order of a factor 2 are visible, but the overall behavior is confirmed. We will see that these small differences have an (equally small) impact on the observables entering $e^\pm$ propagation.

Magnetic field configurations

Model	ref.	B_0 [μG]	r_D [kpc]	z_D [kpc]
MF1	[280]	4.78	10	2
MF2	[276, 281]	5.1	8.5	1
MF3	[282]	9.5	30	4

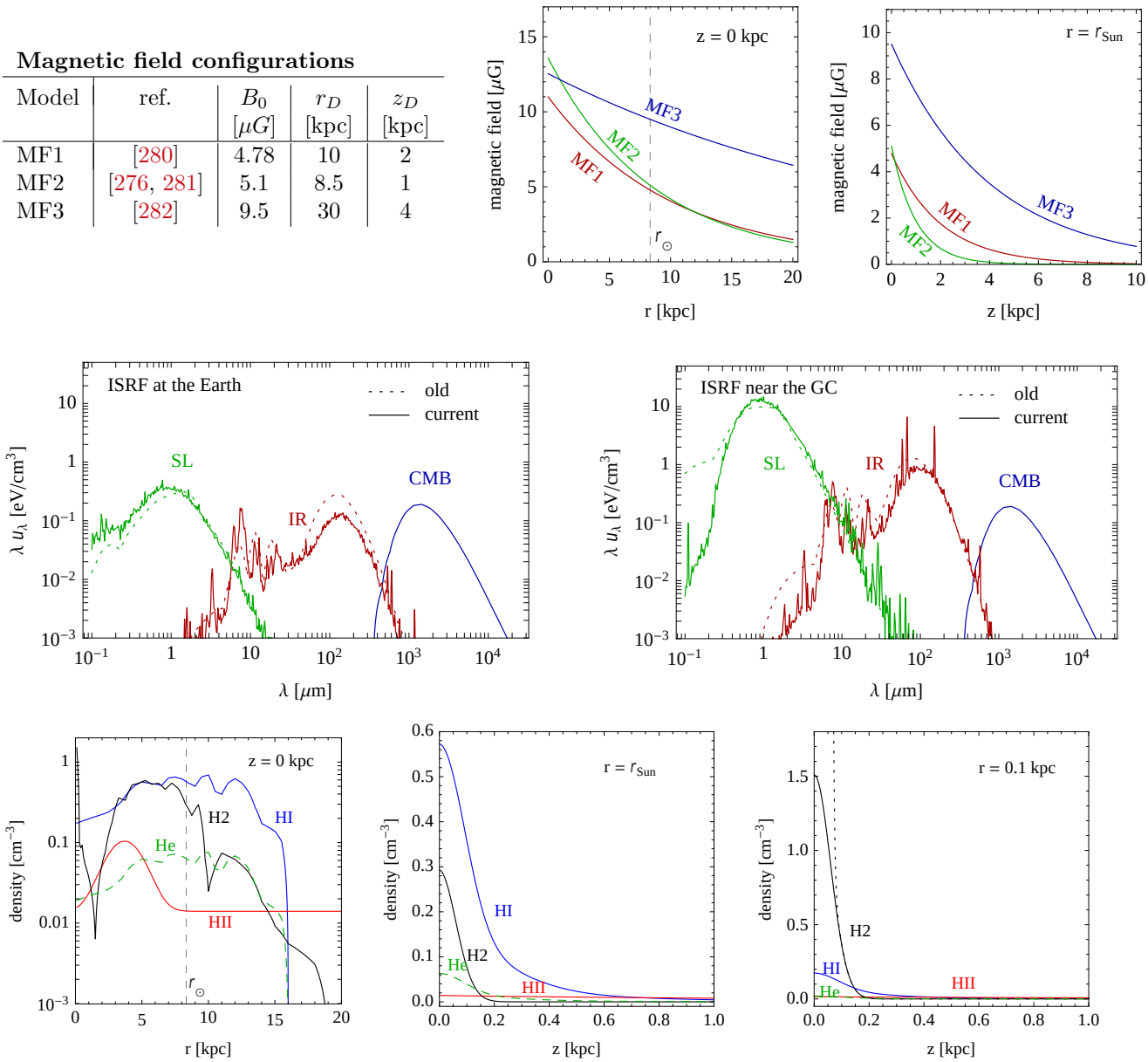

Figure 4.1: Collection of the **astrophysical ingredients** we use. Top row: magnetic field configurations. Second row: illustration of the ISRF in two sample locations. Bottom row: illustration of the galactic gas densities (figure from [260]).

- **Gas maps**. Electrons and positrons also lose energy by processes occurring on the interstellar atomic and molecular gas (Coulomb interactions, ionization, bremsstrahlung). We use the gas maps described in [284] and already used in [260]. We refer to the latter for some discussion. They are illustrated in figure 4.1. The relevant species are atomic (HI) and molecular (H_2) neutral hydrogen, ionized hydrogen (HII), neutral atomic helium (He) and ionized helium (which is however irrelevant for all practical purposes). As discussed in particular in [260], these maps represent a reliable description of the coarse grained distribution of gas in the Galaxy, but miss important features at small scales. In particular, they do not take into account the regions characterized by a much higher gas density (up to 2 or 3 orders of magnitude with respect to the coarse grained maps) which are known to exist close to the galactic center (typically at $r \lesssim 200$ pc scales). For the purpose of the general tools that we are developing in this work, we do not correct by hand the coarse-grid maps by adding the high density regions (contrary to what was done in [260]) but we will allow the user to change the overall normalization of the gas density in the energy loss function that we will describe below.

4.3 Technical outputs

Here we present tools that can be downloaded from the PPPC4DMID website and can be used by the community. First, we have to determine the energy-loss function for $e^{\pm}$, then compute the propagation function of $e^{\pm}$ from DM annihilation or decay in the diffusion model and finally obtain the halo functions for their secondary radiation.

4.3.1 An improved energy loss function for $e^{\pm}$ in the Galaxy

Using the ingredients described above, we compute a function describing the energy losses of electrons and positrons during their propagation in the Galaxy, improving the one of the previous PPPC4DMID. It includes energy losses by Coulomb interactions with the interstellar gas, by ionization of the same gas, by bremsstrahlung on the same gas, by ICS (using the updated ISRF presented in section 4.2.2) and by synchrotron emission, with the choice of the three magnetic field models discussed in section 4.2.1. Schematically:

$$b_{\rm tot}(E,r,z) \equiv -\frac{{\rm d}E}{{\rm d}t} = b_{\rm Coul+ioniz} + b_{\rm brem} + b_{\rm ICS} + b_{\rm syn} \tag{4.2}$$

where E is the energy of the electron or positron and r and z are cylindrical galactic coordinates. Such a function is provided on the website [285] in the format `btot[E,r,z,gasnorm,MF]`, where `gasnorm` allows to change the overall normalization of the gas densities and `MF` is a flag selecting the magnetic field model. We now recall the different components of this function [1] and illustrate its main features in figures 4.2 and 4.3. Details can be found in standard references such as [286, 287] as well as in [9, 270].

- **Energy losses by Coulomb interaction and ionization** on neutral matter are described by

$$b^{\rm neut}(E,r,z) = \frac{9}{4}\, c\, \sigma_{\rm T}\, m_e \sum_i n_i Z_i \left(\log\frac{E}{m_e} + \frac{2}{3}\log\frac{m_e}{\Delta E_i} \right) \tag{4.3}$$

[1] Notice that we will always limit ourselves to the case of relativistic electrons.

where c is the speed of light, $\sigma_T = 8\pi r_e^2/3$, with $r_e = \alpha_{\rm em}/m_e$, is the Thompson cross-section, n_i is the number density of gas species i with atomic number Z_i and ΔE_i is its average excitation energy (it equals 15 eV for hydrogen and 41.5 eV for helium).

On ionized matter, one has

$$b^{\rm ion}(E,r,z) = \frac{3}{4}\, c\, \sigma_{\rm T}\, m_e\, n_e \left(\log\frac{E}{m_e} + 2\log\frac{m_e}{E_{\rm pla}}\right) \tag{4.4}$$

where n_e is the electron density and $E_{\rm pla} = \sqrt{4\pi\, n_e\, r_e^3}\, m_e/\alpha$ corresponds to the characteristic energy of the plasma.

The total energy losses for Coulomb interactions and ionization processes, $b_{\rm Coul+ioniz} = b^{\rm neut} + b^{\rm ion}$, will therefore be given by the sum of equation 4.3 and equation 4.4 with, respectively, the densities of ionized and neutral gas species. In both cases, energy losses are *essentially independent* of E, since the constant terms in the brackets are numerically dominant.

- **Energy losses by bremsstrahlung** are described by

$$b_{\rm brem}(E,r,z) = c\sum_i n_i(r,z)\int_0^E {\rm d}E_\gamma\, E_\gamma\, \frac{{\rm d}\sigma_i}{{\rm d}E_\gamma}\,, \tag{4.5}$$

where E_γ corresponds to the energy of the gamma-ray emitted in each bremsstrahlung process. The differential cross-section reads

$$\frac{{\rm d}\sigma_i(E,E_\gamma)}{{\rm d}E_\gamma} = \frac{3\,\alpha_{\rm em}\sigma_T}{8\pi\, E_\gamma}\left\{\left[1+\left(1-\frac{E_\gamma}{E}\right)^2\right]\phi_1^i - \frac{2}{3}\left(1-\frac{E_\gamma}{E}\right)\phi_2^i\right\}\,, \tag{4.6}$$

where $\phi_{1,2}^i$ are scattering functions dependent on the properties of the scattering system. For a completely ionized gas plasma with charge Z one has

$$\phi_1^{\rm ion}(E,E_\gamma) = \phi_2^{\rm ion}(E,E_\gamma) = 4(Z^2+Z)\left\{\log\left[\frac{2E}{m_e\, c^2}\left(\frac{E-E_\gamma}{E_\gamma}\right)\right] - \frac{1}{2}\right\}\,, \tag{4.7}$$

and thus the energy losses in this regime ('weak shielding') read

$$b_{\rm brem}^{\rm ion} = \frac{3}{2\pi} c\, \alpha_{\rm em}\, \sigma_{\rm T}\, n_i\; Z(Z+1)\left(\log\left(2\,\frac{E}{m_e}\right) - \frac{1}{3}\right) E\,. \tag{4.8}$$

On the other hand, for atomic neutral matter the scattering functions have a more complicated dependence, which is usually parameterized in terms of the quantity $\Delta = E_\gamma m_e/\left(4\alpha_{\rm em}E(E-E_\gamma)\right)$. For the relativistic regime we are interested in, since $E \gtrsim 1$ MeV always, one basically cares for the limit $\Delta \to 0$ for which these functions are constant and take the following numerical values:

$$\begin{aligned}
\phi_1^{\rm H}(\Delta=0) &\equiv \phi_{1,\rm ss}^{\rm H} = 45.79,\\
\phi_2^{\rm H}(\Delta=0) &\equiv \phi_{2,\rm ss}^{\rm H} = 44.46,\\
\phi_1^{\rm He}(\Delta=0) &\equiv \phi_{1,\rm ss}^{\rm He} = 134.60,\\
\phi_2^{\rm He}(\Delta=0) &\equiv \phi_{2,\rm ss}^{\rm He} = 131.40,\\
\phi_{(1,2)}^{\rm H_2}(\Delta=0) &\simeq 2\,\phi_{(1,2),\rm ss}^{\rm H}.
\end{aligned} \tag{4.9}$$

The subscript $_{\rm ss}$ in this notation refers to the fact that this regime is usually called 'strong-shielding' because the atomic nucleus is screened by the bound electrons and the impinging $e^{\pm}$ have to force the shield. In this limit the energy losses read

$$b_{\rm brem}^{\rm neut} = \frac{3}{8\pi} c\, \alpha_{\rm em}\, \sigma_{\rm T}\, n_i \left(\frac{4}{3}\phi_{1,\rm ss}^i - \frac{1}{3}\phi_{2,\rm ss}^i \right) E\,. \tag{4.10}$$

The total energy losses for bremsstrahlung will therefore be given by the sum of equation 4.8 and equation 4.10 with, respectively, the densities of ionized and neutral gas species. In both cases, at leading order, energy losses are *linearly dependent* on E. A further logarithmic dependence arises for scattering in ionized medium, while a small additional energy dependence is also found in neutral medium if one accounts for the effect of finite Δ.

- **Energy losses by Inverse Compton Scattering** are described, in exact form, by

$$b_{\rm ICS} = 3c\,\sigma_{\rm T} \int_0^\infty d\epsilon\, \epsilon \int_{1/4\gamma^2}^1 dq\; n(\epsilon) \frac{(4\gamma^2 - \Gamma_\epsilon)q - 1}{(1+\Gamma_\epsilon q)^3} \left[2q \ln q + q + 1 - 2q^2 + \frac{1}{2}\frac{(\Gamma_\epsilon q)^2}{1+\Gamma_\epsilon q}(1-q) \right], \tag{4.11}$$

where $n(\epsilon, r, z)$ is the number density (per unit volume and unit energy) of photons of the ISRF, with energy ϵ, $\gamma = E/m_e$ is the relativistic factor of the electrons and positrons and $\Gamma_\epsilon = 4\epsilon\gamma/m_e$.

In the Thomson limit (valid for low electron energies), they reduce to the particularly compact expression

$$b_{\rm ICS} = \frac{4\,c\;\sigma_{\rm T}}{3\,m_e^2}\, E^2 \int_0^\infty d\epsilon\;\epsilon\; n(\epsilon, r, z) \qquad \text{[Thomson limit]}, \tag{4.12}$$

which makes the energy density in the photon bath $u_{\rm ISRF} = \int d\epsilon\, \epsilon\, n(\epsilon, r, z)$ apparent.

The ICS energy losses are *proportional to* E^2 (as evident in the Thomson expression, but also in equation 4.11 noting that $4\gamma^2 q$ is the dominant piece at the numerator) for small E. For large E, the dependence softens.

- **Energy losses by synchrotron emission** are described by

$$b_{\rm syn} = \frac{4\,c\;\sigma_{\rm T}}{3\,m_e^2}\, E^2\, \frac{B^2}{8\pi} \tag{4.13}$$

where B is the strength of the magnetic field. This formula is in close analogy to the one for ICS losses: the integral term in equation 4.12 and the B^2 term in equation 4.13 correspond to the energy density in the photon bath and in the magnetic field respectively. In particular, synchrotron energy losses are also *proportional to* E^2.

In figure 4.3, left panel, we plot the different energy losses discussed above, at the location of the Earth. The different dependences on the $e^{\pm}$ energy are clearly shown. Hence, the dominant process in the different energy ranges are, in order, ionization (including Coulomb), bremsstrahlung, ICS and synchrotron. In figure 4.2, we plot the total energy loss function in

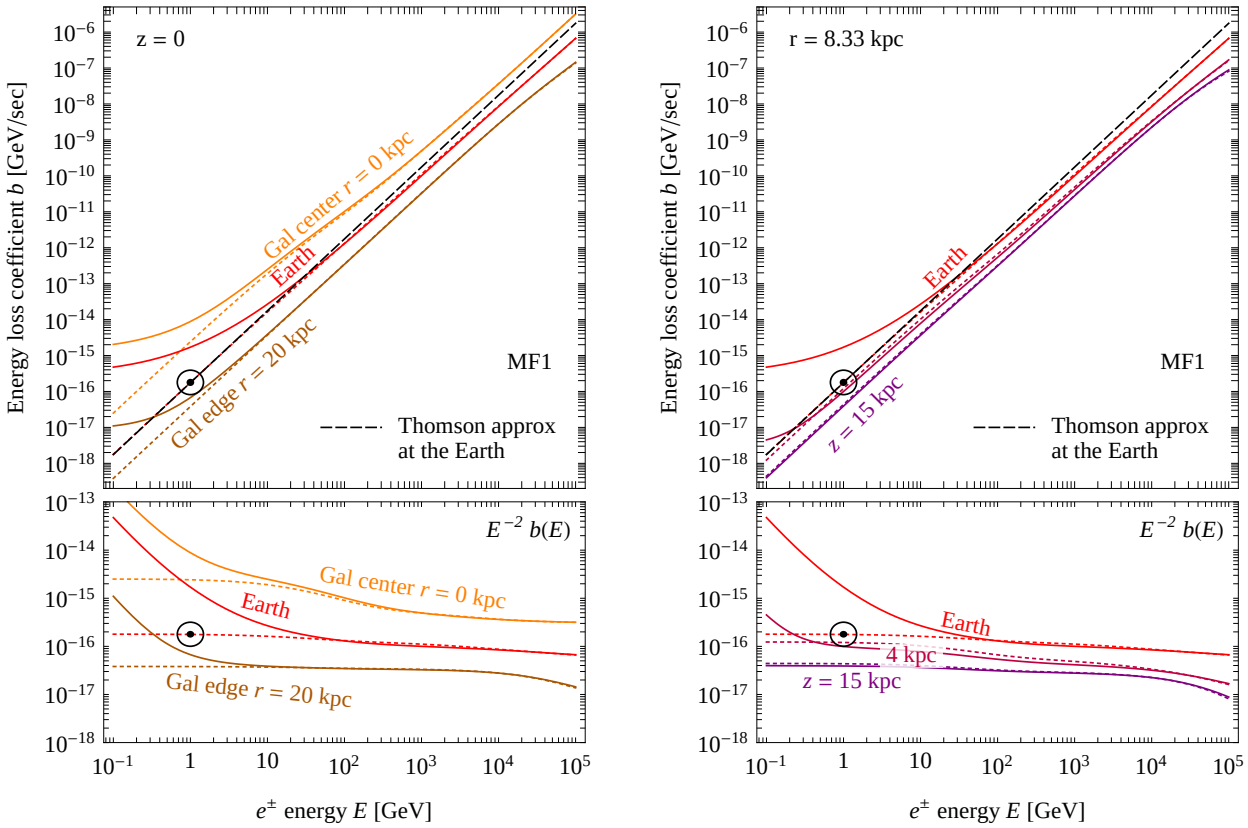

Figure 4.2: **Energy loss function for electrons and positrons in the Milky Way.** Left panel: in the galactic disk ($z = 0$), at several locations along the radial coordinate r. Right panel: above (or below) the location of the Earth along the coordinate z. Here the magnetic field model MF1 has been fixed for definiteness. The circled dot identifies the constant value sometimes adopted. The dotted colored lines are the same function before the improvements listed in section 4.3.1. This figure replaces the analogous one (figitgure 5) of [9].

several locations in the galactic plane (left panel) and at several galactic altitudes at the location of the Earth (right panel). We compare it with the previous version of the same function not including the improvements listed at the beginning of this section (dashed colored lines). The main modification is apparent at low energies and it is due to the inclusion of bremsstrahlung, ionization and Coulomb losses. Being related to the presence of gas, it disappears at the locations outside of the galactic disk.

The modifications due to the use of the new ISRF is minimal and mostly concentrated at low energies, so it is hidden by the dominant bremsstrahlung, ionization and Coulomb losses in most cases except well outside of the plane where the absence of gas makes it indeed visible (see the slight difference between the solid and dashed purple lines corresponding to $z = 15$ kpc in the right panel). While in figure 4.3 left and in figure 4.2 we have chosen the MF1 for definiteness, in figure 4.3 right we explore the impact of changing the magnetic field model. Not surprisingly, in $(r, z) = (3, 0)$ kpc the synchrotron energy losses are larger than at $(r, z) = (8.33, 1)$ kpc, and the ordering reflects the intensity of the magnetic field in the corresponding model (see figure 4.1).

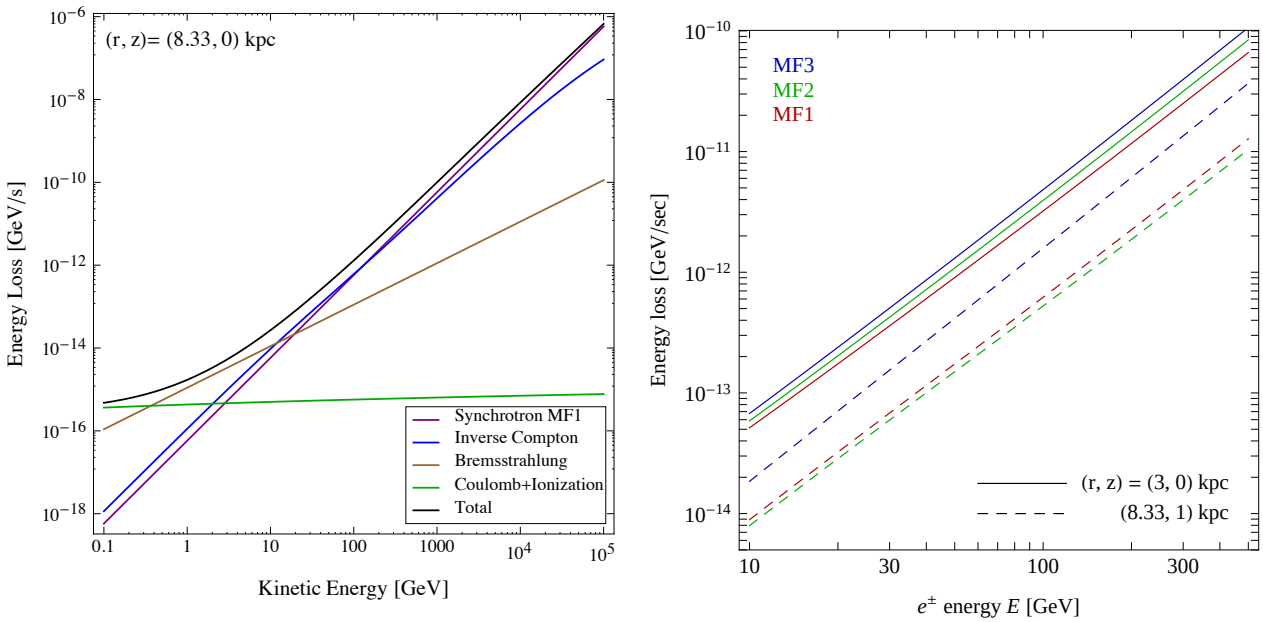

Figure 4.3: Left panel: the **different processes** contributing to the energy loss function, at the location of the Earth. Right panel: the dependence of the energy loss coefficient function on the **choice of magnetic field model**, in two locations.

4.3.2 Revised halo functions for $e^{\pm}$ in the Galaxy

Now, we employ this improved energy loss function to compute the halo functions for electrons and positrons in the Galaxy. We recall that the number density $f(E, r, z)$ of electrons or positrons at the position (r, z) per unit energy E is obtained solving the steady-state diffusion-loss differential equation 2.66, in which we can neglect convection and second-order Fermi acceleration, since we are dealing with $e^{\pm}$,

$$-\mathcal{K}_0 \left(\frac{E}{\mathrm{GeV}}\right)^{\delta} \nabla^2 f - \frac{\partial}{\partial E}\Big(b(E, r, z)\, f\Big) = Q(E, r, z). \tag{4.14}$$

The first term is expressed in terms of the diffusion parameters described in section 2.4.4. As for antiprotons from DM (see section 3.3.1), the source term Q reads

$$Q = \begin{cases} \dfrac{1}{2}\left(\dfrac{\rho}{M_{\mathrm{DM}}}\right)^2 \displaystyle\sum_f \langle\sigma v\rangle_f \frac{dN^f_{e^{\pm}}}{dE} & \text{(annihilation)} \\ \left(\dfrac{\rho}{M_{\mathrm{DM}}}\right) \displaystyle\sum_f \Gamma_f \frac{dN^f_{e^{\pm}}}{dE} & \text{(decay)} \end{cases} . \tag{4.15}$$

The function $dN_{e^{\pm}}/dE$ is the electrons or positron spectrum from DM annihilations in a given final state channel f.

The solution for f, or rather for the energy spectrum of electrons or positrons $d\Phi_{e^{\pm}}/dE$, can be cast [9] in terms of a convolution of the injection spectrum $dN_{e^{\pm}}/dE$ with the *generalized halo functions* $I(E, E_s, r, z)$, which are essentially the Green's functions from a source energy

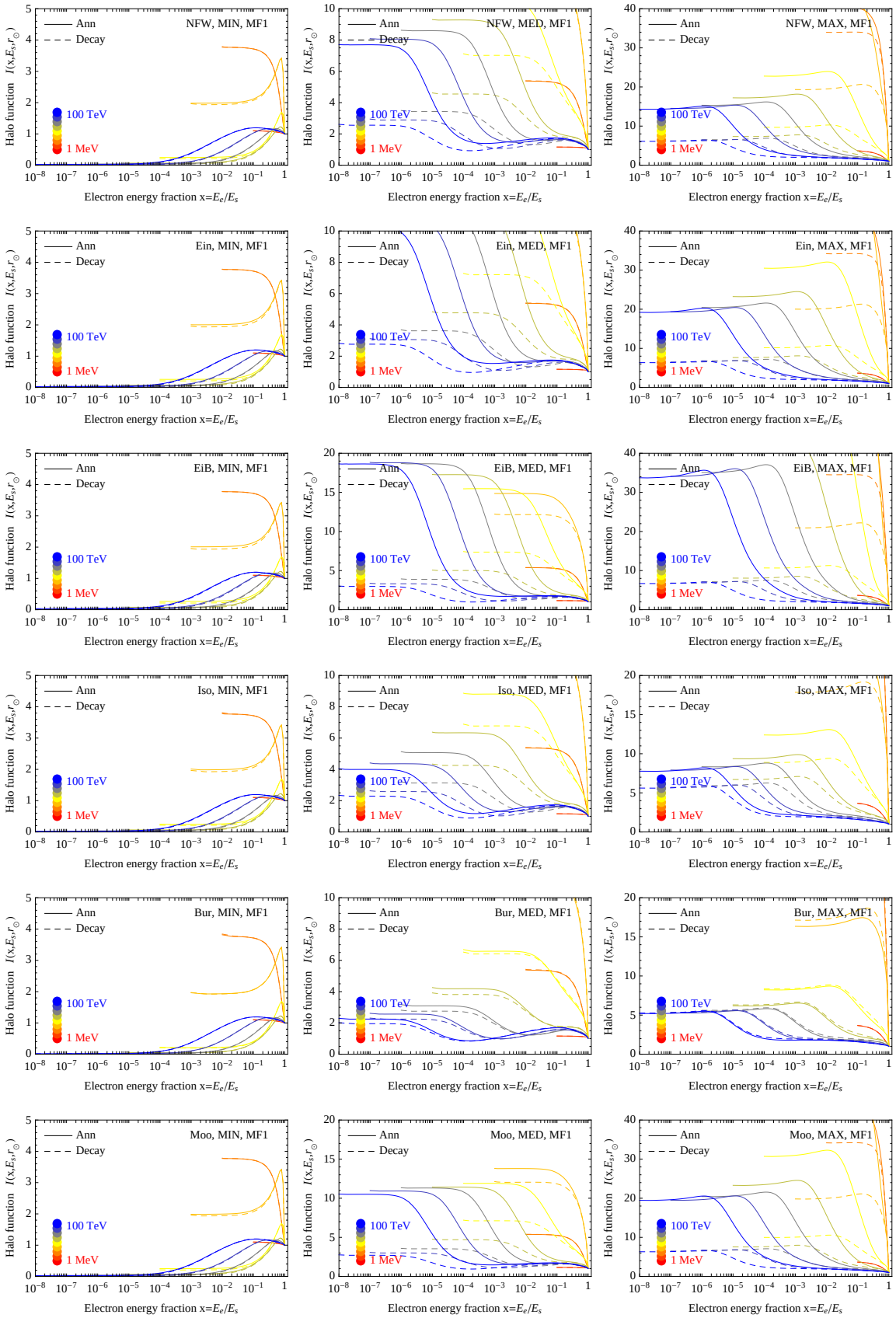

Figure 4.4: **Generalized halo functions for electrons or positrons**, for several different values of the injection energy E_s (color coded). This figure replaces the analogous one (figure 6) of [9].

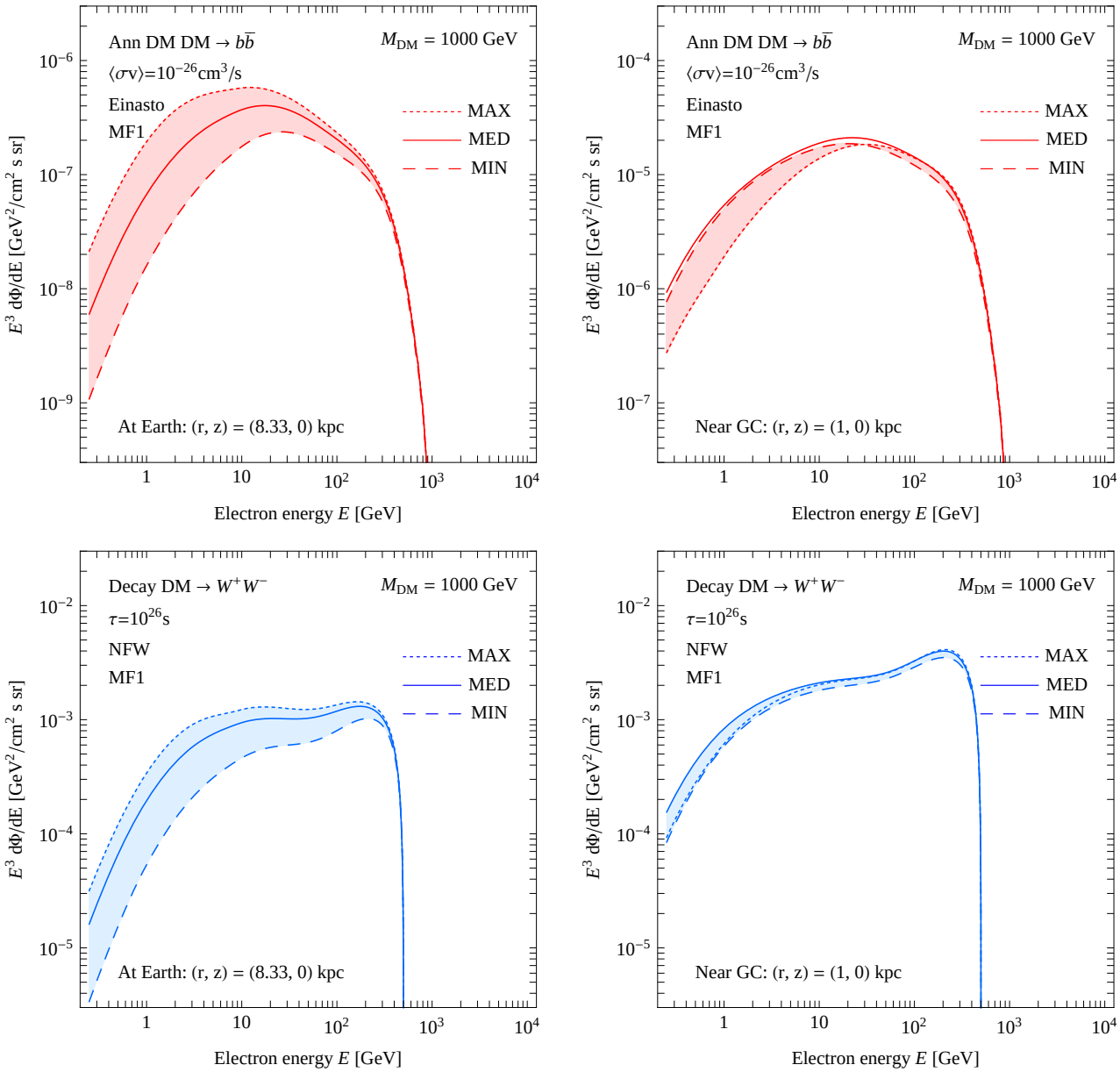

Figure 4.5: **Fluxes of electrons or positrons, after propagation**, for the case of annihilations (top row) and decay (bottom row), shown at two different locations.

E_s to the energy E:

$$\frac{d\Phi_{e^\pm}}{dE}(E,r,z) \equiv \frac{c}{4\pi} f(E,r,z) =$$

$$= \frac{c}{4\pi\, b(E,r,z)} \begin{cases} \frac{1}{2}\left(\frac{\rho}{M_{\rm DM}}\right)^2 \sum_f \langle\sigma v\rangle_f \int_E^{M_{\rm DM}} dE_s \frac{dN^f_{e^\pm}}{dE}(E_s)\cdot I(E,E_s,r,z) & \text{(annihilation)} \\ \left(\frac{\rho}{M_{\rm DM}}\right) \sum_f \Gamma_f \int_E^{M_{\rm DM}} dE_s \frac{dN_{e^\pm}}{dE}(E_s)\cdot I(E,E_s,r,z) & \text{(decay)} \end{cases} \tag{4.16}$$

The halo functions I, which replace those in [9], are available on the website [285], in the format `ElectronHaloFunctGalaxyAnn[halo,propag,MF][log10x,log10Es,r,z]` (and analogously `ElectronHaloFunctGalaxyDec` for decay) where $x = E/E_s$. These functions, particularized at the location of the Earth, are plotted in figure 4.4 for reference. Comparing with the equivalent functions presented in [9], the main difference consists in the evident rise towards small values of the electron energy fraction x,[2] which is the direct consequence of the additional, low-energy losses. For small injection energies (warmer colors), the rise occurs 'early' while moving towards small x, consistently with the fact that the new losses are already relevant. For large injection energies (cold colors) the rise occurs at small x when $E \sim 10$ GeV (the regime at which the new losses set in). For MIN the rise does not happen for large injection energy, as $e^{\pm}$ are not efficiently confined on the characteristic scale of the energy losses. At a location closer to the Galactic Center (not plotted), where energy losses are more relevant, the rise is present.

In figure 4.5 we show the electron spectra, for a few cases. These are in direct correspondence with the left panels of figure 13 of [9]. The differences amount to a factor of a few, up to almost one order of magnitude, especially at low energies (where indeed the new losses are effective). In the right panels of figure 4.5 we show the spectra computed in a location closer to the GC. It is curious to note that, in this case, the fluxes do not follow the intuitive normalization ordering MIN $\rightarrow$ MED $\rightarrow$ MAX; in fact, MAX yields the most suppressed flux. This is just a consequence of the relative importance of the various propagation parameters which is different in the Earth's local neighborhood with respect to that location. Indeed, MIN, MED and MAX are determined as the sets that minimize/maximize the fluxes *at Earth*.

4.3.3 Synchrotron halo functions

In this subsection we want to obtain the *generalized halo functions for synchrotron emission*. We first review the basics of synchrotron emission and then come to the definition of the functions we need.

The synchrotron power (in erg s^{-1} Hz^{-1}) emitted in a certain frequency ν by an isotropic distribution of relativistic electrons with energy E in a uniform magnetic field is

$$\mathcal{P}_{\rm syn}(\nu, E, \alpha) = \sqrt{3}\,\frac{e^3\,B\sin\alpha}{m_e\,c^2}F(x) \tag{4.17}$$

with

$$x = \nu/\nu_c', \qquad \nu_c' = \frac{1}{2}\nu_c \sin\alpha, \qquad \nu_c = \frac{3}{2\pi}\frac{e}{m_e c}B\gamma^2.$$

Here B is the strength of the magnetic field, α the angle between the line of sight and the magnetic field direction and $\gamma = E/m_e$ the Lorentz factor of the electron or positron. The synchrotron kernel $F(x)$ is

$$F(x) = x\int_x^\infty K_{5/3}(x')dx'$$

where K_n is the modified Bessel function of the second kind of order n. In presence of a randomly oriented magnetic field, which is the case of our interest, the synchrotron power has

[2] The functions are defined down to the value of x corresponding to $E = 1$ MeV, to avoid the regime of highly non-relativistic electrons.

to be averaged over the pitch angle μ:

$$\mathcal{P}_{\rm syn}(\nu, E) = \frac{1}{2}\int_0^{\pi} d\mu\, \sin(\mu)\, \mathcal{P}_{\rm syn}(\nu, E, \mu) \tag{4.18}$$

For relativistic electrons ($\gamma \geq 2$) this corresponds to [**?**]:

$$\mathcal{P}_{\rm syn}(\nu, E) = 2\sqrt{3}\,\frac{e^3\,B}{m_e c^2} y^2 \left[K_{4/3}(y)K_{1/3}(y) - \frac{3}{5}y\Big(K_{4/3}(y)^2 - K_{1/3}(y)^2\Big)\right] \tag{4.19}$$

with $y = \nu/\nu_c$. Integrating this quantity over ν yields the total power emitted by an electron of energy E in all frequencies, i.e. equation 4.13.

Next, the synchrotron emissivity has to be computed convolving the synchrotron power in equation 4.19 with the number density of electrons per unit energy $f(E, r, z)$ (in cm^{-3} GeV^{-1}) discussed in section 4.3.2

$$j_{\rm syn}(\nu, r, z) = 2\int_{m_e}^{M_{\rm DM}(/2)} dE\; \mathcal{P}_{\rm syn}(\nu, E)\, f(E, r, z) \tag{4.20}$$

where the minimal and maximal energies of the emitting electrons are determined by the electron mass and the mass of the DM particle. The '/2' notation applies to the decay case. The overall factor 2 takes into account that, besides the electrons, an equal population of positrons radiates.

Finally, the observable in which we are interested is the intensity $\mathfrak{I}$ of the synchrotron emission (in erg cm^{-2} s^{-1} Hz^{-1} sr^{-1}) from a certain direction of observation. This is obtained by integrating the emissivity of equation 4.20 along the line-of-sight. Schematically:

$$\mathfrak{I}(\nu, b, \ell) = \int_{\rm l.o.s.} ds\, \frac{j_{\rm syn}(\nu, r, z)}{4\pi} \tag{4.21}$$

where it is intended that a point in (r, z) is identified by the the parameter s along the line of observation individuated by the galactic latitude b and longitude ℓ: $r(s, \ell, b), z(s, \ell, b)$. Recollecting equation 4.21 and equation 4.16, the synchrotron intensity $\mathfrak{I}$ at a given frequency ν and for given galactic coordinates (b, ℓ) can be cast as:

$$\mathfrak{I}(\nu, \ell, b) = \frac{r_\odot}{4\pi}\begin{cases} \dfrac{1}{2}\left(\dfrac{\rho_\odot}{M_{\rm DM}}\right)^2 \displaystyle\int_{m_e}^{M_{\rm DM}} dE_s \sum_f \langle\sigma v\rangle_f \frac{dN^f_{e^\pm}}{dE}(E_s)\; I_{\rm syn}(E_s, \nu, \ell, b) & \text{(annihilation)} \\ \left(\dfrac{\rho_\odot}{M_{\rm DM}}\right) \displaystyle\int_{m_e}^{M_{\rm DM}/2} dE_s \sum_f \Gamma_f \frac{dN^f_{e^\pm}}{dE}(E_s)\; I_{\rm syn}(E_s, \nu, \ell, b) & \text{(decay)} \end{cases} \tag{4.22}$$

with the *generalized synchrotron halo function* $I_{\rm syn}(\nu, E_s, \ell, b)$ defined as

$$I_{\rm syn}(E_s, \nu, \ell, b) = \int_{\rm l.o.s.} \frac{ds}{r_\odot}\left(\frac{\rho(r, z)}{\rho_\odot}\right)^\eta\; 2\int_{m_e}^{E_s} dE \frac{\mathcal{P}_{\rm syn}(\nu, E)}{b(E, r, z)}\; I(E, E_s, r, z), \tag{4.23}$$

where $\eta = 1, 2$ for the decay or annihilation cases respectively and again implicitly $r(s, \ell, b)$, $z(s, \ell, b)$. The units of $I_{\rm syn}$ are erg/Hz. The synchrotron halo functions $I_{\rm syn}$ are available on the website [285], in the format `ISynAnnI[halo,propag,MF][log10Es,log10ν,ℓ,b]` (and

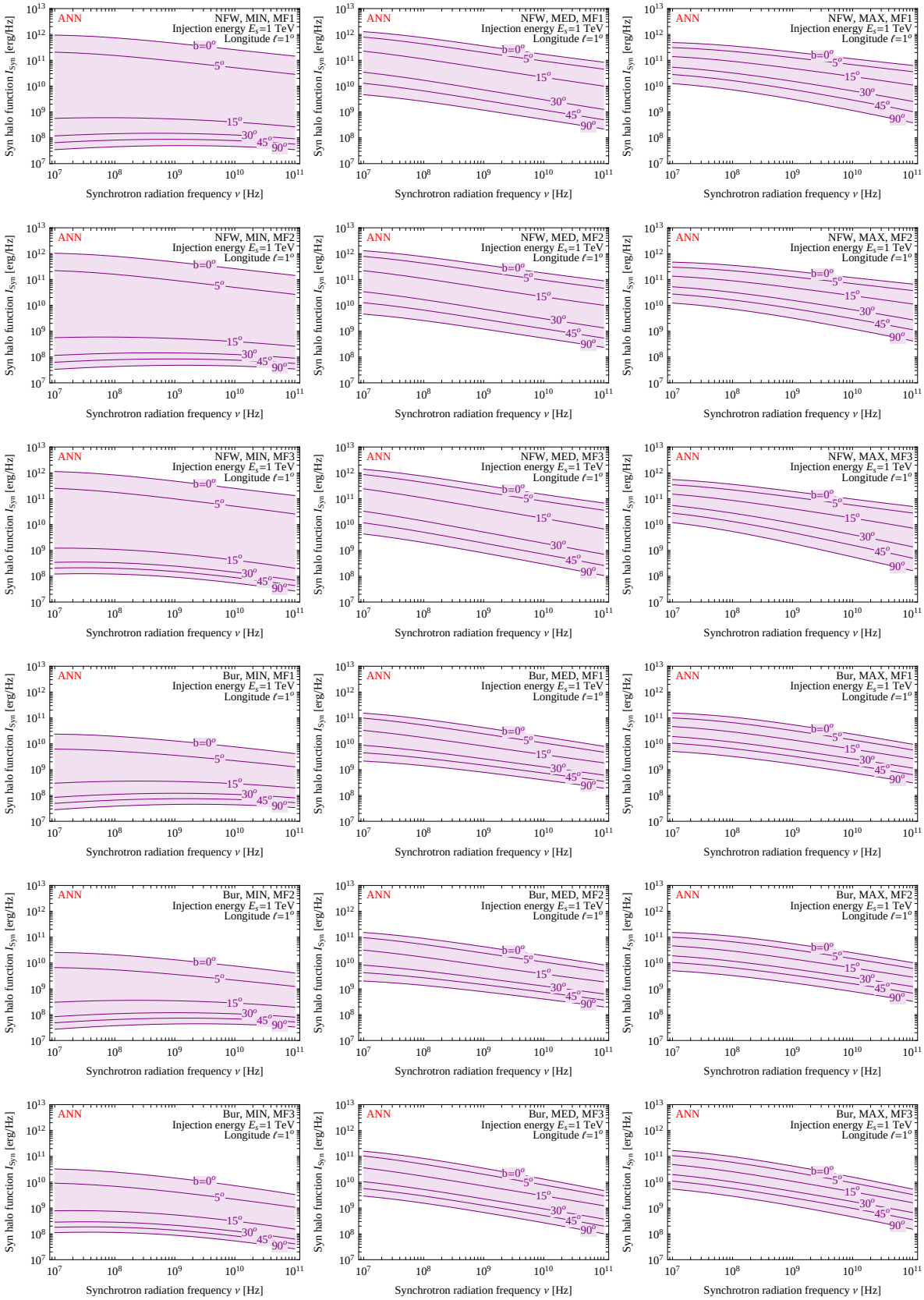

Figure 4.6: **Generalized synchrotron halo functions**, for the DM annihilation case. The upper 9 panels correspond to an NFW profile, the lower 9 to Burkert; the columns correspond to a fixed propagation model, the rows to a fixed magnetic field model.

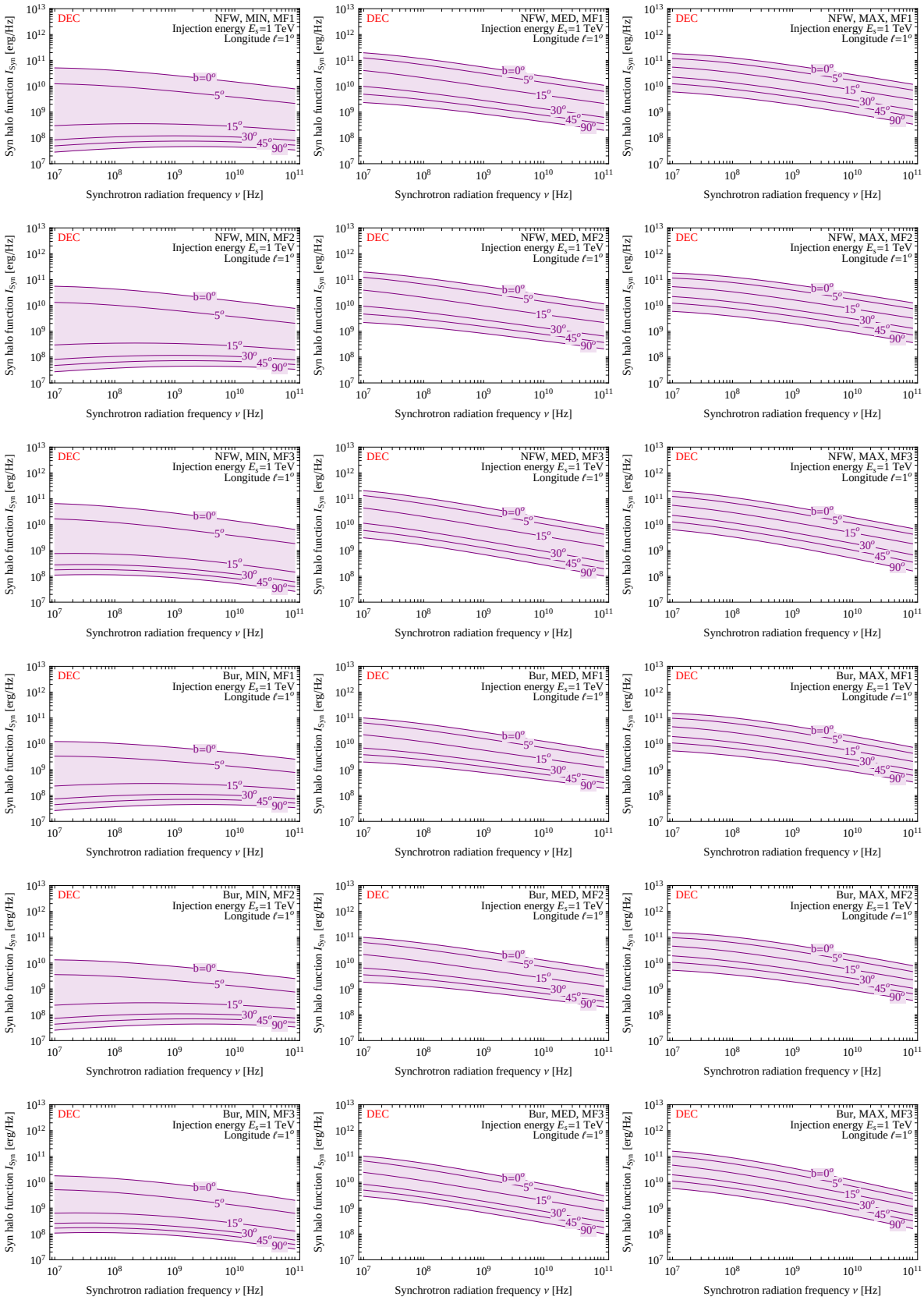

Figure 4.7: **Generalized synchrotron halo functions**, for the DM decay case.

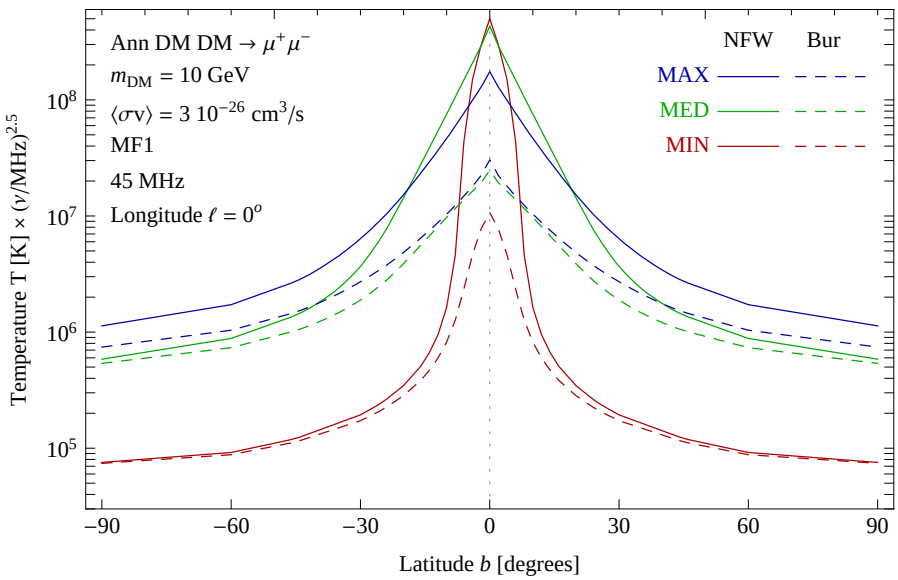

Figure 4.8: **Synchrotron signal** (temperature) at 45 MHz, plotted against the galactic latitude, for several choices of DM profile and propagation scheme.

analogously `ISynDecI` for decay). They are also plotted, for reference, in figure 4.6 for the annihilation case and in figure 4.7 for the decay case.

The last step needed in order to make contact with actual radio surveys consists in expressing the synchrotron signal in terms of brightness temperature $T(\nu)$ (in K) which is defined as:

$$T(\nu) = \frac{c^2\,\mathfrak{I}(\nu)}{2\,\nu^2\,k_B} \tag{4.24}$$

with k_B the Boltzmann constant. In figure 4.8, we plot such quantity for a few different choices of profiles and propagation parameters. Although a comparison with previous results (e.g. in [250] and [255]) is not possible in full details, we have checked that, removing our additional refinements, we recover those previous results in most cases [3].

4.3.4 Bremsstrahlung halo functions

In this subsection, in turn, we want to obtain the *generalized halo functions for bremsstrahlung emission*. The computation follows quite closely the one for synchrotron in the previous subsection, using also the formalism for bremsstrahlung spelled out in section 4.3.1. We summarize here the main ingredients for completeness.

In close analogy with equation 4.22, the bremsstrahlung differential flux (in GeV^{-1}cm^{-2}s^{-1}sr^{-1})

[3] We cannot however fully reproduce the dependence on the choice of profile in [255]: we find that the synchrotron signal is independent on the choice of profile at large latitudes (as we expect from the self-similarity of such profiles at large radii) while their plot show a sizable residual difference.

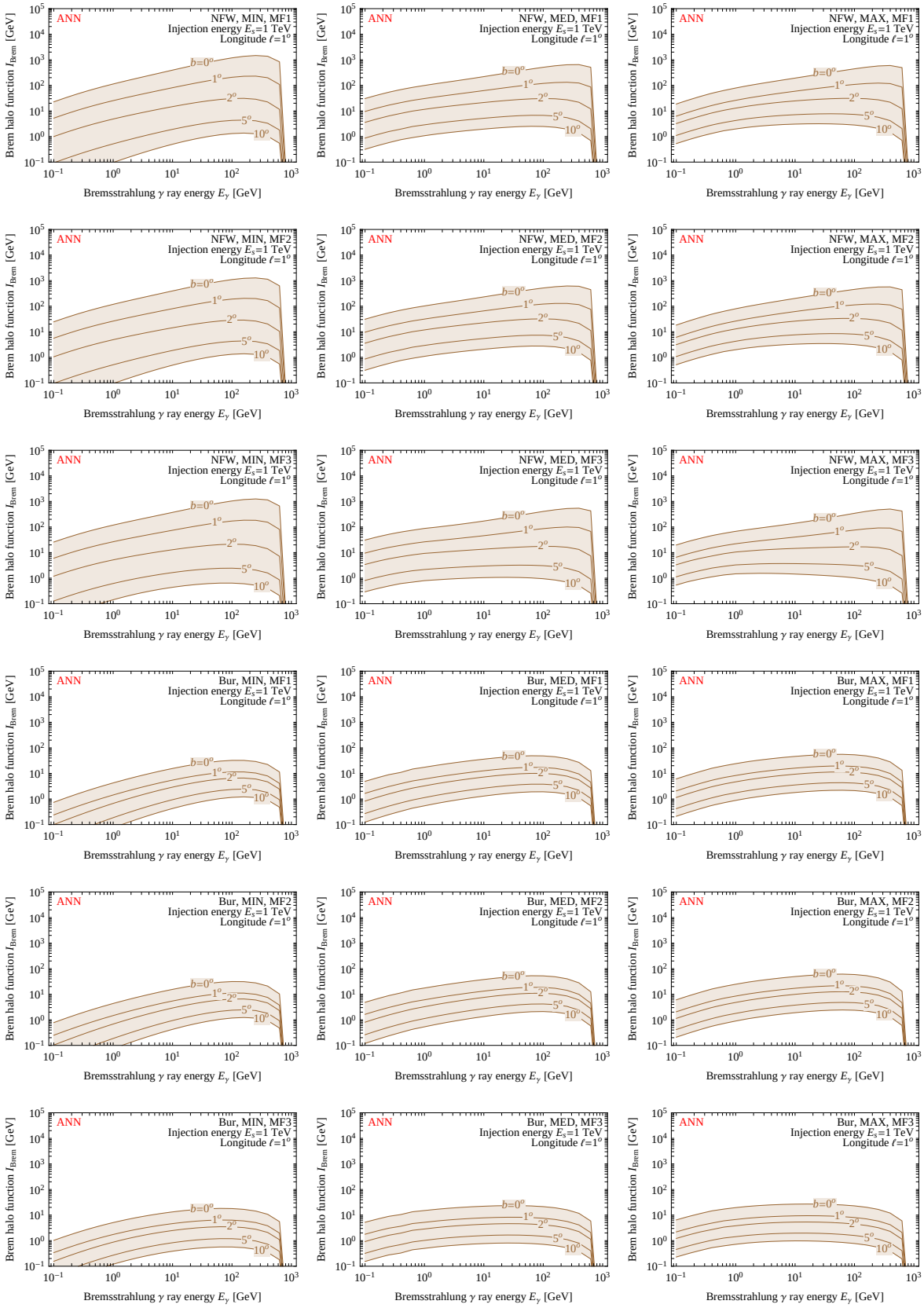

Figure 4.9: **Generalized bremsstrahlung halo functions**, for the DM annihilation case. Analogously to fig. 4.6, the upper 9 panels correspond to an NFW profile, the lower 9 to Burkert; the columns correspond to a fixed propagation model, the rows to a fixed magnetic field model.

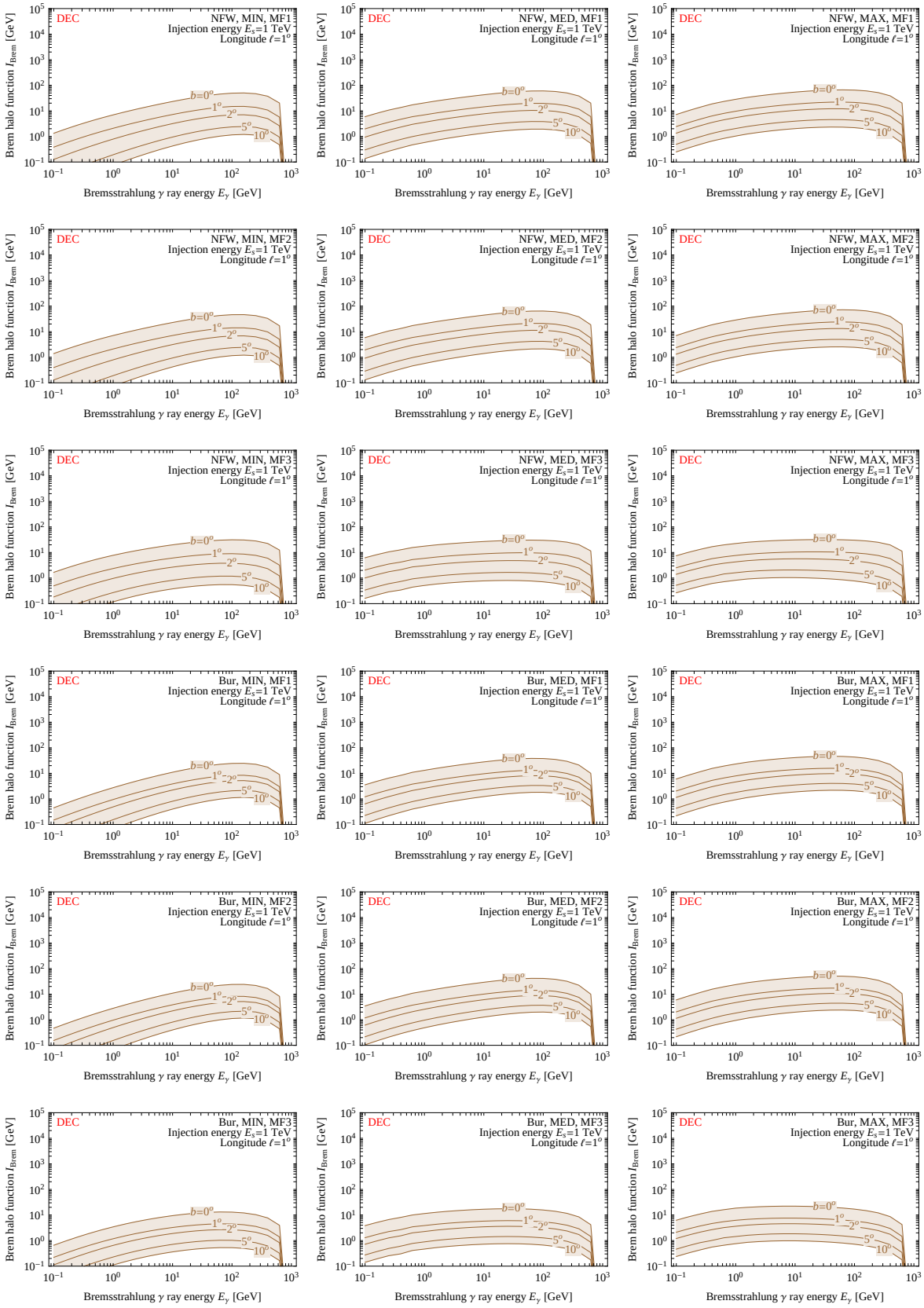

Figure 4.10: **Generalized bremsstrahlung halo functions**, for the DM decay case.

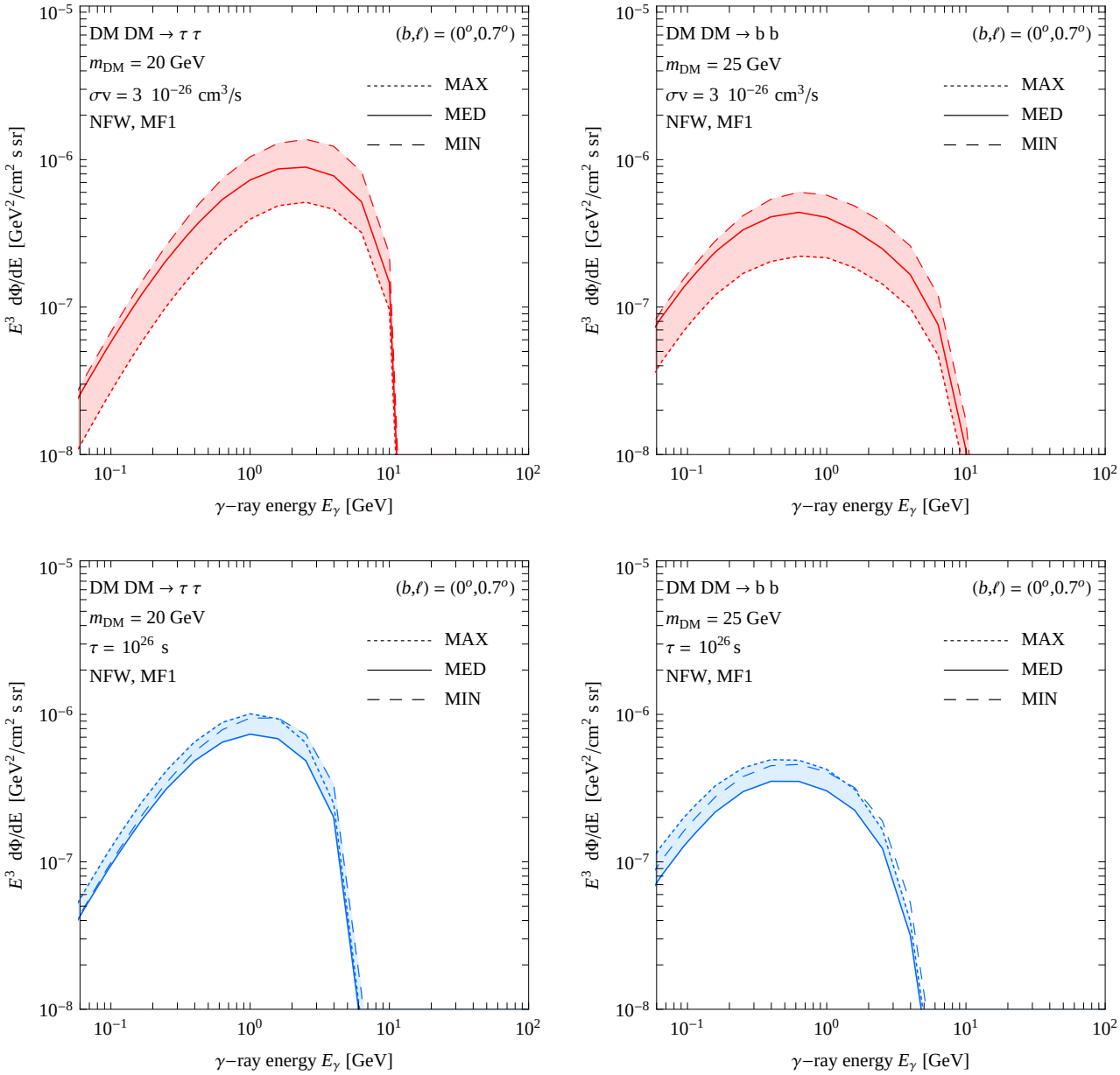

Figure 4.11: **Bremsstrahlung γ-ray fluxes** for the case of annihilations (top row) and decay (bottom row), shown for two different channels.

reads:

$$\frac{d\Phi_{\mathrm{brem}\gamma}}{dE_\gamma\, d\Omega} = \frac{1}{E_\gamma^2}\frac{r_\odot}{4\pi}\begin{cases} \dfrac{1}{2}\left(\dfrac{\rho_\odot}{M_{\mathrm{DM}}}\right)^2 \displaystyle\int_{m_e}^{M_{\mathrm{DM}}} dE_{\mathrm{s}} \sum_f \langle\sigma v\rangle_f \frac{dN^f_{e^\pm}}{dE}(E_{\mathrm{s}})\, I_{\mathrm{brem}}(E_{\mathrm{s}}, E_\gamma, \ell, b) & \text{(annihilation)} \\ \dfrac{\rho_\odot}{M_{\mathrm{DM}}} \displaystyle\int_{m_e}^{M_{\mathrm{DM}}/2} dE_{\mathrm{s}} \sum_f \Gamma_f \frac{dN^f_{e^\pm}}{dE}(E_{\mathrm{s}})\, I_{\mathrm{brem}}(E_{\mathrm{s}}, E_\gamma, \ell, b) & \text{(decay)} \end{cases} \tag{4.25}$$

where now (in analogy with equation 4.23) the *generalized halo function for bremsstrahlung*

$I_{\rm brem}\ (E_{\rm s}, E_\gamma, \ell, b)$, which has units of GeV, is defined as

$$I_{\rm brem}(E_{\rm s}, E_\gamma, \ell, b) = 2\, E_\gamma \int_{\rm l.o.s.} \frac{ds}{r_\odot} \left(\frac{\rho(r,z)}{\rho_\odot}\right)^\eta \int_{m_e}^{E_{\rm s}} dE\, \frac{\mathcal{P}_{\rm brem}(E_\gamma, E, r(s,\theta))}{b(E, r(s,\theta))}\, I(E, E_{\rm s}, r, z). \quad (4.26)$$

The bremsstrahlung power consists in

$$\mathcal{P}_{\rm brem}(E_\gamma, E, \vec{x}) = c\, E_\gamma \sum_i n_i(\vec{x}) \frac{d\sigma_i(E_\gamma, E)}{dE_\gamma} \quad (4.27)$$

where n_i are the number densities of the gas species and the bremsstrahlung cross-section was given in equation (4.6). The bremsstrahlung halo functions $I_{\rm brem}$ are again available on the website [285], in the format `IBremAnnI[halo,propag,MF][log10Es,log10Eγ,ℓ,b]` (and analogously `IBremDecI` for decay). They are plotted in figures 4.9 and 4.10 (annihilation and decay cases), for reference.

In figure 4.11 we plot the resulting bremsstrahlung line-of-sight γ-ray fluxes, for a few cases. The agreement with previous calculations (notably [260]) has been verified. We also cross checked with fully numerical computations done using `GammaSky` [167, 288]. While the spectral shape is in very good agreement, we find a difference in overall normalization of the fluxes along lines of sight passing close to the Galactic Center. This is due to the fact that `GammaSky`, like `GalProp`, corrects the bremsstrahlung emissivities by adjusting the normalization of the gas densities in each galactocentric ring, in particular close to the GC (see [289], and [260] for a short discussion). We decide to instead use consistently the same maps for energy losses and bremsstrahlung emission.

4.4 Summary

In summary, we have here focussed on the secondary radiations from electrons and positrons and presented several upgraded and new results. The upgradings concern: i) an improved energy loss function which fully includes low energy losses (Coulomb, ionization and bremsstrahlung) and ii) the revised halo functions for electrons and positrons. The new results consist in: iii) the synchrotron halo functions (section ; iv) the bremsstrahlung halo functions. All the results are provided in numerical form on the PPPC4DMID website [285].

These state-of-the-art tools allow to compute the secondary radiation signal (synchrotron, bremsstrahlung and Inverse Compton) from any arbitrary DM weak-scale model and will be precious and hopefully instrumental in the current era of precision DM indirect searches.

Chapter 5

The Galactic Center excess: charged particles at their best

5.1 Introduction

We now present a concrete application of the multi-messenger approach of charged CR, using antiprotons presented in chapter 3 as well as secondary emissions from electrons and position investigated in chapter 4.

Due to the very high density of DM particles that is predicted in the inner part of the Galaxy, the GC region is expected to be one of the brightest sources of radiation coming from DM annihilation or decay. For this reason, the very accurate gamma-ray maps and spectra provided by the Fermi-LAT collaboration have been investigated in detail by the DM community, in order to find some hint of an excess with respect to the expected emission from astrophysical processes. The complexity of the region and the abundance of sources make however the task of separating the emission by DM annihilation/decay from backgrounds extremely challenging. In spite of that, several authors have reported since 2009 the detection of a gamma-ray signal from the inner few degrees around the GC [290, 261]. Its spectrum and morphology are claimed to be compatible with those expected from annihilating DM particles: to fix the ideas, we recall the results of the most recent analysis [262], which confirms the presence of this excess at an incredibly high level of significance (if taken at face value) and finds this signal to be best fit by 31-40 GeV DM particles distributed according to a (contracted) NFW profile and annihilating into $b\bar{b}$ with $\langle\sigma v\rangle = 1.4 \div 2 \times 10^{-26}$ cm^3/s. These results have understandably spurred an intense model building activity from the community [291], possibly because the main features of this potential signal are very close to widespread expectations (GC origin, close-to-thermal annihilation cross-section, 'conventional' mass and annihilation channel, matching to one of the most popular DM distribution profiles...). Some models may also provide an interesting connection with other recent astroparticle anomalies such as the Dama/Libra and Integral signals [292]. In the light of these points, it is interesting and timely to assess the robustness of the DM claims against associated constraints, as we set out to do.

Two important cautionary remarks are in order. Firstly, one should not forget that, in very general terms, the identification of an 'excess' strongly relies on the capability of carefully assessing the background over which the excess is supposed to emerge. As we already implicitly suggested above, the claim under scrutiny constitutes no exception, quite the contrary. The extraction of the residuals strongly relies on the modeling of the diffuse gamma-ray background (in particular the one publicly made available by the Fermi collaboration) as well as on ad-

ditional modeling of astrophysical emissions, e.g. from FERMI bubbles, isotropic component, unresolved point sources, molecular gas... While this is probably the best that can be done, it is not guaranteed to be (and in general is not expected to be) the optimal strategy.

Secondly, one should not forget that there might be alternative astrophysical explanations for the excess. A population of milli-second pulsars has been extensively discussed since the beginning [293], as well as the possibility of a spectral break in the emission of the central Black Hole [294]. More recently, the possibility has been suggested that isolated injections of charged particles (electrons [295] or protons [296]) sometime in the past, possibly connected with the activity of the central Black Hole, can produce secondary radiation able to account for the anomalous signal. While reproducing with these models all the details of the observed emission might be not easy, they represent plausible and useful counterexamples to the DM interpretation.

Keeping these points in mind, we wish to insist on the tantalizing DM hypothesis and we wish to explore ways to confirm or disprove the result within the DM framework. To this purpose, it is useful to follow a multi-messenger approach. In particular, given the alleged hadronic origin of the signal, it is very useful to analyze the antiproton channel to put constraints on the DM interpretation of such excess. The antiprotons are a precious cross check in this context for several reasons: first of all, as we have seen in chapter 3, in most non-leptophilic WIMP scenarios, the ratio between the exotic signal and the astrophysical background is noticeably large in this channel; moreover, the astrophysical background is known with a considerable level of precision: it depends on the proton flux and, apart from an unavoidable uncertainty on the production cross-section, it is not highly affected by the choice of a diffusion setup among those allowed by light nuclei ratios and other observables. On the other hand, the signal coming from a light DM particle is expected to lie in an energy range where the effect of solar modulation is very important, making the task of identifying an extra signal much more complicated.

Very recently, [232] performed an analysis of antiprotons constraints which partially overlaps with our scope. We will compare in detail our respective results later on; now we can anticipate that we adopt a different strategy concerning solar modulation, we use different tools (in particular we adopt numerical packages such as `DRAGON` and `GammaSky`), and, overall, we find less stringent and more conservative bounds.

Another key issue in the analysis of the GC residuals is the role of the secondary gamma radiation (via Bremsstrahlung and Inverse Compton processes, respectively on the Galactic gas and ambient light) emitted from the particles originating from DM annihilation. Already in [260] it was pointed out that, for the ranges of energies under discussion and for the gas-rich regions close to the GC, Bremsstrahlung is the dominant process of energy loss for the electrons and positrons produced by DM annihilation, resulting in an important contribution to the gamma ray emission. Reference [263] has analyzed the issue in further detail, showing that leptonic channels can actually provide a better fit of the GC excess when the secondary emissions are included. However, that study still implements an approximated framework for energy losses. In the analysis of [261] and [262], the impact of Bremsstrahlung is discussed too, although only at the level of an estimate. Here we go one step further: we employ `DRAGON` [159] and `GammaSky` [167, 288] in order to compute realistic and accurate gamma-ray spectra including all secondary radiations for annihilations into a couple of exemplar leptonic channels. We then compare the spectra with data, as extracted from [262] and determine the best fit regions. This is not intended as a fully thorough analysis (in particular because the data are extracted using templates that do not account for secondary emissions), but it provides a useful example of how important a proper calculation of the full DM gamma-ray emission can be. Moreover, in

the light of the antiprotons constraints disfavoring the hadronic channels, it will be important to assess the viability of the alternative leptonic channels.

5.2 Dark Matter and Cosmic Rays: setups and tools

In this section we briefly present the basic ingredients that we will need for the subsequent computations, both in terms of physics assumptions and in terms of technical tools.

5.2.1 DM Galactic distribution and DM gamma-ray flux

As we have seen in section 1.1.3, the DM distribution ρ in the Galaxy is unknown and is actually source of significant uncertainty. In this specific case, however, it is claimed that the morphology of the GC excess signal allows to determine ρ quite precisely. The best choice, which we also adopt, appears to be a generalized Navarro-Frenk-White profile (gNFW) [4] defined as

$$\rho_{\rm gNFW}(r) = \rho_\odot \left(\frac{r}{r_\odot}\right)^{-\gamma} \left[\frac{1+(r/R_s)^\alpha}{1+(r_\odot/R_s)^\alpha}\right]^{-\frac{(\beta-\gamma)}{\alpha}} , \tag{5.1}$$

with $\rho_\odot = 0.3$ GeV/cm^3, $r_\odot = 8.5$ kpc, $R_s = 20$ kpc, $\alpha = 1$, $\beta = 3$. The parameter γ controls the inner slope of the profile. For the standard NFW profile one has $\gamma = 1.0$, as described in section 1.1.3. The GC excess is better fit by a profile with $\gamma = 1.20$ or 1.26 [262], corresponding to an inner portion steeper than the standard one (i.e. 'contracted'), and therefore we will use these two values in the following.

The prompt gamma-ray differential flux from DM annihilation from a given angular direction $d\Omega$ is given by

$$\frac{d\Phi}{dE_\gamma d\Omega} = \frac{r_\odot}{8\pi}\left(\frac{\rho_\odot}{M_{\rm DM}}\right)^2 \; J \sum_f \langle\sigma v\rangle_f \frac{dN_\gamma^f}{dE_\gamma} , \tag{5.2}$$

with the J-factor

$$J \equiv \int_{\rm l.o.s.} \frac{ds}{r_\odot}\left[\frac{\rho_{\rm gNFW}(r(s,\theta))}{\rho_\odot}\right]^2 , \tag{5.3}$$

and $r(s,\theta) = (s^2 + r_\odot^2 - 2sr_\odot\cos\theta)^{1/2}$, θ being the aperture angle between the direction of the line of sight and the axis connecting the Earth to the GC. We take the input spectra dN_γ^f/dE_γ for a final state f (for instance $b\bar{b}$) from the `PPPC4DMID` [9]. They include ElectroWeak radiations and other refinements with respect to previous computations, although these are mostly not relevant in our case as we are interested in the low DM mass case.

DM also emits secondary gamma-rays, as presented in chapter 4. In practice, we compute here the IC and Brem γ-ray fluxes using `GammaSky`. This numerical package is interfaced to `DRAGON` and computes the line of sight integral of the the gamma-ray, synchrotron and neutrino emissions originating from the interactions of the CRs (output by `DRAGON`) with the interstellar gas, the magnetic field and the diffuse radiation field (from microwaves to UV). Some realistic magnetic field distributions (as described in [167, 288]), gas and interstellar radiation field (ISRF) models are implemented. In particular, the gas and ISRF we use here are the same as in the latest public version of `GalProp` [158]. One should recall that the gas distributions have large uncertainties and are known to map only approximatively the regions close to the GC (see e.g. the discussion in [260]), although in practice this will have a limited impact on our work as we consider areas far enough from the GC.

The code will be published soon; some results obtained with this tool can be found in [167, 288]. For this work we have also cross checked the output of the code, for specific cases, against the semi-analytic calculations mentioned above, finding a very good agreement.

5.2.2 Charged cosmic rays propagation

For propagating charged CR in the Galaxy (electrons, positrons, protons and antiprotons), we use `DRAGON` [159]. The code can perform computations in 2D, 3D isotropic and 3D anisotropic mode; since the impact of three-dimensional structures in the Galaxy is not relevant for the antiproton channel in which we will be mainly interested, we will work in 2D mode. Again, we use the propagation equation 2.66, but this time with the parameters described in table 2.2. The uncertainty on the diffusion parameters produce a modest spread in predictions for the antiproton flux coming from p-p and p-He collisions, while the impact on the flux coming from DM annihilations is much larger.

As pointed out e.g. in [171] (among others), the most relevant uncertainty for this kind of analysis is the thickness of the diffusion zone z_t: a thinner halo corresponds to a much lower signal for the antiprotons coming from DM annihilation, hence one anticipates that the constraints obtained using this setup will be much weaker. In order to investigate more carefully different choices for the thickness of the diffusion zone, we define two more THN-type models with, respectively, $z_t = 2$, 3 kpc.

	γ	ϕ_F^p [GV]	$\chi^2_{\rm min}$/dof (p in [221])
KRA	2.35	0.650	0.462
KOL	1.78/2.45	0.335	0.761
CON	1.62/2.35	0.282	1.602
THK	2.35	0.687	0.516
THN	2.35	0.704	0.639
THN2	2.35	0.626	0.343
THN3	2.35	0.623	0.339

Table 5.1: **Additional parameters needed for the DM signal:** best-fit values of the inner slope of the halo profile the solar modulation potential for protons ϕ_F^p obtained against the proton data in [221] for the 5 standard profiles of [171] as well as of the modified 'thin' setups that we will use in the following.

In order to model the solar modulation effects on charged particles, we continue to use the force-field approximation, presented in equation 2.82. For each propagation setup we fit the solar modulation potential ϕ_F^p against the PAMELA proton data in [221] (we report the resulting values in the table 5.1). We show the result of this analysis in figure 5.1. Since the modulation process – due to relevant drift effects – depends on the charge of the particle (including its sign), we will adopt several strategies for the antiproton Fisk potential discussed in section 5.4.

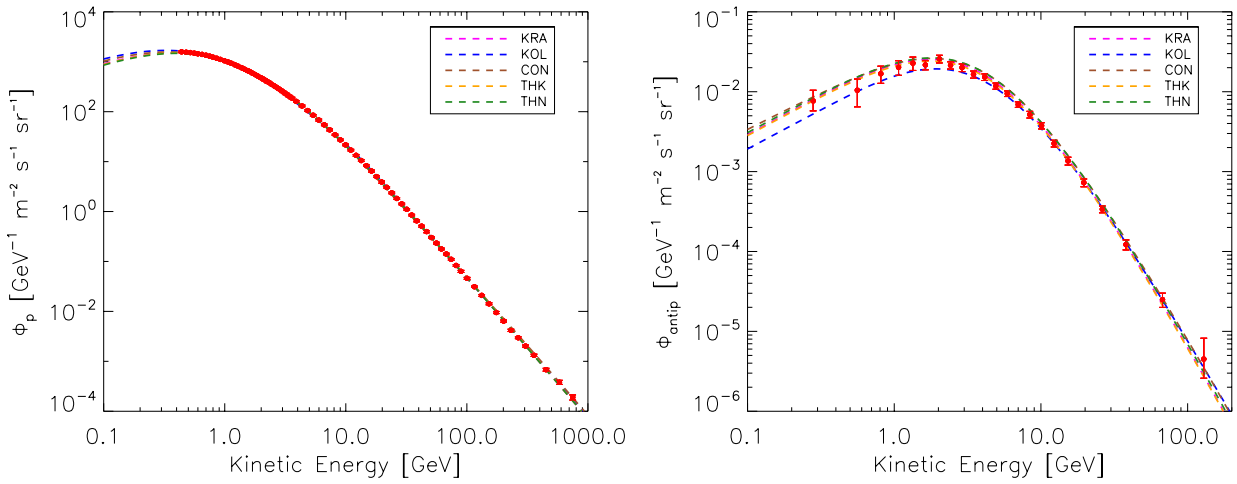

Figure 5.1: **Cosmic-ray proton (left panel) and antiproton (right panel) flux** measured by the PAMELA experiment. We superimpose to the experimental data – taken, respectively, from ref. [221] and ref. [297] – the background estimations obtained using the five propagation models defined in table 2.2. Fitting the proton data we determine the best solar modulation potential ϕ_F^p for each setup (we give the corresponding values in table 5.1). For the purpose of this figure we modulate the $\bar{p}$ flux with the same value.

5.3 Fits of the gamma-rays from DM annihilation in the GC

We focus on two benchmark cases: 100% DM annihilation into $b\bar{b}$ final state and annihilation into leptons in some specific mixtures of flavors as indicated in table 5.2. The latter ones are chosen since, as we will see, they are very close to producing the best fit to the data with which we will be comparing. But since such data depend on the details of the analysis and might change as more refined background subtractions are developed, they can just be considered as typical examples for a leptonic channel.

Following the results of [262], we analyze two different sets of residual data describing the gamma-ray emission associated with DM. In the 'Galactic Center' analysis the region of interest is defined as the region $|b| < 5°$, $|l| < 5°$, while the 'Inner Galaxy' analysis is based on a full-sky fit (masking 1° in latitude around the galactic plane). In the first setup the best-fit value for the slope of the gNFW profile in equation 5.1 turns out to be $\gamma = 1.2$, while the second approach seems to prefer a slightly larger value, $\gamma = 1.26$. In both cases we compute – using the corresponding values of γ – the differential flux from DM annihilation considering one specific l.o.s. with $\theta = 5°$ and compare with the data presented in [262], which are normalized under this assumption [298].

A comment concerning the morphology of the different emissions is now in order. The prompt gamma-ray flux is of course spherically symmetric. For the secondary emissions, in order to have a better insight on their morphology we plot in figure 5.2 –considering the DM annihilation into leptons, where the impact of this kind of emission is larger– the Brems and IC emission as a function of the Galactic latitude (upper-left panel, averaging on $|l| \leqslant 5°$) and longitude (upper-right panel, averaging on $|b| \leqslant 5°$) for two representative values of the

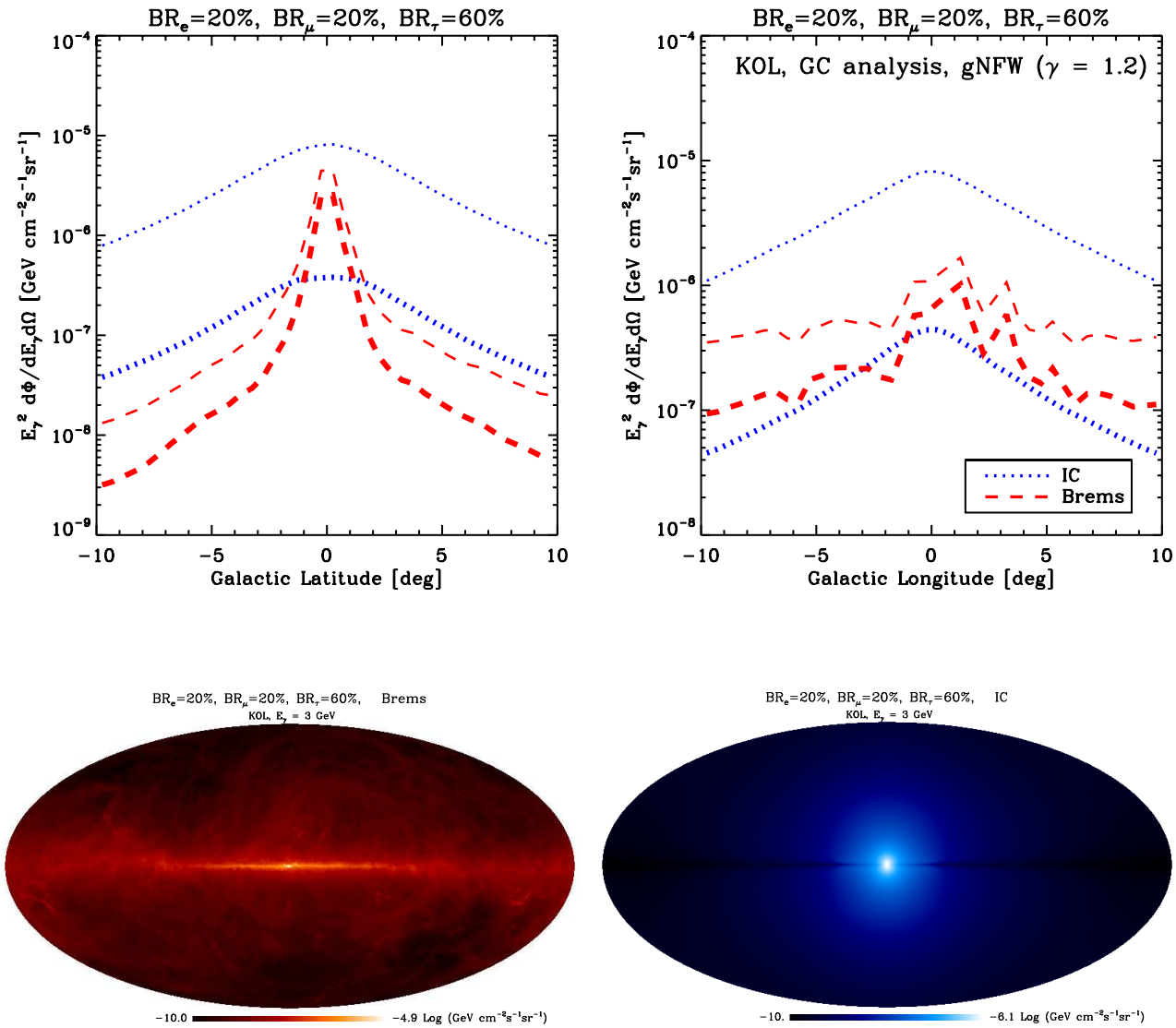

Figure 5.2: Upper panels: latitude- and longitude-dependence of **Brems and IC emissions from DM annihilation** into leptons with $\langle \sigma v \rangle = 3 \times 10^{-26}$ cm^3 s^{-1} and branching ratios as given in table 5.2. We show secondary emissions for $E_\gamma = 3$ GeV (thicker lines) and $E_\gamma = 0.5$ GeV (thinner lines). Lower panels: representative sky maps for Brems (left) and IC (right) emission, for the same choices of parameters.

energy, $E_\gamma = 0.5$ GeV (thinner lines) and $E_\gamma = 3$ GeV (thicker lines). For completeness, we also show in the lower panel of figure 5.2 the corresponding sky maps for $E_\gamma = 3$ GeV. This allows to see that, while the IC emission is to a good approximation spherically symmetric too, the Brems emission, which is correlated with the gas density in the Galactic Plane, is far from being so, not surprisingly. In order to meaningfully compare with the data in [262], derived under the assumption of spherical symmetry, we take the averaged value of the differential flux in a Galactocentric disk with $\theta \in [4.8°, 5.2°]$. A more accurate treatment, which is however out of the scope of our current analysis, would consist in extracting the data by including secondary emission, especially Brems, in the DM template used to fit the residual.

We show the impact of secondary emissions in figure 5.3 for $b\bar{b}$ final state (upper panels), and annihilation into one of the leptonic channels (lower panels). We consider, in each case, two

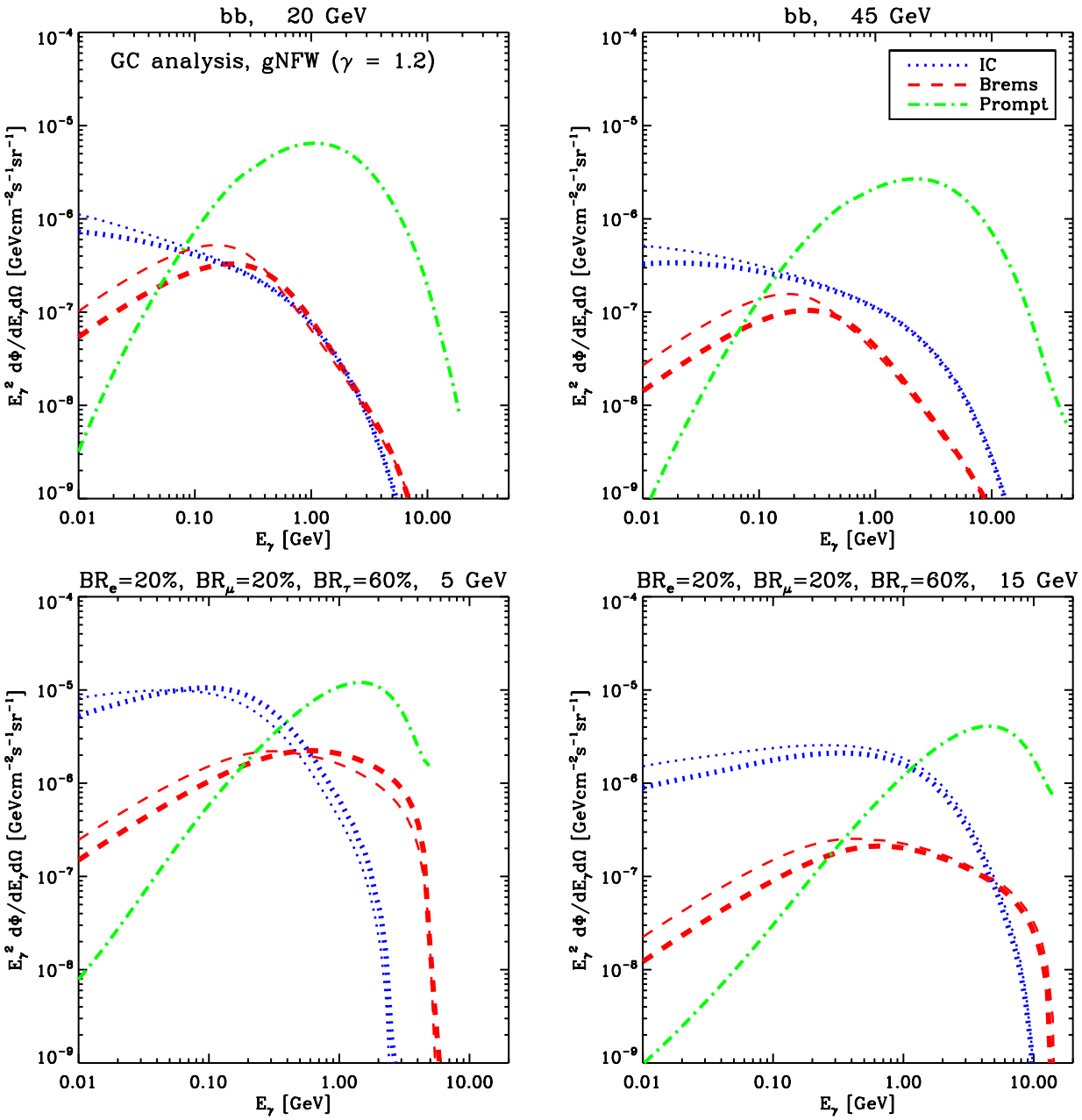

Figure 5.3: **Gamma-ray spectrum from DM annihilation in the GC** We consider 100% DM annihilation into $b\bar{b}$ final state (upper panels) and DM annihilation into leptons with branching ratios as given in table 5.2 (lower panels). We separately show prompt, IC and Brems emissions for four different representative values of the DM mass. We assume a gNFW profile with $\gamma = 1.2$, and we take $\langle \sigma v \rangle = 3 \times 10^{-26}$ cm^3 s^{-1}. Thicker (thinner) lines correspond to the KOL (THN) propagation model.

different values for the DM mass, and we explore two different propagation setups, namely the KOL (thicker lines) and the THN (thinner lines) models. One sees that, as expected, secondary emissions are relevant for the leptonic channel already at an energy corresponding to a fraction of the DM mass. For the $b\bar{b}$ channel, instead, secondary emissions affect more marginally the spectrum and at smaller energies.

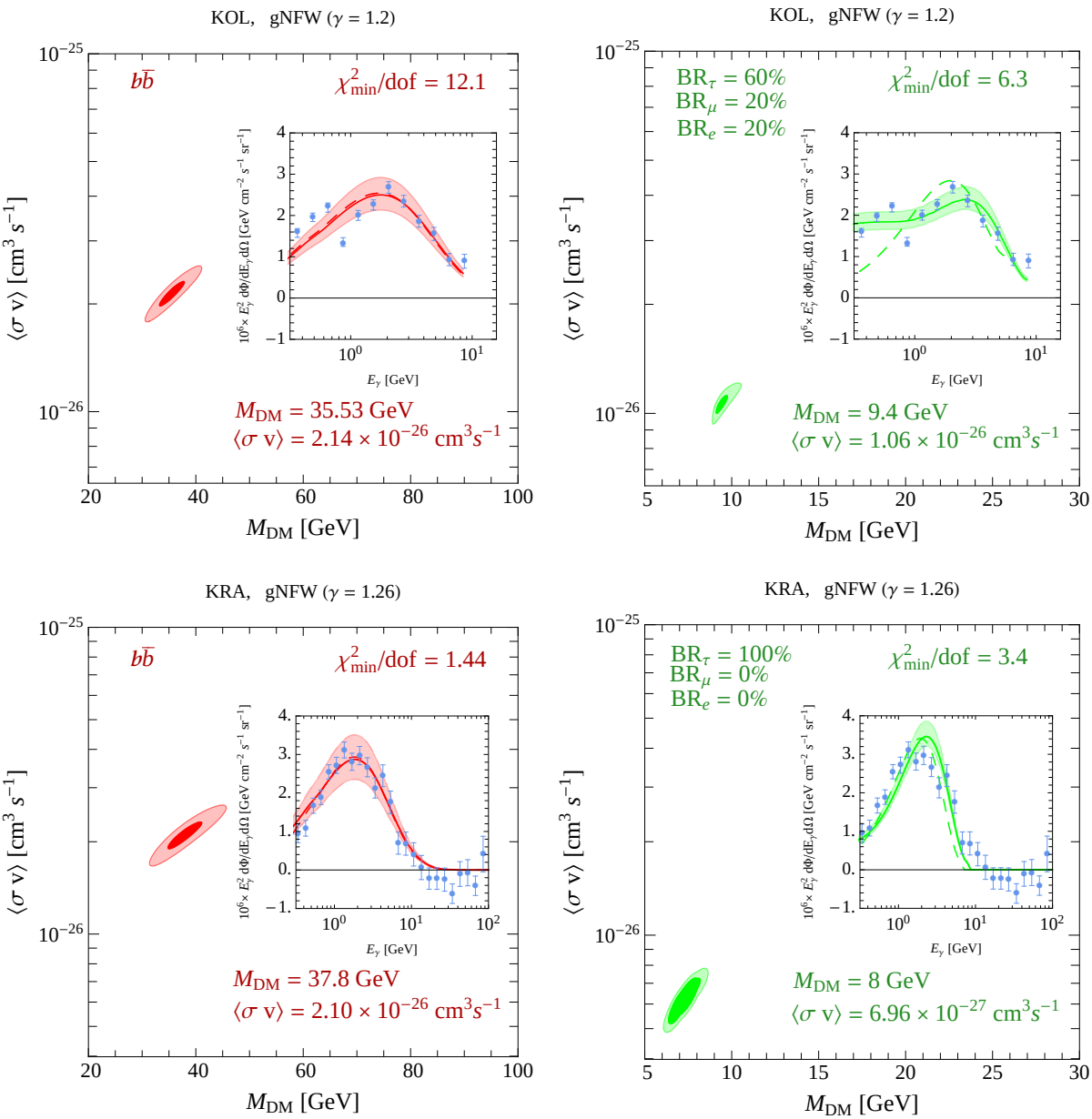

Figure 5.4: **χ-square fit of the GC excess** We include secondary emissions from DM annihilation, and we show the 1-σ and 3-σ confidence regions corresponding to 100% DM annihilation into $b\bar{b}$ (left panels) and DM annihilation into leptons (right panels). In the inset plot, we compare the best-fit gamma-ray spectrum with the residual data; for illustrative purposes, the shaded region represents the 3-σ band obtained by varying the annihilation cross-section in the corresponding confidence interval (but keeping $M_{\rm DM}$ fixed to the best-fit value). As far as the $b\bar{b}$ final state is concerned, secondary emissions do not play a significant role. Considering DM annihilation into leptons, on the contrary, the inclusion of secondary emissions can significantly improve the goodness of the fit; for comparison, in the inset plots the dashed lines represent the best-fit spectra obtained considering only the prompt emission.

In figure 5.4, we show the results of our fits to GC excess including secondary emissions from DM annihilation, and table 5.2 reports the results of our χ-square analysis. We fit the

Analysis	Final State	Setup	$M_{\rm DM}$ [GeV]	$\langle\sigma v\rangle$ [cm^3 s^{-1}]	$\chi^2_{\rm min}$/dof
'Gal Center', $\gamma = 1.2$	$b\bar{b}$	KOL	35.53	2.14×10^{-26}	12.1
	leptonic mix $^{(\star)}$	KOL	9.4	1.06×10^{-26}	6.3
'Inner Gal', $\gamma = 1.26$	$b\bar{b}$	KRA	37.8	2.10×10^{-26}	1.44
	$\tau^+\tau^-$	KRA	8	6.96×10^{-27}	3.4

$^{(\star)}$ leptonic mix = 20% e^+e^- + 20% $\mu^+\mu^-$ + 60% $\tau^+\tau^-$

Table 5.2: **Results of the χ-square analysis** for the fit of the GC excess.

'Galactic Center' data found in ref. [262] (fig. 7 of ref. [262], left panel) and the 'Inner Galaxy' data (figure 5 in ref. [262], right panel). Concerning the 'Galactic Center' analysis, we see that our exemplar leptonic channel with 60% $\tau^+\tau^-$, 20% $\mu^+\mu^-$ and 20% e^+e^- provides a better fit to the data (upper right panel of figure 5.4), mainly thanks to the low energy tail provided by secondary emissions. This is consistent with the findings of [263] and their results are therefore confirmed by our more accurate (in terms of energy losses and computation of the emissions) analysis. On the other hand, the shape of the spectrum of the 'Inner Galaxy' analysis selects the $b\bar{b}$ channel as a better fitting possibility, although a 100% DM annihilation into $\tau^+\tau^-$ can also provide a decent fit (lower right panel of figure 5.4). One could also consider mixed hadronic/leptonic channels (dubbed e.g. 'democratic fermions'), but the qualitative conclusions would remain the same. Changing the propagation setup would change these results only marginally. For completeness, we anyway specify in table 5.2 the employed setup.

In summary, this part of our analysis does not want to exhaust or systematically scan all the fitting possibilities. However it illustrates an important point: the specific conclusions that one can draw on the nature of the DM particle responsible for the excess have a critical dependence on (i) the method of extraction of the data and (ii) an accurate computation of the DM gamma-ray flux (including secondary radiation). On the other hand, the choice of the propagation setup for electrons and positrons at the origin of the secondary emissions has a small impact.

5.4 Antiproton bound on $b\bar{b}$ final state

In light of the results of the previous section, it becomes crucial to investigate the DM interpretation of the GC excess from a different but complementary perspective. DM annihilation into $b\bar{b}$ final state copiously produces antiprotons giving rise, in principle, to a detectable signal on Earth. Leptonic annihilation channels, on the contrary, do not feature this property (at least considering values of the DM mass smaller than $\sim$ 100 GeV where electroweak radiative corrections – otherwise able to produce antiprotons via emission of $W^\pm$, Z bosons – play no significant role [299, 300, 208]). This means that the measurement of the antiproton flux provides a powerful way to scrutinize the hadronic interpretation of the GC excess. To achieve this goal, however, one has to rely on a careful understanding of the astrophysics involved.

Let us summarize the main points of our approach used already in section 3.4.2. First, following the discussion outlined in section 5.2.2, we compute the astrophysical antiproton flux originated from p-p and p-He collisions, for each one of the propagation setups defined in table 5.1. Second, we compute the antiproton flux from DM annihilations assuming 100% an-

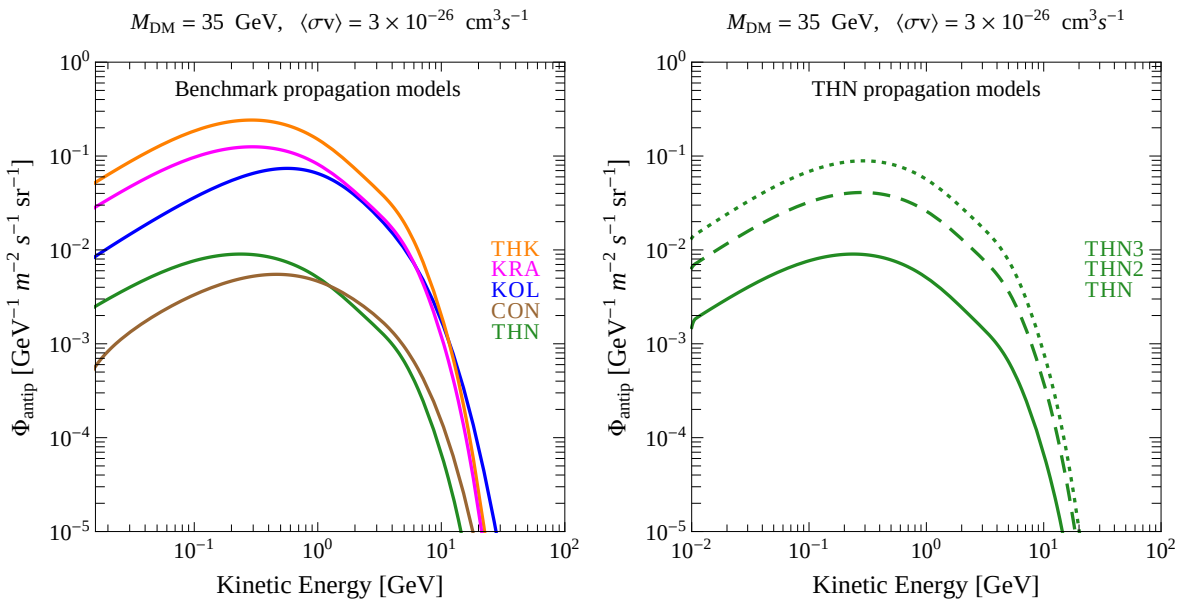

Figure 5.5: **Antiproton flux from DM annihilation** into $b\bar{b}$ final state with $M_{\rm DM} = 35$ GeV and $\langle\sigma v\rangle = 3\times10^{-26}$ cm^3 s^{-1}. We show the flux at the location of the Earth, after propagation in the Galaxy. We use the gNFW profile with $\gamma = 1.26$. In the left panel we use the five benchmark propagation models defined in table 2.2. In the right panel we explore alternative choices for the scale height z_t that defines the THN model (THN2, dashed; THN3, dotted, see table 5.1).

nihilation into $b\bar{b}$ final state, and we propagate it according to the same setup (we plot example fluxes in figure 5.5). We assume a gNFW density profile with $\gamma = 1.26$ (see equation 5.1). We then constrain this additional DM contribution using the PAMELA data [1]. Since we start from a best fit of the antiproton flux, the constraints are not the most conservative that one can get (more conservative upper limits on DM models may come making no assumption at all about the background astrophysical fluxes) but turn out to be very realistic. Using the antiproton data in reference [297], we extract a 3-σ exclusion contour[2] in the plane $(M_{\rm DM}, \langle\sigma v\rangle)$.

One crucial ingredient in this kind of analysis is the impact of solar modulation on the total antiproton flux, parametrized by the Fisk potential $\phi_F^{\bar{p}}$. Here, we aim to give an accurate discussion of this delicate issue, and we explore three different approaches, motivated by the dedicated analysis presented in section 2.5.2:

A. We fix the solar modulation potential $\phi_F^{\bar{p}}$ to the value obtained from the fit of the proton data (see table 5.1); we show the corresponding result in the top panels of figure 5.6.

B. We marginalize over $\phi_F^{\bar{p}}$ considering the interval $\phi_F^{\bar{p}} = \phi_F^{p} \pm 50\%$; we show the corresponding result in the middle panels of figure 5.6.

C. We marginalize over a wider range of values, namely $\phi_F^{\bar{p}} \in [0.1, 1.1]$; we show the corresponding result in the lower panels of fig. 5.6.

Let us now further motivate these choices, and discuss in detail our results.

[1] This analysis was done before the presentation of $\bar{p}/p$ by the AMS collaboration

[2] In chapter 3, we were computing $\Delta\chi^2 > 4$ exclusion regions

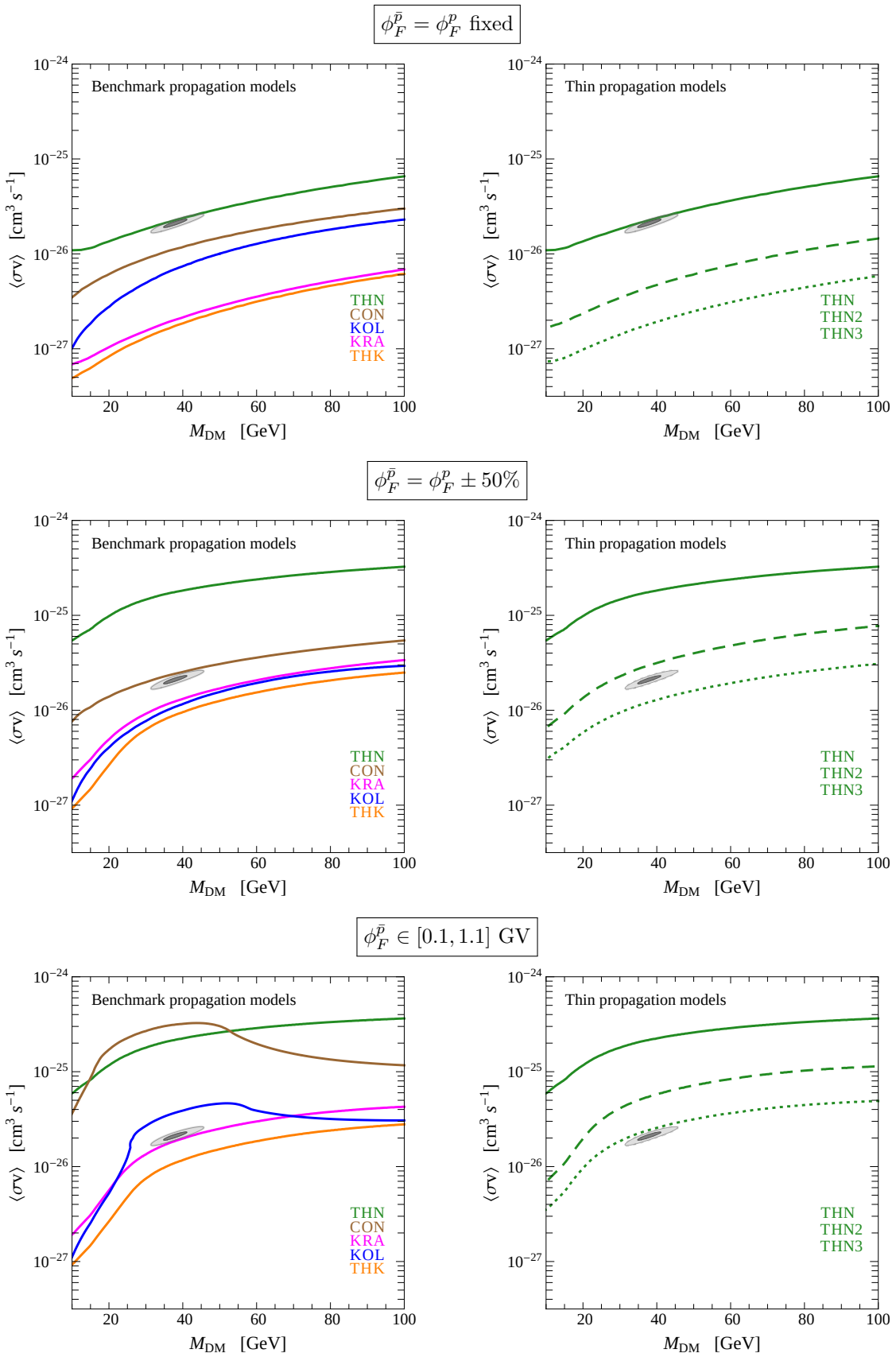

Figure 5.6: **3-σ exclusion contours on** $\langle \sigma v \rangle$ for 100% DM annihilation into $b\bar{b}$, for the three approaches to solar modulation discussed in the text. Left panels: the five benchmark propagation setups. Right panels: alternative choices for the scale height z_t that defines the THN setup (THN2, dashed; THN3, dotted). The gray area is the best-fit region identified in section 5.3.

A. Choosing $\phi_F^{\bar{p}} = \phi_F^p$ is a very constrictive assumption, and it corresponds to neglecting completely any charge-dependent effect in the description of solar modulation, which is the basic assumption behind the force-field approximation. The results obtained in this setup, as a consequence, must be taken with a pinch of salt and lead to the most stringent bound one can obtain from the antiproton data, since there is no freedom to vary the Fisk potential in order to counterbalance – in particular at low energies – the impact of DM on the total flux.

In the top left panel of figure 5.6 all the propagation setup but THN rule out the DM explanation of the GC excess, represented by the 1- and 3-σ confidence regions shaded in gray. As we know, the THN model, based on a thin diffusion zone with $z_t = 0.5$ kpc, is strongly disfavored by recent studies on synchrotron emission, radio maps and low energy positron spectrum. Therefore, taking into account these results, the exclusion plots shown in the upper left part of figure 5.6 turn out to strongly disfavor the DM interpretation of the gamma-ray excess. In order to assess more carefully the validity of this claim, we explore in the upper right panel of figure 5.6 different choices for the halo height that defines the THN model. We compute the antiproton bound corresponding to the THN2 ($z_t = 2$ kpc) and THN3 ($z_t = 3$ kpc) propagation models and we see that the DM interpretation of the GC excess is excluded for both of them.

In summary, within this approach the DM interpretation of the excess requires unrealistically thin ($\lesssim 1$ kpc) diffusive halos, which are at odds with several other measurements, and is therefore strongly disfavored.

B. As mentioned at the beginning, however, this strong conclusion cannot be the ending point of a careful analysis. Protons and antiprotons are likely to be subject to different modulations under the influence of the Sun, and the requirement $\phi_F^{\bar{p}} = \phi_F^p$ will be seldom realized (see table 2.3). For this reason, let us abandon the condition $\phi_F^{\bar{p}} = \phi_F^p$, go beyond the initial force-field approximation and investigate how the antiproton bound changes as soon as solar modulation is marginalized away in the fit.

In the middle portion of fig. 5.6, we marginalize over $\phi_F^{\bar{p}}$ considering the interval $\phi_F^{\bar{p}} = \phi_F^p \pm 50\%$ (we recall that ϕ_F^p is fixed for each setup, values are given in table 5.1). We chose this particular range based on the use of the dedicated analysis presented in table 2.3, using `HelioProp`.

By comparing the results in the middle panels of figure 5.6 – obtained with this range – with the upper panels, it is evident that in this case the antiproton bound becomes less stringent. Intuitively, this happens since as soon as the DM contribution becomes large enough to overshoot the low-energy data, it can be compensated by increasing the value of the Fisk potential. Nevertheless, we find that also in this case the THK, KOL and KRA propagation models as well as the THN3 model (with $z_t = 3$ kpc) rule out the $b\bar{b}$ DM interpretation of the signal. The bounds corresponding to the CON propagation model and the THN2 model (with $z_t = 2$ kpc), on the contrary, are weakened to the extent that the best-fit region of the GeV excess falls into the allowed region.

C. Finally, in the lower panels of figure 5.6 we present even more conservative bounds. Here we choose to marginalize over $\phi_F^{\bar{p}}$ in the interval $\phi_F^{\bar{p}} \in [0.1, 1.1]$ GV (for all propagation setups, irrespectively of the values for ϕ_F^p they possess). This is a very generous range that most certainly brackets even extreme variations for this parameter. One can look for instance at [301], in which the authors reconstructed the value of the modulation potential over the period from July 1936 through December 2009: according to that analysis, the value of the potential

exceeded our upper limit only during a few very pronounced solar maxima around 1990, 1982 and 1959; in the current century the Fisk potential that they derive reached but never exceeded 1.05 GV. We remind once again that the Fisk potential is model dependent and the assumption on the local interstellar spectrum has a strong impact on its value; nevertheless, since PAMELA took data during a period of extremely low modulation, the range we adopt appears extremely conservative anyway.

The bounds obtained under these assumptions are of course much weaker: models with large convection or reacceleration such as CON and KOL do not exclude the DM interpretation, as well as models with halo height lower than 3 kpc. We notice however that models with large halo height, favored by synchrotron analyses, still rule it out.

5.5 Final comments

Very recently, the authors of [232] have also discussed the antiproton bounds. They find that the antiproton data can be marginally consistent with the GeV excess only if the very conservative MIN model from [218] is used (a model roughly corresponding to our THN). We differ from [232] since: **1)** we consider a comprehensive set of propagation models, including several 'thin' models with different halo height, and models with high reacceleration or convection together with others where these effects are less important; **2)** we fully include the subtleties associated to solar modulation: this turns out to be crucial since the more the Fisk potential for the antiprotons is allowed to vary the less stringent the bounds become.

Our overall conclusions are the following: adopting the most realistic propagation models and well motivated choices for the solar modulation potential, the hadronic ($b\bar{b}$) DM interpretation for the GeV excess is definitely in strong tension with the antiproton data. Nevertheless, given that our knowledge of CR diffusion both in the Galaxy and in the heliosphere is far from being accurate and complete, there are still conservative choices of the parameters involved that do not result in ruling it out, namely thin halo models and large solar modulation potentials. In addition, leptonic channels can provide good fits to the data (although critically dependent on a proper computation of secondary emissions) and avoid antiproton constraints. In any case, as we have concluded in chapter 3, more precise data, and a deeper understanding of CR propagation and modulation, are required for antiprotons, in particular in order to test convincingly the DM origin of this signal. While it is difficult to compare constraints obtained using `DRAGON` with those computed in section 3.5.2, propagation models still allowed by the preliminary AMS-02 $\bar{p}/p$ data, such as MED and MAX, increase the tension between the DM interpretation of the excess and antiproton constraints in the most conservative case of solar modulation. It is however difficult to predict if propagation models such as KOL and CON still leave room for a DM signal. In the future, data from AMS-02 on other CR species is needed in order to help pinning down new propagation setups.

Chapter 6

Conclusion and discussion

Since the 1930's, the evidence for the existence of Dark Matter has only been gravitational. Other manifestations are actively searched for and a particularly promising one would consists in detecting excess cosmic rays as a signature of Dark Matter annihilations or decays. This is the main focus of this thesis work.

After reminding the main reasons for the need of Dark Matter in astrophysics and cosmology, we reviewed briefly theories that contain Dark Matter candidates: particle physics models beyond the Standard Model, such as Super Symmetry, extra dimensions or sterile neutrinos, provide viable ones. In particular, a very popular class of candidates consists of WIMPs, massive particles that interact weakly (in the sense of the weak interactions of Standard Model of particle physics). Their annihilations or decays can produce fluxes of cosmic rays in the typical GeV to TeV range of energy and that can be detected at Earth on top of the astrophysical contributions. Focussing first on charged cosmic rays, we presented the derivation of their transport equation in the Galaxy and described their propagation in the heliosphere. In fact, dedicated codes can model the effects of the solar wind on the energy spectrum of cosmic rays particles, but in order to use a more practical and simple way to account for this effect, we introduced the force-field approximation, used extensively for our analysis of antiprotons.

In the quest for Dark Matter, it is important to exploit all possible strategies. In indirect searches, in particular, it is important to be able to exploit the multi-messenger and multi-wavelength nature of the possible signals. For this reason, we examined charged cosmic rays in a model independent approach, starting with antiprotons, followed by secondary emissions from electrons and positrons and presented an example of the interplay between charged cosmic rays by analyzing the Galactic Center excess.

We focused on cosmic ray antiprotons in particular because they have been regarded since long as a powerful probe for Dark Matter annihilations (or decay) in the Galaxy. Indeed, because the physics that controls their production and propagation in the Galaxy as well as the astrophysical background are under relatively better control than for other species, and because experimental data in the antiproton channel are impressively accurate. The results we have obtained have followed (and sometimes anticipated) the developments of the experimental activity in the field. First, we used PAMELA data in a simplified approach and showed the potential of antiprotons to constraint Dark Matter. Then, for the sake of comparing with ever more precise data, the accuracy of the theoretical predictions had to be improved. We have reassessed the computation of the astrophysical and Dark Matter antiproton fluxes by including effects such as $\bar{p}$ Energy Losses (including tertiary component) and Diffusive Reacceleration

('ELDR'), as well as Solar Modulation ('SMod'). These effects are often perceived as subdominant, but they can actually have an important impact, especially at low energies (hence in particular for small Dark Matter masses, $m_{\rm DM} \lesssim 50$ GeV). We have obtained the updated astrophysical background fluxes, which we provide in terms of approximation functions, as well as the Dark Matter $\bar{p}$ fluxes, which we provide in the new release of Poor Particle Physicist Cookbook Book 4 Dark Matter Indirect Detection (PPPC4DMID Release 4.0). We have then employed these ingredients to derive improved constraints based on PAMELA data and sensitivities for AMS-02, before applying our methods to study the preliminary $\bar{p}/p$ AMS-02 data.
By carefully treating the uncertainties on the astrophysical background (slope of the primary fluxes, production cross-sections, propagation in the Galaxy and solar modulation), we concluded that the AMS-02 $\bar{p}/p$ can be explained by astrophysics and does not show the need for an exotic component. The data prefer a propagation model with a mild energy dependence of the diffusion coefficient, such as MAX while the MIN model does not provide a good fit.

In addition to antinuclei (and antiprotons in particular), leptons also constitute messengers for Dark Matter annihilation or decay in the halo of our Galaxy. However, positrons exhibit an excess that could be due to Dark Matter or other astrophysical sources. We turned therefore to gamma rays and secondary emissions from electrons and positrons produced by Dark Matter annihilation or decay. We improved the previous calculation of energy losses in the Pppc4dmid by adding ionization and bremsstrahlung losses, as well as improved inverse Compton losses by replacing the Interstellar Radiation Field with a more detailed model, also used in the numerical code `GalProp`. In addition, for synchrotron losses, we proposed three different models for the global magnetic field of the Galaxy, motivated by different studies. In order to work in a coherent frame, we use the same propagation parameters (MIN, MED and MAX) and halo profiles (NFW, Einasto, EinastoB, Isothermal, Burkert and Moore) as for other potential Dark Matter signatures in cosmic rays. With the improved energy loss function, we then computed the electron and positron halo functions from Dark Matter annihilation and decay, which can be convoluted with the injection spectrum to obtain the electron and positron flux at each point in the Galaxy. Finally, we also computed the halo functions for the secondary emissions: inverse Compton, synchrotron and bremsstrahlung. These emissions fall at different wavelength and should be used to crosscheck potential discoveries. All of these functions can be downloaded from the Pppc4dmid website.

Finally, we turned towards the Galactic Center, a region known to be one of the most promising targets for indirect Dark Matter search. Several recent works have pointed to a gamma-ray excess in Fermi-LAT data from that region in the latest years. We have discussed two key issues related to this presumed Dark Matter detection. The first point is the relevance of the secondary gamma radiation emitted by particles originating from Dark Matter annihilation. We use the numerical packages `DRAGON` and `GammaSky` in order to compute in a realistic way this contribution and, once this emission is taken into account, we find the best fit regions corresponding to the gamma excess in the (Dark Matter mass - cross-section) parameter space. We conclude that the secondary emission is relevant for the leptonic channels in a wide energy range. Hence any conclusion on the Dark Matter nature of the signal critically depends on this contribution.

The second issue we have analyzed is the possibility of confirming or disproving the Dark Matter nature of this excess using the antiproton channel. We find that the uncertainties on the propagation model, and in particular on the halo height, play a major role, as expected.

Moreover, we have discussed in detail the role of the solar modulation. The main conclusion is that the interpretation of the Galactic Center excess in terms of a Dark Matter annihilating into $b\bar{b}$ is in tension with antiproton bounds. The Dark Matter interpretation survives when relaxing the assumptions on solar modulation effects and only for "extreme" propagation models, such as with convection (CON), diffusive reaccelerating (KOL) or models with halo hight smaller than 3 kpc (THIN).

The work reported in this thesis shows that Dark Matter indirect detection with antiprotons has revealed itself to be a more difficult exercise than expected: with more sensitive data, the energy spectrum starts to discriminate between propagation models. In fact, the traditional MIN-MED-MAX schemes are based on past cosmic rays data and are not necessarily guaranteed to work in describing the current status. Looking for Dark Matter on top of inadequate schemes can lead to non-robust or even wrong conclusions. Hence, one of the most crucial issues in the field is to update the uncertainty ranges of ordinary astrophysics in view of the more recent and precise experimental results, in order to build the Dark Matter search on a more solid basis. For the time being, the search for Dark Matter signatures has to be pursued with the utmost care. As illustrated in our analysis of the GC excess, astrophysical uncertainties dominate our calculations leaving enough room to evade constraints. This is where the AMS-02 experiment will play a key role in the near future: with the data on light nuclei, radioactive elements and secondary to primary ratios, we will be able to revisit the propagation models. In particular, the thin halo predicted by MIN or THN has already been seriously disfavored by different studies of cosmic rays. Observations prefer halo height larger than $2-3$ kpc. This is very encouraging for Dark Matter indirect detection, since large values of L imply a larger cosmic rays flux from Dark Matter annihilation or decay detected at Earth. In fact, more annihilation (decay) products are trapped inside the diffusion halo.

Another important uncertainty in our calculations is solar modulation. Since AMS-02 will be taking data for two decades, the experiment will probe two entire 11-year solar cycles, both with $A > 0$ and $A < 0$ heliosphere magnetic field configurations. Solar modulation models will be tested with high precision. If we include drift effects, solar modulation of antiprotons during $A > 0$ cycles should behave in the same way as protons during $A < 0$ cycles. Thus proton data measured today can be used in 11 years to model the solar modulation of antiprotons.

Concerning gamma-rays, the Fermi satellite is still collecting data and identifying new point sources, as well as faint dwarf galaxies. Understanding astrophysical sources in gamma rays is a crucial point towards building robust background models for the search of WIMP annihilations or decays in our and neighboring Galaxies and in particular at the center of the Milky Way.

Aiming towards deriving even more precise models and finding new clues on the nature of Dark Matter, the future of indirect searches lies in the next generation of experiments. Different projects have been proposed, while others are already under construction. In addition to AMS-02 other experiments are planned to be deployed on space stations: the International Space Station will host the experiment ISS-CREAM, designed to measure nuclei species, and CALET, an electron telescope. On the other hand, HERD will be attached to the Chinese Space Station in order to measure charged cosmic rays as well as gamma rays. Other space-based missions include GAPS, an experiment dedicated to the search of antideuteron. In fact, the detection of only one antideuteron would be a very strong indication for WIMP annihilations. In gamma ray astronomy, Gamma 400, the successors of the Fermi mission will continue to study cosmic rays, gamma ray sources and gamma ray bursts. In addition,

the DAMPE satellite is a project devoted to Dark Matter indirect searches, measuring cosmic rays, electrons and high energy gamma rays.
Future ground based experiments and successors of HESS, MAGIC and VERITAS consist of CTA and HAWC. Both are Cherenkov telescopes measuring gamma rays and cosmic rays interacting in the atmosphere. HAWC is currently under construction in Mexico on the flank of the Sierra Negra volcano at an altitude of 4100m. CTA is a project with two arrays at two locations: one in the norther and one in the southern hemisphere.
Finally, numerous direct detection experiments using different target masses and different detection techniques are testing the WIMP scenario. In the near future, experiments will start to be limited by the coherent scattering of neutrinos, marking the irreducible background and the maximum sensitivity of direct detection. Finally, the LHC has been upgraded and will push the center of mass energy up to 14 TeV, testing the Standard Model of particle physics in unprecedented regimes, searching for new physics such as Dark Matter particles.

We are living in a very exciting time for Dark Matter searches with various detection hints, constraining bounds and creative models explaining the potential signals while evading constraints. During the next decade, we should be able to confirm or exclude the WIMP paradigm. However, the absence of an indisputable WIMP signal does not imply the nonexistence of Dark Matter particles. In fact, WIMPs only represent a small fraction of possible Dark Matter candidates. Many other models and detection techniques exist in order to reveal the mystery of the nature of Dark Matter.

We can only see a short distance ahead, but we can see plenty there that needs to be done (Alan Turing).

Appendix

General Relativity : definitions

For a metric $g_{\mu\nu}$, the Christoffel symbols are defined as

$$\Gamma^{\mu}_{\nu\sigma} = \frac{1}{2} g^{\mu\lambda} \left(\frac{g_{\sigma\lambda}}{\partial x^{\nu}} + \frac{g_{\nu\lambda}}{\partial x^{\sigma}} - \frac{g_{\sigma\nu}}{\partial x^{\lambda}} \right), \tag{1}$$

Now, we can define the Riemann curvature tensor

$$R^{\mu}_{\nu\sigma\gamma} = \frac{\partial \Gamma^{\mu}_{\nu\gamma}}{\partial x^{\sigma}} - \frac{\partial \Gamma^{\mu}_{\nu\sigma}}{\partial x^{\gamma}} + \Gamma^{\mu}_{\alpha\sigma}\Gamma^{\alpha}_{\gamma\nu} - \Gamma^{\mu}_{\alpha\gamma}\Gamma^{\alpha}_{\sigma\nu}. \tag{2}$$

Then, the Ricci tensor and scalar are

$$R_{\mu\nu} = R^{\sigma}_{\mu\nu\sigma} \text{ and } R = R^{\mu}_{\mu}. \tag{3}$$

The Einstein equations can then be defied from the Einstein Hilbert action

$$S_{EH} = -\frac{1}{16\pi G} \int dx^4 \sqrt{-g}(R + 2\Lambda), \tag{4}$$

with $g = det(g_{\mu\nu})$. The total action has two part, the first one due to gravity, S_{EH}, and the second one due to the matter content of the universe S_M:

$$S = S_{EH} + S_M = -\frac{1}{16\pi G} \int dx^4 \sqrt{-g}(R + 2\Lambda) + \frac{1}{2} \int d^4x \sqrt{-g} T_{\mu\nu} g^{\mu\nu}. \tag{5}$$

$T_{\mu\nu}$ his the energy-momentum tensor.

In a homogeneous and isotropic universe, the redshift z can be defined by

$$1 + z = \frac{\lambda_0}{\lambda_e} = \frac{a(t_0)}{a(t_e)}, \tag{6}$$

λ_0 is the observed wavelength, λ_e the wavelength at emission, and $a(t_0)$ and $a(t_e)$ the scale factors at the time of the observation and emission.

Quantum Field Theory: definitions

Free fields

If ϕ is a scalar field with mass m, the lagrangian is

$$\mathcal{L}_{sca} = \frac{1}{2} \partial_{\mu}\phi \partial^{\mu}\phi - \frac{1}{2} m^2 \phi^2. \tag{7}$$

Varying the action $S_{sac} = \int d^4x \; \mathcal{L}_{sca}$ leads to the Klein-Gordon equation

$$\partial_\mu \partial^\mu \phi - m^2 \phi = 0. \tag{8}$$

For a massive vector field B^μ, we define the field tensor $B^{\mu\nu} = \partial^\mu B^\nu - \partial^\nu B^\mu$ and the lagrangian is

$$\mathcal{L}_{vec} = -\frac{1}{4} B_{\mu\nu} B^{\mu\nu} + \frac{m^2}{2} B_\mu B^\mu \tag{9}$$

and the equation of motion is

$$\partial^\mu B_{\mu\nu} + m^2 B_\nu = 0. \tag{10}$$

For a spinor ψ, we define the γ-matrices

$$\gamma^0 = \begin{pmatrix} 0 & \mathbb{1} \\ \mathbb{1} & 0 \end{pmatrix} \quad \text{and} \quad \gamma^i = \begin{pmatrix} 0 & \sigma^i \\ -\sigma^i & 0 \end{pmatrix} \tag{11}$$

, where σ^i are the Pauli matrices, and $\bar{\psi} = \psi^\dagger \gamma^0$, where $\psi^\dagger = \psi^{*T}$. The lagrangian for a Dirac spinor

$$\mathcal{L}_{dir} = \bar{\psi} \left(i\gamma^\mu \partial_\mu - m \right) \psi, \tag{12}$$

and the equation of motion is the Dirac equation

$$\left(i\gamma^\mu \partial_\mu - m \right) \psi = 0. \tag{13}$$

The fifth γ-matrix is $\gamma^5 = i\gamma^0\gamma^1\gamma^2\gamma^3$ and we can define the left- and right-chiral fields

$$\psi^L = \frac{\mathbb{1} - \gamma_5}{2} \psi \quad \text{and} \quad \psi^R = \frac{\mathbb{1} + \gamma_5}{2} \psi. \tag{14}$$

Standard model fields and interactions

In the standard model, the matter fields are fermion fields: the left-handed quark doublet Q_α, the right-handed up-type quark singlets U_α, the right-handed down-type quark singlets D_α, the left-handed lepton doublet L_α and the right-handed charged lepton singlets E_α. There are three generations of each field (index $\alpha = 1, 2, 3$).

Since the standard model group is $SU(3)_c \otimes SU(2)_L \otimes U(1)_Y$, the bosons sector contains: eight gluon fields G^a, four electroweak bosons W^1, W^2, W^3, B and one complex two-component Higgs field $H = (\phi^+, \phi^0)/\sqrt{2}$. For the case of the electroweak group $SU(2)_L \otimes U(1)_Y$, the fermion fields couple to the electroweak bosons, the derivative ∂_μ is promoted t a covariant derivative D_μ and the lagrangian becomes

$$\mathcal{L}_{EW} = \sum_\psi \bar{\psi} \gamma^\mu (i\partial_\mu - g' \frac{1}{2} Y_W B_\mu - g \frac{1}{2} \vec{\sigma} \cdot \vec{W}_\mu) \psi, \tag{15}$$

where Y_W is the weak hyper charge, g' the $U(1)_Y$ coupling and g the $SU(2)_L$ coupling. The Higgs lagrangian is

$$\mathcal{L}_H = \left[(\partial_\mu - igW^a_\mu t^a - ig' Y_H B_\mu) H \right]^2 + \mu^2 H^\dagger H - \lambda (H^\dagger H)^2 \tag{16}$$

with t^a the generators of the group, $\lambda > 0$ and $\mu^2 > 0$ which leads to spontaneous symmetry breaking. In the unitarity, we can set $\phi^+ = 0$ and make ϕ^0 real. The non-vanishing vacuum expectation value of Higgs field is $\langle \phi^0 \rangle = v$ and h the residual Higgs field.

The electroweak massless bosons mix into one massless neutral boson γ, one massive neutral boson Z^0 and two massive charged bosons $W^\pm$

$$\begin{aligned} A_\mu &= W^3_\mu \sin\theta_W + B_\mu \cos\theta_W, \\ Z\mu &= W^3_\mu \cos\theta_W - B_\mu \sin\theta_W, \\ W^\pm_\mu &= \frac{1}{\sqrt{2}}(W^1_\mu \mp iW^2_\mu), \end{aligned} \tag{17}$$

where θ_W is the Weinberg angle. The Higgs mechanism gives rise to masses of the W and Z

$$M_W = \frac{1}{2}v|g| \quad \text{and} \quad M_Z = \frac{1}{2}v\sqrt{g^2 + g'^2}. \tag{18}$$

and fermions get mass through the Yukawa coupling G_μ in the term $G_\mu \bar{\psi}\phi\psi$ in the lagrangian of the SM.

Bibliography

[1] F. Zwicky, Helv. Phys. Acta **6**, 110 (1933).

[2] V. C. Rubin, N. Thonnard and W. K. Ford, Jr., Astrophys. J. **238**, 471 (1980).

[3] T. S. van Albada, J. N. Bahcall, K. Begeman and R. Sancisi, Astrophys. J. **295**, 305 (1985).

[4] J. F. Navarro, C. S. Frenk and S. D. M. White, Astrophys. J. 462 (1996) 563 [arXiv:astro-ph/9508025].

[5] U. Haud and J. Einasto, TARTU-A-10-1986.

[6] A. W. Graham, D. Merritt, B. Moore, J. Diemand and B. Terzic, Astron. J. 132 (2006) 2685 [arXiv:astro-ph/0509417].

[7] J. F. Navarro *et al.*, arXiv:0810.1522 [astro-ph].

[8] P. B. Tissera, S. D. M. White, S. Pedrosa and C. Scannapieco, Mon. Not. Roy. Astron. Soc. **406** (2010) 922 [arXiv:0911.2316 [astro-ph.CO]].

[9] M. Cirelli, G. Corcella, A. Hektor, G. Hutsi, M. Kadastik, P. Panci, M. Raidal and F. Sala *et al.*, JCAP **1103** (2011) 051 [arXiv:1012.4515 [hep-ph]].

[10] A. Burkert, IAU Symp. 171 (1996) 175 [Astrophys. J. 447 (1995) L25] [arXiv:astro-ph/9504041].

See also: P. Salucci and A. Burkert, Astrophys. J. **537** (2000) L9 arXiv:astro-ph/0004397. G. Gentile, P. Salucci, U. Klein, D. Vergani and P. Kalberla, Mon. Not. Roy. Astron. Soc. 351 (2004) 903 [arXiv:astro-ph/0403154] and P. Salucci, A. Lapi, C. Tonini, G. Gentile, I. Yegorova and U. Klein, Mon. Not. Roy. Astron. Soc. 378 (2007) 41 [arXiv:astro-ph/0703115].

[11] B. Moore, T. R. Quinn, F. Governato, J. Stadel and G. Lake, Mon. Not. Roy. Astron. Soc. **310**, 1147 (1999) [astro-ph/9903164].

[12] M. Milgrom, Astrophys. J. **270**, 365 (1983).

[13] J. D. Bekenstein, Phys. Rev. D **70**, 083509 (2004) [Phys. Rev. D **71**, 069901 (2005)] [astro-ph/0403694].

[14] M. Markevitch, A. H. Gonzalez, D. Clowe, A. Vikhlinin, L. David, W. Forman, C. Jones and S. Murray *et al.*, Astrophys. J. **606** (2004) 819 [astro-ph/0309303].

[15] S. W. Randall, M. Markevitch, D. Clowe, A. H. Gonzalez and M. Bradac, Astrophys. J. **679**, 1173 (2008) [arXiv:0704.0261 [astro-ph]].

[16] P. Tisserand *et al.* [EROS-2 Collaboration], Astron. Astrophys. **469**, 387 (2007) [astro-ph/0607207].

[17] M. Moniez, arXiv:0901.0985 [astro-ph.GA].

[18] M. Cirelli, A. Strumia *et al*, work in progress

[19] A. A. Penzias and R. W. Wilson, Astrophys. J. **142**, 419 (1965).

[20] http://lambda.gsfc.nasa.gov/product/cobe/

[21] http://map.gsfc.nasa.gov/

[22] http://www.esa.int/Our_Activities/Space_Science/Planck

[23] http://asd.gsfc.nasa.gov/archive/arcade/cmb_intensity.html

[24] http://wmap.gsfc.nasa.gov/universe/bb_cosmo_fluct.html

[25] P. A. R. Ade *et al.* [Planck Collaboration], Astron. Astrophys. **571**, A15 (2014) [arXiv:1303.5075 [astro-ph.CO]].

[26] P. A. R. Ade *et al.* [Planck Collaboration], arXiv:1502.01589 [astro-ph.CO].

[27] http://www.mpoweruk.com/nuclear_theory.htm

[28] http://map.gsfc.nasa.gov/universe/bb_tests_ele.html

[29] A. L. Maroto and J. Ramirez, astro-ph/0409280.

[30] W. J. G. de Blok, Adv. Astron. **2010**, 789293 (2010) [arXiv:0910.3538 [astro-ph.CO]].

[31] B. A. Bassett and R. Hlozek, Dark Energy, Ed. P. Ruiz-Lapuente (2010, ISBN-13: 9780521518888) [arXiv:0910.5224 [astro-ph.CO]].

[32] W. Hu, R. Barkana and A. Gruzinov, Phys. Rev. Lett. **85**, 1158 (2000) [astro-ph/0003365].

[33] S. Tremaine and J. E. Gunn, Phys. Rev. Lett. **42**, 407 (1979).

[34] C. Dvorkin, K. Blum and M. Kamionkowski, Phys. Rev. D **89** (2014) 2, 023519 [arXiv:1311.2937 [astro-ph.CO]].

[35] B. W. Lee and S. Weinberg, Phys. Rev. Lett. **39** (1977) 165.

[36] K. Griest and M. Kamionkowski, Phys. Rev. Lett. **64** (1990) 615.

[37] K. Griest and D. Seckel, Phys. Rev. D **43**, 3191 (1991).

[38] http://ned.ipac.caltech.edu/level5/Sept05/Gondolo/Gondolo2.html

[39] C. Kraus, B. Bornschein, L. Bornschein, J. Bonn, B. Flatt, A. Kovalik, B. Ostrick and E. W. Otten *et al.*, Eur. Phys. J. C **40**, 447 (2005) [hep-ex/0412056].

[40] M. C. Gonzalez-Garcia, M. Maltoni, J. Salvado and T. Schwetz, JHEP **1212**, 123 (2012) [arXiv:1209.3023 [hep-ph]].

[41] http://home.physics.ucla.edu/~arisaka/home/Dark_Matter/

[42] T. Asaka, S. Blanchet and M. Shaposhnikov, Phys. Lett. B **631**, 151 (2005) [hep-ph/0503065].

[43] S. Dodelson and L. M. Widrow, Phys. Rev. Lett. **72**, 17 (1994) [hep-ph/9303287].

[44] R. D. Peccei and H. R. Quinn, Phys. Rev. Lett. **38**, 1440 (1977).

[45] S. Weinberg, Phys. Rev. Lett. **40**, 223 (1978).

[46] F. Wilczek, Phys. Rev. Lett. **40**, 279 (1978).

[47] G. Bertone, D. Hooper and J. Silk, Phys. Rept. **405**, 279 (2005) [hep-ph/0404175].

[48] J. Edsjo, hep-ph/9704384.

[49] M. Mori *et al.* [Kamiokande Collaboration], Phys. Rev. D **48**, 5505 (1993).

[50] D. Hooper, J. March-Russell and S. M. West, Phys. Lett. B **605**, 228 (2005) [hep-ph/0410114].

[51] S. P. Martin, Adv. Ser. Direct. High Energy Phys. **21**, 1 (2010) [hep-ph/9709356].

[52] C. Arina, M. E. C. Catalan, S. Kraml, S. Kulkarni and U. Laa, JHEP **1505**, 142 (2015) [arXiv:1503.02960 [hep-ph]].

[53] T. Kaluza, Sitzungsber. Preuss. Akad. Wiss. Berlin (Math. Phys.) **1921**, 966 (1921).

[54] G. Servant and T. M. P. Tait, Nucl. Phys. B **650**, 391 (2003) [hep-ph/0206071].

[55] D. J. H. Chung, E. W. Kolb and A. Riotto, Phys. Rev. D **59**, 023501 (1999) [hep-ph/9802238].

[56] V. Kuzmin and I. Tkachev, JETP Lett. **68**, 271 (1998) [Pisma Zh. Eksp. Teor. Fiz. **68**, 255 (1998)] [hep-ph/9802304].

[57] S. W. Hawking, Nature **248**, 30 (1974).

[58] K. Griest, A. M. Cieplak and M. J. Lehner, Phys. Rev. Lett. **111** (2013) 181302 [arXiv:1307.5798 [astro-ph.CO]].

[59] F. Capela, M. Pshirkov and P. Tinyakov, Phys. Rev. D **87**, no. 12, 123524 (2013) [arXiv:1301.4984 [astro-ph.CO]].

[60] D. M. Jacobs, G. D. Starkman and B. W. Lynn, [arXiv:1410.2236 [astro-ph.CO]].

[61] P. H. Frampton, arXiv:1003.3356 [astro-ph.CO].

[62] P. H. Frampton, M. Kawasaki, F. Takahashi and T. T. Yanagida, JCAP **1004**, 023 (2010) [arXiv:1001.2308 [hep-ph]].

[63] G. B. Gelmini, L. J. Hall and M. J. Lin, Nucl. Phys. B **281**, 726 (1987).

[64] S. Nussinov, Phys. Lett. B **165** (1985) 55.

[65] A. Kusenko and M. E. Shaposhnikov, Phys. Lett. B **418**, 46 (1998) [hep-ph/9709492].

[66] J. L. Feng, AIP Conf. Proc. **1516**, 170 (2012) [arXiv:1211.3116 [astro-ph.HE]].

[67] D. R. Tovey, R. J. Gaitskell, P. Gondolo, Y. A. Ramachers and L. Roszkowski, Phys. Lett. B **488** (2000) 17 [hep-ph/0005041].

[68] M. J. Reid, Ann. Rev. Astron. Astrophys. **31**, 345 (1993).

[69] E. I. Gates, G. Gyuk and M. S. Turner, Astrophys. J. **449** (1995) L123 [astro-ph/9505039].

[70] L. M. Widrow, B. Pym and J. Dubinski, Astrophys. J. **679** (2008) 1239 [arXiv:0801.3414 [astro-ph]].

[71] F. J. Kerr and D. Lynden-Bell, Mon. Not. Roy. Astron. Soc. **221**, 1023 (1986).

[72] D. G. Cerdeno and A. M. Green, In *Bertone, G. (ed.): Particle dark matter* 347-369 [arXiv:1002.1912 [astro-ph.CO]].

[73] C. E. Aalseth *et al.* [CoGeNT Collaboration], Phys. Rev. D **88** (2013) 1, 012002 [arXiv:1208.5737 [astro-ph.CO]].

[74] R. Bernabei, P. Belli, F. Cappella, V. Caracciolo, S. Castellano, R. Cerulli, C. J. Dai and A. d'Angelo *et al.*, Eur. Phys. J. C **73** (2013) 12, 2648 [arXiv:1308.5109 [astro-ph.GA]].

[75] L. Baudis, Phys. Dark Univ. **1** (2012) 94 [arXiv:1211.7222 [astro-ph.IM]].

[76] S. C. Kim, H. Bhang, J. H. Choi, W. G. Kang, B. H. Kim, H. J. Kim, K. W. Kim and S. K. Kim *et al.*, Phys. Rev. Lett. **108** (2012) 181301 [arXiv:1204.2646 [astro-ph.CO]].

[77] E. Aprile *et al.* [XENON100 Collaboration], Phys. Rev. Lett. **109** (2012) 181301 [arXiv:1207.5988 [astro-ph.CO]].

[78] D. S. Akerib *et al.* [LUX Collaboration], Phys. Rev. Lett. **112** (2014) 091303 [arXiv:1310.8214 [astro-ph.CO]].

[79] P. Agnes *et al.* [DarkSide Collaboration], Phys. Lett. B **743** (2015) 456 [arXiv:1410.0653 [astro-ph.CO]].

[80] G. Angloher *et al.* [CRESST-II Collaboration], Eur. Phys. J. C **74** (2014) 12, 3184 [arXiv:1407.3146 [astro-ph.CO]].

[81] Z. Ahmed *et al.* [CDMS-II Collaboration], Phys. Rev. Lett. **106** (2011) 131302 [arXiv:1011.2482 [astro-ph.CO]].

[82] E. Armengaud *et al.* [EDELWEISS Collaboration], Phys. Lett. B **702** (2011) 329 [arXiv:1103.4070 [astro-ph.CO]].

[83] E. Behnke *et al.* [COUPP Collaboration], Phys. Rev. D **86** (2012) 5, 052001 [Phys. Rev. D **90** (2014) 7, 079902] [arXiv:1204.3094 [astro-ph.CO]].

[84] M. C. Piro [PICASSO Collaboration], arXiv:1005.5455 [astro-ph.IM].

[85] P. Cushman, C. Galbiati, D. N. McKinsey, H. Robertson, T. M. P. Tait, D. Bauer, A. Borgland and B. Cabrera *et al.*, arXiv:1310.8327 [hep-ex].

[86] J. Diemand, M. Kuhlen, P. Madau, M. Zemp, B. Moore, D. Potter and J. Stadel, Nature **454** (2008) 735 [arXiv:0805.1244 [astro-ph]].

[87] M. Kuhlen, N. Weiner, J. Diemand, P. Madau, B. Moore, D. Potter, J. Stadel and M. Zemp, JCAP **1002** (2010) 030 [arXiv:0912.2358 [astro-ph.GA]].

[88] P. J. Fox, J. Liu and N. Weiner, Phys. Rev. D **83** (2011) 103514 [arXiv:1011.1915 [hep-ph]].

[89] E. Del Nobile, G. B. Gelmini, P. Gondolo and J. H. Huh, Phys. Procedia **61** (2015) 45 [arXiv:1405.5582 [hep-ph]].

[90] G. Aad *et al.* [ATLAS Collaboration], Phys. Rev. D **90** (2014) 5, 052004 [arXiv:1406.3827 [hep-ex]].

[91] CMS Collaboration [CMS Collaboration], and studies of the compatibility of its couplings with the standard model," CMS-PAS-HIG-14-009.

[92] G. Aad *et al.* [ATLAS Collaboration], Phys. Rev. D **90** (2014) 1, 012004 [arXiv:1404.0051 [hep-ex]].

[93] J. Goodman, M. Ibe, A. Rajaraman, W. Shepherd, T. M. P. Tait and H. B. Yu, Phys. Rev. D **82**, 116010 (2010) [arXiv:1008.1783 [hep-ph]].

[94] D. Racco, A. Wulzer and F. Zwirner, JHEP **1505** (2015) 009 [arXiv:1502.04701 [hep-ph]].

[95] CMS Collaboration [CMS Collaboration], CMS-PAS-EXO-12-047.

[96] S. Maruyama [CMS and ATLAS Collaborations], arXiv:1411.0204 [hep-ex].

[97] O. Tibolla [MAGIC Collaboration], arXiv:1201.2295 [astro-ph.HE].

[98] B. Zitzer [VERITAS Collaboration], arXiv:1503.00743 [astro-ph.HE].

[99] A. Abramowski *et al.* [HESS Collaboration], Phys. Rev. Lett. **114**, no. 8, 081301 (2015) [arXiv:1502.03244 [astro-ph.HE]].

[100] A. Albert [Fermi-LAT Collaboration], Phys. Procedia **61**, 6 (2015).

[101] P. Sreekumar *et al.* [EGRET Collaboration], Astrophys. J. **494**, 523 (1998) [astro-ph/9709257].

[102] L. Goodenough and D. Hooper, arXiv:0910.2998 [hep-ph].

[103] C. Weniger, JCAP **1208**, 007 (2012) [arXiv:1204.2797 [hep-ph]].

[104] M. Su and D. P. Finkbeiner, arXiv:1206.1616 [astro-ph.HE].

[105] M. Ackermann *et al.* [Fermi-LAT Collaboration], arXiv:1503.02641 [astro-ph.HE].

[106] A. Geringer-Sameth, M. G. Walker, S. M. Koushiappas, S. E. Koposov, V. Belokurov, G. Torrealba and N. W. Evans, arXiv:1503.02320 [astro-ph.HE].

[107] A. Achterberg *et al.* [IceCube Collaboration], Astropart. Phys. **26**, 155 (2006) [astro-ph/0604450].

[108] M. Ageron *et al.* [ANTARES Collaboration], Nucl. Instrum. Meth. A **656**, 11 (2011) [arXiv:1104.1607 [astro-ph.IM]].

[109] J. Conrad, arXiv:1411.1925 [hep-ph].

[110] I. Masina, P. Panci and F. Sannino, JCAP **1212** (2012) 002 [arXiv:1205.5918 [astro-ph.CO]].

[111] A. D. Avrorin *et al.* [Baikal Collaboration], Astropart. Phys. **62** (2014) 12 [arXiv:1405.3551 [astro-ph.HE]].

[112] http://www.ams02.org/

[113] http://www.ams02.org/2013/04/first-results-from-the-alpha-magnetic-spectrometer-ams-experiment/

[114] O. Adriani *et al.* [PAMELA Collaboration], Phys. Rev. Lett. **105** (2010) 121101 [arXiv:1007.0821 [astro-ph.HE]].

[115] O. Adriani *et al.* [PAMELA Collaboration], Nature **458**, 607 (2009) [arXiv:0810.4995 [astro-ph]].

[116] L. Bergstrom, J. Edsjo and G. Zaharijas, Phys. Rev. Lett. **103**, 031103 (2009) [arXiv:0905.0333 [astro-ph.HE]].

[117] M. Di Mauro, F. Donato, N. Fornengo, R. Lineros and A. Vittino, JCAP **1404** (2014) 006 [arXiv:1402.0321 [astro-ph.HE]].

[118] H. Yuksel, M. D. Kistler and T. Stanev, Phys. Rev. Lett. **103**, 051101 (2009) [arXiv:0810.2784 [astro-ph]].

[119] S. Profumo, Central Eur. J. Phys. **10**, 1 (2011) [arXiv:0812.4457 [astro-ph]].

[120] A. Ibarra and S. Wild, JCAP **1302** (2013) 021 [arXiv:1209.5539 [hep-ph]].

[121] H. Fuke, T. Maeno, K. Abe, S. Haino, Y. Makida, S. Matsuda, H. Matsumoto and J. W. Mitchell *et al.*, Phys. Rev. Lett. **95**, 081101 (2005) [astro-ph/0504361].

[122] L. Arruda, F. Barao and R. Pereira, arXiv:0710.0993 [astro-ph].

[123] K. Mori, C. J. Hailey, E. A. Baltz, W. W. Craig, M. Kamionkowski, W. T. Serber and P. Ullio, Astrophys. J. **566**, 604 (2002) [astro-ph/0109463].

[124] C. J. Hailey, W. W. Craig, F. A. Harrison, J. Hong, K. Mori, J. Koglin, H. T. Yu and K. P. Ziock, Nucl. Instrum. Meth. B **214** (2004) 122 [astro-ph/0306589].

[125] M. Cirelli, N. Fornengo, M. Taoso and A. Vittino, JHEP **1408**, 009 (2014) [arXiv:1401.4017 [hep-ph]].

[126] T. R. Slatyer, N. Padmanabhan and D. P. Finkbeiner, Phys. Rev. D **80**, 043526 (2009) [arXiv:0906.1197 [astro-ph.CO]].

[127] D. P. Finkbeiner, S. Galli, T. Lin and T. R. Slatyer, Phys. Rev. D **85** (2012) 043522 [arXiv:1109.6322 [astro-ph.CO]].

[128] A. Boyarsky, O. Ruchayskiy, D. Iakubovskyi and J. Franse, Phys. Rev. Lett. **113** (2014) 251301 [arXiv:1402.4119 [astro-ph.CO]].

[129] E. Bulbul, M. Markevitch, A. Foster, R. K. Smith, M. Loewenstein and S. W. Randall, Astrophys. J. **789** (2014) 13 [arXiv:1402.2301 [astro-ph.CO]].

[130] T. E. Jeltema and S. Profumo, Mon. Not. Roy. Astron. Soc. **450**, 2143 (2015) [arXiv:1408.1699 [astro-ph.HE]].

[131] V. F. Hess, Phys. Zeitschr. XIII (1912) 1084

[132] C. D. Anderson, Phys. Rev. **43**, 491 (1933).

[133] K. Greisen, Phys. Rev. Lett. **16**, 748 (1966).

[134] G. T. Zatsepin and V. A. Kuzmin, JETP Lett. **4**, 78 (1966) [Pisma Zh. Eksp. Teor. Fiz. **4**, 114 (1966)].

[135] G. A. Medina-Tanco, Astrophys. J. **510**, L91 (1999) [astro-ph/9810366].

[136] R. U. Abbasi *et al.* [HiRes Collaboration], Phys. Rev. Lett. **100**, 101101 (2008) [astro-ph/0703099].

[137] J. Abraham *et al.* [Pierre Auger Collaboration], Phys. Rev. Lett. **101** (2008) 061101 [arXiv:0806.4302 [astro-ph]].

[138] http://www.physics.utah.edu/ whanlon/spectrum.html

[139] M. Casolino [Pamela Collaboration], arXiv:0904.4692 [astro-ph.HE].

[140] N. Hayashida *et al.* [AGASA Collaboration], Astropart. Phys. **10**, 303 (1999) [astro-ph/9807045].

[141] http://courses.atlas.illinois.edu/fall2009/astr/astr596npa/LECTURES/Lect38.html

[142] R. Weyer, http://www-brs.ub.ruhr-uni-bochum.de/netahtml/HSS/Diss/WeyerRalf/diss.pdf

[143] W. Baade,F. Zwicky, Proceedings of the National Academy of Sciences **20** (1934) 259

[144] http://www.nasa.gov/multimedia/imagegallery/image_feature_460.html

[145] http://auger.cnrs.fr/presse/0197swordybox2.html

[146] Y. Sekido, T. Masuda, S. Yoshida, M.. Wada, Phys. Rev. **83** (1951) 658

[147] K. Koyama, R. Petre, E. V. Gotthelf, U. Hwang, M. Matsuura, M. Ozaki and S. S. Holt, Nature **378**, 255 (1995).

[148] W. R. Binns, M. E. Wiedenbeck, M. Arnould, A. C. Cummings, G. A. de Nolfo, S. Goriely, M. H. Israel and R. A. Leske *et al.*, Space Sci. Rev. **130** (2007) 439 [arXiv:0707.4645 [astro-ph]].

[149] H. E. Mitler SAO Special Report # 330 (1970) Cosmic-Ray Production of Deuterium, He^3, Lithium, Beryllium and Boron in the Galaxy

[150] M. Lemoine and G. Sigl, (Lecture notes in physics. 576)

[151] R. Schlickeiser Springer, Berlin (2001)

[152] R. Blandford and D. Eichler, Phys. Rept. **154**, 1 (1987).

[153] F. Casse, M. Lemoine and G. Pelletier, Phys. Rev. D **65**, 023002 (2002) [astro-ph/0109223].

[154] J. Lavalle and P. Salati, Comptes Rendus Physique **13**, 740 (2012) [arXiv:1205.1004 [astro-ph.HE]].

[155] S. D. Hunter, D. L. Bertsch, J. R. Catelli, T. M. Digel, S. W. Dingus, J. A. Esposito, C. E. Fichtel and C. E. Hartman *et al.*, Astrophys. J. **481**, 205 (1997).

[156] A. W. Strong ans J. R. Mattox, Astronomy and Astrophysics **308**, 21 (1996)

[157] K. M. Ferriere, Rev. Mod. Phys. **73**, 1031 (2001) [astro-ph/0106359].

[158] GALPROP's website.

[159] C. Evoli, D. Gaggero, D. Grasso and L. Maccione, JCAP **0810** (2008) 018 [arXiv:0807.4730 [astro-ph]]. D. Gaggero, L. Maccione, G. Di Bernardo, C. Evoli and D. Grasso, Phys. Rev. Lett. **111** (2013) 2, 021102 [arXiv:1304.6718 [astro-ph.HE]]. DRAGON's website.

[160] D. Maurin, 12th ICATPP Conference

[161] D. Maurin, F. Donato, R. Taillet and P. Salati, Astrophys. J. **555**, 585 (2001) [astro-ph/0101231].

[162] I. V. Moskalenko and A. W. Strong, Astrophys. J. **493**, 694 (1998) [astro-ph/9710124].

[163] A. W. Strong and I. V. Moskalenko, Astrophys. J. **509**, 212 (1998) [astro-ph/9807150].

[164] T. Delahaye, R. Lineros, F. Donato, N. Fornengo and P. Salati, Phys. Rev. D 77 (2008) 063527 [arXiv:0712.2312].

[165] F. Donato, N. Fornengo, D. Maurin and P. Salati, Phys. Rev. D 69 (2004) 063501 [arXiv:astro-ph/0306207].

[166] J. J. Engelmann, P. Ferrando, A. Soutoul, P. Goret and E. Juliusson, Astron. Astrophys. **233**, 96 (1990).

[167] G. Di Bernardo, C. Evoli, D. Gaggero, D. Grasso and L. Maccione, JCAP **1303**, 036 (2013) [arXiv:1210.4546 [astro-ph.HE]].

[168] R. Trotta, G. Johannesson, I. V. Moskalenko, T. A. Porter, R. R. de Austri and A. W. Strong, Astrophys. J. **729**, 106 (2011) [arXiv:1011.0037 [astro-ph.HE]].

[169] M. Ackermann *et al.* [Fermi-LAT Collaboration], Astrophys. J. **761** (2012) 91 [arXiv:1205.6474 [astro-ph.CO]].

[170] J. Lavalle, D. Maurin and A. Putze, Phys. Rev. D **90**, 081301 (2014) [arXiv:1407.2540 [astro-ph.HE]].

[171] C. Evoli, I. Cholis, D. Grasso, L. Maccione and P. Ullio, Phys. Rev. D **85** (2012) 123511 [arXiv:1108.0664 [astro-ph.HE]].

[172] T. Bringmann, F. Donato and R. A. Lineros, JCAP **1201** (2012) 049 [arXiv:1106.4821 [astro-ph.GA]].

[173] E. Orlando and A. Strong, arXiv:1309.2947 [astro-ph.GA].

[174] N. Fornengo, R. A. Lineros, M. Regis and M. Taoso, JCAP **1404** (2014) 008 [arXiv:1402.2218 [astro-ph.CO]].

[175] E.C. Stones, A.C. Cummings, F.B. McDonald, B.C. Heikkila, N. Lal, W.R. Webber Science **309**, 2017 (2005)

[176] E.C. Stones, A.C. Cummings, F.B. McDonald, B.C. Heikkila, N. Lal, W.R. Webber, Nature **454**, 71 (2008)

[177] K. Scherer, H. Fichtner, E. Marsch, Copernicus Gesellschaft e. V., Katlenburg-Lindau (2000)

[178] H. Moraal, Space Sci. Rev. **176**, 299 (2013).

[179] E.N. Parker, Planet. Space Sci. **13**, 9 (1965)

[180] J. R. Jokipii, H. Levy and W.B. Hubbard Astrophys. J. **213**, 861 (1977).

[181] M. S. Potgieter, E. E. Vos, M. Boezio, N. De Simone, V. Di Felice and V. Formato, Solar Phys. **289**, 391 (2014) [arXiv:1302.1284 [astro-ph.SR]].

[182] L. Maccione, Phys. Rev. Lett. **110**, no. 8, 081101 (2013) [arXiv:1211.6905 [astro-ph.HE]].

[183] J. P. Roberts, arXiv:1211.0691 [astro-ph.HE].

[184] M. Potgieter, Living Rev. Solar Phys. **10**, 3 (2013) [arXiv:1306.4421 [physics.space-ph]].

[185] M. S. Potgieter ?ICRC July 2013 (icrc2013-0119)

[186] L. J. Gleeson and W. I. Axford, Astrophys. J. **154**, 1011 (1968).

[187] R. A. Caballero-Lopez and H. Moraal, Journal of Geophysical Research: Space Physics **109**, 2156 (2004).

[188] L. J. Gleeson and I. H. Urch, Astrophysics and Space Science **25**, 387 (1973).

[189] L. J. Gleeson and I. H. Urch, Astrophysics and Space Science **11**, 288 (1971).

[190] L. A. Fisk, J. Geophys. Res **76**, 221 (1971).

[191] M. N. Mazziotta and F. Loparco, arXiv:1302.5359 [astro-ph.HE].

[192] I. G. Usoskin, G. A. Kovaltsov, O. Adriani, G. C. Barbarino, G. A. Bazilevskaya, R. Bellotti, M. Boezio and E. A. Bogomolov *et al.*, Adv. Space Res. **55**, 2940 (2015).

[193] O. Adriani, G. C. Barbarino, G. A. Bazilevskaya, R. Bellotti, M. Boezio, E. A. Bogomolov, M. Bongi and V. Bonvicini *et al.*, Astrophys. J. **765**, 91 (2013) [arXiv:1301.4108 [astro-ph.HE]].

[194] D. Gaggero, D. Grasso, L. Maccione, G. Di Bernardo and C. Evoli, Phys. Rev. D **89**, 083007 (2014) [arXiv:1311.5575 [astro-ph.HE]].

[195] R. D. Strauss, M. S. Potgieter and S. E. S. Ferreira, Adv. Space Res. **49** (2012) 392.

[196] D. Gaggero, private communications.

[197] J. Silk, M. Srednicki, Phys. Rev. Lett. 53 (1984) 624.

[198] M. Cirelli, M. Kadastik, M. Raidal and A. Strumia, Nucl. Phys. B 813 (2009) 1 [Addendum-ibid. B 873 (2013) 530] [arXiv:0809.2409 [hep-ph]].

F. Donato, D. Maurin, P. Brun, T. Delahaye and P. Salati, Phys. Rev. Lett. 102 (2009) 071301 [arXiv:0810.5292 [astro-ph]].

M. Garny, A. Ibarra and S. Vogl, JCAP 1107 (2011) 028 [arXiv:1105.5367 [hep-ph]].

X. Chu, T. Hambye, T. Scarna and M. H. G. Tytgat, Phys. Rev. D 86 (2012) 083521 [arXiv:1206.2279 [hep-ph]].

G. Belanger, C. Boehm, M. Cirelli, J. Da Silva and A. Pukhov, JCAP 1211 (2012) 028 [arXiv:1208.5009 [hep-ph]].

N. Fornengo, L. Maccione and A. Vittino, JCAP 1404 (2014) 003 [arXiv:1312.3579 [hep-ph]].

V. Pettorino, G. Busoni, A. De Simone, E. Morgante, A. Riotto and W. Xue, arXiv:1406.5377 [hep-ph].

J. A. R. Cembranos, V. Gammaldi and A. L. Maroto, arXiv:1410.6689 [astro-ph.HE].

A. Urbano and W. Xue, arXiv:1412.3798 [hep-ph].

[199] T. Bringmann, M. Vollmann and C. Weniger, Phys. Rev. D **90** (2014) 123001 [arXiv:1406.6027 [astro-ph.HE]].

[200] Ya.B. Zeldovich, A.A. Klypin, M.Yu. Khlopov and V.M. Chechetkin Yadernaya Fizika (1980) V. 31, PP. 1286-1294. [English translation: Sov.J.Nucl.Phys. (1980) V.31, PP. 664-669]. V.M. Chechetkin, M.G. Sapozhnikov, M.Yu. Khlopov and Ya.B. Zeldovich, Phys. Lett. (1982), V. 118B, PP. 359-362. V.M. Chechetkin, M.Yu. Khlopov and M.G. Sapozhnikov, Rivista Nuovo Cimento (1982) , V. 5, N-10, PP. 1-80.

[201] D. G. Cerdeno, T. Delahaye and J. Lavalle, Nucl. Phys. B **854** (2012) 738 [arXiv:1108.1128 [hep-ph]].

[202] T. Delahaye and M. Grefe, JCAP **1312** (2013) 045 [arXiv:1305.7183 [hep-ph]].

[203] G. Belanger, C. Boehm, M. Cirelli, J. Da Silva and A. Pukhov, arXiv:1208.5009 [hep-ph].

[204] T. Bringmann and P. Salati, Phys. Rev. D **75** (2007) 083006 [astro-ph/0612514].

[205] P. Blasi and P. D. Serpico, Phys. Rev. Lett. **103** (2009) 081103 [arXiv:0904.0871 [astro-ph.HE]].

[206] P. Blasi, E. Amato and P. D. Serpico, Phys. Rev. Lett. **109** (2012) 061101 [arXiv:1207.3706 [astro-ph.HE]].

[207] F. Donato and P. D. Serpico, Phys. Rev. D **83** (2011) 023014 [arXiv:1010.5679 [astro-ph.HE]].

[208] P. Ciafaloni, D. Comelli, A. Riotto, F. Sala, A. Strumia and A. Urbano, JCAP **1103** (2011) 019 [arXiv:1009.0224 [hep-ph]].

[209] M. Ackermann *et al.* [Fermi-LAT Collaboration], Phys. Rev. Lett. **107** (2011) 241302 [arXiv:1108.3546 [astro-ph.HE]].

[210] A. Geringer-Sameth and S. M. Koushiappas, Phys. Rev. Lett. **107** (2011) 241303 [arXiv:1108.2914 [astro-ph.CO]].

[211] M. Cirelli, E. Moulin, P. Panci, P. D. Serpico and A. Viana, Phys. Rev. D **86** (2012) 083506 [arXiv:1205.5283 [astro-ph.CO]].

[212] S. Ting, talk at SpacePart12.

[213] M. Pato, D. Hooper and M. Simet, JCAP **1006** (2010) 022 [arXiv:1002.3341 [astro-ph.HE]].

[214] V. Choutko, Nucl. Phys. B (Proc.Suppl.) **113** (2002) 170-176.

[215] A. G. Malinin [AMS Collaboration], Phys. Atom. Nucl. **67**, 2044 (2004).

[216] L. C. Tan, L. K. Ng, Phys. Rev. D 26 (1982) 1179.

[217] L. C. Tan and L. K. Ng, Nucl. Phys. B 9 (1983) 227.

[218] F. Donato, D. Maurin, P. Salati, A. Barrau, G. Boudoul and R. Taillet, Astrophys. J. 563 (2001) 172 [astro-ph/0103150].

[219] K. Mannheim and R. Schlickeiser, Astron. Astrophys. **286**, 983 (1994) [astro-ph/9402042].

[220] L. Bergström, J. Edsjö and P. Ullio, Astrophys. J. 526 (1999) 215 [arXiv:astro-ph/9902012].

[221] O. Adriani *et al.* [PAMELA Collaboration], Science **332**, 69 (2011) [arXiv:1103.4055 [astro-ph.HE]].

[222] Timur Delahaye, private communication.

[223] I. Yusifov and I. Küçük, Astron. Astrophys. 422 (2004) 545 [astro-ph/0405559].

[224] G. Bernard, T. Delahaye, P. Salati and R. Taillet, Astron. Astrophys. 544 (2012) A92 [arXiv:1204.6289 [astro-ph.HE]].

[225] M. di Mauro, F. Donato, A. Goudelis and P. D. Serpico, arXiv:1408.0288 [hep-ph].

[226] H. Fischer, et al. [NA49 Collaboration], Heavy Ion Phys. 17 (2003) 369.

[227] R. Kappl, M. W. Winkler, arXiv:1408.0299 [hep-ph].

[228] D. Hooper, T. Linden and P. Mertsch, arXiv: 1410.1527 [astro-ph.HE].

[229] I. V. Moskalenko, A. W. Strong, J. F. Ormes and M. S. Potgieter, Astrophys. J. 565 (2002) 280 [astro-ph/0106567].

G. Di Bernardo, C. Evoli, D. Gaggero, D. Grasso and L. Maccione, Astropart. Phys. 34 (2010) 274 [arXiv:0909.4548 [astro-ph.HE]].

H. B. Jin, Y. L. Wu and Y. F. Zhou, arXiv:1410.0171 [hep-ph].

[230] C. Evoli, I. Cholis, D. Grasso, L. Maccione and P. Ullio, Phys. Rev. D 85 (2012) 123511 [arXiv:1108.0664 [astro-ph.HE]].

G. Di Bernardo, C. Evoli, D. Gaggero, D. Grasso and L. Maccione, Astropart. Phys. 34 (2010) 274 [arXiv:0909.4548 [astro-ph.HE]].

F. Donato, N. Fornengo and D. Maurin, Phys. Rev. D 78 (2008) 043506 [arXiv:0803.2640 [hep-ph]].

[231] D. Gaggero, A. Urbano, M. Valli and P. Ullio, arXiv:1411.7623 [astro-ph.HE].

[232] T. Bringmann, M. Vollmann and C. Weniger, arXiv:1406.6027 [astro-ph.HE].

[233] See e.g. the talk by Anderson at the Fermi Symposium 2014, Nagoya, Japan.

[234] M. Aguilar *et al.* [AMS Collaboration], Phys. Rev. Lett. **110**, no. 14, 141102 (2013).

[235] L. Accardo *et al.* [AMS Collaboration], Phys. Rev. Lett. **113** (2014) 121101.

[236] O. Adriani, G. C. Barbarino, G. A. Bazilevskaya, R. Bellotti, M. Boezio, E. A. Bogomolov, L. Bonechi and M. Bongi *et al.*, Astropart. Phys. **34** (2010) 1 [arXiv:1001.3522 [astro-ph.HE]].

[237] M. Ackermann *et al.* [Fermi LAT Collaboration], Phys. Rev. Lett. **108** (2012) 011103 [arXiv:1109.0521 [astro-ph.HE]].

[238] M. Aguilar *et al.* [AMS Collaboration], Phys. Rev. Lett. **113** (2014) 221102.

[239] M. Aguilar *et al.* [AMS Collaboration], Phys. Rev. Lett. **113** (2014) 121102.

[240] M. Cirelli, Pramana **79** (2012) 1021 [arXiv:1202.1454 [hep-ph]].

[241] P. D. Serpico, Astropart. Phys. **39-40**, 2 (2012) [arXiv:1108.4827 [astro-ph.HE]].

[242] M. Boudaud, S. Aupetit, S. Caroff, A. Putze, G. Belanger, Y. Genolini, C. Goy and V. Poireau *et al.*, Astron. Astrophys. 575, A67 (2015) [arXiv:1410.3799 [astro-ph.HE]].

[243] AMS-02 Collaboration, Talks at the 'AMS Days at CERN', 15-17 april 2015.

[244] M. Aguilar [AMS Collaboration], Phys. Rev. Lett. **114**, no. 17, 171103 (2015).

[245] R. P. Duperray, C.-Y. Huang, K. V. Protasov and M. Buenerd, Phys. Rev. D **68**, 094017 (2003) [astro-ph/0305274].

[246] C. Evoli, D. Gaggero and D. Grasso, arXiv:1504.05175 [astro-ph.HE].

[247] V. Pettorino, G. Busoni, A. De Simone, E. Morgante, A. Riotto and W. Xue, JCAP **1410** (2014) 10, 078 [arXiv:1406.5377 [hep-ph]].

[248] R. Aloisio, P. Blasi and A. V. Olinto, JCAP **0405** (2004) 007 [astro-ph/0402588]. G. Bertone, E. Nezri, J. Orloff and J. Silk, Phys. Rev. D **70** (2004) 063503 [astro-ph/0403322]. M. Regis and P. Ullio, Phys. Rev. D **78** (2008) 043505 [arXiv:0802.0234 [hep-ph]]. G. Bertone, M. Cirelli, A. Strumia and M. Taoso, JCAP **0903** (2009) 009 [arXiv:0811.3744 [astro-ph]]. L. Bergstrom, G. Bertone, T. Bringmann, J. Edsjo and M. Taoso, Phys. Rev. D **79** (2009) 081303 [arXiv:0812.3895 [astro-ph]]. R. M. Crocker, N. F. Bell, C. Balazs and D. I. Jones, Phys. Rev. D **81** (2010) 063516 [arXiv:1002.0229 [hep-ph]]. C. Boehm, J. Silk and T. Ensslin, arXiv:1008.5175 [astro-ph.GA]. I. Cholis, D. Hooper and T. Linden, arXiv:1408.6224 [astro-ph.HE].

[249] P. Blasi, A. V. Olinto and C. Tyler, Astropart. Phys. **18** (2003) 649 [astro-ph/0202049].

[250] N. Fornengo, R. A. Lineros, M. Regis and M. Taoso, JCAP **1201** (2012) 005 [arXiv:1110.4337 [astro-ph.GA]].

[251] E. Borriello, A. Cuoco and G. Miele, Phys. Rev. D **79** (2009) 023518 [arXiv:0809.2990 [astro-ph]].

[252] E. Borriello, A. Cuoco and G. Miele, Nucl. Phys. Proc. Suppl. **190** (2009) 185 [arXiv:0812.2932 [astro-ph]].

[253] T. Delahaye, C. Boehm and J. Silk, Mon. Not. Roy. Astron. Soc. Lett. **422** (2012) L16 [arXiv:1105.4689 [astro-ph.GA]].

[254] T. Linden, D. Hooper and F. Yusef-Zadeh, Astrophys. J. **741** (2011) 95 [arXiv:1106.5493 [astro-ph.HE]].

[255] Y. Mambrini, M. H. G. Tytgat, G. Zaharijas and B. Zaldivar, JCAP **1211** (2012) 038 [arXiv:1206.2352 [hep-ph]].

[256] N. Fornengo, R. Lineros, M. Regis and M. Taoso, Phys. Rev. Lett. **107** (2011) 271302 [arXiv:1108.0569 [hep-ph]].

[257] N. Fornengo, R. Lineros, M. Regis and M. Taoso, JCAP **1203** (2012) 033 [arXiv:1112.4517 [astro-ph.CO]].

[258] D. Hooper, A. V. Belikov, T. E. Jeltema, T. Linden, S. Profumo and T. R. Slatyer, Phys. Rev. D **86** (2012) 103003 [arXiv:1203.3547 [astro-ph.CO]].

[259] E. Carlson, D. Hooper, T. Linden and S. Profumo, JCAP **1307** (2013) 026 [arXiv:1212.5747 [astro-ph.CO]].

[260] M. Cirelli, P. D. Serpico and G. Zaharijas, JCAP **1311** (2013) 035 [arXiv:1307.7152].

[261] K. N. Abazajian, N. Canac, S. Horiuchi and M. Kaplinghat, Phys. Rev. D **90** (2014) 2, 023526 [arXiv:1402.4090 [astro-ph.HE]].

[262] T. Daylan, D. P. Finkbeiner, D. Hooper, T. Linden, S. K. N. Portillo, N. L. Rodd and T. R. Slatyer, arXiv:1402.6703 [astro-ph.HE].

[263] T. Lacroix, C. Boehm and J. Silk, arXiv:1403.1987 [astro-ph.HE].

[264] K. N. Abazajian, N. Canac, S. Horiuchi, M. Kaplinghat and A. Kwa, arXiv:1410.6168 [astro-ph.HE].

[265] D. Eichler and I. Maor, astro-ph/0501096.

[266] I. Cholis, G. Dobler, D. P. Finkbeiner, L. Goodenough and N. Weiner, Phys. Rev. D **80** (2009) 123518 [arXiv:0811.3641 [astro-ph]].

[267] J. Zhang, X. J. Bi, J. Liu, S. M. Liu, P. F. Yin, Q. Yuan and S. H. Zhu, Phys. Rev. D **80** (2009) 023007 [arXiv:0812.0522 [astro-ph]].

[268] E. Borriello, A. Cuoco and G. Miele, Astrophys. J. **699** (2009) L59 [arXiv:0903.1852 [astro-ph.GA]].

[269] V. Barger, Y. Gao, W. Y. Keung, D. Marfatia and G. Shaughnessy, Phys. Lett. B **678** (2009) 283 [arXiv:0904.2001 [hep-ph]].

[270] M. Cirelli and P. Panci, Nucl. Phys. B **821** (2009) 399 [arXiv:0904.3830 [astro-ph.CO]].

[271] P. Baratella, M. Cirelli, A. Hektor, J. Pata, M. Piibeleht and A. Strumia, JCAP **1403** (2014) 053 [arXiv:1312.6408 [hep-ph]].

[272] R. Beck, AIP Conf. Proc. **1381**, 117 (2011) [arXiv:1104.3749 [astro-ph.CO]].

[273] R. Jansson, G. R. Farrar, A. H. Waelkens and T. A. Ensslin, JCAP **0907** (2009) 021 [arXiv:0905.2228 [astro-ph.GA]].

[274] M. S. Pshirkov, P. G. Tinyakov, P. P. Kronberg and K. J. Newton-McGee, Astrophys. J. **738** (2011) 192 [arXiv:1103.0814 [astro-ph.GA]].

[275] R. Beck and R. Wielebinski, in 'Planets, Stars and Stellar Systems. Volume 5: Galactic Structure and Stellar Populations', ed. T.D. Oswalt, G. Gilmore, Springer (2013), [arXiv:1302.5663 [astro-ph.GA]].

[276] X.Sun, W.Reich, A.Waelkens, T.Enßling, A&A **477**, 573 (2008) [arXiv:0711.1572 [astro-ph]].

[277] R. Jansson and G. R. Farrar, Astrophys. J. **761** (2012) L11 arXiv:1210.7820 [astro-ph.GA].

[278] R. Jansson and G. R. Farrar, Astrophys. J. **757** (2012) 14 [arXiv:1204.3662 [astro-ph.GA]].

[279] X. Sun and W. Reich, Res. Astron. Astrophys. **10** (2010) 1287 [arXiv:1010.4394 [astro-ph.GA]].

[280] A. W. Strong, I. V. Moskalenko and O. Reimer, Astrophys. J. **537**, 763 (2000) [Erratum-ibid. **541**, 1109 (2000)] [astro-ph/9811296].

[281] J.L. Han, R.N. Manchester, A.G. Lyne, G.J. Qiao and W. van Straten, Astrophys. J. **642**, 868 (2006) [astro-ph/0601357].

[282] A.W. Strong, E. Orlando and T.R. Jaffe, Astron. Astrophys. **534**, A54 (2011) [arXiv:1108.4822 [astro-ph.HE]].

[283] The files are available on GALPROP's website. As discussed in A. E. Vladimirov, S. W. Digel, G. Johannesson, P. F. Michelson, I. V. Moskalenko, P. L. Nolan, E. Orlando and T. A. Porter *et al.*, Comput. Phys. Commun. **182** (2011) 1156 [arXiv:1008.3642 [astro-ph.HE]], the newest files are based on calculations using the FRANKIE code (Fast Radiation transport Numerical Kode for Interstellar Emission), described in T. A. Porter, I. V. Moskalenko, A. W. Strong, E. Orlando and L. Bouchet, Astrophys. J. **682** (2008) 400 [arXiv:0804.1774 [astro-ph]].

[284] I. Moskalenko, A. Strong, J. Ormes, M. Potgieter, Astrophys. J. **565** (2002) 280 [astro-ph/0106567].

[285] www.marcocirelli.net/PPPC4DMID.html

[286] G. R. Blumenthal and R. J. Gould, Rev. Mod. Phys. **42** (1970) 237.

[287] Reinhard Schlickeiser, 'Cosmic ray astrophysics', Springer, 2002.

[288] C. Evoli, D. Gaggero, D. Grasso and L. Maccione, Phys. Rev. Lett. **108** (2012) 211102F [arXiv:1203.0570 [astro-ph.HE]].

[289] [Fermi-LAT Collaboration], Astrophys. J. **750** (2012) 3 [arXiv:1202.4039 [astro-ph.HE]].

[290] L. Goodenough and D. Hooper, arXiv:0910.2998 [hep-ph].

D. Hooper and L. Goodenough, Phys. Lett. B **697** (2011) 412 [arXiv:1010.2752 [hep-ph]].

D. Hooper and T. Linden, Phys. Rev. D **84** (2011) 123005 [arXiv:1110.0006 [astro-ph.HE]].

D. Hooper, Phys. Dark Univ. **1** (2012) 1 [arXiv:1201.1303 [astro-ph.CO]].

K. N. Abazajian and M. Kaplinghat, Phys. Rev. D **86** (2012) 083511 [arXiv:1207.6047 [astro-ph.HE]].

D. Hooper and T. R. Slatyer, Phys. Dark Univ. **2** (2013) 118 [arXiv:1302.6589 [astro-ph.HE]].

C. Gordon and O. Macias, Phys. Rev. D **88** (2013) 083521 [arXiv:1306.5725 [astro-ph.HE]].

W.-C. Huang, A. Urbano and W. Xue, arXiv:1307.6862 [hep-ph].

V. Vitale *et al.* [Fermi/LAT Collaboration], arXiv:0912.3828 [astro-ph.HE].

[291] W.-C. Huang, A. Urbano and W. Xue, JCAP **1404** (2014) 020 [arXiv:1310.7609 [hep-ph]].

C. Boehm, M. J. Dolan, C. McCabe, M. Spannowsky and C. J. Wallace, JCAP **1405** (2014) 009 [arXiv:1401.6458 [hep-ph]].

A. Hektor and L. Marzola, arXiv:1403.3401 [hep-ph].

A. Alves, S. Profumo, F. S. Queiroz and W. Shepherd, arXiv:1403.5027 [hep-ph].

A. Berlin, D. Hooper and S. D. McDermott, arXiv:1404.0022 [hep-ph].

P. Agrawal, B. Batell, D. Hooper and T. Lin, arXiv:1404.1373 [hep-ph].

E. Izaguirre, G. Krnjaic and B. Shuve, arXiv:1404.2018 [hep-ph].

S. Ipek, D. McKeen and A. E. Nelson, arXiv:1404.3716 [hep-ph].

C. Boehm, M. J. Dolan and C. McCabe, arXiv:1404.4977 [hep-ph].

P. Ko, W.-I. Park and Y. Tang, arXiv:1404.5257 [hep-ph].

M. Abdullah, A. DiFranzo, A. Rajaraman, T. M. P. Tait, P. Tanedo and A. M. Wijangco, arXiv:1404.6528 [hep-ph].

A. Martin, J. Shelton and J. Unwin, arXiv:1405.0272 [hep-ph].

T. Basak and T. Mondal, arXiv:1405.4877 [hep-ph].

C. Cheung, M. Papucci, D. Sanford, N. R. Shah and K. M. Zurek, arXiv:1406.6372 [hep-ph].

[292] C. Boehm, P. Gondolo, P. Jean, T. Lacroix, C. Norman and J. Silk, arXiv:1406.4683 [astro-ph.HE].

C. Arina, E. Del Nobile and P. Panci, arXiv:1406.5542 [hep-ph].

[293] K. N. Abazajian, JCAP **1103** (2011) 010 [arXiv:1011.4275 [astro-ph.HE]].

D. Hooper, I. Cholis, T. Linden, J. Siegal-Gaskins and T. Slatyer, Phys. Rev. D **88** (2013) 083009 [arXiv:1305.0830 [astro-ph.HE]].

Q. Yuan and B. Zhang, arXiv:1404.2318 [astro-ph.HE].

[294] A. Boyarsky, D. Malyshev and O. Ruchayskiy, Phys. Lett. B **705** (2011) 165 [arXiv:1012.5839 [hep-ph]].

[295] J. Petrovic, P. D. Serpico and G. Zaharijas, arXiv:1405.7928 [astro-ph.HE].

[296] E. Carlson and S. Profumo, arXiv:1405.7685 [astro-ph.HE].

[297] O. Adriani, G. A. Bazilevskaya, G. C. Barbarino, R. Bellotti, M. Boezio, E. A. Bogomolov, V. Bonvicini and M. Bongi *et al.*, JETP Lett. **96** (2013) 621 [Pisma Zh. Eksp. Teor. Fiz. **96** (2012) 693].

[298] T. Slatyer, private communication.

[299] M. Kachelriess, P. D. Serpico and M. A. .Solberg, Phys. Rev. D **80**, 123533 (2009) [arXiv:0911.0001 [hep-ph]].

[300] P. Ciafaloni and A. Urbano, Phys. Rev. D **82** (2010) 043512 [arXiv:1001.3950 [hep-ph]].

[301] Usoskin, I. G., G. A. Bazilevskaya, and G. A. Kovaltsov (2011), J. Geophys. Res., 116, A02104.